FABRICATION AND CHARACTERIZATION OF NANOSTRUCTURED CERAMIC THIN FILMS FROM SINGLE SOURCE AND MIXED MOLECULAR PRECURSORS

MUHAMMAD ALI EHSAN

A THESIS SUBMITTED IN FULFILLMENT OF THE REQUIREMENT FOR THE DEGREE OF DOCTOR OF PHILOSOPHY

DEPARTMENT OF CHEMISTRY
FACULTY OF SCIENCE
UNIVERSITY OF MALAYA
KUALA LUMPUR
2014

UNIVERSITI MALAYA

ORIGINAL LITERARY WORK DECLARATION

Name of Candidate: **Muhammad Ali Ehsan**

Registration/Matric No: **SHC100080**

Name of Degree: **Doctor of Philosophy (Ph.D.)**

Title of Project Paper/Research Report/Dissertation/Thesis ("this Work"): **Fabrication and Characterization of Nanostructured Ceramic Thin Films from Single Source and Mixed Molecular Precursors**
Field of Study: **Inorganic Chemistry**

I do solemnly and sincerely declare that:

(1) I am the sole author/writer of this Work;
(2) This Work is original;
(3) Any use of any work in which copyright exists was done by way of fair dealing and for permitted purposes and any excerpt or extract from, or reference to or reproduction of any copyright work has been disclosed expressly and sufficiently and the title of the Work and its authorship have been acknowledged in this Work;
(4) I do not have any actual knowledge nor do I ought reasonably to know that the making of this work constitutes an infringement of any copyright work;
(5) I hereby assign all and every rights in the copyright to this Work to the University of Malaya ("UM"), who henceforth shall be owner of the copyright in this Work and that any reproduction or use in any form or by any means whatsoever is prohibited without the written consent of UM having been first had and obtained;
(6) I am fully aware that if in the course of making this Work I have infringed any copyright whether intentionally or otherwise, I may be subject to legal action or any other action as may be determined by UM.

Candidate's Signature Date

Subscribed and solemnly declared before,

Witness's Signature Date

Name: **Dr. Muhammad Mazhar**

Designation: **Professor**

Abstract

This work describes some general procedures for the preparation and characterization of heterobimetallic complexes $[Fe_2Ti_4(\mu\text{-}O)_6(TFA)_8(THF)_6]$ (**1**), $[Co_2Ti(\mu_3\text{-}O)(TFA)_6(THF)_3]$ (**2**) and a series of metal dithiocarbamate $[Bi(S_2CNEt_2)_3]_2$ (**3**), $[In(S_2CNCy_2)_3]\bullet 2py$ (**4**), $[In(S_2CN(^{i}Pr)_2)_3]\bullet 1.5py$ (**5**), $[In(S_2CPip)_3]\bullet 0.5py$ (**6**), $[In(S_2CNBzMe)_3]$ (**7**), $[Ag_4\{S_2CNEt_2\}_3(py)_2]_n\cdot nNO_3\cdot 2nH_2O$ (**8**), $[Cd(S_2CNCy_2)_2(py)]$ (**9**), $[Zn(S_2CNCy_2)_2(py)]$ (**10**), $[Zn(S_2CNBzMe)_2(py)]$ (**11**), $[Pd(S_2CNBz_2)_2]\bullet py$ (**12**) $[Pd(S_2CNCy_2)_2]\bullet py$ (**13**), $[Pd(S_2CN^{n}Hex_2)_2]$ (**14**), $[Pd(S_2CNCyMe)_2]$ (**15**) and their disposal for the growth of thin films of ceramic oxide composites and metal sulphides. The physical properties of these complexes have been studied by means of fusion point determination, microanalysis, Fourier transform infrared spectrophotometry (FTIR) and proton nuclear magnetic resonance (^{1}H-NMR) spectroscopy, X-ray single crystal and thermogravimetric and derivative thermogravimetric (TG/DTG) analyses. Thermogravimetric studies prove that all the complexes (**1**)-(**15**) undergo facile thermal decomposition at relatively low temperature and are well suited single source precursors for the fabrication of ceramic oxide and sulphide thin films by aerosol assisted chemical vapour deposition. The particle size, phases and crystallinity of the deposited films were determined by X-ray power diffraction (XRPD) while scanning electron microscopy (SEM) and energy dispersive X-ray (EDX) spectrometry were used for investigating the surface morphologies, crystallite size, shape and elemental compositions.

XRPD and EDX analyses revealed the formation of impurity free composite oxides Fe_2TiO_5-TiO_2 and $CoTiO_3$-CoO films at relatively low temperature of 500 °C on glass substrate from precursors (**1**) and (**2**) respectively. SEM results showed that fabricated films are crack free, crystalline and possess nanosized features with clear boundaries and architectures.

Single source metal dithiocarbamate precursors (**3**), (**4**)-(**7**), (**8**), (**9**), (**10**)-(**11**) and (**12**)-(**15**) have been found suitable for deposition of Bi_2S_3, β-In_2S_3, Ag_2S, CdS, ZnS and PdS thin films on fluorine doped tin oxide (FTO) coated conducting glass substrate at temperature range of 300-500 °C and the energy bandgaps (E_g) of the Bi_2S_3, β-In_2S_3, Ag_2S, CdS, ZnS and PdS thin films determined from UV-Vis spectrophotometry are valued at 1.80, 2.20, 1.05, 2.40, 3.40 and 1.70 eV, respectively, indicating the direct band gap nature of the metal sulphide materials.

The photoelectrochemical (PEC) characteristics of the Bi_2S_3, β-In_2S_3, CdS, ZnS, PdS and Ag_2S thin films electrodes measured from photocurrent potential plot recorded under Air Mass 1.5G illuminations exhibit anodic photocurrent densities of 1.90, 1.25, 1.20, 8.0×10^{-3} and 4.0×10^{-3} , 0.22, mA/cm^2 at 0.23 and 0.0 V vs. Ag/AgCl, respectively. The photoelectrochemical performances indicate that the newly synthesised precursors are highly advantageous in fabricating metal sulphide electrodes for solar energy harvesting and optoelectronic application.

Abstrak

Kerja penyelidikan ini menerangkan sintesis beberapa oksida heterodwilogam, $[Fe_2Ti_4(\mu\text{-}O)_6(TFA)_8(THF)_6]$ (**1**), $[Co_2Ti(\mu_3\text{-}O)(TFA)_6(THF)_3]$ (**2**) dan satu siri logam dithiokarbamat $[Bi(S_2CNEt_2)_3]_2$ (**3**), $[In(S_2CNCy_2)_3]\bullet 2py$ (**4**), $[In(S_2CN(^iPr)_2)_3]\bullet 1.5py$ (**5**), $[In(S_2CPip)_3]\bullet 0.5py$ (**6**), $[In(S_2CNBzMe)_3]$ (**7**), $[Ag_4\{S_2CNEt_2\}_3(py)_2]_n\cdot nNO_3\cdot 2nH_2O$ (**8**), $[Cd(S_2CNCy_2)_2(py)]$ (**9**), $[Zn(S_2CNCy_2)_2(py)]$ (**10**), $[Zn(S_2CNBzMe)_2(py)]$ (**11**), $[Pd(S_2CNBz_2)_2]\bullet py$ (**12**) $[Pd(S_2CNCy_2)_2]\bullet py$ (**13**), $[Pd(S_2CNHex_2)_2]$ (**14**) dan $[Pd(S_2CNCyMe)_2]$ (**15**) prakursor bagi penjanaan berfungsi oksida dan sulfida seramik bahan. Ciri-ciri fizikal kompleks ini telah dikaji melalui penentuan titik terlakur mikroanalisis , spektroskopi inframerah (IR) dan proton resonans magnetik nukleus (^1H - NMR) spektroskopi , sinar- X hablur tunggal dan analisis termogravimetri (TG / DTG). Kajian termogravimetri membuktikan bahawa kompleks (**1**)-(**15**) menjalani penguraian terma yang mudah diperolehi pada suhu yang rendah dan adalah prakursor sumber pemendapan wap kimia dibantu aerosol tunggal yang sesuai untuk pembikinan oksida seramik dan filem tipis sulfida. Fasa dan penghabluran bagi filem-filem yang terendap telah ditentukan oleh kuasa pembelauan sinar-X (PXRD) manakala mikroskop pengimbasan elektron (SEM) dan tenaga serakan sinar-X (EDX) telah digunakan untuk menyiasat morfologi permukaan dan komposisi unsur.

Analisis PXRD dan EDX mendedahkan pembentukan komposit oksida Fe_2TiO_5-TiO_2 dan filem $CoTiO_3$-CoO yang bebas bendasing pada substrat kaca daripada prakursor (1) dan (2) masing-masing. Keputusan SEM menunjukkan bahawa filem-filem yang terbikin adalah bebas retak berhablur dan mempunyai ciri-ciri saiz nano dengan sempadan dan seni bina yang jelas.

Prakursor sumber (**3**), (**4**) - (**7**), (**8**), (**9**), (**10**) - (**11**) dan (**12**) - (**15**) telah didapati sesuai bagi pemendapan filem tipis Bi_2S_3, β-In_2S_3 , Ag_2S, CdS, ZnS dan PdS keatas substrat

kaca bersalut timah oksida (FTO) didopkan fluorin yang dijalankan pada julat suhu 300-500 °C. Sifat- sifat filem tipis sulfida logam seperti darjah penghabluran, penentuan fasa, morfologi permukaan, komposisi dan jurang jalur optik telah diperiksa masing-masing menerusi PXRD, SEM, EDX dan UV-Vis spektroskopi. Tenaga ruang jalur langsung bagi filem tipis Bi2S3, β-In_2S_3, Ag_2S, CdS, ZnS dan PdS yang ditentukan melalui UV-Vis spektrofotometri bernilai 1.80, 2.20, 1.05, 2.40, 3.50 dan 1.70 eV masing-masing, menunjukkan sifat ruang jalur langsung bagi bahan-bahan logam sulfida.

Ciri-ciri photoelektrokimia (PEC) elektrod filem tipis logam sulfida diukur dengan plot potensi arusfoto yang direkodkan di bawah iluminasi Air Mass 1.5 mempamerkan ketumpatan anodik arusfoto 1.90, 1.25, 1.20, 8 $\times 10^{-3}$ dan 0.22, 4 $\times 10^{-3}$ mA/cm^2 pada 0.23 dan 0.0 V lawan Ag / AgCl untuk elektrod-elektrod Bi_2S_3, β-In_2S_3, CdS, ZnS, dan Ag_2S, PdS bagi prakursor (**3**), (**4**), (**9**), (**11**), (**13**) dan (**8**), (**13**) masing-masing. Prestasi photoelektrokimia menunjukkan bahawa prakursor yang baru disintesis amat berfaedah dalam pembikinan elektrod logam sulfida bagi penuaian tenaga solar dan aplikasi optoelektronik.

Dedication

In cherished and loving memories of the departed souls of my dearly beloved parents and to all those who martyred (Shuhada) in ruthless terrorist attacks in Pakistan.

(May Allah grant them eternal rest, (Ameen))

Acknowledgment

All praises, graces and thanks be to Almighty Allah (Subhanahu Wa Taalaa), The Owner and Giver of bountiful blessings and gifts. Prayers and peace of Allah be upon the Holy Prophet Hazrat Muhammad who designated *"The superiority of the learned over the devout is like that of the moon, on the night when it is full, over the rest of the stars".*

I am indebted to many people who have been instrumental in completion of this thesis and supported me with their cooperation and timely help.

Foremost, I wish to express my most heartfelt gratitude to my research supervisor, Dr. Muhammad Mazhar, Meritorious Professor for giving me the opportunity to pursue my doctoral degree with his group, for introducing to me the interesting research theme for the present work and for his indispensable expertise and wisdom, enlightening discussions, endless encouragement, admiringly placid manner to listen to my problems throughout the course of the completion of this research work.

I equally express my sincere gratitude to my co-supervisor Professor Zainudin Bin Arifin for providing support in preparation of various manuscripts for publications and for his unlimited moral and intellectual help at many steps in the last three years.

I am very grateful to all my respected teachers in school, during under graduation and masters and who have extended fruitful suggestions whenever needed.

I would like to extend my gratitude to the Chairman and all the Professors of the Chemistry Department for all the support granted to me throughout my program. I am also thankful to Professor Misni Misran and his research group for sharing the laboratory facilities in the beginning of my Ph.D. I am extremely thankful to Dr. K.M. Lo and Dr. Hamid Khaledi for the determination of molecular structures by single crystal X-ray technique. Also, My sincere thanks to Dr. Huang Nay Ming for his invaluable technical support with analytical measurements such as (XRD, SEM and EDX) which were vital for the success of my research project.

I am highly indebted to our foreign collaborators in UK, Professor Upul Wijayantha, Professor Vickie McKee, Loughborough University and Dr. Asif Ali Tahir, University of Exeter for their excellent feedback, valuable discussions, immense help and co-operation for material characterization.

Special thanks must go to my seniors in Pakistan, Dr. Mazhar Hamid, Dr. Qaisar Malik, Dr. Muhammad Sultan and Dr. Muhammad Faizan for being there unconditionally and for their constant encouragement throughout the Ph.D course. I will

forever be grateful to Dr. Zubair Ahmad at University of Malaya for showing his kindness and sympathy during my tough time.

I have many thanks for my fellows and friends for cooperation and providing enjoyable moments especially Mr. Muhammad Adil Mansoor, Mr. Farhan Dawood and Mr. Haris Rasheed.

I gratefully acknowledge the funding sources, High Impact Research (HIR) grant, University of Malaya Research Grant (UMRG) and Pakistan Science Foundation (PSF) that made my Ph.D work possible.

Finally, my deepest gratitude goes to my deceased parents for their unflagging love, numerous sacrifices and support throughout my life and their thoughts and prayers gave me strength and motivation with positive energy to prosper myself in the life. It is a great honour for me to appreciate the encouragement, generosity, patience and sense of sharing extended to me by my loving sisters and sweet brothers. This is a tribute to their affection, support and prayers which enabled me to complete this task. In the end, I acknowledge the role of those important characters whose names could not be displayed in the words but will always remain in my memories.

Muhammad Ali Ehsan

Table of Contents

List of Figures

List of Tables

List of Symbols and Abbreviations

AACVD	aerosol-assisted chemical vapor deposition
Å	Angstrom
acac	2,4-pentandionate
acacH	2,4-pentandione
ADPs	atomic displacement parameters
ALD	atomic layer deposition
Bz	benzyl
CBD	chemical bath deposition
CHN	carbon hydrogen nitrogen analysis
CVD	chemical vapour deposition
Cy	cyclohexyl
DMSO	dimethyl sulfoxide
Dmae	N,N-dimethylaminoethanolato
dmaeH	N,N-dimethylaminoethanol
EDX	energy dispersive X-ray spectroscopy
E_f	fermi energy
Et	ethyl
E_g	bandgap
e.g	exempli gratia
et al	et alia
etc	et cetra
eV	electron volt
FEG	field emission gun
FTO	fluorine doped tin oxide
GC	gas chromatography
Hfacac	hexafluoroacetylacetonate
^{i}Pr	isopropyl
ICDD	International center for diffraction data
KeV	kilo electron Volt

K	Kelvin
MBE	molecular beam epitaxy
mmol	milli mole
mL	milli liter
mp.	melting point
MS	mass spectrometry
MEMS	micro electromechanical systems
Me	methyl
NMR	nuclear magnetic resonance
OAc	acetate
PEC	photoelectrochemical
Ph	Phenyl
Pip	piperidine
PVD	physical vapour deposition
PXRD	powder X-ray diffraction
Py	pyridine
PZT	lead zirconate titanate
SEM	scanning electron microscopy
SOFC	solid oxide fuel cell
T_C	Curie temperature
TN	Neel temperature
TFA	trifluoroacetic acid
THF	tetrahydrofuran
TGA	thermogravimetry analysis
TMS	trimethylsilane
MOCVD	metal-organic chemical vapour deposition
LPCVD	low-pressure chemical vapour deposition
SSP	single source precursors
UV/Vis	ultra violet/ visible
WDS	wavelength dispersive X-ray

List of Appendices

Preface

The thesis “Fabrication and characterization of nanostructured ceramic thin films from single source and mixed molecular precursors” is divided into five different chapters. Chapter 1 highlights the importance of our synthetic strategy towards the development of the nano-engineered functional ceramic thin films.

Chapter 2 provides a background to ceramics with specific details given to advanced functional ceramic and examines the fabrication technologies used for the development of nanostructured ceramic thin films as well as the concepts of Aerosol- Assisted Chemical Vapour Deposition (CVD). A detailed history of design, preparation, characterization and usage of single source heterobimetallic oxides and classes of metal sulphide precursors for the deposition of relevant material thin films have been described.

The materials used and methods adopted have been given in Chapter 3. This chapter presents our synthetic procedures and physico-chemical methods used for characterization of bimetallic cobalt-titanium, iron-titanium oxides and bismuth, indium, silver, cadmium, zinc and palladium dithiocarbamate precursors and subsequent utilization in AACVD trials to fabricate functional material thin films and their investigations by sophisticated analytical techniques.

Chapter 4 is divided into eight sections. The initial two sections deal with discussion on the chemistry of bimetallic precursors and their conversion to composite oxide thin films. A discussion of each bimetallic precursor and the resultant composite oxide material has been treated individually. The remaining sections elaborate the synthetic chemistry of metal dithiocarbamate and their disposal for deposition of metal sulphide thin films with special reference to their optical and photoelectrochemical properties. A discussion of each precursor and corresponding metal sulphide has been described separately because of large variation in their characteristics. At the end of the thesis, conclusions regarding this research work have been given in Chapter 5 that also includes recommendations for further research.

CHAPTER 1

INTRODUCTION

The development of innovative strategies for the fabrication of nanostructured ceramic films and coatings centers on nanoclusters, nanowires, nanorods and nanotubes because of their potential applications in the field of science and technology. Nanocrystalline advanced functional ceramics display enormous and unique dielectric, ferroelectric, piezoelectric, pyroelectric, ferromagnetic, magnetoresistive, ionical, electronical, superconducting, electro-optical, and gas-sensing properties (Khalil, 2012) as a result of the very high fraction of atoms that reside in the grain boundaries when sizes reduce to nanometer scale. Such superior combinations of properties are fundamental to the development of smart and functional material thin films which are attractive candidate for optics, optoelectronics, magnetism, catalysis, biomedicines, next generation computer memories, gate dielectric layers, infrared detectors, optical wave guiders, electro-optic storages and environmental applications (Goel, 2004; Ramesh, 2001). To meet the criteria of such sophisticated and advanced technological applications, functional ceramic materials are specifically tailored to possess well-arranged and established nanofeatures, with controlled size, shape, composition, and crystallographic orientation. These requirements summarize one of the outstanding challenges in the area of nanoscience and nanotechnology, which is the need for cheap and cost-effective nanomanufacturing processes that can develop, ordered surfaces with the desired attributes, such as size, shape and dimensionality that lead to various novel applications.

In this context, the molecular route to advanced ceramic materials offers precise control over purity, composition, homogeneity and nanostructure of the resulting materials. The molecular precursor approach for the development of ceramic materials

in gas or solution phases demand well-defined starting molecules with metal ratios that are compatible with the targeted ceramic materials. The composition and microstructure of advanced functional materials determine their properties. Factors that control composition and structure are thus of obvious importance for preparing thin films with desired properties. One of the basic requirements for the fabrication of advanced functional ceramic thin films is the availability of elegant precursors with appropriate physical properties and decomposition characteristics, but there are problems associated with many of the existing precursors. Therefore, in order to exploit the full potential of chemical vapour deposition (CVD) it is compulsory to tailor the physico-chemical properties of precursor in order to optimize process parameters. To achieve this, the molecular structure design approach is based on the choice of a proper molecular structure type and completing it with ligands providing the necessary number of donor atoms. The development of materials with complex composition at nanometer level define the morphology and physical properties focus recently on single source precursor (SSP) comprising of molecules containing all the necessary elements in the proper ratios and decomposable in a controllable manner under mild conditions.

The current research work therefore, focuses on the design and development of single source precursors of mixed metal oxide and monometallic sulphide for aerosol assisted chemical vapour deposition (AACVD) to fabricate nanostructured advanced metal oxide and sulphide ceramic thin films for technological applications.

CHAPTER 2

LITERATURE REVIEW

2.1 Ceramics

Ceramics constitute a wide class of materials and broadly defined as inorganic, solids usually made either of oxides, carbides, nitrides or silicates of metals (Callister, 2012; Riedel, 2011). Metallic and non-metallic atoms (often ions) in ceramic materials behave mostly like either positive or negative ions, and are bound by very strong Coulomb forces between them. The advantageous properties of ceramics are chemical inertness, non-conductors of heat and electricity, hardness, rigidity, abrasive toughness and low density. Ceramics, either in the form of fine powders, thin films, single crystals, polycrystals or composites, display significant and diversified role in electronics, chemical, energy and manufacturing industries (Rahaman, 2003, 2006).

Ceramics are generally classified into, Traditional and Advanced ceramics (Heimann, 2010).

Advanced ceramics are highly refined and sophisticated materials tailored to possess exceptional properties such as superior mechanical properties, corrosion/oxidation resistance, thermal, electrical, optical or magnetic properties by controlling their composition and internal structure by new fabrication techniques. Metal oxides and sulphides are classes of materials belonging to this category. However, other carbides and nitrides material are also included in the group. Advanced ceramics, based on their technical applications, can be divided into advanced structural and advanced functional ceramics (Riedel, 2011).

Advanced structural ceramics have potential to bear mechanical and thermal loading subject to tribological, aggressive, harsh chemical and thermal environments. They are materials that unify the properties and advantages of traditional ceramics, such as

chemical inertness, high temperature capability and rigidity, with the potential to carry significant mechanical stress. Advanced structural ceramics are more costly than traditional ceramics and are based on silicon nitride (Si_3N_4), silicon carbide (SiC), zirconia, (ZrO_2) and alumina, Al_2O_3. They typically obtained excellent combination of high temperature capabilities, high strength, toughness or flaw tolerance, high hardness, mechanical strength retention at high temperatures, wear resistance, corrosion resistance, thermal shock resistance, creep resistance, and long-term durability. The lifespan of ceramics in various structural applications is particularly sensitive to rare events including brittle failure during mechanical or thermal loading, pitting by corrosion, dielectric breakdown, fatigue crack initiation and by analogy over longer time and distance scales, earthquakes. Therefore, the correlation between processing and properties is especially critical for advanced structural ceramics because subsequent fruitful operation in extreme environments frequently demands carefully controlled compositions and microstructures. Fabrication generally involves four steps: powder processing, consolidation/forming, densification and finishing with attention focused on applications for gas turbine, diesel, and spark-ignited engines. Advanced structural ceramics are also under investigation for employment in various high performance applications including metal-cutting and shaping tools, and numerous military applications. Within the advanced ceramics group, structural ceramics are wear-resistant, corrosion- resistant and lightweight materials, and are superior to many materials with respect to stability in high-temperature environments. Because of these broad and unique characteristics, advanced structural ceramics are particularly valuable to resolve a wide number of today's material challenges in process industries, power generation, aerospace, transportation and military applications (Morrell, 2011; Riley, 2009).

Advanced functional ceramics are being designed for application of microstructural effects in bulk (volume), grain boundaries and surfaces of materials (Heimann, 2010; Riedel, 2011; Rohrer, 2012). Many functional ceramic materials possess outstanding electric, magnetic and optical properties and find widespread applications in optics, optoelectronics, catalysis and sensors. A variety of deposition techniques, such as liquid phase epitaxial growth, chemical vapour deposition, molecular beam epitaxial growth, sputtering, laser, ablation and chemical solution deposition have been utilized to manufacture advanced functional ceramic thin films with desired properties. Among these approaches, the chemical solution deposition method presents the advantages of excellent homogeneity, ease of compositional control, low temperature synthesis, and large area and versatile shaping with integrated functionalities over vacuum deposition technologies. Furthermore, the processing of nanostructured functional ceramic particles/organic hybrids generates novel materials has the potential to develop into an emerging area.

Advanced functional ceramics are of technical interest due to their ability to interact with the surrounding territory to detect, act upon and generate power (Dorey, 2008). However, to make effective use of these materials, it is necessary to consolidate them with other materials and to structure these materials in order to construct a functioning device that can be applied to do useful work. Moreover, by shrinking the dimensions of the resultant devices, development in terms of sensitivity, efficiency and portability can be improved. It is for these reasons that microsystems, or micro electromechanical systems (MEMS), have been extensively utilized for technological applications. For example, Lead Zirconate Titanate (PZT), a renowned piezo/ferroelectric material, faces synthetic challenges that are common to most other advanced functional ceramics. PZT is a solid solution of lead titanate and lead zirconate that displays a variety of composition and has been applied in a range of devices including ultrasound

transducers, actuators and sensors. Functional oxide and sulphide materials present the broadest range of chemistry, bonding and structures which are among the hot research topics in the field of photoelectrochemistry and photocatalysis.

2.2 Physical Properties of Advanced Functional Ceramic

Advanced functional ceramics exist in variety of compositions and crystallographic structure and exhibit numerous fascinating and useful properties which can be exploited for nanotechnology. The nanostructured materials have the potential for revolutionizing the ways in which materials and products are fabricated and the range and nature of functionalities that can be accessed. The two main reasons why materials at the nano scale level can reveal altered properties are increased relative surface area and new quantum effects. Nanosized materials acquire much greater surface area to volume ratio than their conventional counterparts, which can lead to better chemical reactivity and improved strength. In addition, at the nano scale level, quantum effects can become much more prominent in defining the materials properties and characteristics, leading to novel optical, electrical and magnetic behaviours.

2.2.1 Transport Properties

Transport properties/electrical conductivity assess well a material accommodates the mobility of the electric charge. It is the ratio of current density to the electric field strength. Electrical conductivity is a very useful property and is determined by chemical composition, stress state and crystalline structure of the material. Functional materials exhibit ionic or mixed ionic/electronic conductivity. The ionic charge carriers comprise of cations, anions and foreign ions (e.g. impurity ions, dopant ions and protons) and the electronic charge carriers are the electrons and holes. The concentration of the charge carriers is directly related to the defect structure of material,

temperature and oxygen pressure. As the movements of electrons and electrons holes are usually much higher than those of ions, so these materials are electronic conductors. The electronic conduction is known as n- or p-hopping type depending on whether the major charge carrier is electrons or holes, respectively. However, some oxide materials become ionic conductors or mixed ionic/electronic conductors depending on the temperature and appropriate doping with foreign ions. Cerium oxide (CeO_2) and cobalt sulphide (CoS_2) exhibits n-type conductivity.

A dielectric material is an electrical insulator that can be polarized by an applied electric field (Kao, 2004). They should possess high dielectric strength i.e. the ability to tolerate maximum electric field intensity without breakdown and becoming electrical conductor. They should have low dielectric loss, i.e. in an electric field, the loss of electric energy should be minimum. By applying alternating potential difference across the dielectric, polarization of charge within the material takes place without long-range movement of ions and electrons. The polarization vanishes as the voltage is removed. When a dielectric material is inserted between two plates of capacitors, the total charge hoarded in the capacitor will change and this change depends on the ability of substance to be polarized under an electric field. The dielectric constant or permittivity of a material regulates the change in charge storage. For high capacity applications a material with a high dielectric constant is required. Dielectric materials also display piezoelectric and ferroelectric properties. In today's high technology era, dielectric ceramics are indispensable for producing capacitors and electronic components that are widely used in products such as computers, televisions and mobile phones. Capacitors assist as "traffic controllers" within an electronic circuit by conducting electricity to certain parts, temporarily obstructing electricity, or blocking only specific types of electrical signals. The strontium hexaferrite and sulphides of main group elements

including zinc (Zn), cadmium (Cd) and mercury (Hg) are the important examples of dielectric material.

Ferroelectric materials (Varghese, 2013) presents an intrinsic electric polarization that can be changed or inverted by an applied electric field as shown in Figure 2.1.

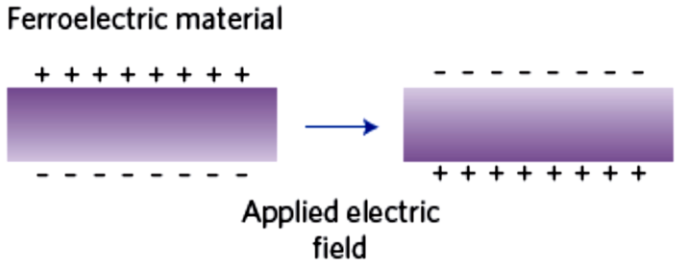

Figure 2.1: Inversion of polarization on the application of an electric field in a ferroelectric material (Keppens, 2013).

The term ferroelectric is used in resemblance to ferromagnetism, in which a material shows a permanent magnetic moment. The prefix *ferro*, meaning iron, was used to narrate the property despite the fact that most ferroelectric materials do not include iron. Ferroelectric material of single crystal or polycrystalline type, experiences a phase transition at the Curie temperature (T_C), from a high-temperature non-polarized paraelectric state to a low-temperature ferroelectric (polarized) state. The spontaneous polarization is a consequence of the structural transformation that takes place at T_C, and usually involves a small symmetry-breaking distortion. The structure of the low-temperature ferroelectric material is always non-centrosymmetric, and therefore does not exhibit inversion symmetry, as this prevents the charge separation intrinsic to the electric polarization. Three necessary conditions have to be met for a crystal to be a ferroelectric material. First, the structural transformation has to be continual; second, the low temperature structure has to be non-centrosymmetric; and third, the low-temperature structure needs to support a unique polar axis (which is a rotational axis of symmetry without a mirror plane perpendicular to it).

Barium titanate, $BaTiO_3$, is a ferroelectric oxide that undergoes a transition from a ferroelectric tetragonal phase to a paraelectric cubic phase upon heating above 130 °C. Sulphide ferroelectric materials include bismuth sulphide, Bi_2S_3 and antimony sulphide, Sb_2S_3. Thin films of ferroelectric materials are widely employed in many devices including transducer, acoustic, sensor and computer accessories (random access memories (RAM), radio-frequency identifications (RFID) cards), multilayer ceramic capacitors, gate dielectrics, waveguide modulators, IR detectors and holographic memory (Ramesh, 2007; Setter, 2006).

An antiferroelectric state is defined as one in which lines of ions in the crystal are spontaneously polarized, but with neighbouring lines polarized in antiparallel directions (Rabe, 2013). In simple cubic lattices the antiferroelectric state is likely to be more stable than the ferroelectric state. The dielectric constant above and below the antiferroelectric Curie point is investigated for both first and second order transitions. In either case the dielectric constant need not be very high but if the transition is second order, κ is continuous across the Curie point. The antiferroelectric state will not be piezoelectric. The thermal anomaly near the Curie point will be of the same nature and magnitude as in ferroelectrics. $PbZrO_3$ is an antiferroelectric material which has a cubic perovskite structure at high temperature and at low temperature it goes through a structural phase transition where in one cell the central atom moves up and in the cell above it the atom moves down so the atoms move against each other and the polarisations are pointing towards each other (Tagantsev, 2013). The result of this is that the macroscopic polarisation is zero. The types of applications this functionality would enable include high-energy storage capacitors, electrocaloric refrigerators, high-strain actuators and transducers (Sukkha, 2014).

Piezoelectricity is the capability of some materials especially crystals and certain ceramics to create an electric potential in response to applied mechanical stress (Figure

2.2). Piezoelectric materials also demonstrate the converse piezoelectric effect (mechanical deformation) upon application of electric charge.

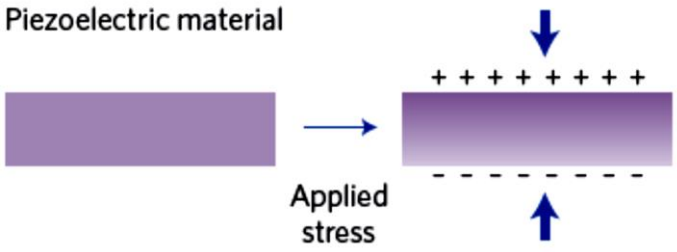

Figure 2.2: Generation of a polarization in piezoelectric material when stress is applied.

The prefix *piezo-* in the word *piezoelectrics* is derived from a Greek word, *piezein*, meaning *pressure*. Crystals comprised of polar molecules with a noncentrosymmetic structure (i.e., without a center of symmetry) will display a piezoelectric effect. This indicates that a mechanical stress applied to the crystal specimen will generate an overall polarization and hence a voltage across it (Yang, 2005). The reverse of the stress direction will cause the inverse of the polarity of the polarization and hence the voltage. This effect arises naturally in quartz crystals, but can be created in other materials, such as specially designed ceramics consisting mainly of lead, zirconium, and titanium (PZT) and cadmium and zinc sulphides.

The piezoelectric effect can be potentially used to fabricate materials for sensor and actuator (Tressler, 1998). Strain, for example, can be measured by capturing the voltage produced across the material when it is strained. As a sensor, these materials can also be applied for damage detection in structures in which they are implanted. Piezoceramics can be employed as actuators because they can strain or displace when an electric field is applied across the poling axis. This makes PZTs attractive applicants for valve actuation or active control systems (Wilson, 2007). Piezoceramics also finds applications as structural dampers because of their potential to convert mechanical energy to electrical energy and vice versa.

Pyroelectricity is the ability to generate induced charges on crystal surfaces when they are heated or cooled (Figure 2.3).

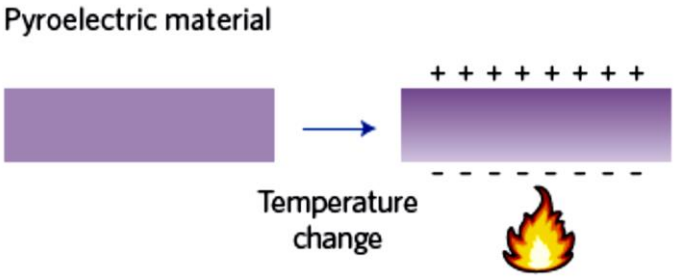

Figure 2.3: Generation of a polarization in pyroelectric material when heat is applied.

The prefix *pyro-* means *fire* in Greek. Due to variation in temperature, slight modifications occur in the atomic positions within the crystal, and as a result, the polarization of the crystal alters. This develops a voltage across the crystal which is not permanent and persists until temperature change remains as such.

All pyroelectric materials also show the piezoelectric property but some piezoelectric materials have a crystal symmetry which does not permit pyroelectric property. Pyroelectric tools have been used for determining temperature changes, thermal imaging and applications in space technology (Lang, 2005; Sebald, 2008; Whatmore, 2000).

Paraelectricity is the ability of many materials, specifically ceramic crystals to become polarized under an applied electric field. Unlike ferroelectricity, this can occur even if there is no permanent electric dipole in the material, and shifting of the electric field results in polarization in the material returning to zero. Paraelectricity arises in the crystal phase in which electric dipoles are unaligned. High temperature quantum paraelectricity in perovskite titanate series $(Ln_{0.5}Na_{0.5})$ TiO_3 has been investigated in relation to their structure (Nakamura, 1998).

2.2.1 Magnetic Properties

Magnetic properties of materials originate from magnetic moments associated with individual electrons. Each electron in an atom has two types of magnetic moments, named as orbital and spin magnetic moments which are associated with its orbital motion around the nucleus and its spin motion respectively, as shown in Figure 2.4. Thus each electron in an atom behaves like a small magnet having permanent orbital and spin magnetic moments. For an atom having completely filled electron shells or subshells, there is total cancellation of both orbital and spin moments, therefore such materials are not capable of being permanently magnetized.

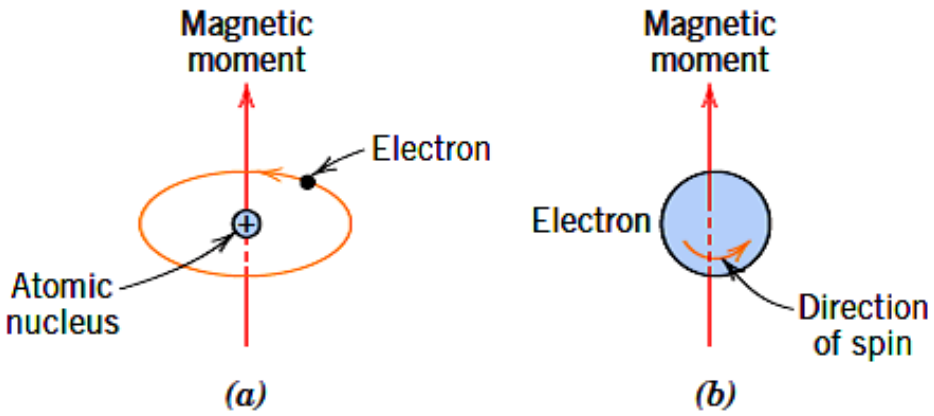

Figure 2.4: Demonstration of the magnetic moment associated with (***a***) an orbiting electron and (***b***) a spinning electron.

Based on magnetic properties such as ordering, sign, magnitude and temperature that influence magnetic susceptibility, all magnetic materials can be categorized into five classes diamagnetic viz. paramagnetic, ferromagnetic, antiferromagnetic and ferromagnetic and have been sequentially discussed here.

Diamagnetism is the property of the materials that do not have inherent magnetic moment but when introduced to an applied magnetic field (H) show negative susceptibility and acquire magnetization (Figure 2.5).

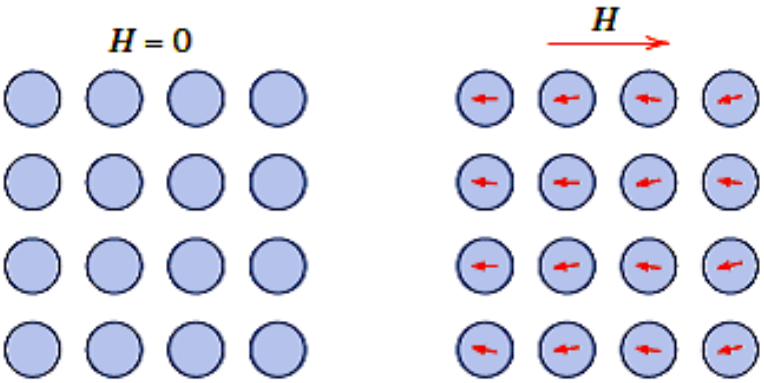

Figure 2.5: The atomic dipole configuration for a diamagnetic material with and without a magnetic field (H).

In diamagnetic materials, the susceptibility nearly has a fixed value and is free of temperature effects. Ionic crystals and inert gas atoms are diamagnetic. These substances have atoms or ions with fully occupied shells, and their diamagnetic character arises due to the fact that a magnetic field acts to distort the orbital motion. Sulphides of main group (i.e., non -transition) elements including Zn, Cd, Hg and pyrite (FeS_2), galena (PbS) are examples of diamagnetic materials (Pearce, 2006).

Paramagnetism occurs only in the presence of an externally applied magnetic field (H). These materials exhibit no net magnetic moment in the removal of an applied magnetic field (Figure 2.6).

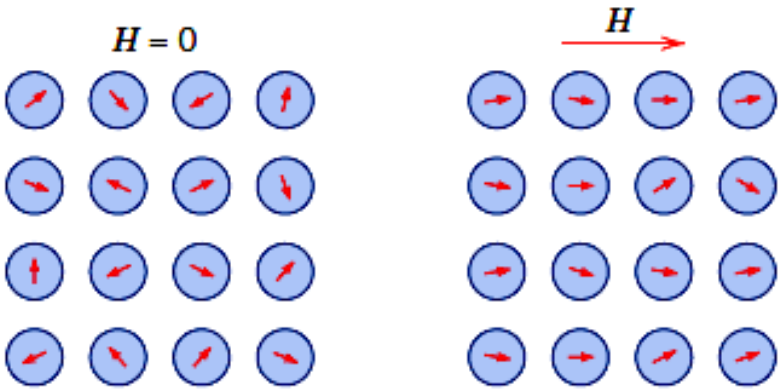

Figure 2.6: Atomic dipole configuration with and without an external magnetic field (H) for a paramagnetic material.

Some of the atoms or ions in the material have a net magnetic moment due to unpaired electrons in partially filled orbital. In such materials, the magnetic moment is non-zero for each atom, but averages to zero over many atoms. If a magnetic field is applied across the material and the atoms are free to oscillate, they will affiliate with the magnetic field, amplifying its strength (Figure 2.6). When the field is removed all moments again return to their random orientation. Bornite (Cu_5FeS_4) and tennantite (Cu, Fe,$ZnAg_{12}$)As_4S_{13} possess paramagnetic behaviour. The susceptibility and magnetization is positive for these materials.

Certain materials possess a permanent magnetic moment in the absence of an applied external field (H), and manifest very large and permanent magnetization which is characteristics of ferromagnetism. Ferromagnetic materials acquire their strong magnetic properties due to the existence of magnetic domains. In such materials, coupling interactions cause net spin magnetic moments of neighbouring atoms to align with one another, even in the absence of an external field, schematically illustrated in Figure 2.7.

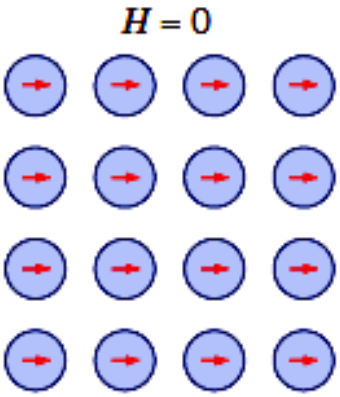

Figure 2.7: Schematic illustration of the mutual alignment of atomic dipoles for a ferromagnetic material, which will exist even in the absence of an external magnetic field.

This mutual spin arrangement occurs over relatively large volume regions of the crystal called domains. When a magnetizing force is employed the domains become aligned to create a strong magnetic field within the part. Iron, nickel and cobalt are examples of ferromagnetic materials. Ferromagnetic susceptibility of a material is quite temperature dependent and exceeding a critical temperature called as *Curie Temperature (T_C),* the material halt to become ferromagnetic and it becomes merely paramagnetic. A number of rare earth sulphides including europium, gadolinium and lanthanum sulphides have ferromagnetic behaviour.

In antiferromagnetic materials, the phenomenon of magnetic moment coupling between adjacent atoms or ions results in an antiparallel alignment, causing the net magnetic moment to vanish (Figure 2.8). This behaviour usually occurs at low temperatures and characterized by the Neel temperature. The temperature at which a transition occurs from antiferromagnetic to paramagnetic behaviour is called Néel Temperature. Manganese oxide (MnO), alabandite (MnS) and chalcocite (Cu_2S), chalcopyrite ($CuFeS_2$) materials display this kind of behaviour.

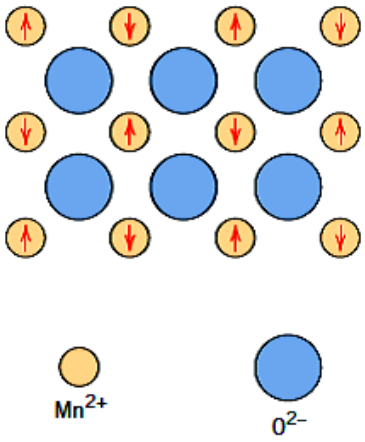

Figure 2.8: Schematic representation of antiparallel alignment of spin magnetic moments for antiferromagnetic manganese oxide.

In ferrimagnetic materials, there are antiparallel spin-coupling interactions between the atoms or ions, similar in character to antiferromagnetism but the net magnetic moment arise from the incomplete cancellation of spin moments (Figure 2.9). Ferrimagnetic materials are also called “Ferrites”, represented by the chemical formula MFe_2O_4 in which M represents any one of several metallic elements. The prototype ferrites are magnetite (Fe_3O_4) and greigite (Fe_3S_4). Almost all of the ferrimagnetic materials are poor conductors of electricity.

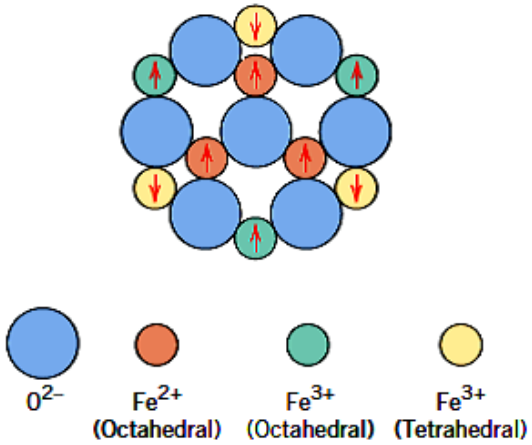

Figure 2.9: Schematic diagram showing the spin magnetic moment configuration for Fe(II) and Fe(III) ions in Fe_3O_4.

2.2.3 Optical Properties

Optical property is a material’s response on exposure to electromagnetic radiation, notably to visible light and is determined by the band structure of the material. Materials are characterized as metals, semiconductors and insulators depending upon their band structures as shown in the Figure 2.10.

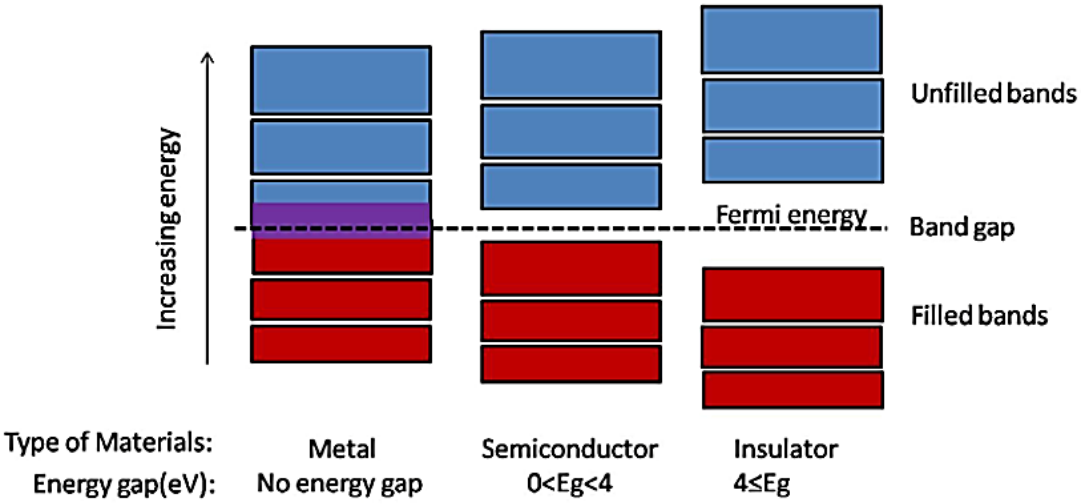

Figure 2.10: Simplified diagram of the electronic band structure of metals, semiconductors and insulators.

In non-metal solids, there is a minimum energy separating the highest filled electron states (valence band) and the lowest empty ones (conduction band), narrated as the energy band-gap. The main absorption phenomenon in semiconductors and dielectrics arises from the interaction of light with electrons. In dielectrics, no electronic transitions occur in the visible region, because the valence electrons are so firmly bound that photons with energy in the ultraviolet are required to free them. Ideally, photons containing energy lesser than the band-gap are not absorbed. Conversely, metals are good reflectors and are transparent to visible and infrared radiation.

The optical properties of semiconductors occur between those of metals and those of insulating dielectrics. Semiconductors are generally transparent in the near infrared and absorbing in the visible region, while the absorption in dielectrics is strong in the ultraviolet. Thus, the fundamental absorption edge of semiconductors lies, approximately, between 0.5 eV ($\lambda \sim 2500$ nm) and 2.5 eV ($\lambda \sim 500$ nm). Within a small energy range around the fundamental absorption edge, semiconductors go, ideally, from high transparency to complete opacity. However, the presence of impurities, free conduction electrons or holes, and/or other defect states may affect the transparency of

semiconductor and dielectric materials at photon energies smaller than the band-gap (Chambouleyron, 2001).

A semiconductor in its pure form has equal number of electrons and holes (n = p) and is known as intrinsic semiconductor such as CdS, GaAs or $CuInS_2$. When an intrinsic semiconductor is doped with some foreign atom (impurity), the carrier concentrations of electron and hole changes and it becomes extrinsic semiconductor. Donor impurity atoms possess more valence electrons than the atoms they substitute in the intrinsic semiconductor lattice. Donor impurities give their extra valence electrons to a semiconductor's conduction band, providing extra electrons to the intrinsic semiconductor. Extra electrons enhance the electron carrier concentration (n_0) of the semiconductor, forming it n-type. Acceptor impurity atoms have fewer valences electron than the atoms they substitute in the intrinsic semiconductor. They receive electrons from the semiconductor's valence band. This provides extra holes to the intrinsic semiconductor. Extra holes rise the hole carrier concentration (p_0) of the semiconductor, producing a p-type semiconductor.

An example of n-type doping is arsenic in silicon. Arsenic has five valence electrons whereas silicon has four. This additional electron generates donor electron levels just below the conduction band (Figure 2.11).

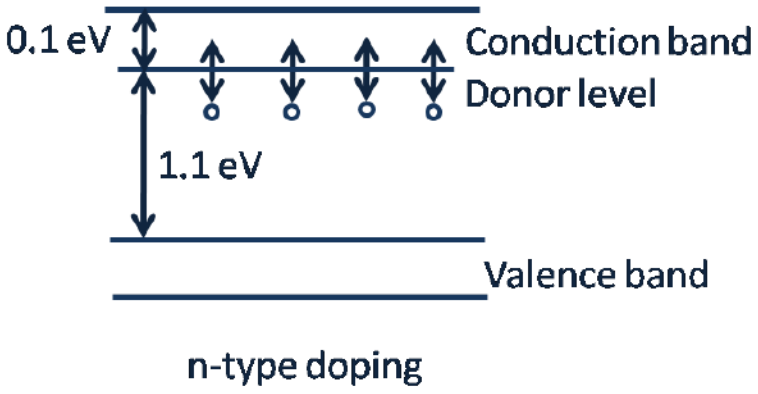

Figure 2.11: Band structure of n-type doped semiconductor.

Thermal excitation can motivate electrons from the new donor levels (rather than the valence band) into the conduction band. The donor levels do not display band-like characteristics and electrons are restricted to move. Conduction is produced by movement of the promoted electrons in the partly filled conduction band. Due to the immediacy of donor levels and the conduction band, electrons can transfer from one to the other more easily than in pure silicon. The bandgap for silicon is 1.1 eV however for arsenic doped silicon the donor level energy is less than 0.1 eV beneath the conduction band. Less thermal energy is needed for arsenic doped silicon to attain the same conductivity level as pure silicon.

An example of p-type doping is gallium in silicon as shown in Figure 2.12.

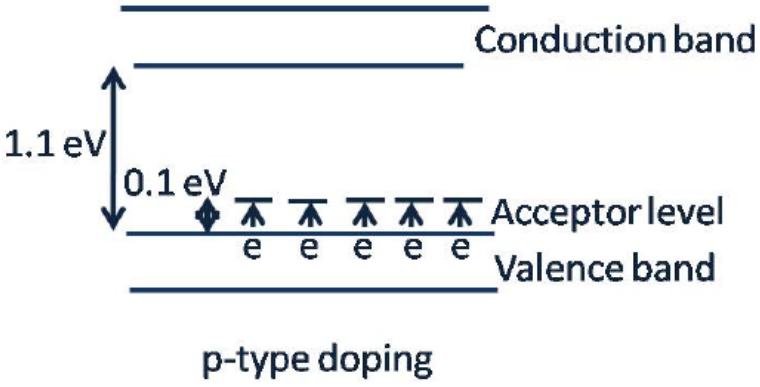

Figure 2.12: Band structure of p-type doped semiconductor

Gallium has three valence electrons whereas silicon has four, and the emerging material is thus deficient by one electron. Acceptor levels produce just above the valence band. Thermal excitation lifts electrons from the valence band to the new acceptor levels (rather than to the conduction band). Similar to the donor levels in n-type materials, the acceptor levels in p-type materials do not have band-like qualities and electrons are not allowed to move (i.e. they are localized energy levels). The motion of electrons from the valence band to the acceptor levels generates positively charged holes in the valence band. The movement of these holes in the valence band causes the

conduction of the material. Due to the immediacy of the valence band and acceptor levels, electrons can transfer from one to the other more easily than in the pure silicon. In gallium-doped silicon the acceptor level energy is ~ 0.1 eV over the valence band (compared to the 1.1 eV bandgap of silicon)

The location of the Fermi level is different for intrinsic n-type and p-type semiconductors. In intrinsic semiconductors the Fermi level (E_f) is always mid-bandgap ($E_f = E_g/2$) and is unaffected by temperature (Figure 2.10). The number of holes in the valence band is always identical to the number of electrons in the conduction band. The Fermi level in n-type materials is temperature sensitive and exists just over the donor level energy (E_d) slightly beneath the conduction band. At low temperature all the electrons are in the donor levels. In this material there are more electrons existing in the conduction band than there are holes in the valence band. In the p-type extrinsic semiconductor the Fermi level is situated slightly below the acceptor energy level (E_a), and just above the valence band. In this kind of material there are more holes present in the valence band than electrons in the conduction band.

Semiconductors can be further categorized according to their electronic structure by the nature of electrons transition from valence to conduction band.

Direct bandgap semiconductors, *i.e.* semiconductors for which the minimum of the conduction band occurs at the same wave vector, *k*, as the maximum of the valence band, have a deep absorption of light as characterized by a larger absorption coefficient. They are also the favourite semiconductors when manufacturing light emitting devices. Indirect bandgap semiconductors, *i.e.* semiconductors for which the minimum of the conduction band does not occur at the same wave vector as the maximum of the valence band, are known to have a smaller absorption coefficient and are seldom used in light emitting devices. The difference between direct and indirect transitions is represented in Figure 2.13.

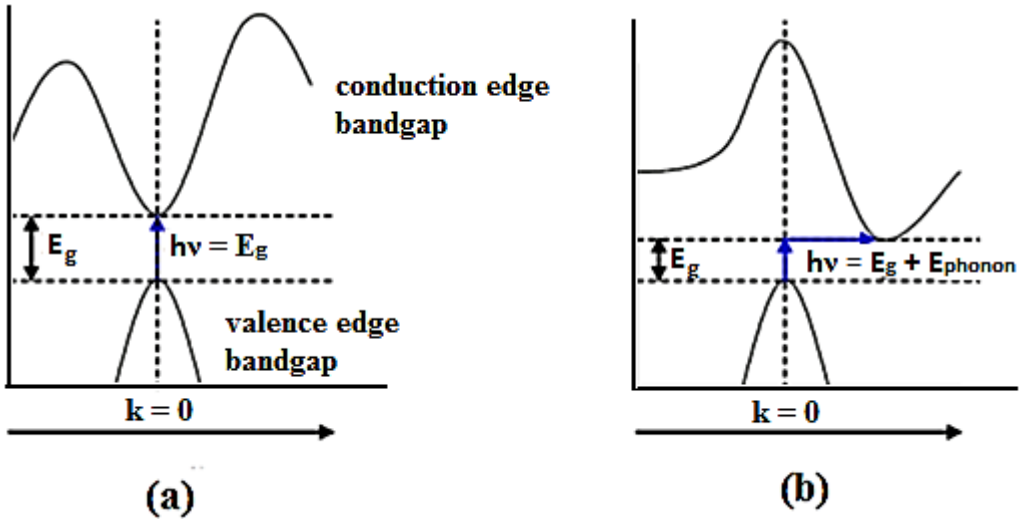

Figure 2.13: E-*k* diagram illustrating (**a**) photon absorption in a direct band gap semiconductor (**b**) photon absorption in a indirect band gap semiconductor.

For a direct bandgap semiconductor the minimum value of energy E(*k*) in the conduction band and maximum value of E(*k*) in the valence band concur at the same value of *k*. For indirect bandgap semiconductor like silicon, an electron cannot be exactly promoted to the conduction band with energy E_g. Extra energy is required in form of lattice vibrational energy (phonon), the electron experiences a change in crystal momentum and we acquire an indirect transition with energy $h\nu = E_g + E_{phonon}$. The phonon energy, E_{ph}, is very small compared to band gap E_g (Sze, 2006).

Indirect transitions need the addition of lattice vibrational energy phonons and hence are obviously dependent on temperature. The absorption coefficient for indirect semiconductors is lower than for direct semiconductors; in result light absorption is a less attractive process for indirect semiconductors. For clarity we have accounted these basics absorption phenomenon for direct and indirect semiconductors, *i.e.* those that occur for light photon of energies similar to the bandgap energy.

Similarly, in the case of light emission, a direct bandgap material is also more likely to emit a photon than an indirect bandgap material. While indirect bandgap materials are

rarely used for some LEDs, they result in low conversion efficiency. Direct bandgap materials are used exclusively for semiconductor laser diodes (Chilla, 2007).

2.3 Fabrication Routes to Functional Ceramic Thin Films

Thin films are material layers in thickness range of a few nanometers to about ten micrometers. The processing of materials into thin films allows easy integration into various types of optoelectronic, photonic and magnetic devices (Eason, 2007; Nalwa, 2000; Singh, 2006). The Synthesis of functional materials on the substrate surface with well-established nanodesigns and architectures represents an area of increasingly high interest and creates new opportunities in field of materials engineering and technologies. However, the extensive utilization of nanostructured materials is often complicated by the conflicting demands for exact control of hyperfine features and large-scale production. The trend towards miniaturization in the electronic and semiconductor industry has set high demands on fabrication technologies and processes which can not only approach the scale of interest, but do so in an efficient manner. The microarchitecture and surface properties of nanoengineered thin films and coatings depend heavily on the fabrication method as well as on the processing route; therefore, the selection of appropriate deposition technique is of utmost importance (Milosevic, 2009).

Nanophase thin films of functional ceramic have been prepared by various deposition methods as summarized in Table 2.1. It is possible to classify these techniques in two ways, either, purely physical, such as evaporation or sputtering methods (Mattox, 2010), or, purely chemical, such as gas- and liquid-phase chemical processes (Krishna, 2008; Mane, 2000; Waser, 2001). Some other thin films techniques fall outside the physical or chemical categories because they rely on a mixture of chemical and physical means (Nalwa, 2002).

Table 2.1: Classifications of thin films deposition techniques

Thin Films Deposition Techniques

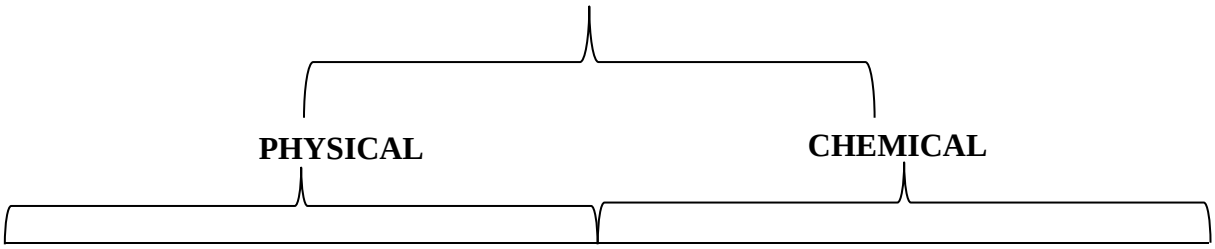

Sputtering	Evaporation	Gas Phase	Liquid Phase
1) Glow discharge DC Sputtering	1) Vacuum evaporation	1) Chemical vapour deposition (CVD)	1) Electro-deposition
2) Triode Sputtering	2) Resistive heating evaporation	2) Atmospheric pressure CVD (APCVD)	2) Chemical bath deposition (CBD)
			3) Arrested precipitation technique (APT)
3) Getter Sputtering	3) Flash Evaporation	3) Low-pressure CVD (LPCVD)	4) Electroless deposition
4) Radio Frequency sputtering	4) Electron beam evaporation	4) Metal-organic CVD (MO-CVD)	5) Anodisation
5) Magnetron sputtering	5) Laser evaporation	5) Photo enhanced CVD (PHCVD)	6) Sol-gel 7) Spin Coating
6) Ion beam sputtering	6) Reactive Evaporation	6) Laser induced CVD (PCVD)	8) Spray-pyrolysis technique (SPT)
7) A.C sputtering	7) Arc Evaporation	7) Electron enhanced CVD	9) Ultrasonic SPT
	8) Molecular beam epitaxy (MBE)		10) Polymer assisted deposition (PAD)

Chemical vapour deposition (CVD) is a versatile technique used to create films by chemical reaction on the surface of a substrate. This technique is capable to produce high-purity, high-performance solid materials and has found potential applications in the semiconductor industry to generate high quality thin films. In a common CVD process, the substrate is heated and exposed to gaseous precursor molecules, which react and /or decompose on the substrate surface to facilitate the desired material. Frequently, volatile unwanted by-products, normally organic species, are also generated, which are cleaned by vacuum pump or gas flow through the reaction chamber (Binions, 2011; Choy, 2003; Jones, 2009; Kodas, 2008; Mathur, 2007).

A number of types of CVD are extensively used and are frequently reported in the literature (Carter, 2013; Dobkin, 2003; Jaeger, 2001). In terms of operating pressure, CVD can be categorized as atmospheric pressure CVD (APCVD) and low pressure CVD (LPCVD) - CVD works at subatmospheric pressures and ultrahigh vacuum CVD (UHVCVD) - CVD processes at a very low pressure, typically below 10^{-6} Pa (~ 10^{-8} torr). Reduced pressures tend to diminish unwanted gas-phase reactions and produces good quality films. Most advanced CVD techniques are either LPCVD or UHVCVD. CVD methods can also be categorized on the basis of physical appearances of the vapour. Aerosol assisted CVD (AACVD) is a CVD variant in which the precursors are conveyed to the substrate in form of a liquid/gas aerosol, which can be generated ultrasonically. This method is suitable for precursors with low volatility. Direct liquid injection CVD (DLICVD) is a CVD technique in which the precursor used is in liquid form (liquid or solid dissolved in a suitable solvent). Liquid solutions are injected in a vaporization compartment towards injectors. Then the precursor's vapours are transferred to the substrate as in classical CVD process. This method is applicable for liquid or solid precursors. Using DLICVD makes high growth rates achievable. CVD

variants also include microwave plasma-assisted CVD (MPCVD), atomic layer CVD (ALCVD), hot wire CVD (HWCVD), rapid thermal CVD (RTCVD), vapor phase epitaxy (VPE) and metal organic chemical vapour deposition (MOCVD).

2.4 Process, Mechanism and Development of Aerosol Assisted Chemical Vapour Deposition (AACVD)

This is a variant of CVD process which utilizes a liquid aerosol to transport the precursor to the substrate. In AACVD, the precursors are firstly dissolved in a solvent, from which an aerosol is generated, or the precursor can be a liquid. Provided that a compound can be dissolved in a suitable solvent there is not much need to rely on the evaporation of the precursor, as is typical with other types of CVD, including atmospheric pressure CVD (APCVD) and LPCVD (Binions, 2011; Hassan, 2013; Hou, 2006; Knapp, 2014; MarchandHassan, 2013).

AACVD involves the process of atomization of a precursor solution into fine, sub-micrometer-sized aerosol droplets that are transported to a heated substrate through a carrier gas. The aerosol is consequently entered into a heated region, where the solvents undergo rapid evaporation and/or decomposition, leaving the precursor vapours at the elevated temperature. Then desired materials can be synthesized by means of decomposition or other chemical reactions of the vaporized precursor.

The series of events commonly occuring in AACVD are schematically illustrated in Figure 2.14. The starting solution may be a pure liquid, single-source precursor or a combination of various liquid chemicals. It may also be prepared by dissolving solid or liquid starting compounds in a solvent. In many cases, the criteria for the selection of solvents for atomization are high solubility of the precursor, low vapor pressure, and low viscosity (Hubert-Pfalzgraf, 1998). The atomization of the starting precursor solution can be performed using various types of aerosol generators. The duty of carrier

gases is to support the generation of aerosol and drive the aerosol to the reactor tube. Compressed air is employed for the creation of oxide materials whereas argon and nitrogen are commonly used for the reason that they are inert carrier gases. Reactive gases such as H_2 may also be presented at this step with other primary carrier gases, to assist the subsequent CVD reaction (Glerup, 2003). After atomization, the precursor aerosol is transported to the heated zone, where evaporation of solvent and vaporization of precursor occur before the major chemical reactions. The vaporization can take place directly from the aerosol mist if the precursor is pure. Because the vaporization of precursor is the key aspect of AACVD, the choice of the starting precursor and the control of deposition parameters are vital to ensure a true CVD process. An unwanted spray pyrolysis process will come to pass in place of an accurate CVD mechanism, if the aerosol droplets approach the heated substrates before entire evaporation and vaporization.

In some cases, initial decomposition of vaporized precursor can occur in the gas phase. The vaporized precursors and their gaseous intermediates then become adsorbed on the surface of the heated substrates, where they endure considerable decomposition and chemical reactions, and deposit the desired materials. External reactive gases may also be introduced into the reaction zone directly to assist the chemical reactions. This procedure is analogous to the heterogeneous CVD reaction which leads to the deposition of high-quality films with good adhesive strength. In other cases, often if the deposition temperature is too high, the major decomposition and/or chemical reactions occur much earlier in the vapour phase, leading to homogeneous nucleation and the formation of fine particles. External reactive gases may also be presented into the homogeneous reaction. If the particles generated in such a way are adsorbed onto the substrate, the subsequent heterogeneous reactions tend to lead to the production of porous films on substrate surface. As an alternative, depending on the processing

parameters, powders can be collected from the gas phase, with the size ranging from the nanometer to micrometer scales. The compound, in an AACVD process, must be in the form of chemical vapour that undergoes homogeneous and/or heterogeneous chemical reactions, as represented in Figure 2.14. This narrative limits various aerosol-based deposition techniques which have been reviewed with reference to a few true CVD processes (Choy, 2000).

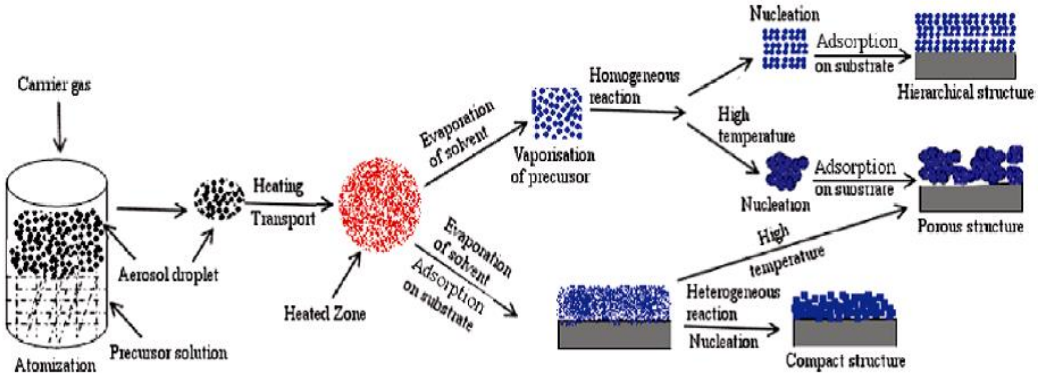

Figure 2.14: Schematic representation of AACVD process for the deposition of thin films.

The main advantage of AACVD over conventional CVD technique is the alleviation of the need for volatile precursors, an obligation which can cause a constraint in the range of potential precursors that can be studied. AACVD is a cost effective process, the humidifier eliminates the need for high vacuums or temperatures which are used in conventional bubbler or vaporisation methods. Additionally, because the system is solution based, it ensures that *in situ* reactions are possible, so that reactants can be mixed together before they transfer to the reaction zone without decomposition occurring. This abolishes the need for several starting 'pots' containing many volatile precursors and why the technique has come to be narrated as the 'one pot' approach. Overall AACVD offers a simplification in the synthesis of multicomponent materials whilst keeping appreciable control over their stoichiometry. This creates more dynamic

surroundings that can allow AACVD process to be carried out at low pressure and even in open air.

2.5 Single-Source Precursor

A major part of tailoring material properties resides in the proper choice of the molecular precursors, whose design strongly affects the nature and morphology of the final product. It is most important to develop the precursors having a set of physical properties such as economical and easy preparation routes, high purity, non-toxicity, high volatility and thermal stability and clean thermal decomposition that make them elegant precursors for preparation of high quality thin films with minimum health hazards and environmental issues (Malik, 2010).

However, the uses of conventional precursors for the CVD process have many disadvantages such as difficulty to control stoichiometry, impurity incorporation, unwanted side reactions and high processing temperature which may cause inter-diffusion of layers. In order to overcome these disadvantages, during the past decades, much attention has been paid to the development of alternative single-source precursors (Bochmann, 1996; O'Brien, 1997).

The single-source molecular precursor route has opened a fruitful way for the controllable synthesis of advanced functional materials (Adeogun, 2007; Afzaal, 2010; Bloor, 2011; MansoorIsmail, 2013; TahirWijayantha, 2009). A single source precursor is a metal-organic molecule which contains all the desired elements for the growth of a material product. The use of such molecular precursor reagents for the CVD process has potential advantages over conventional precursors. First of all, it offers the distinct advantages of mildness, safety and simplified fabrication procedure and equipment, and delivers exact control over stoichiometry as compared to the conventional or multiple sources. Another key incentive for consuming single-source molecular precursors may

be found in the observation of unusual crystal growth selectivity or metastable phase formation of the final products, which are sometimes unachievable via the conventional synthesis techniques (Marchand Carmalt, 2013; Pickett, 2001). For these reasons, the single-source molecular precursor method, which is precisely defined and can thus enable a much higher degree of synthetic control during the reaction, has proven to be a useful route to synthesize high quality materials (McElwee-White, 2006; McElwee-White, 2009) .

2.5.1 Oxide Ceramic Thin Films

In order to fabricate advance functional oxides with certain specifications such as homogeneity, high purity, and narrow particle-size distribution over large area, it is indispensable that the precursor chemistry is well understood with as far as possible precursors having matched thermal properties and reasonable vapour pressures. In CVD methods, molecular precursors must shed the ligands that contributed to their volatility and clean controlled thermal decomposition on the substrates without incorporation of carbon from the ligands or solvent to yield material thin films. The suitable tailor-made precursors for monometallic oxides are molecules having already M-O bonds, namely metal alkoxides $M(OR)_n$, or oxoalkoxide $MO(OR)_n$ (R = saturated and unsaturated organic group, alkyl or aryl), metal carboxylates $M(O_2CR)_n$, and β-diketonates$(β\text{-dik})_n$ (β-dik RCOCHCOR'). The most commonly used precursors of oxides are alkoxides due to their commercial availability and high liability of the M-OR bond allowing facile tailoring in situ during process.

Heterobimetallic compounds are of huge interest as they present a variety of structural architectures in addition to remarkable chemical properties as compared to their monometallic analogues. Research in this area is also inspired by their applications as single source precursor for the fabrication of bi-multimetallic advance materials

(Szafert, 2008). Pyrolysis of distinct and well-defined bi- or multimetallic compounds as single-source precursors (SSPs) has been shown to furnish the correct crystalline oxide phases at low temperatures and in higher purity than what is attainable by traditional solid-state techniques. The ordinary conditions required for the formation of crystalline oxides from molecular complexes results in the ability to create and isolate metastable phases and allow for the formation of materials with unique morphologies. The ease of crystallization of oxides obtained from SSPs has been ascribed to the direct atomic ordering of the two or more metal centres with respect to one another in the molecular lattice. Moreover, these molecular precursor complexes frequently exhibit other interesting properties including high solubility in common organic solvents, increased hydrolytic stability, ease of purification and in some cases, volatility. This combination of physical and chemical characteristics generally allows SSPs to be used simultaneously with well-defined deposition techniques for the growth of thin or thick oxide films such as metal-organic decomposition (MOD), metal-organic chemical vapor deposition (MOCVD), and sol-gel techniques.

The general synthetic procedures for heterometallic derivatives and the chemical concepts which are involved are as follows:

2.5.1.1 Lewis Acid–Base Interactions

The heterobimetallic complexes generally follow the Lewis acid–base neutralization reaction mechanism. The electronegativity difference between two or more metal species in a complex compound suggests that one metal atom will act as a strong acceptor of the electron density and the other will act as the donor to develop a heterometallic complex. These compounds can be obtained by simple mixing of the component alkoxides as shown in chemical equation (1) (Veith, 2000) . Although some of the reactions do not constitute pure Lewis acid-base interactions as the product

formation involves inclusion or liberation of neutral molecules; however, their similar formation is on the basis of donor-acceptor interaction of two component alkoxides (Veith, 2001).

$$1/n\,[Ba(OBu^t)_2]_n + Zr(OBu^t)_4 \xrightarrow{THF} 1/m[BaZr(OBu^t)_6(THF)_2]_m \quad (1)$$

$$[Ln\{N(SiMe_3)_2)_3\}] + 3[Al(OPri)_3]_4 \xrightarrow{Pr^iOH/C_7H_8} [Ln\{Al(OPri)_4\}_3(Pr^iOH)] \quad (2)$$

Ln = Pr; Nd

Bismuth salicylate $[Bi(Hsal)_3]_n$ carries a significant Lewis acidity and react with transition metal alkoxides to produce stable heterobimetallic complexes including $Bi_2M_2(sal)_4(Hsal)_4(OPr^i)_4$ and $Bi_2M_2(sal)_4(Hsal)_4(OEt)_4$ (M = Nb, Ta)) under very mild conditions and in good yields and complexes are converted into mixed metal oxides products $BiMO_4$ (M = Nb, Ta) at 500 °C (Thurston, 2002).

In a different study, bismuth(III) salicylate reacts readily with the trivalent metal β-diketonate $M(acac)_3$ (M = Al, V, Cr, Co, Fe) via direct Lewis acid-base adduct formation and the resultant coordination compounds undergo facile thermal decomposition at 475 °C to generate bimetallic oxide materials (Thurston, 2004).

$$[Bi(Hsal)_3]_2 + M(acac)_3 \longrightarrow [Bi(Hsal)_3]_2 \cdot M(acac)_3 \quad (3)$$

M = V, Al, Fe, Co, Cr

Metal β-diketonates are attractive reagents as MOCVD precursors for the synthesis of oxide material because of their prospective advantages in comparison with other ligands, such as higher volatility, stronger resistance to hydrolysis, and easier structural control of precursors. The possibility of utilizing Lewis acid-base interactions for the synthesis of heterometallic β-diketonates have been recently explored through low temperature solid state methods which employ coordinatively unsaturated metal fragments for the formation of bismuth transition metal $Bi_2M(hfac)_8$ (M = Mn, Fe, Co,

Ni, Cu, and Zn; hfac = hexaflouroacetylacetonate) (Dikarev, 2005) and manganese-containing MnM $(hfac)_6$ (In, Cd, Hg and Pb) (Zhang, 2009) heterometallic diketonates. These compounds exhibit high volatility, clean, low-temperature decomposition, and retention of heterometallic structures upon sublimation-deposition as well as in solutions of non-coordinating solvents.

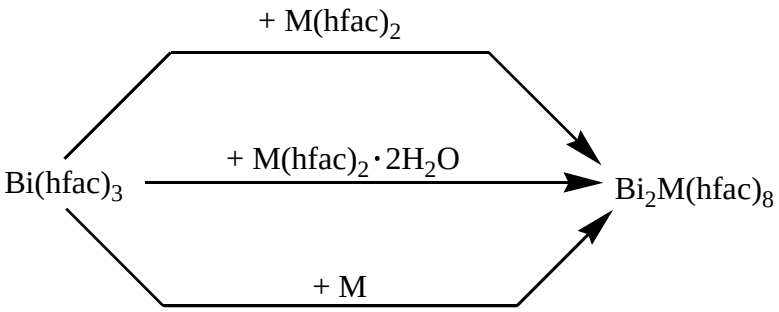

(4)

M = Mn, Fe, Co, Ni, Cu, Zn

$$M + 2\,Mn(hfac)_3 \longrightarrow MMn_2(hfac)_6 \qquad (5)$$

M = In, Cd, Hg, Pb

$$Pb(hfac)_2 + Mn(hfac)_2 \longrightarrow PbMn(hfac)_4 \qquad (6)$$

Extensive work on the development of heterobimetallic complexes of titanium and other metals have been carried out and precursors such as $[Sr_2Ti_2(\beta\text{-dik})_4(OR)_8]$, $M_2[Ti_2(OPr^i)_8(thd)_4]$ (M = Ba and Sr, thd = 2,2,6,6-tetramethylheptanedionate) (Hubert-Pfalzgraf, 1997), $[BaTiO(OPr^i)_4]_4 \cdot 3.5^iPrOH$ (Yanovsky, 1991), $[Ba_2Ti_2(thd)_4(OEt)_8] \cdot 2EtOH$ (Kessler, 1994) and $[M_2Ti_2(acac)_4(OMe)_8]$ (M = Mg and Co) (Seisenbaeva, 2004), have been synthesized. The other heterometallic β-diketonates complexes such as $[Co_2Ti_2(acac)_2(OPr^i)_{10}]$, $[MAl_2(OPr^i)_4(acac)_4]$ [M = Co, Ni, Mg], $[Zn_2Al_2(OPr^i)_6\ (acac)_4]$ (Kessler, 2003), $[NiTi(OEt)_2(\mu\text{-}OEt)_6(acac)_4]$ (TahirMazhar, 2009) and $MW(acaca)_2(OMe)_{10}]$ (where M = Co, Ni, Mg, Zn) (Choujaa, 2013) have also been described in literature.

$$Ni(acac)_2 + Ti(OEt)_4 \xrightarrow[R.T]{Toluene} 1/2[Ni_2Ti_2(OEt)_2(\mu\text{-}OEt)_6(acac)_4] \quad (7)$$

$$M(acac)_2 + 2W(O)(OMe)_4 \xrightarrow{Toluene} 1/2M_2W_2(acac)_2(OMe)_{10} \quad (8)$$

or

$$+ W(O)(OMe)_3(acac)_2$$

M = Co, Ni, Mg, Zn

2.5.1.2 Metathesis Reactions

Another credible mechanism through which heterobimetallic derivatives could be prepared is a salt elimination or metathesis reaction, in which component parts of different molecules are exchanged to construct new structures. The alkali metal compounds are elegant reagents to transfer metallic ligands of the type to an electropositive metal center and have been used as building blocks for the construction of a variety of heterometal alkoxides (Veith, 2005; Veith, 2001) .

$$ZnCl_2 + 2\,NaFe(OR)_4 \longrightarrow Zn[Fe(OR)_4]_2 + 2\,NaCl \quad (9)$$

$R = Bu^t, Pr^i$

$$ZnCl_2 + 2/n\,[K\{Al(OR)_4\}]_n \longrightarrow [Zn\{Al(OPr^i)_4\}]_2 + 2KCl \quad (10)$$

The reaction of Et_2Zn with $NaOCH_2CH_2OH$ yielded a bimetallic zinc complex $NaOCH_2CH_2{\cdot}OZnEt$ which further reacts with Ph_3SnCl, Cp_2TiCl_2, and $Cp_2LuCl(THF)$ to produce corresponding heterobimetallic complexes (Nikitinskii, 2004).

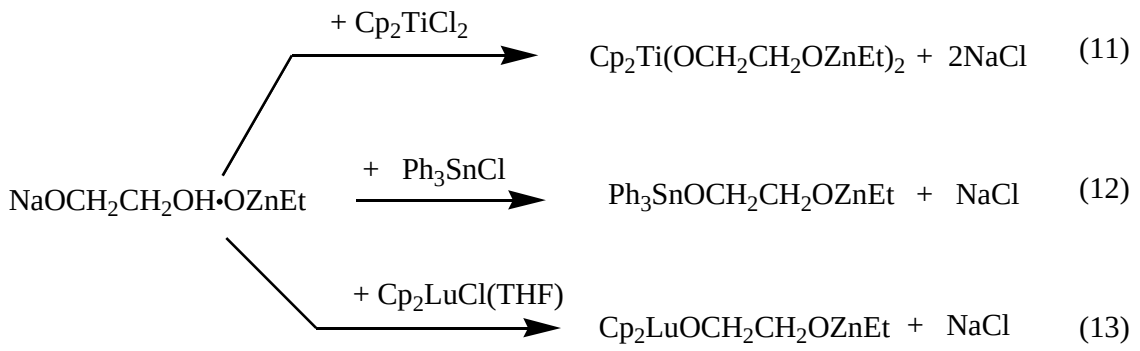

Similarly a series of iodide heterobimetallic isopropoxides $[I_2Sn\{Al(OPr^i)_4\}$, $[I_2Sn\{Ti(OPr^i)_5\}_2]$, $[I_2Sn\{Nb(OPr^i)_6\}_2]$ and $[I_3Sn\{Zr(OPr^i)_5(Pr^iOH)\}]$ is obtained on reacting SnI_4 with stoichiometric amounts of alkali-metal reagents $[KAl(OPr^i)_4]_n$, $[KTi(OPri)_5]_n$, $[KZr(OPr^i)_5]_n$, and $[KNb(OPr^i)_6]_n$, respectively, is reported (Veith, 1998).

In addition, examples may also be cited of a few other novel type of bimetallic alkoxometallate, which have been described in literature: $MTi(OPr^i)_5$ (M= Li, Na, K); $BaCu_6(OCEt_3)_8$; $Na_2Cu\{OCH(CF_3)_2\}_4$; $Ba\{Cu(OCMe(CF_3)_2)_3\}_2$; $Cu(I)_2Zr_2(OPr^i)_{10}$; $MZn(OBu)^t)_3$ (M = Na, K); and $M[Sn_2(OPr^i)_9\}_2$ (M = Ba, Zn, Cd).

2.5.1.3 Elimination Reactions

A more attentive choice to the development of advanced heterobimetallic is the elimination of small molecules (ester, alcohol, and water as a volatile by-product) through condensation as shown in chemical equations (14) (Mathur, 2001), (15) (Kumar, 2014) and (16) (Mathur, 2004). As a wide-ranging aspect, dissolution of anhydrous acetate in the presence of metal alkoxides, proceeds with the formation of adducts or of oxoacetatoalkoxides owing to liability of dialkyether. Sometimes heating is required for dissolution of some metal acetates and condensation occur with elimination of ester.

$$[Zn\{N(SiMe_3)_2\}_2] + 1/2\,[\{Al(OR)_3\}_4] \xrightarrow{ROH} [Zn\{Al(OR)_4\}_2\} + 2HN(SiMe_3)_2 \quad (14)$$

$$Mg(OAc)_2 + 2\,Ti(OPri)_4 \xrightarrow[190\ ^oC]{\text{decalin, xylene}} [MgO_2Ti_2(OPr^i_6] + 2\,AcOPr^i \quad (15)$$

$$2[Y_3(OBut)_9(ButOH)_2] + 3[Fe_2(OBut)_6] \xrightarrow[Pr^iOH\ (excess)]{} 3[YFe(OPri)_6(PriOH)]_2 + 40\,ButOH \quad (16)$$

Bismuth saliyclate $[Bi(Hsal)_3]_n$ is a very useful starting material for the synthesis of heterobimetallic compounds with the metal alkoxide $Ti(OPr^i)_4$ via alcohol elimination reactions and by following this synthetic strategy various heterobimetallic species including $Bi_2Ti_3(sal)_8(Hsal)_2$, $Bi_2Ti_4(sal)_{10}(Hsal)(OPr^i)\cdot H_2O$, $BiTi_4(sal)_7(OPr^i)_6$, $Bi_4Ti_4(sal)_{10}(OPr^i)_8$ and $Bi_8Ti_8(sal)_{20}(OPr^i)_{16}$ have been designed (Thurston, 2004).

Condensation reaction may take place between N-substituted diethanolaminate and metal alkoxide (Ghadwal, 2005)

$$Nb(PhDEA)_2(PhDEAH) + M(OPr^i)_3 \xrightarrow[\text{reflux, 2 h}]{C_6H_6} Nb(PhDEA)_3\{M(OPr^i)_2\} + Pr^iOH \quad (17)$$

$$PhDEA = PhN(CH_2CH_2\bar{O})_2\,;\ M = Al, Ga, Sb, Ti\ Ge, Ta$$

Condensation reaction also occurs between aminoalkoxides and metal carboxylate (Bakar, 2012; Hamid, 2007a; Shahid, 2009).

$$4\ Ti(dmae)_4 + 6\ Cu(OAc)_2{\cdot}2H_2O$$

$$\downarrow \text{ Toluene} \quad (18)$$

$$Ti_4(dmae)_6(\mu\text{–}OH)(\mu\text{ -}O)_6(OAc)_9{\cdot}H_2O\ 1.5(C_6H_5\text{ -}CH_3)$$

$$+3\ HOAc + 5\ H_2O + 10\ (dmaeH)$$

$$4\ Cd(OAc)_2\ 2H_2O \ + \ 4Ti(OEt)_4 \ + 4dmaeH \ + \ 8\ TFAH$$

$$\xrightarrow[R.T]{THF}$$

$$[Cd_4Ti_4(dmae)_4(TFA)_8(OAc)_4O_6] + \ 16EtOH \ + \ 4AcOH \ + 2H_2O \ + \ 2H_2 \qquad (19)$$

$$3\ M(OAc)_2 \cdot 2H_2O \ + \ 4Cu(dmae)_2$$

$$\downarrow$$

$$M_2(OAc)_6(\mu\text{-}O)Cu_4(dmae)_4 \cdot xH_2O \ + \ M(dmae)_2 \ + 2dmaeH \ + yH_2O \qquad (20)$$

$$M = Cd,\ x = 1,\ y = 4$$

$$M = Zn,\ x = 3,\ y = 2$$

2.5.2 Sulphide Ceramic Thin Films

To date, numerous classes of compounds have been synthesized and subsequently employed as SSPs for the preparation of metal sulphide thin films and a detail literature survey has been described here.

Cadmium and zinc dialkyldithiocarbamates have been widely investigated for the preparation of cadmium and zinc sulphide thin films by MOCVD. It is well known that the solid state pyrolysis of dithiocarbamate complexes under inert atmosphere generally yield the corresponding metal sulphide. However, the stoichiometry and phase of the metal sulphide deposited are greatly influenced by the pyrolysis conditions (Sharma, 1986). Single crystal X-ray investigations of various dialkyldithiocarbamates, either symmetrically as $[M(S_2CNR_2)_2]$ (M = Zn, Cd; R = Me, Et, or ^{i}Pr) (Bonamico, 1965; Klug, 1966; Miyamae, 1979) or unsymmetrically substituted as $[M(S_2CNMeR)_2]$ (M = Cd, Zn; R = Et, ^{n}Pr, ^{i}Pr, or ^{n}Bu) (Domenicano, 1968) have shown dimeric nature in the

solid-state (Figure 2.15) but are apparently monomeric in the vapour phase, as established by mass spectra (Motevalli, 1996).

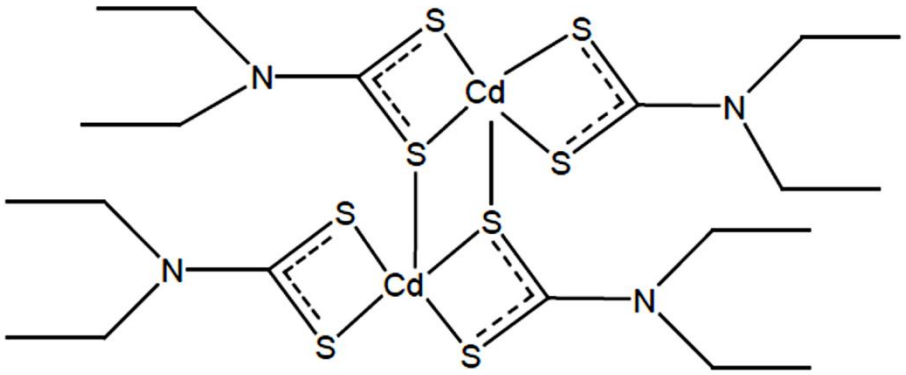

Figure 2.15: Structure of cadmium diethyldithiocarbamate.

Saunders *et al.* used diethyldithiocarbamate complexes of Zn and Cd as a single source precursor for the growth of ZnS, CdS films by Low Pressure (LP) CVD. Polycrystalline and hexagonal CdS films were deposited by MOCVD on glass substrate but thin epitaxial layers were obtained on InP (100) and GaAs (100) substrates. Such compounds can be used for the low-cost preparation of photovoltaic materials. The quality of the ZnS films was generally inferior than that of the CdS films as shown by Frigo *et al.* in a hot wall reactor (Frigo, 1989a).

Wold and co-workers reported the detailed study of the deposition of ZnS films by MOCVD using toluene solution of diethyldithiocarbamate in a sonicated spray evaporator. The influence of various parameters on the crystalline nature of the ZnS deposit was discussed and the epitaxial growth of cubic ZnS could be observed on GaAs (100) substrates at growth temperatures of 460-520 °C. The thermal decomposition of the precursor was also examined by pyrolysis GC-MS at pyrolyser temperature 400-500 °C. These evolved pyrolysates matched well with the earlier

results obtained from thermogravimetric (TG) decomposition of dithiocarbamates. The decomposition path is presented in Scheme (21) (Pike, 1993).

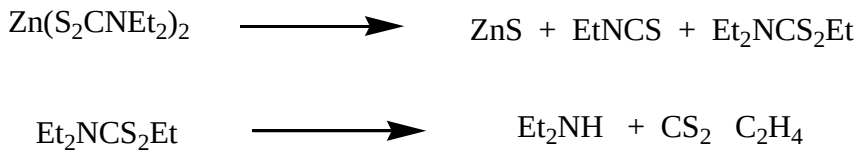

(21)

Nomura *et al.* developed the cubic β-ZnS zinc blende phase epitaxially on Si (111) by OMPVE, using the precursor $[Zn(S_2CN(Et)_2)_2]$ in a cold wall horizontal reactor. It has been observed that depositions conducted without carrier gas produced hexagonal α-ZnS films of poor crystallinity and morphology. The introduction of carrier gas (N_2) improved the film quality and allowed (111)-oriented β-ZnS to grow strongly (Nomura, 1995). Motevalli *et al.* investigated the deposition behaviour of unsymmetrically substituted zinc dithiocarbamate complexes. In trial volatilization experiments it was observed that at 150 °C, unsymmetrically substituted $[Zn(S_2CN(Me)Et)]_2$, $[Zn(S_2CN(Me)^nPr)]_2$ and $[Zn(S_2CN(Me)^nBu)]_2$ sublime above their melting points, whereas symmetrical derivate $[Zn(S_2CNEt_2]_2$ sublimes as a solid. The Precursor $[Zn(S_2CN(Me)^nBu)]_2$ successfully deposited ZnS on glass substrate, in a cold wall, LPCVD reactor, with the source at 150 °C and with a substrate temperature range of 450-490 °C. A film of hexagonal phase with highly oriented (0001) peak was obtained in a two hour run at 470 °C. A similar comparative study of $[Cd(SCNEt_2)_2]$ and $[Cd(SCN(Me)^nBu)_2]$ has confirmed the latter to be by far the more volatile (O'Brien, 1996).

The volatility of dithiocarbamate complexes can be enhanced by making associates of alkyl ligand, so as to form heteroleptic compounds of general formula $[M(R)(S_2CNR'_2)]$, (Me)Zn(diethyldithiocarbamate) (Hursthouse, 1991). These complexes were first synthesized by Noltes using the insertion reactions (22) and (23)

$$2\ MeZn(NEt_2) + 2CS_2 \longrightarrow [MeZn(S2CNEt_2) \quad (22)$$

Such compounds can be conveniently prepared via comproportionation or symproportionation reaction.

$$Me_2Zn + Zn(S_2CNEt_2) \longrightarrow [MeZn(S_2CNEt_{2)})]_2 \quad (23)$$

Alkyldithiocarbamate complexes with general formula $[M(R)(S_2CNR'_2)]$ (R or R' = Me or Et, M = Zn; R = Me, R' = Et, M = Cd) have been shown to sublime under mild conditions (100-150 °C). Films of ZnS have been grown by LPCVD on glass substates at 450 °C from $[(R)Zn(S_2CNEt_2)]_2$ with (R = Me, Me_3C and Me_3CCH_2), in a hot wall reactor (Hursthouse, 1991; Malik, 1992). CdS films deposited from $[(Me)Cd(S_2CNEt_2)]_2$ at 425 °C were of better quality than those prepared from $[(Me_3CCH_2)Cd(S_2CNEt_2)]_2$. Heteroleptic bis(dialkyldithiocarbamate) compounds of general formula $[LM(R_2NCS_2)_2]$ (M = Zn, Cd, Mn, Mn:Zn, or Zn:Cd and L = 1, 10–phenanthroline or 2,2'-bipyridine or 4,4' bipyridine) adducts were employed as single source precursors for the deposition of ZnS, CdS, (Zn, Cd)S, or (Zn, Mn)S films by MOCVD (Zemskova, 1996).

Zink *et al.* developed ZnS films from zinc xanthate (bis(O-isopropyldithiocarbonato)zinc(II)) precursor by thermal and photolytic MOCVD comparatively. Both series of depositions were carried out under low pressure, using glass plates and silicon wafers as substrates, the precursor being vapourised at 120 °C. Thermal depositions were effected at 350 °C. They grew polycrystalline, highly (0002) oriented, hexagonal ZnS-films. Photolytic depositions were run at an overall temperature of 120 °C using a XeCl excimer laser which afforded pure hexagonal ZnS films in contrast to the thermal CVD method (CheonTalaga, 1997b) . Nanophase ZnS and CdS films were developed on SiO_2 and SiO_2/Si(100) substrates in N_2 atmosphere in

temperature range of 250-400 °C by CVD using xanthate ($M(S_2COR_2)$ (M = Zn; R = ethyl and M = Zn, Cd and R = isopropyl) precursors (Barreca, 2004; Barreca, 2003).

Hampden-Smith co-workers reported the deposition of CdS, ZnS and $Cd_xZn_{1-x}S$ films from the precursors of general formula $M(SOCR)_2$ (tmeda) (tmeda = N,N,N,N-tetramethylehylenediamine), R being a methyl or a tert-butyl group, by AACVD (Nyman, 1996; Nyman, 1998). Single crystal structures of $[Zn(SOCCH_3)_2(tmeda)]$ and $[Cd(SOCCH_3)_2(tmeda)]$ displayed that they are isostructural, monomeric with the metal atom in a distorted tetrahedral coordination environment containing two nitrogens and two sulphurs. Good quality films of CdS and ZnS have been deposited from toluene solutions of these complexes at minimum temperatures of 125 °C. $Cd_xZn_{1-x}S$ films were grown at 175 °C from solutions of the precursors mixed in Cd/Zn ratios of 6:4, 5:5, 4:6 and 2.5:7.5. Compared to the solutions, the films appeared Cd-deficient by ca. 5-10% under deposition conditions. Thermally more-stable precursors of thiopivalate analogues of $[M(SOCC(CH_3)_3)_2$ (tmeda)] (M = Zn, Cd) were used to develop films of $Cd_xZn_{1-x}S$ with the stoichiometry of the solution (Cd/Zn =1).(Xu, 1995)

Thiophosphinates are another variety of compound that has been implemented as single-source precursors for the deposition of zinc and cadmium sulphide materials. CdS thin films were prepared using dimethylthiophosphinates and it was found that doping of excess phosphorus on n-type CdS films would lead to highly compensated semi insulating material (Takahashi, 1980). Thin films of ZnS and CdS were grown from $[M(S_2P^iBu_2)_2]_2$ (M = Zn, Cd) using homemade cold-wall low-pressure reactor (Byrom, 2000). Recently O'Brien et al reported the AACVD of ZnS and CdS using dithiobiurets $[M(N(SCNR_2)_2)_2]$ [M = Zn, Cd and R = methyl , ethyl] and thiobiurets $[M(SON(CNR_2)_2)_2]$ [M = Zn, Cd and R = isopropyl] as single source precursors at various temperatures between 300 to 450 °C resulted in high purity films with well oriented surface architectures (Ramasamy, 2011).

Nomura *et al.* effectively synthesized volatile precursors of alkyl indium thiolates $[(^{n}Bu)_2In(S^{i}Pr)]$ and $[(^{n}Bu)In(S^{i}Pr)_2]$, which are liquids at room temperature (Nomura, 1991). Low-pressure CVD experiments using these precursors produced tetragonal β-In_2S_3 on (111)-Si or quartz substrates. β-In_2S_3 was obtained amorphous at 300 °C and crystalline in the range 350-400 °C with strong (103) orientation, on (111)-Si at 400 °C. At 450°C, a mixture of In_6S_7 and β-In_2S_3 was acquired with predominantly In_6S_7. Barron and co-workers have deposited a novel metastable cubic GaS phase from the $[^{t}BuGaS]_4$ cube, at temperatures of 400 °C; and draw a correlation between the cubic phase observed and the cubane structure of the precursor (MacInnes, 1992). In a comparative MOCVD experiment three structurally distinct complexes, dimeric $[(^{t}Bu)_2Ga(\mu_2\text{-}S^{t}Bu)]_2$, tetrameric $[(^{t}Bu)Ga(\mu_3\text{-}S)]_4$ and heptameric $[(^{t}Bu)Ga(\mu_3\text{-}S)]_7$ were used as precursors in order to investigate phase control by molecular design. As expected, $[(^{t}Bu)Ga(\mu_3\text{-}S)]_4$ gave the cubic GaS at about 400 °C. At the same temperature $[(^{t}Bu)_2Ga(\mu_2\text{-}S^{t}Bu)]_2$, yielded poorly crystalline films of hexagonal GaS (MacInnes, 1993).

O'Brien and co-workers explored the precursor chemistry of indium and gallium dithioarbamates to deposit respective metal sulphide (Lazell, 2000; Lazell, 1999). Indium sulphide thin films were developed from dimethyl, diethyl or dineopentyl-indium diethyldithiocarbamates $[R_2In(S_2CNEt_2)]$ with (R = Me, Et, or Np) on GaAs substrate, using a cold wall low-pressure reactor. The phases generated from $Me_2InS_2CNEt_2$ were either β-In_2S_3 at 325 °C, In_6S_7 at 350 °C and 375 °C or InS + In_6S_7 at 400 °C and 425 °C. $[Et_2In(S_2CNEt_2)]$ produced β-In_2S_3 at 350 °C and 400 °C, whereas $[Np_2In(S_2CNEt_2)]$ yielded In_6S_7 at 375 and 400°C. The ethyl derivative differs from the other two, both by its aptitude for β-H elimination, and the growth of single phase cubic β-In_2S_3 over the whole temperature range studied. The analogous gallium compounds proved less efficient to obtain gallium sulphide thin films. Unsymmetrically

substituted indium (III) dialkyldithiocarbamates [$In(S_2CN(Me)R)_3$] (were R = n-butyl or n-hexyl) have been used as precursors for the growth of In_2S_3 on glass, (100)-GaAs or (111)-InP substrates using cold wall reactor under low pressure at 450-500 °C (O'Brien, 1998b). Symmetrically substituted indium trischelate complex of dibenzyldithiocarbamate $In(S_2CNBz_2)_3$ has been found as a potential SSP for the deposition of β-In_2S_3 films through CVD for photovoltaic applications (Hehemann, 2005).

Complexes [$In(SOCNR_2)_3$] (R= ethyl and isopropyl) were utilised as a single-source precursors for the deposition of tetragonal β-In_2S_3 by LP-MOCVD (Horley, 1999; Horley, 1998). Hampden-Smith and co-workers have taken the facile elimination of thioacetic anhydride from polyether adducts of group 2 metal thioacetates and employed it to adducts of gallium and indium thioacetates (Kunze, 1996). Gallium thioacetates adducts, [$Ga(SCOMe)_2(CH_3)(dmp)$] and [$Ga(SCOMe)_3(dmp)$] (dmp = 3,5-dimethylpyridine) (ShangHampden-Smith, 1996) and an ionic indium thioacetate complex, $[Hdmp]^+[In(SCOCH_3)_4]^-$ have been implemented in aerosol-assisted MOCVD experiments to prepare thin films of the metal sesquisulfides (ShangKunze, 1996). The respective proposed decomposition patterns for the gallium complexes are presented in schemes (24) and (25).

$$2Ga(SCOMe)_2(CH_3)(dmp) \longrightarrow 2dmpy + [MeC(O)SC(O)Me] + 2\,(Me_2CO) + Ga_2S_3 \quad (24)$$

$$2Ga(SCOMe)3(dmp) \longrightarrow 2dmpy + 3[MeC(O)SSC(O)Me] + Ga_2S3 \quad (25)$$

Tin and lead sulphides are narrow bandgap semiconductor materials. It is only recently that efforts have been made to produce them as thin films from single-source precursors. Cubic PbS thin films have been fabricated from lead dithiocarbamates: [$Pb(S_2CNEt_2)_2$] yielded PbS films in the temperature range of 425-500 °C by LPCVD

and in the temperature range of 230-300°C, by remote plasma-enhanced MOCVD (Fainer, 1996). Trindade and O'Brien employed $[Pb(S_2CN^nBu_2)_2]$ to obtain PbS films on glass and (100) Si in the temperature range of 400-600 °C, in a cold wall, low-pressure MOCVD reactor (Trindade, 1997). Similarly Afzaal *et al.* synthesized a series of lead dithiocarbamate complexes of general formula $[Pb(S_2CNRR')_2]$ (R = Me, Et; R' = ^{i}Pr, ^{n}Bu) and applied them to deposit cubic PbS films by AA and LPCVD on glass substrates (AfzaalEllwood, 2004). Furthermore, another series of symmetrically substituted complexes $[Pb(S_2CNR_2)_2]$ (where R = Me, benzyl, heptyl, octadecyl, dioctyl, Hex, Et or ^{n}Pr) was developed and utilized to deposit thin films of lead sulphide by AACVD (Akhtar, 2010).

The benzyl-substituted tin thiolates $[(R_3Sn)_2S]$ and $[R_2SnS]_3$ have been designed and studied as single-source precursors to tin sulphide (Boudjouk, 1996). Pyrolysis of compounds at 450 °C gave gray or black powders and dibenzyl as the main products. The powders obtained were characterized as SnS with some contamination from elemental tin. Thermal decomposition of $[Ph_2Sn(S_2CN(CH_2)_4)_2]$ and $[Ph_3Sn(S_2CN(CH_2)_4)]$ generated a mixture of orthorhombic Sn_2S_3 and SnS (Menezes, 2004). Similarly APCVD of $[Me_2Sn(S_2CN(C_4H_9)CH_3)]$ and $[BuSn(S_2CN(C_4H_9)CH_3)_3]$ at 350–550 °C in the presence of H_2S, resulted in formation of SnS and Sn_2S_3 films on glass (Kana, 2001). In an attempt to find a mild, low-temperature route to the preparation of SnS thin films, the APCVD reaction of $[nBu_3SnO_2CCF_3]$ with H_2S has been investigated. Tin (II) sulphide films were deposited at 350–600°C under nitrogen, and no impurity from fluorine was detected in the resulting films (Price, 2000). Recently, a series of diorganotin complexes of dithiocarbamates $[Sn(C_4H_9)_2(S_2CN(RR')_2)_2]$ (R, R' = ethyl; butyl and R = methyl, R' = butyl; R = methyl, R' = hexyl) and $[Sn(C_6H_5)_2(S_2CN(R\ R')_2)_2]$ (R, R' = ethyl; butyl; R = methyl, R' = butyl; R = methyl, R' = hexyl) have been synthesized and used as single source precursors for

the deposition of phase pure orthorhombic SnS thin films by AACVD at temperatures from 400 °C to 530 °C (Ramasamy, 2013).

Bi_2S_3 and Sb_2S_3 are important class of semiconductors that are already used in numerous technological components as e.g. photoconducting targets, electronic and optoelectronic devices, thermoelectric devices, hydrogen storage materials and sensors. An example of a single-source route is carried out on the deposition of thin films of Bi_2S_3 from bismuth dithiocarbamates, $[Bi(S_2CNRR')_3]$ (R = Et, Me, R′ = hexyl) by LP-MOCVD (Monteiro, 2001; Monteiro, 2000). Molloy et al studied Sb_2S_3 thin films by AACVD using a variety of single source precursors including antimony dithiocarbamates $Sb(S_2CNR_2)_3$ (R = Et, Pip and MeCy), dithiophosphates $Sb(S_2P(OR)_2)_3$ (R = Et, ^{i}Bu) and xanthate $Sb(S_2COR_2)_3$ (R= ^{n}Pr, ^{i}Bu) (Castro, 2008).

Titanium and molybdenum sulphide find applications as lubricant coatings, electrode materials or catalysts. TiS_2 and MoS_2 thin films were fabricated using $[M(S^tBu)_4]$ as the precursor through conventional hot wall LP-MOCVD. The precursor was heated to 45 °C and the substrate in the range 150-270 °C for TiS_2 and 110-350 °C for MoS_2 (CheonGozum, 1997) . Winter *et al.* have deposited TiS_2 using adducts of titanium tetrachloride with cycloalkanethiols $[TiCl_4(HSC_6H_{11})_2]$. The films were produced on silicon and glass substrates in a hot wall reactor using sublimation temperature of 50 °C and deposition temperatures in the range 200-600 °C (Winter, 1993). $[(\eta^5\text{-}C_5H_5)_2Ti(S^tBu)_2]$ and $[(\eta^5\text{-}C_5H_5)_2Ti(SEt)_2]$ have been employed in hot wall LP-MOCVD trails with helium as the carrier gas, the films had S/Ti elemental ratios in the range of 0.5-1.5, depending on the type of precursor and deposition temperature which was varied from 400-650 °C (Senocq, 1996). Gold colour and reflective TiS_2 films have been grown using precursor $[Ti(SBu^t)_4]$ solutions in hexanes, dichloromethane or toluene through AACVD on glass substrate at temperatures between 150 and 300 °C (Carmalt, 2004). Thin films of nickel sulphide and palladium sulphide have been

developed from metal complexes of bis(isopropylxanthate) [$M(S_2COCHMe_2)_2$] (M = Ni or Pd) (CheonTalaga, 1997a). The precursors were sublimed at 95 °C (Ni) and 110 °C (Pd) under 10^{-2} Torr and depositions occurred on glass or silicon wafers at 300°C for NiS and 350 °C for PdS. In addition, thin films of nickel sulfide ($NiS_{1.03}$, NiS_2,α-Ni_7S_6) and palladium sulfide (PdS, $Pd_{16}S_7$, Pd_{4S},) were obtained from AACVD using dithiocarbamate precursors of the type $M(S_2CNRR')_2$ (M= Ni, Pd; RR' =Et_2, MeEt, Me^{n}Bu, or Me^{n}Hex) on glass substrates at temperatures of 400–525 °C (O'Brien, 2006). Moreover Alam *et al* designed a series of nickel butylxanthate pyridine adducts [$Ni(S_2CO^nBu)_2$ $(py)_2$] (py) = pyridine derivatives) and tested as single-source precursors for the growth of phase-pure thin films of rhombohedral NiS on several substrates (plane glass, FTO and TiO_2 and porous ceramic) by AACVD (Alam, 2008).

Dithiocarbamate complexes of several transition metals including Fe, Co, Ni and Cu have been studied as single source precursors for metal sulphide thin films. Nomura *et al.* have produced copper-deficient $Cu_{1.96}S$ films by LP-MOCVD from copper(II) bis(diethyl-dithiocarbamate) [$Cu(S_2CNEt_2)_2$] using N_2 as the carrier gas with source temperature of 200 °C and deposition temperature of 400 °C on a silica substrate (Nomura, 1996). The same precursor has been tested in RPECVD experiments to develop Cu_2S films at the deposition temperature range of 200-400 °C under helium(Rumyantsev, 1999). Films obtained on fused silica were a mixture of hexagonal and cubic phases, whereas films deposited on silica were in the cubic phase. O'Brien and co-workers have fabricated high-purity Cu_2S thin films from the [$Cu(S_2CN(Me)Hex)_2$] precursors respectively (McAleese, 1998). In a recent investigation thiobiuret complex [$Cu(SON(CN^iPr_2)_2)_2$] was also used for the deposition of nanostructured copper sulfide thin films by AACVD (Abdelhady, 2011). Pyrite FeS_2 thin films have been grown from symmetrical and unsymmetrical dialkyl dithiocarbamate complexes of iron [$Fe(S_2CNRR')_3$] R = Me, ^{n}Bu; R' = ^{i}Pr, ^{n}Bu by

AACVD in the temperature range of 375-450 °C (O'Brien, 1999). Several iron thiobiurets complexes [$Fe(SON(CN^{i}Pr_2)_2)_3$, $Fe_2(\mu\text{-}OMe)_2(SON(CNEt_2)_2)_2$, $Fe(SON(CNEt_2)_2)_3$, and $Fe(SON(CNMe_2)_2)_3$] were employed as AACVD precursors but none of them could generate phase pure pyrite (FeS_2) at any temperature from 300 to 450 °C (K Ramasamy, 2010). Cubic manganese sulphide thin films were developed from [$Mn(S_2CN(Me)Hex)_3$] on a glass substrate in argon atmosphere (flow rate of 200 sccm) in the temperature range of 475-500°C (Srouji, 2005). Similarly thin films of cobalt sulphides were deposited from cobalt complex of methylhexyldithiocarbamate in the temperature range of 375-475°C on glass substrate by AACVD and yielded mixtures of $Co_{1-x}S$, CoS_2 and $Co_3S_{4.89}$. AACVD experiments were also carried out from cobalt(III) dithiobiuret [$Co\{N\text{-}(SCNMe_2)_2\}_3$], [$Co\{N\text{-}(SCNEt_2)_2\}_3$] and cobalt(II) thiobiuret [$Co\{N(SOCN^{i}Pr_2)_2\}_2$] to obtain $Co_{1-x}S$ and Co_3S_4 films respectively at the temperature range of 350-500 °C(Karthik Ramasamy, 2010) .

2.6 Characterization Techniques

2.6.1 Characterization of Precursors

2.6.1.1 Elemental Analysis

Elemental analysis is the qualitative detection and quantitative determination of chemical elements (atoms, ions) in a sample. Elemental analysis results may pose difficulties in deciding at the exact composition of heterometallic complexes due to the change in metal ligand ratio. However with the support of atomic absorption analysis of metallic elements, the CHN results may become productive to find the stoichiometry of the heterometallic compounds. The conformation of the predictions is further made from single crystal X-ray analysis.

2.6.1.2 Infrared (IR) Spectroscopy

Infrared (IR) spectroscopy is a versatile analytical technique used for the detection of organic and inorganic compounds. An infrared spectrum is recorded by passing IR radiation through a sample and measuring the absorption frequencies that correlate with the structural features of the molecule. This spectroscopic technique mainly focuses on the detection of chemical functional groups present in a compound. As a principle different functional groups attached to a molecule produce characteristic absorption in IR spectrum. Thus infrared spectroscopy is an important and popular tool for structural interpretation and compound identification.

The IR spectrum ranges from 14,000 cm^{-1} to 10 cm^{-1} can be divided into far-, mid- and the near-infrared regions. The region of most attention for chemical investigation is the mid-infrared region (4000–400 cm^{-1}) which relates to changes in vibrational energies within the molecules. The far infrared region (400–10 cm^{-1}) is valuable for molecules comprising heavy atoms such as inorganic compounds but needs rather specialized experimental methods (Coates, 2000).

Although IR data, presents useful information for the compounds with functionalized ligands, it faces problems in structural examination of heterometallic systems because of the screening of important bands. Occasionally a spectrum becomes very complex because of the congested ligand environment and specific absorption band cannot be easily resolved. Nevertheless, IR spectroscopy has been used as a supporting technique for the identification of the functional groups existing in the heterometallic compounds rather than the complete structural analysis.

The nature of O-H group, whether it is bonded with metal center or is a part of ligand can be recognized by the absorption frequency. The coordination behaviour of carboxylate to metal can be proposed by determining the factor $\Delta\nu = [\nu(COO)_{asym}$ and $\nu(COO^{-})_{sym}$ by IR spectroscopy; if $\Delta\nu < 200$ cm^{-1}, the carboxylate behave as a bridging

ligand (Deacon, 1985). This technique has also been used to determine the presence of several alkoxy groups as every metal-ligand bond produces a characteristic absorption such as $\nu_{OMe} \cong 1180$; $\nu_{OEt} \cong 1025$ and 1070; $\nu_{OPr} \cong 840$, 1125 and 1160 cm^{-1}, respectively in various mixed metal alkoxides. The terminal and bridging alkoxy groups in various heterometallic species may be identified on the basis of IR absorption bands present in the area around 1020-1180 and 940-1070 cm^{-1}, respectively. Heterometallic β –diketonates shows two absorption bands around 1567-1575 cm^{-1} due to C⁻⁻⁻⁻⁻⁻O and 1509-1512 cm^{-1} due to C⁻⁻⁻⁻⁻⁻C stretching vibrations. A band detected in the region less than 500 cm^{-1} may be correspond to M-O stretching vibrational band for these compounds.

In case of inorganic materials IR spectroscopy is very useful in finding the nature of material and added impurities both in bulk material and thin films. IR is also helpful for measuring the thickness and of epitaxial layers particularly when substrate and layers are of similar types (Si). Furthermore, FTIR has enormous applications like determination of bonding in diamond like carbon films (Dischler, 1983), determination of H-content and moisture absorption on plasma deposited films, determination of the B and P concentration in borosilicate (Krishnan, 1995), and phososilicate (Zearing, 1981) passivation layers, H concentration in silicon nitride passivation layers and carbon impurity concentration in GaAs. The infrared spectroscopy has proved to be a useful analytical technique for industrial applications including pharmaceutical, food, agricultural, pulp and paper, paint and environmental fields.

2.6.1.3 Nuclear Magnetic Resonance (NMR)

Multinuclear NMR is a widely applied spectroscopic technique for the structural and sterochemical elucidation of monometallic complexes, and may also useful for oligometallic derivatives comprising more than one metallic center provided that metal

species are NMR active, in addition to ^{1}H and ^{13}C. By the use of specific probes and careful data collection we may able for the determination of coordination environment around the metal atoms in heterometallic species both in solution and solid state (Mehrotra, 1994).

2.6.1.4 Mass Spectrometry (MS)

Mass spectrometry provides useful information on the structural details of single source precursor compounds subject to their stability with respect to disproportionation reaction in vapour phase. The mass spectral results have proven that fast atom bombardment mass spectrometry (FABMS) can be widely employed for the characterization of heterometallic precursors particularly for non-volatile polymeric precursors. Mass spectrometry is helpful in finding the molecular formula of the complexes where crystal data is not available especially for the low molecular weight stable oligomers (Hamid, 2006).

2.6.1.5 Thermogravimetric Analysis (TGA)

Thermogravimetric analysis (TGA) is an analytical technique used to access the material's thermal stability and its fraction of evolved components by observing the weight changes, that occurs as a sample is heated (Prime, 2009). TG investigations are generally made in air or in inert atmosphere such as Helium or Argon, and the loss in weight is measured as a function of increasing temperature. Sometimes measurements are carried out in presence of lean oxygen (1 to 5% O_2 in N_2 or He) to slow down oxidation. Moreover, some instruments can also record the temperature difference between the sample and reference pans (differential thermal analysis or DTA), or the heat flow into the sample pan compared to that of reference pan (differential scanning

calorimetry or DSC). The latter can be used to measure the energy released or absorbed via chemical reactions during heating process.

During TG analysis, when materials are heated they can lose weight either by a simple drying process or in the result of complicated chemical reactions that release gases while increase in weight in certain materials is due to reaction with the atmosphere in the testing environment. We study TGA to investigate the decomposition temperature of the precursor to give stable ceramic oxide or sulphide material. By calculating the percentage of residue amount, we may be able to decide about the final oxide or sulphide product. However, the assignment of the released fragments simply based upon TGA without coupled device is impossible.

2.6.1.6 X-ray Crystallography

X-ray crystallography is a powerful tool that can see inside of crystals and allow the detailed determination of their structures, geometries and unit cells size. Based on the diffraction pattern obtained from X-ray scattering off the orderly arranged molecules or atoms in the crystal, the electron density map can be refined to generate valuable information about their atomic positions, bond lengths and angles and disorder.

The most precise method of X-ray crystallography is the single crystal X-ray diffraction, in which X-ray beam is reflected from regularly spaced planes of a single crystal, constructing a diffraction pattern of spots called reflections. Each reflection relates to one set of planes with in the crystal and the density of electrons is determined from position and brightness of the numerous reflections collected as the crystal is steadily rotated in X-ray beam. This density along with supplementary data, allows to be inferred the atomic positions and chemical bonds. For single crystals of adequate purity and uniformity, X-ray diffraction data can estimate the mean chemical bond lengths and angles to within a few thousands of an Å and within a few tenths of a

degree, respectively. The data also permit to determine the static and dynamic disorder in the atomic positions, which is generally less than a few tenths of an Å . At its most basic level, X-ray crystallography is advantageous in finding known materials, characterizing new materials and in discriminating materials that appear analogous by other experiments.

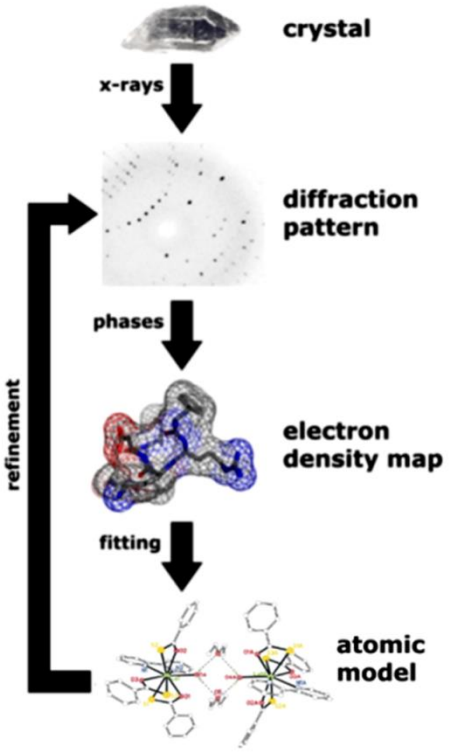

Figure 2.16: Schematic presentation of crystal analysis and refinement.

The technique of single crystal X-ray crystallography involves three basic steps to model the crystal structure. The first and most important step is to develop a suitable crystal of the material under investigation. The crystal should be adequately large, pure in composition and regular in structure, free of imperfections such as cracks or twinning. The second step is the mounting of the crystal in an intense beam of monochromatic X-rays, generating the organized pattern of reflections. The third step is refinement of the thousands of the reflections intensities composed by the full rotation of the crystal. The reflection data are combined computationally with corresponding

chemical details to develop and refine a model of the positioning of atoms with in the crystal and final refined model is named as crystal structure as shown in Figure 2.16.

2.6.2 Characterization of Thin films

2.6.2.1 Film Adhesion Test

The most simple and frequently used test for adhesive bonding is peel test and a variant of the peel test is the tape test in which adhesive tape is fixed on the film surface and then a peel test is applied. This test defines the adhesion quality of film that is for distinguishing poor adhesion (upto about 1000 psi). This test largely depends on the parameters including type of tape, method of application of the tape, pull angle, pull rate etc. Practically a line is scratched on the film (cut crosshatched) beneath the tape to provide an edge on which the tape pulls. If the quality of the films is poor, it is pulled out with the tape from substrate.

2.6.2.2 X-Ray Powder Diffractions

X-ray powder diffraction (XRPD) is a non-destructive technique used for the identification of crystalline phase and measuring the degree of crystallinity of thin films. The diffraction pattern obtained allows the identification of the chemical compound or phase composition of the film, texture of the film, preferred orientation of crystallites, the crystallite size and presence of film stress.

The crystal structure is tough to resolve for the systems other than simple high symmetry crystals. Accordingly it is mostly used as a finger print method for identifying the presence of a known compound or phase in a material. A huge library of powder pattern of known compounds is available at JCPDS (Joint Committee for Powder Diffraction standards) files. When the powder pattern of the specimen has been

collected and both d_{hkl} spacing and intensity of lines recorded, these can be compared with the patterns of known compounds in the library.

2.6.2.3 Scanning Electron Microscope (SEM) and Energy Dispersive X-ray Analysis (EDX)

Scanning electron microscopy (SEM) uses a focused electron probe to extract structural and chemical information point-by-point from an area of interest in the sample. The high spatial resolution of an SEM makes it a powerful tool to characterise a wide range of specimens at the nanometre to micrometre length scales. SEM offers higher magnification with greater depth resolution than optical microscopes. SEM images may be deformed by the surface potential which develops on insulators edge effects at sharp contours. Non-conductive samples may be coated with a thin conductive layer of Au, Pt or carbon to disperse the surface charge. SEM images at less than 20A resolution have been obtained with several hundred thousand times magnification.

One of the most common analytical extensions to the SEM is the energy dispersive X-ray spectrometer (EDX). The useful energy extent for EDX systems is from 1.0 to 220 KeV, which limits the analysis to elements with $Z > 9$. EDX detectors with thin protective layers or without protective layer, when worked in ultra-high vacuum systems, enable the analysis of the lighter elements down to B. The analysis depth is dependent on the path length of the X-rays, not on the primary electron beam. As a result EDX signals may originate from depths of 0.5μm or more. Due to pulse counting mode of EDX system, it has capability to detect the characteristic X-rays for all elements above F in the periodic table. Therefore, EDX system takes a much shorter time to scan the complete spectrum as compared with wavelength dispersive X-ray (WDX) analyser. Moreover, EDX analyser has a resolution of approximately 150 eV, whereas a WDX analyser has a resolution of 5eV. The detector used with EDX is of Li-

doped Si that requires liquid nitrogen cooling to keep the Li from diffusing and rapidly degrading the detectors performance.

2.7 Applications of Functional Ceramic Thin Films and Coatings

Nanostructured thin films of metal oxides and sulphides have shown their revival of interest in the fabrication of energy saving and harvesting devices such as lithium ion batteries (Dillon, 2008; Lai, 2010; Lai, 2009; Lee, 2009), fuel cells(Asamoto, 2009; Grgicak, 2007), solar cells (Colodrero, 2009; X. Li, 2010; J.-C. Wang, 2010), transistors/FETs (Han, 2012; Kim, 2011; Moon, 2010; Park, 2012), light emitting devices (LEDs) (Gang, 2012; Smet, 2010; Van den Eeckhout, 2011), hydrogen production by water photolysis and its storage, (MansoorEhsan, 2013; Tahir, 2013; Tseng, 2012; Zhang, 2013) water and air purification by degradation and adsorption of organic/inorganic pollutants and toxic gases (De Melo, 2012; Jo, 2012; Xu, 2012; Zhao, 2012), environmental monitoring by their applications in the fabrication of gas, humidity and temperature sensors (Gong, 2011; Karami, 2013; Sen, 2010; Zhao, 2008), UV-screening and photodetectors (Afsal, 2012; Fang, 2010; L. Li, 2010). They have also fabulous applications in biological and medical sciences such as drug delivery, cancer treatments, fluorescent imaging, bio labeling and bio tagging etc (Alessio, 2011; Farrer, 2011; Im, 2010). Nanoarchitectural functional oxides and sulphides films have strong ferromagnetism with high Curie temperature and are used as magnetic read, write heads and data storage devices. Transition metal doped nanostructured oxides such as ZnO, TiO_2 etc (Cong, 2009; Tuan, 2004) and sulphides $Co_xZn_{1-x}S$ (Lai, 2012) are called diluted magnetic semiconductors (DMS) and are applicable in the fabrication of spin based nanoscale electronic devices i.e. spintronics spin light-emitting diodes, nonvolatile memory and spinvalve transistors (Fabian, 2007; Pearton, 2004).

Similarly Zn, Cd sulphides and rare earth elements such as Eu, Nd oxides are usually used as phosphor materials for the fabrication of LEDs, displays and laser materials (Gao, 2013; Saha, 2013). One of the salient features of oxide/sulphides nanomaterials is bio compatibility which opens an avenue for interdisciplinary research between physicists and biotechnologists. Fluorine doped SnO_2 film have potential application in architectural glass applications due to its low emissivity for thermal infrared heat. SnO_2, WO_3 and ZnO nanomaterials are regarded as the most important sensor materials for detecting leakage of several inflammable environmental polluting gases (CO, NO_2) (Chen, 2013; Liu, 2011; Shi, 2013) and species such as ethanol for breath analyser (Beckers, 2013) owing to their high sensitivity to low gas concentrations. SnS, ZnS and CdS nanostructures exhibit excellent photoelectrical properties for near-infrared detectors, photovoltaics and photodetectors applications (Y. Chen, 2012; Jiang, 2012; Saha, 2013; Sahraei, 2010). β-In_2S_3 and Indium-doped tin oxide films are potential materials for flat panel displays because of their high electrical conductivity and sensitivity (Qiu, 2011; Štengl, 2012).

2.7.1 Photochemistry of Metal Sulphide Thin films for Energy Applications

Energy and environmental problems are the major challenges facing mankind in the twenty-first century. Currently, energy demands are being met by the conventional energy sources such as carbon-based fuel and the fossil reserves. The resource accrued over millions of years is swiftly being exhausted and the combustion has led to pollution severity and environment fluctuations. It is widely believed that CO_2 (besides CH_4 and NO_x) profoundly contributes to the greenhouse effect (X. Chen, 2012). Due to dangerous consequences of climate change and fossil fuel consumption, there is growing interest for evolution of renewable energy (Abbasi, 2011) sources such as solar, wind, ocean tides and sea stream energies, in addition to the thermal energy from

hot water springs and volcanoes. Hydrogen is believed to be clean, promising and sustainable energy carrier that can be used in mobile and stationary applications (Chen, 2010; Osterloh, 2013). Hydrogen can be made from a wide range of domestic resources such as (i) reforming natural gas (CH_4), methanol (CH_3OH), gasoline (C_8H_{18}), ethanol (C_2H_3OH) and (ii) water based hydrogen generation through electrochemical, photoelectrochemical (PEC) and photobiological routes. Out of all possible sources, production of hydrogen from water using solar energy seems to be the most attractive idea. However, in order to use hydrogen as a commercial fuel, it must be produced and made available at low priced without creating global warming and ecological imbalance. Solar energy driven photoelectrochemical, (PEC) water splitting combines several attractive features for energy utilization. Both the energy source (sun) and the reactive media (water) are readily available and are renewable, and the resultant fuel (generated H_2) and the emission with fuel consumption (water) are each environmentally benign (Shen, 2012; Shen, 2011). Photoelectrochemical (PEC) solar cells for the generation of hydrogen have been extensively studied and are the matter of great attention during last two decades.

An investigation of photoelectrochemical (PEC) cells, converting solar energy to electrical energy or chemical energy was initiated by Honda and Fujishima in 1972. They succeeded in water splitting by illumination of TiO_2 photoelectrode. However, these systems resulted in low efficiencies as only the UV portion of the solar spectrum was used. Since then, photoelectrochemical properties of semiconductors have been intensively studied (Cho, 2011; Iwashina, 2011; Li, 2011; Wheeler, 2012). In order to improve the efficiency of a PEC cells some of the prime requirements for semiconductor photoelectrode materials should be considered for an efficient photo cleavage of water:

(i) Bandgap width and position of the conduction and valence band

(ii) Stability to photocorrosion

(iii) Absorption coefficient must be large

(iv) Hole's diffusion length should be small

(v) Space-charge layer should be relatively large

In the photoelectrochemical process, the light absorbed in a semiconductor is used to decompose water molecules in molecular hydrogen and oxygen. Light absorbed by the semiconductor generates electron-hole pairs that in turn help the Oxidation-Reduction reactions, at the photoanode and the photocathode, to produce oxygen and hydrogen respectively. The net photochemical reaction can be summarized as

$$H_2O + \text{Light} \longrightarrow H_2 + 1/2\ O_2 \quad (26)$$

Photons having energy greater than the band gap, E_g are absorbed by the semiconductor generating electron-hole pair

$$2h\nu \longrightarrow 2\bar{e} + 2\bar{h} \quad (27)$$

The electrons and holes are separated due to the potential generated at the interface of the semiconductor-electrolyte due to the band bending. The holes move to the interface and react with water to producing oxygen:

$$2\,\bar{h}^{+} + H_2O \longrightarrow 1/2\ O_2\ (gas) + 2\overset{+}{H}\ (aq) \quad (28)$$

The electrons travel in the external circuit and arrive at the interface between the counter electrode and electrolyte. There, the reduce the H ions to H_2.

$$2\bar{e} + 2\ \overset{+}{H}(aq) \longrightarrow H_2(gas) \quad (29)$$

The complete reaction is absorption of photon and splitting of water into hydrogen and oxygen as illustrated in Figure 2.17

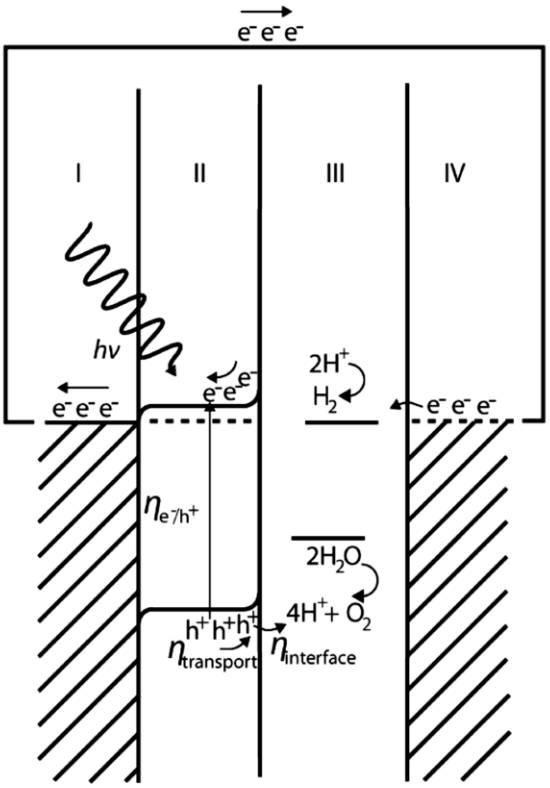

Figure 2.17: Band diagram of a photoelectrochemical water-splitting cell, illustrating the various processes of photon absorption, electron-hole excitation, charge transport, and interfacial reactions. Region I represents an ohmic contact. Region II is a single band gap n-type semiconductor. Region III is the aqueous electrolyte. Region IV is the counter electrode. A connection between the ohmic contact and the counter electrode completes the circuit.

The oxidation/reduction potential for this reaction is about ~1.23 eV (G = +237.7KJ/mol). This corresponds to photon below about 1000nm (Figure 1.19) which covers a large part of spectrum. Kinetic and thermodynamic considerations however, mean that initiation of this reaction requires a potential to increase this energy up to ~1.4-1.6eV (840nm). In order to perform successful water splitting upon irradiation, the valence band of semiconductor has to be located at a lower energy level than the chemical potential of O_2 evolution (H_2O/O_2) in solution, and the conduction band has to be positioned at a higher energy level than the chemical potential of H_2 evolution

(H_2/H). If the position of the energy levels of the valance and conduction band is not fulfilled an external bias has to be applied in order to induce the photo-oxidation process.

Figure 2.18 shows band levels of various semiconductor materials and only two oxides materials α-Fe_2O_3 and WO_3 possess suitable band structures to fulfil the requirements for the PEC cell. Although CdS having a suitable band structure and a narrow band gap as compared to metal oxides seems attractive candidate for visible light responsive photocatalysis. However, S^{2-} in CdS is easily oxidized by photogenerated holes and accompanied by the elution of Cd^{2+} into the solution, such photocorrosion is in fact a demerit of a metal sulphide photocatalyst (Zhu, 2009).

$$CdS + 2h^{+} \longrightarrow Cd^{2+} + S \qquad (30)$$

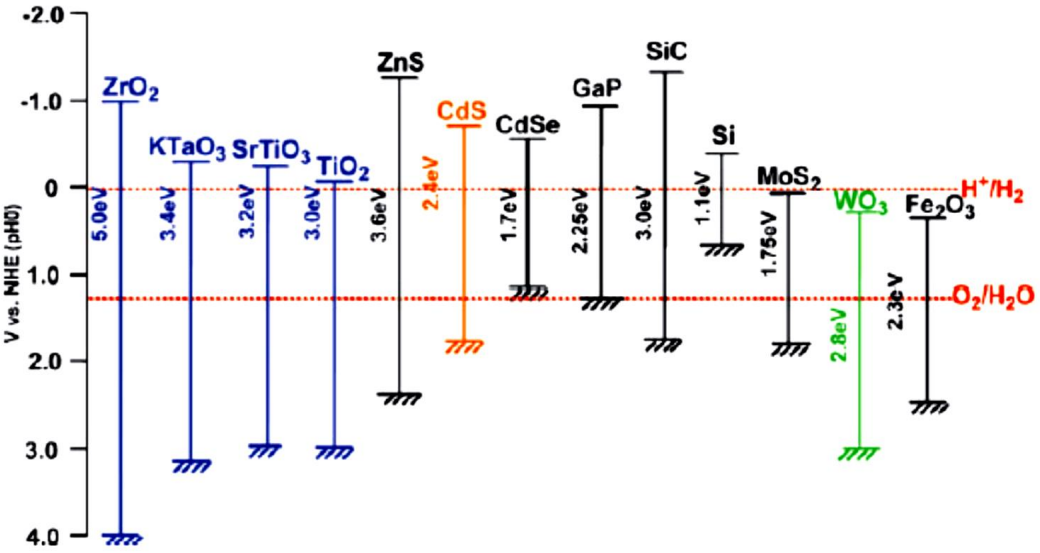

Figure 2.18: Relationship between band structure of semiconductor and redox potentials of water splitting (Choudhary, 2012).

Sacrificial reagents (S^{2-} or SO_3^{2-}) are often employed to evaluate the photocatalytic activity of metal sulphides for water splitting (Kudo, 2009; Li, 2011; Tsuji, 2010; L. Wang, 2010). Photoelectrochemical (PEC) studies of metal sulphide photocatalyst is

carried out in aqueous solutions including easily oxidizable reducing reagents such as alcohol and SO_3^{2-} or S^{2-}, photogenerated holes irreversibly oxidize the reducing reagents instead of water. This makes the photocatalyst electron rich and a H_2 evolution reaction is enhanced (Figure 2.19) .

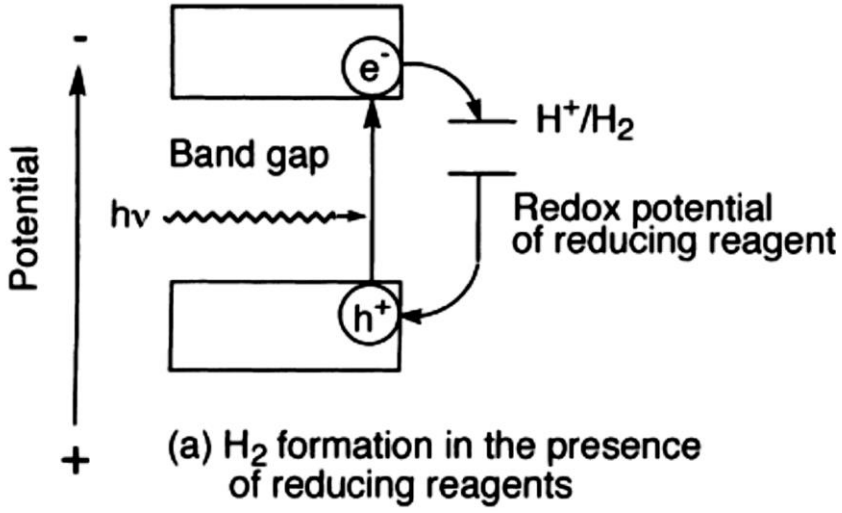

Figure 2.19: Photocatalytic H_2 evolution in the presence of sacrificial reagents

CHAPTER 3

MATERIALS AND METHODS

3.1 General Consideration

$AgNO_3$, $Bi(NO_3)_3{\cdot}5H_2O$, $Co(OAc)_2{\cdot}4H_2O$, $Cd(NO_3)_2{\cdot}H_2O$, $Fe(NO_3)_3{\cdot}9H_2O$, $InCl_3$, , $Pd(NO_3)_2{\cdot}2H_2O$, $Ti(Pro^i)_4$, $ZnCl_2$, sodium acetate trihydrate, trifluoroacetic acid bezylmethylamine, cyclohexylmethylamine, diethylamine, dicyclohexylamine, di-iso-propylamine, dihexylamine, piperidine were purchased from Sigma-Aldrich chemicals. Acetone, chloroform, methanol, pyridine, toluene, tetrahydrofuran were purchased from Fisher chemicals.

The syntheses were executed under an inert atmosphere using a double manifold vacuum line, attached to a RZ 6 ROTARY VANE PUMP (Model: 698132) vacuum pump and a dry argon gas cylinder. All flasks were evacuated and then purged with argon at least three times prior to usage, with external heat applied where deemed necessary. Liquid air-sensitive reagents were shifted to Schlenk type flask either by cannula or using disposable syringes. Solvents were rigorously dried over sodium bezophenonate and distilled immediately before use.

Tetrakis(2-ethoxyethanalato)titanium(IV) (Johnson, 2001) and $[Fe_3O(OAc)_6(H_2O)_3]NO_3{\cdot}4H_2O$ (Turte, 1994) were prepared according to reported procedures and were used without any further characterization. The dithiocarbamate ligands were generated as described in literature (Brewer, 1994).

Melting points of complexes (**1**)-(**3**) and (**4**)-(**15**) were recorded on a Mitamura Riken Kogyo and Gallenkamp MPD350.BM3.5 apparatus respectively and are uncorrected. Elemental analyses of complexes (**1**)-(**3**) and (**4**)-(**15**) were performed using CHN Analyzer LECO model CHNS-932 and Perkin Elmer CHNS/O Analyzer series II 2400, respectively. Infrared spectrum was recorded on a Perkin Elmer Spectrum 400 FT-

IR/FT-FIR spectrometer. Controlled thermal analyses of complexes (**1**)-(**3**) were investigated using Perkin Elmer Thermogravimetric Analyzer TGA-7 with computer interface while complexes (**4**)-(**15**) were analysed by using a METTLER TOLEDO TGA/ SDTA 851e Thermogravimetric Analyzer. The thermal measurements were carried out in an alumina crucible under an atmosphere of flowing nitrogen gas (25 mL min^{-1}) with a heating rate of 10 ^{o}C min^{-1}. The proton nuclear magnetic resonance (^{1}H-NMR) spectra were recorded using a Bruker AC300 FT-NMR spectrometer, using $CDCl_3$ as solvent. ^{1}H NMR spectra were referenced to the solvent signal and the chemical shifts are reported relative to Me_4Si.

Film surface morphology and composition were determined by field-emission gun scanning electron microscope (FE-SEM, FEI Quanta 400) operated at an accelerating voltage of 20 kV and a working distance of 9.2 mm. Metallic elemental ratios were recorded on EDX analyzer Inca 200 of Oxford instruments UK. The phase and crystallinity of deposited films were characterized by a PANanalytical, X'Pert HighScore diffractometer with primary monochromatic high intensity Cu-K_α(λ = 1.54184 Å) radiation. The data were collected by scanning from 10° to 90° in a step size of 0.026° operated at 40 kV and 40 mA to cover all possible diffraction peaks of the deposited material. The diffraction patterns were then compared to the documented patterns in the ICDD index.

Optical absorption measurements were performed using a Lambda 35 Perkin-Elmer UV-Vis spectrophotometer. A FTO coated glass substrate was placed in the reference optical path, thus the absorbance spectra included the contributions only from the deposited material.

3.2 Syntheses

3.2.1 Iron Titanium Bimetallic Oxide Complex, $[Fe_2Ti_4(\mu\text{-}O)_6(TFA)_8(THF)_6]$ (1)

0.50 g (0.703 mmol) $[Fe_3O(OAc)_6(H_2O)_3]\ NO_3 \cdot 4H_2O$ were suspended in 10 mL of THF in a 50 mL Schlenk tube fitted with vacuum line adapter and magnetic stirrer. 0.27 mL (4.90 mmol) tetrakis(2-ethoxyethanalato)titanium(IV) was added drop by drop via syringe to the suspension. 0.20 mL (2.59 mmol) of trifluoroacetic acid (TFA) was added to the reaction mixture and the contents were stirred for 1 hour. The reaction mixture was evaporated to dryness under vacuum and the solid was re-dissolved in 5 mL of THF. The solution was filtered through cannula to remove any traces of solid residue and was placed in a freezer at -10 °C for crystallization. Red colored crystals were obtained after three days with 85% yield. mp. 148 °C. Elemental analysis found: C, 29.40; H, 3.23%; $C_{44}H_{56}F_{24}Fe_2O_{29}Ti_4$ requires: C, 29.00; H, 3.20%. IR (ν_{max}/cm^{-1}): 1672s, 1538w, 1435w, 1198s, 1146s, 1051w, 833w, 794s, 721m, 419w. TGA: 30-100 °C (10.17% wt. loss); 100-223 °C (9.74% wt. loss); 223-378 °C (50.30% wt. loss); 378 °C-500 °C (13.27% wt. loss); residue mass of 26.69%, calcd for Fe_2TiO_5-TiO_2: 26.76%.

3.2.2 Cobalt Titanium Bimetallic Oxide Complex, $[Co_2Ti(\mu_3\text{-}O)(TFA)_6(THF)_3]$ (2)

Complex (**2**) was prepared as red coloured crystals by following the procedure as described for (**1**).

The quantities used were: 0.20 g (0.803 mmol) $Co(OAc)_2 \cdot 4H_2O$; 0.24 mL (0.809 mmol) of Ti $(Pro^i)_4$ and 0.2 mL (2.00 mmol) of trifluoroacetic acid. Yield (82%) mp. 115 °C. Elemental analysis found: C, 26.96; H, 2.47%; $C_{24}H_{24}Co_2F_{18}O_{16}Ti$ requires: C, 26.76; H, 2.23%. IR (ν_{max}/cm^{-1}): 1713s, 1672s, 1584m, 1468s, 1426m, 1198s, 1146s, 1026m, 897w, 793s, 721s, 618s, 522s, 461w. TGA: 129-246 °C (28.58% wt. loss); 259-

363 °C (46.16% wt. loss); 363-480 °C (3.50% wt. loss); residual mass of 21.76%, calcd for $CoTiO_3$-CoO: 21.76%.

3.2.3 Tris - (*N,N'*-diethyldithiocarbamato)bismuth(III) Complex, $Bi_2[(S_2CNEt_2)_3]_2$ (3)

1.16 g (6.17 mmol) $K(S_2CNEt_2)$ dissolved in acetone (20 mL) was stirred with 1.0 g (2.06 mmol) of $Bi(NO_3)_3 \cdot 5H_2O$ for 1 h to give a yellow colored solution. Filtration and slow evaporation gave the target compound as yellow crystals after 2 days. Yield: (83 %). mp. 199 °C. Elemental analysis found: C, 27.41; H, 4.60; N, 6.46 %; $C_{15}H_{30}BiN_3S_6$ requires: C, 27.56; H, 4.59; N, 6.43%; ^{1}H-NMR δ_H (400 MHz, $CDCl_3$): 1.34 (6H, t, $CH_2(CH_3)$ and 3.77 (4H, q, $CH_2(CH_3)$) ppm. IR (ν_{max}/cm^{-1}) 2937w, 2929w, 1488s, 1431s, 1374s, 1352s, 1264w, 1199w, 1138bs 162s, 982s, 907s, 831s, 775w, TGA: 232-332 °C (58.6% wt. loss); residual mass 40.8%, calcd for Bi_2S_3: 39.32%.

3.2.4 Tris-(*N,N'*-dicyclohexyldithiocarbamato)indium(III)dipyridine Complex, $[In(S_2CNCy_2)_3]$•2py (4)

0.50 g (1.80 mmol) $Na(S_2CNCy_2)$ was dissolved in methanol (20 mL) and placed in a three-necked round bottom flask (100 mL) fitted with a dropping funnel, reflux condenser and inert gas line followed by addition of $InCl_3$ 0.13 g (0.60 mmol).The resultant milky white solution was stirred for 30 min. At this point 30 mL pyridine was added to give a clear and colourless solution and stirring was continued for another hour. Filtration and slow evaporation of the reaction mixture afforded $[In(S_2CNCy_2)_3]$•2py (**4**) as colourless crystals; yield (78%), mp. 255-260 °C (decomposition). Elemental analysis found: C, 56.73; H, 7.83; N, 6.32%; $C_{49}H_{76}InN_5S_6$ requires: C, 56.46; H, 7.34; N 6.71%. IR (ν_{max}/cm^{-1}): 2925s, 2853s, 1579m, 1471w, 1440s, 1378w,1361s, 1346m, 1332w, 1300s, 1266m, 1241s, 1166s, 1148s, 1105s,

1020w, 997s, 949s, 922s, 895s, 882w, 748w, 746m, 705s, 658s, 612s, 602m, 503w, 492w, 473s; ^{1}H-NMR δ_H (400 MHz, $CDCl_3$): 1.13–2.17(60H, m, 3($C_{10}H_{20}$)), 3.12 (2H, s, (NC*H*), 3.40 (2H, s, (NC*H*), 4.82 (2 H, s, (NC*H*) and 7.30–8.63 (10H, m, 2(NC_5H_5)) ppm; TGA: 55-110 °C (11.60% wt. loss); 230-400 °C (73.21% wt. loss); residual mass of 15.19%, calcd for β-In_2S_3: 15.64%.

Complexes (**5**), (**6**), (**7**), (**9**), (**10**) and (**11**) were prepared as colourless crystals while (**8**) and (**12**)-(**15**) were appeared as light and dark yellow crystalline solids respectively by adopting the method used for synthesis of (**4**).

3.2.5 Tris-(*N,N'*-di-iso-propyldithiocarbamato)indium(III) one and half pyridine Complex, $[In(S_2CN(^{i}Pr)_2)_3]$•1.5py (5)

The quantities used were: 0.50 g (2.50 mmol) $Na(S_2CN^{i}Pr_2)$ and 0.19 g (0.83 mmol) $InCl_3$; yield (80%), mp. 265-270 °C(decomposition) Elemental analysis found: C, 43.72; H, 6.69; N, 7.94%; $C_{28.5}H_{49.5}InN_{4.5}S_6$ requires: C, 44.90; H, 6.54; N, 8.26%. IR (ν_{max}/cm^{-1}): 2971m, 2931w, 1581w, 1480s, 1460w, 1444s, 1369s, 1321s, 1192s, 1142s, 1117w, 1036s, 991w, 942s, 906s, 848s, 789s, 748w, 705s, 614m, 582s, 529s, 476s; ^{1}H-NMR δ_H (400 MHz, $CDCl_3$): 1.48–1.68 (36H, br d, 6CH(CH_3)$_2$), 3.95 (2H, br s, C*H*(CH_3)$_2$), 5.16 (4H, br s, C*H*(CH_3)$_2$) and 7.27–8.60 (7.5H, m, 1.5(NC_5H_5)) ppm; TGA: 55-115 °C (15.50% wt. loss); 230-400 °C (64.25% wt. loss); residual mass of 20.25%, calcd for β-In_2S_3 21.36%).

3.2.6 Tris-(Piperidinedithiocarbamato)indium(III) half pyridine Complex, $[In(S_2CPip)_3]$•0.5py (6)

The quantities used were: 0.50 g (2.73 mmol) $Na(S_2CN(CH_2)_5)$ and 0.20 g (0.90 mmol) $InCl_3$; yield (83%), mp. 280-283 °C (decomposition). Elemental analysis found: C, 37.70; H, 5.05; N, 7.40%; $C_{20.5}H_{32.5}InN_{3.5}S_6$ requires: C, 38.76; H, 5.15; N, 7.71%.

IR (ν_{max}/cm^{-1}): 2937s, 2853m, 1581w, 1484s, 1456w, 1436s, 1359w, 1346w, 1278m, 1258m, 1232w, 1132m, 1109s, 1069w, 1022m, 1001m, 970s, 948m, 883s, 855m, 743w, 703m, 613m, 559m, 514s, 464m; ^{1}H-NMR δ_H (400 MHz, $CDCl_3$): 1.53–1.86 (18H, m, 3(CH_2)), 3.78–4.15 (12H, m, 3(NCH_2)) and 7.27–8.61 (2.5H, m, 0.5(NC_5H_5)) ppm; TGA: 45-110 °C (6.84% wt. loss); 230-400 °C (69.31% wt. loss); residual mass of 23.85%, calcd for β-In_2S_3: 25.64%).

3.2.7 Tris-(*N*-benzyl-*N′*-methyldithiocarbamato)indium(III) Complex, [In(S_2CNBzMe)$_3$] (7)

The quantities used were: 0.5 g (2.28 mmol) Na(S_2CNBzMe) and 0.17 g (0.76 mmol) $InCl_3$; yield (85%), mp.180 °C. Elemental analysis found: C, 45.70; H, 4.33; N, 6.05% $C_{27}H_{30}InN_3S_6$ requires: C, 46.08; H, 4.29; N, 5.96%. IR (ν_{max}/cm^{-1}): 3027w, 2927w, 1491s, 1453s, 1433m, 1392s, 1357w, 1348w, 1301w, 1267w, 1242s, 1196s, 1157w, 1088s, 1070w, 1029m 983m, 955s, 817w, 745s, 732s, 694s, 624s, 569s, 549s, 485s; ^{1}H-NMR δ_H (400 MHz, $CDCl_3$): 3.35 (9H, s, 3(CH_3)), 5.10 (6H, s, 3(CH_2)) and 7.26–7.42 (15H, m, aromatic 3(C$_6H_5$)) ppm; TGA: 230-400 °C (wt loss 74.60%); residual mass of 25.40%, calcd for β-In_2S_3 : 23.15%).

3.2.8 n-tris(*N,N′* diethyldithiocarbamato)-bis(pyridine)argentate(+n)n-nitrate di-n-hydrate Cluster, [$Ag_4(S_2CNEt_2)_3(py)_2]_n \cdot nNO_3 \cdot 2nH_2O$ (8)

The quantities used were: 0.50 g (2.92 mmol) of Na(S_2CNEt_2) and 0.66 g (3.88 mmol) $AgNO_3$; yield (75%), mp. 90 °C. Elemental analysis found: C, 25.91; H, 3.77; N, 7.23%; $C_{25}H_{44}Ag_4N_6O_5S_6$ requires: C, 26.51; H, 3.91; N, 7.42%. IR (ν_{max}/cm^{-1}): 3424bs, 2981s, 2936s, 2874w, 2364 w, 1632bs, 1591s, 1496s, 1456s, 1427s, 1338s, 1296s, 1270s, 1214s, 1196s, 1146s, 1096s, 1064s, 1033s, 1000s, 973s, 901s, 828s, 778w, 749s, 699s, 615s, 552s, 507s. ^{1}H-NMR δ_H (400 MHz, $(CD_3)_2SO$): 1.20 (3H, t,

CH_2CH_3), 3.98(2H, q, CH_2CH_3), 3.68 (2H, S, H_2O) and 7.39-8.66 (5H, m, C_5H_5N) ppm. TGA: 40-75 °C (1.99% wt. loss); 75-90 °C (1.13% wt. loss); 90-130 °C (8.08% wt. loss); 130-175 °C (1.95% wt. loss); 175-191 °C (7.29% wt. loss); 191-210 °C (5.64% wt. loss); 210-400 °C (29.40% wt. loss); residual mass of 44.52%, calcd for Ag_2S: 43.76%.

3.2.9 Bis(*N,N'*-dicyclohexyldithiocarbamato)(pyridine)cadmium(II) Adduct, [Cd(S_2CNCy_2)$_2$(py)] (9)

The quantities used were: 2.0 g (7.16 mmol) Na(S_2CNCy_2) and 1.10g (3.58 mmol) $Cd(NO_3)_2 \cdot 2H_2O$; yield (85%), mp. 220 °C (decomposition). Elemental analysis found: C, 50.92; H, 6.679; N, 6.36%; $C_{31}H_{49}CdN_3S_4$ requires: C, 52.81; H, 6.95; N 5.96%. IR (ν_{max}/cm^{-1}): 1474s, 1441s [ν(C—N)]; 997s [ν(C—S)]. ^{1}H-NMR δ_H (400 MHz, $CDCl_3$): 1.13–2.05 (40H, m, 2($C_{10}H_{10}$)), 3.12(2H, s, (NC*H*)), 5.02(2H, s, (NC*H*)) 7.32–8.67 (5H, m, NC_5H_5) ppm. TGA: 89-123 °C (9.67% wt. loss); 128-270 °C (7.45% wt. loss); 271-349 °C (61.49% wt. loss); residual mass of 21.39%, calcd for CdS: 20.30%.

3.2.10 Bis(*N,N'*-dicyclohexyldithiocarbamato)(pyridine)zinc(II) Adduct, [Zn(S_2CNCy_2)$_2$(py)] (10)

The quantities used were: 1.0 g (3.58 mmol) of Na(S_2CNCy_2) and 0.24 g (1.76 mmol) $ZnCl_2$; yield (88%), mp. 230 °C (decomposition). Elemental analysis found: C, 55.31; H, 8.52; N, 6.05%; $C_{31}H_{49}ZnN_3S_4$ requires: C, 56.64; H, 7.51; N 6.39%. IR (ν_{max}/cm^{-1}): 2926s, 2851s, 1591w, 1473s, 1441s, 1364s, 1346s, 1302s, 1264s, 1241s, 1168s, 1149s, 1102s, 1069s, 1029s, 997s, 944s, 921s, 896s, 785s, 754s, 703s, 692w, 655s, 636s, 610s, 470s; ^{1}H-NMR δ_H (400 MHz, $CDCl_3$): 1.14–2.10 (40H, m, 2($C_{10}H_{20}$)), 3.16 (2H, s, (NC*H*)), 5.00 (2H, s, (NC*H*)) and 7.31–8.70 (5H, m, (NC_5H_5)) ppm. TGA: 75-115 °C (11.60% wt. loss); 270-375 °C (73.26% wt. loss); residual mass

of 15.14%, calcd for ZnS 14.83%.

3.2.11 Bis-(*N*-benzyl-*N′*-methyldithiocarbamato)(pyridine)zinc(II) Adduct, [Zn(S_2CN(BzMe)$_2$(py)] (11)

The quantities used were: 1.0g (4.56 mmol) Na(S_2CNBzMe) and 0.31 g (2.27 mmol) $ZnCl_2$; yield (85%), mp.125 °C. Elemental analysis found: C, 51.56; H, 4.81; N, 7.88%; $C_{23}H_{25}ZnN_3S_4$ requires: C, 51.42; H, 4.69; N 7.82%. IR (ν_{max}/cm^{-1}): 2931s, 1604s, 1583w, 1482s, 1446s, 1428s, 1390s, 1352w, 1261s, 1247s, 1212s, 1199s, 1151s, 1089s, 1068s, 1041s, 995s, 975s, 945s, 884s, 755s, 732s, 704s, 691s, 629s, 571s, 551s, 496s, 481s. ^{1}H-NMR δ_H (400 MHz, $CDCl_3$): 3.40 (6H, s, 2(CH_3)), 5.19 (4H, s, 2(CH_2), 7.25–7.37 (10H, m, aromatic 2(C_6H_5)) and 7.48-9.03 (5H, m, NC_5H_5) ppm. TGA: 70-122 °C (3.10% wt. loss); 126-146 °C (2.62% wt. loss); 146-210 °C (wt. loss 11.20%); 210-260 °C (wt. loss 6.50%); 260-375 °C (wt. loss 57.16%); residual mass of 19.42 %, calcd for ZnS: 18.15%.

3.2.12 Bis-(*N*,*N′*-dibenzyldithiocarbamato)palladium(II)pyridine Complex, [Pd(S_2CNBz$_2$)$_2$]•py (12)

The quantities used were: 0.50 g (1.70 mmol) Na(S_2CNBz$_2$) and 0.23 g (0.86mmol) $Pd(NO_3)_2{\cdot}2H_2O$; yield (83%) mp. 225-228 °C. Elemental analysis found: C, 57.91; H, 4.33; N, 5.52%; $C_{35}H_{33}PdN_3S_4$ requires C, 57.51; H, 4.51; N 5.75%. IR (ν_{max}/cm^{-1}): 3062w, 3026m, 2922w, 2322w, 2067brw, 1884brw, 1804w, 1604m, 1585w, 1491s, 1452s, 1427m, 1357s,1312w, 1253s, 1145s, 1076s, 1030s, 989s, 929s, 901w, 882s, 822m, 744s, 736s, 691s, 639w, 626m 585s, 557s, 538s, 516s. ^{1}H-NMR δ_H (400 MHz, $CDCl_3$): 4.81 (8H, s, 4(CH_2)), 7.26–7.42 (20H, m, 4(C_6H_5)) and 7.66–8.62 (5H, m, (NC_5H_5)) ppm. TGA: 66-139 °C (6.02% wt. loss); 238-500 °C (76.35% wt. loss); residual mass of 17.70%, calcd for PdS: 18.90%.

3.2.13 Bis(*N,N'*-dicyclohexyldithiocarbamato)palladium(II)pyridine Complex, [Pd(S_2CNCy_2)$_2$]•py (13)

The quantities used were: 0.50 g (1.80mmol) Na(S_2CNCy_2) and 0.24 g (0.90 mmol) Pd(NO_3)$_2$·2H_2O; yield (78%) mp. 265-270 °C (decomposition). Elemental analysis found: C, 52.86; H, 7.31; N, 5.84%; $C_{31}H_{49}PdN_3S_4$ requires: C, 53.26; H, 7.01; N, 6.01%. IR (ν_{max}/cm^{-1}): 2927s, 2854s, 2657w, 2091brw, 1596w, 1579m, 1475s, 1460w, 1447w, 1435w, 1366s, 1348s, 1302s, 1270s, 1164s, 1152w, 1108s, 1065w, 1028m, 998s, 949m, 924s, 895s, 883w, 844w, 800w, 747s, 708s, 663s, 613s, 596w, 504w, 489m, 470m. ^{1}H-NMR δ_H (400 MHz, $CDCl_3$): 1.10–1.78 (40H, m, 2($C_{10}H_{20}$)), 2.87 (2H, s, (NC*H*,), 3.42 (2H, s, (NC*H*), 4.74 (2H, s, (NC*H*) and 7.42–8.71 (5H, m, (NC_5H_5)) ppm. TGA: 75-163 °C (8.38% wt. loss); 252-500 °C (72.05% wt. loss); residual mass of 19.20%, calcd for PdS: 19.77%.

3.2.14 Bis(*N,N'*-di-n-hexyldithiocarbamato)palladium(II) Complex, [Pd($S_2CN^nHex_2$)$_2$] (14)

The quantities used were as follows, 0.50 g (1.76mmol) Na($S_2CN^nHex_2$) and 0.23 g, (0.88 mmol) Pd(NO_3)$_2$·2H_2O; yield (74%) mp. 61-64 °C. Elemental analysis found: C, 49.79; H, 8.10; N, 4.51%; $C_{26}H_{52}PdN_2S_4$ requires: C, 49.73; H, 8.28; N, 4.46%. IR (ν_{max}/cm^{-1}): 2954m, 2923s, 2854s, 1510s, 1459w, 1429s, 1371s, 1300s, 1278w, 1234m, 1219w, 1199m, 1151s, 1119w, 1100s, 1109w, 1100m, 1054w, 1029m, 1006w, 972brs, 880br, 793w, 724s, 626w, 606m, 575w, 534w, 518w, 478w. ^{1}H-NMR δ_H (400 MHz, $CDCl_3$): 0.87 (12H, m, 4((CH_2)$_5$C*H*$_3$)), 1.27 (24H, m, 4(CH_2CH_2(C*H*$_2$)$_3CH_3$); 1.64 (8H, m, 4(CH_2C*H*$_2$(CH_2)$_3CH_3$) and 3.79(8H, t, 2(C*H*$_2$(CH_2)$_4CH_3$)) ppm; TGA: 200-515 °C (78.22% wt. loss); residual mass of 21.78%, calcd for PdS: 22.00%.

3.2.15 Bis(*N*-cyclohexyl-*N'*-methyldithiocarbamato)palladium(II) Complex, [Pd(S_2CNCyMe)$_2$] (15)

The quantities used were: 0.5 g (2.36mmol) of Na(S_2CNCyMe) and 0.31 g (1.18 mmol) Pd(NO_3)$_2$·2H_2O; yield (69%) mp.185 °C Elemental analysis found: C, 40.17; H, 5.89; N, 5.93% $C_{16}H_{28}PdN_2S_4$ requires: C, 39.75; H, 5.79; N, 5.79%; IR (ν_{max}/cm^{-1}): 2933s, 2855s, 1490s, 1447m, 1397s, 1373m, 1345w, 1322s, 1251s, 1213s, 1188m, 1147s, 1112w, 1078s, 1058w, 1031m, 1005s, 966s, 955s, 913s, 892s, 874w, 786w, 746w,703w, 669s, 570s, 516s, 461s; ^{1}H-NMR δ_H (400 MHz, $CDCl_3$): 1.49–2.16 (10H, m, C*H*$_2$), 3.26 (3H, s, C*H*$_3$) and 4.74 (1H, s, NCH) ppm; TGA: 210-500 °C (72.47% wt loss); residual mass of 27.40%, calcd for PdS: 28.57%.

3.3 X-ray Crystallography and Structure Refinement

The data for complex [Fe_2Ti_4(μ-O)$_6$(TFA)$_8$(THF)$_6$] (**1**) and [Co_2Ti(μ_3-O)(TFA)$_6$(THF)$_3$] (**2**) were collected on a Bruker AXS SMART APEX CCD diffractometer at 100 (2) K using Mo Kα radiation (0.71073 Å). The unit cell was determined using SMART and SAINT (Bruker, 1997-2003) and the data were corrected for absorption using SADABS in SAINT. The structures were solved by direct methods and refined by full matrix least squares against F^2 with all reflections using SHELXTL (Bruker, 2003). All non-hydrogen atoms were refined anisotropically.

In structure of complex (**1**) the ratio of the two moieties refined to 0.630(1) to 0.370(1). In case of a 1:1 ratio, the structure would have been centrosymmetric with the space group *P*bca instead of the observed space group *P*ca2$_1$. The structure is also racemically twinned with a twin ratio of 0.69(2) to 0.31(2). Refinement attempts with other unit cell orientations in the alternative *P*ca2$_1$ setting did result in 1:1 disorder, perfect racemic twinning and did give worse refinement results than in the chosen orientation. Due to the excessive disorder of large sections of the structure a series of

restraints and constrained were applied to achieve a meaningful and stable refinement. All carboxylate units were restrained to be flat. All C-F bonds were restrained to be of approximately the same length. The same was done with all C-O and all C-C bonds within the THF molecules. All minor TFA anions were restrained to have the same geometry as their major moiety counterparts. All ADPs of C, F and O were restrained using DELU, ISOR and SADI commands as defined in SHELXTL with standard deviations of 0.05 each. ADPs of heavily overlapping minor moiety atoms with very ill-behaved ADPs were constrained to be the same as that of their major component counterparts.

The molecule (**2**) is situated on a crystallographic mirror plane cutting through the Ti atom, the central oxo atom, one of the THF molecules and two of the TFA molecules. One of these TFA anions shows rotational disorder of the CF_3 group with an occupancy ratio of 0.672(19) to 0.328(19). The THF molecule on the mirror plane is disordered over two symmetry equivalent positions.

Single crystal X-ray diffraction data of complexes $[In(S_2CNCy_2)_3]$•2py (**4**), $[In(S_2CPip)_3]$.0.5py (**6**) and $[In(S_2CNBzMe)_3]$ (**7**) were collected on a Bruker D8 Apex II diffractometer and on an Agilent SuperNova Dual for $[In(S_2CN(^iPr)_2)_3]$•1.5py (**5**) and $[Cd(S_2CNCy_2)_2(py)]$ (**9**) with use of an Oxford low temperature apparatus. Multi-scan methods for absorption correction were applied (Sheldrick, 2004). The structures of (**4**), (**5**), (**6**) and (**7**) were solved by direct methods and difference Fourier synthesis and refined by full-matrix least-squares based on all data (Scheldrick, 2008).

The structure of complex (**9**) was solved by heavy-atom methods Patterson and refinement was on F^2 (SHELXL97) using data that had been corrected for absorption effects with an empirical procedure with non-hydrogen atoms modelled with anisotropic displacement parameters, with hydrogen atoms in their calculated positions, and using a weighting scheme of the form $w = 1/[\sigma^2(F_o^2) + (aP)^2]$ where $P = (F_o^2 + 2F_c^2)/3)$.

Disorder was resolved for the NCy_2 residue rings of one dithiocarbamate ligand in (**9**) so that two distinct positions were determined for each atom. Refinement showed that each component had a similar site occupancy factor so this was fixed at 0.5 in the final cycles of refinement. Chemically equivalent atoms were assigned equivalent anisotropic displacement parameters, and the fragments were refined with soft constraints using the SADI, ISOR and DFIX commands in SHELX97. Finally, two reflections, *i.e.* ($\bar{1}$ 3 2) and (4 -6 7), were omitted from the final cycles of refinement owing to poor agreement. Data analyses were performed with WinGX (Farrugia, 1999) and PLATON (Spek, 2003).

X-ray diffraction data for $[Ag_4\{S_2CN(C_2H_5)_2\}_3(C_5H_5N)_2]_n \cdot nNO_3 \cdot 2nH_2O$ (**8**) $[Zn(S_2CNCy_2)_2(py)]$ (**10**) and $[Zn\{S_2CN(CH_2Ph)(Me)\}_2(py)]$ (**11**) were recorded at 296 K with a Bruker SMART Apex II CCD area-detector diffractometer (graphite-monochromated Mo-*Kα* radiation, λ = 0.71073 Å). The orientation matrix, unit-cell refinement, and data reduction were all handled by the Apex2 software (SAINT integration, SADABS absorption correction) (Bruker, 2007).

The crystal structure of (**8**) was solved using Patterson method in the program SHELXS-97 and was refined by the full matrix least-squares method on F^2 with SHELXL-97 (Spek, 2010). The non-hydrogen atoms were refined anisotropically and the hydrogen atoms were added geometrically and refined with a riding model. The structure contains disordered solvent molecules which could not be satisfactorily modeled. The data were therefore treated with the SQUEEZE routine of PLATON (Version, 2007).

The crystal structures of (**10**) and (**11**) were solved using direct methods in the program SHELXS-97 and were refined by the full matrix least-squares method on F^2 with SHELXL-97 (Sheldrick, 2004). The non-hydrogen atoms were refined anisotropically and the hydrogen atoms were added geometrically and refined with a

riding model. Molecular graphics were prepared using XSEED software (Barbour, 2001).

The data for complexes (**12**)-(**15**) were collected at 150(2)K on a Bruker Apex II CCD diffractometer using MoK_α radiation (λ = 0.71073Å). The structure was solved by direct methods and refined on F^2 using all the reflections. Except where described below, all the non-hydrogen atoms were refined using anisotropic atomic displacement parameters and hydrogen atoms were inserted at calculated positions using a riding model. The pyridine solvate molecule in complex $[Pd(S_2CNCy_2)_2]\cdot py$ (**13**) is disordered over a centre of symmetry; the nitrogen atom is therefore necessarily disordered and was modelled with 50% occupancy of two positions. There is some disorder in one of the four independent alkyl chains of $[Pd(S_2CN^nHex_2)_2]$ (1**4**). The four terminal carbon atoms of this chain were modelled with 74:26% occupancy of two orientations and the minor component was refined isotropically.

3.4 Aerosol-Assisted Chemical Vapour Deposition (AACVD) Studies

Thin films were deposited on soda glass and fluorine doped tin oxide (FTO) coated conducting glass substrates using a self-designed Aerosol Assisted Chemical Vapour deposition assembly described in Figure 3.1. Substrates were cleaned prior to use by ultrasonically washing with distilled water, acetone, isopropanol and ethanol and dried in air. In a typical deposition, a 0.05M solution of the precursor was taken in a two necked 50 mL round-bottom flask with a gas inlet that allowed the carrier gas (argon 99.00% purity) to pass into the solution to aid the transport of the aerosol. This flask was connected to the reactor tube by a piece of reinforced tubing. The argon flow rate was controlled by a L1X linear flow meter. Four glass substrates (approx. 1 x 2 cm^2) were placed inside the reactor tube, which is placed in a CARBOLITE (Model No. 10/25/130) (6"L × 1"D) tube furnace. The precursor solution in a round-bottom flask

was kept in a water bath above the piezoelectric modulator of a PIFCO ultrasonic humidifier (Model No. Cool Mist-plus serial No. ADV-CMP-85956) operated at 50 Hz frequency. The aerosol droplets of the precursor thus generated were transferred into the hot wall zone of the reactor by carrier gas. Both the solvent and the precursor were evaporated and the precursor vapour reached the heated substrate surface where thermally induced reactions and film deposition took place. The exhaust from reactor was vented directly into the extraction system of a fume cupboard. Towards the end of the experiment, the aerosol line was closed and carrier gas was passed over the substrate. The glass substrate was allowed to cool to ca. 60 °C before it was removed from the reactor.

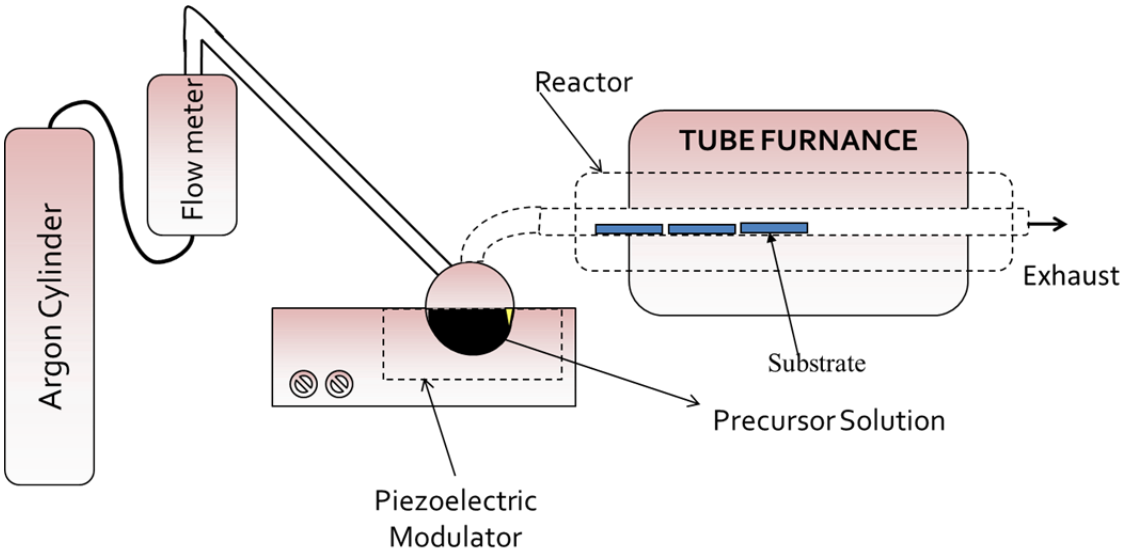

Figure 3.1: Schematic diagram of aerosol-assisted chemical vapour deposition (AACVD) process.

Table 3.1**:** Parameters for thin film growth from different precursors and on different substrates

Precursor Formula	**Solvent**	**Deposition Temperature (°C)**	**Substrate**	**Carrier Gas/ (mL/min.)**	**Deposition time (mints)**	**Composition of Deposited Thin Films**
$[Fe_2Ti_4(\mu\text{-}O)_6(TFA)_8(THF)_6]$(**1**)	Toluene	500	Plane glass	Ar/150	45	Fe_2TiO_5-TiO_2
$[Co_2Ti(\mu_3\text{-}O)(TFA)_6(THF)_3]$(**2**)	Toluene	500	Plane glass	Air/150	45	$CoTiO_3$-CoO
$Bi_2[(S_2CNEt_2)_3]_2$ (**3**)	Chloroform/ Dichloromethane	350, 400, 450	FTO	Ar /150	30	Bi_2S_3
$[In(S_2CNCy_2)_3]$•2py (**4**) $[In(S_2CN(^iPr)_2)_3]$•1.5py (**5**) $[In(S_2CPip)_3]$•0.5py (**6**) $[In(S2CNBzMe)_3]$ (**7**)	THF	300, 350, 400	FTO	Ar/120	30	β-In_2S_3

$[Ag_4\{S_2CN(C_2H_5)_2\}_3(C_5H_5N)_2]_n$ ·nNO_3·$2nH_2O$ (**8**)	Pyridine	350, 400	FTO	Ar/100	50	Ag_2S
$[Cd(S_2CNCy_2)_2(py)]$ (**9**)	Pyridine, Toluene and THF	350, 400, 450	FTO, Soda glass	Ar/100	35	CdS
$[Zn(S_2CNCy_2)_2(py)]$ (**10**) $[Zn\{S_2CN(CH_2Ph)(Me)\}_2(py)]$ (**11**)	Toluene	375, 450, 475	FTO	Ar	40	ZnS
$[Pd(S_2CNBz_2)_2]$•py (**12**) $[Pd(S_2CNCy_2)_2]$•py (**13**) $[Pd(S_2CNHex_2)_2]$ (**14**) $[Pd(S_2CNCyMe)_2]$ (1**5**)	Pyridine	400, 450, 500	FTO	Ar /100	60	PdS

3.5 General Procedure for Photoelectrochemical (PEC) Characterization of Photoelectrodes

The photoelectrochemical (PEC) properties of metal sulphide films were measured using the standard three electrodes electrochemical cell fitted with a quartz window. An Ag/AgCl electrode and Pt were employed as the reference and counter electrodes, respectively. Generally an aqueous Na_2SO_4 (0.05M) and Na_2S (0.10M) electrolyte was used to measure the PEC properties of metal sulphide electrodes. The bare SnO_2 area of photoelectrode was used to make the electrical contact which was made with a gold–coated crocodile clip above the electrolyte. The potential of the photoelectrode was controlled by a potentiostat (Eco Chemie micro-Autolab, type III). In the electrochemical cell light enters through a quartz window and travels about a 5 mm path length in the electrolyte before illuminating the photoelectrode. The photo electrode was illuminated through the electrolyte side and the illumination area was 1 cm^2. The illumination source was an AM1.5 Class A solar simulator (Solar Light 16S – 300 solar simulator) at 100 mW cm^{-2} light intensity, calibrated by a silicon pyranometer (Solar Light Co., PMA2144 Class II). The voltage scan speed was 0.01 V/s and light was manually chopped at regular intervals in order to record the behavior of photoelectrodes.

CHAPTER 4

RESULTS AND DISCUSSION

Functional materials thin films are often found in various compositions and crystal structures and exhibit diverse physical and electrical properties, leading to numerous potential applications in advanced material technology. They offer a significant role in the field of microelectronics and telecommunications such as next generation computer memories, fuel cells, gate dielectric layers, infrared detectors, optical wave-guides, and in the field of electro-optic storage. The evolution of modern technologies with their appeal for miniaturization and efficient performances has driven the research's interest to find alternative ways for the production of advanced functional materials thin films. A variety of newly developed synthetic routes are now capable to yield desired products under mild conditions and known as the Soft Chemistry Approach (Corriu, 2001; Hubert-Pfalzgraf, 2003). These techniques include sol- gel, metal organic chemical vapour deposition (MOCVD), metal organic deposition (MOD) and others involve the utilization of metal-organic compounds or metal complexes with organic ligands such as alkoxide, metal carboxylates, β-diketonates, dithiocarbamates and xanthates. These metal complexes can be easily hydrolytically or thermally decomposed and are usually narrated as molecular precursors. Single Source Precursor (SSP) is a molecule containing all necessary elements required by the final material in a proper ratio have proven extremely versatile as they often decompose cleanly under mild conditions and in a controllable manner.

The synthesis of oligomeric homo-or hetero bi/trimetalic molecular precursor is usually carried out by solution mixing of readily available reactants such as metal carboxylates, β-diketonates, metal alkoxides and aminoalkoxides that have bridging or bridging–chelating coordination capabilities. The heterobimetallic oxide precursors

$[Fe_2Ti_4(\mu\text{-}O)_6(TFA)_8(THF)_6]$ (**1**) and $[Co_2Ti(\mu_3\text{-}O)(TFA)_6(THF)_3]$ (**2**) (TFA = trifloroacetate, THF = tetrahydrofuran) were synthesized using a Lewis-acid base adduct approach which is a unique method for the design of homo and heterobimetallic precursors (Bradley, 1978). This type of synthetic strategy aims to coordinately saturate each metal center by use of chelating ligands like carboxylate and functionalized alcohol etc., that enhance the stability, solubility, volatility and shelf life of heterobimetallic precursors (Hamid, 2008). We used trifluoroacetate rather than simply acetate as a ligand to enhance the solubility of the precursor, as transition metal trifluoroacetate derivatives are commonly known for their higher volatility and solubility when compared to simple acetates, a fact that is made use of in many applications such as e.g. catalysis. The trifluoroacetate ligand is also known to be able to change its coordination from bi to monodentate, according to the electronic and steric requirements of the central metal atom, thus improving the chances to obtain a stable well defined bimetallic precursor complex (Marchetti, 2007).

The metal dithiocarbamates precursors $[Bi(S_2CNEt_2)_3]_2$ (**3**), $[In(S_2CNCy_2)_3]\bullet 2py$ (**4**), $[In(S_2CN(^{i}Pr)_2)_3]\bullet 1.5py$ (**5**), $[In(S_2CPip)_3]\bullet 0.5py$ (**6**), $[In(S_2CNBzMe)_3]$ (**7**), $[Ag_4\{S_2CNEt_2\}_3(py)_2]_n\cdot nNO_3\cdot 2nH_2O$ (**8**), $[Cd(S_2CNCy_2)_2(py)]$ (**9**), $[Zn(S_2CNCy_2)_2(py)]$ (**10**), $[Zn(S_2CNBzMe)_2(py)]$ (**11**), $[Pd(S_2CNBz_2)_2]\bullet py$ (**12**) $[Pd(S_2CNCy_2)_2]\bullet py$ (**13**), $[Pd(S_2CN^{n}Hex_2)_2]$ (**14**) and $[Pd(S_2CNCyMe)_2]$ (**15**) are conveniently prepared via metathetical reaction of the metal chloride or nitrates and sodium dithiocarbamate in acetone- pyridine solutions. Our approach in developing SSPs differs from those previously used methods (Brewer, 1994) in the synthesis of dithiocarbamate complexes, in that we used a Lewis base (pyridine) as a solvent for crystallization of complexes (**3**)-(**15**). The dithiocarbamates with Lewis bases are a class of precursor compounds with versatile properties that include: air stability, ease of synthesis at room temperature, enhanced volatility and facile decomposition at relatively low temperatures. However,

in some case, pyridine did not coordinate with the metal centre but exists as solvate molecules in the crystal lattices of (**4**), (**5**), (**6**) (**12**) and (**13**).

4.1 Iron Titanium Bimetallic Oxide Complex $[Fe_2Ti_4(\mu\text{-}O)_6(TFA)_8(THF)_6]$ (1)

The heterobimetallic precursor $[Fe_2Ti_4(\mu\text{-}O)_6(TFA)_8(THF)_6]$ (**1**) was synthesized in good yield under mild conditions by the reaction of $[Fe_3O(OAc)_6(H_2O)_3]NO_3{\cdot}4H_2O$ with tetrakis(2-ethoxyethanalato)titanium(IV) in dry THF by addition of a few drops of TFA. Precursor (**1**) as crystallized from THF has an iron to titanium ratio of (1:2), is stable in air and soluble in common organic solvents such as toluene or tetrahydrofuran. Precursor (**1**) was characterized by its melting point, elemental analysis, IR, (data presented in Chapter 3, Section 3.2.1 at page 64) TGA and single crystal X-ray analysis. In the IR spectrum, two characteristic bands appear at 1652 and 1435 cm^{-1}: CO_2 ν_{asym} at 1652 cm^{-1} and ν_{sym} vibration at 1435 cm^{-1}. The difference between the two values of approximately 200 cm^{-1} suggests the presence of a bridging TFA ligand (Veith, 2005).

4.1.1 Single Crystal X-ray Structure of $[Fe_2Ti_4(\mu\text{-}O)_6(TFA)_8(THF)_6]$ (1)[1]

The crystal structure of precursor (**1**) is shown in Figure 4.1. The crystal data and refinement parameters are listed in Table 4.1 while selected bond distances and angles are given in Table 4.2. The structure exhibits partial pseudo-inversion symmetry due to complete molecular disorder by a pseudo-inversion center located in the middle of the molecule. The two molecules occupying the site of the complex are chemically and geometrically identical, thus only the major moiety will be described in detail. In the structure, half of the molecule is related to the other half through a non-crystallographic two-fold rotation axis and the entire precursor comprises of four titanium and two iron centers linked together by oxygen atoms, which are doubly or triply bridged between

[1] Published: **Ehsan, M.A**.; Tahir, A.A.; Hamid, M.; Mazhar, M.; Wijayantha, K.; Zeller, M. (2011). Deposition of iron titanate/titania ceramic composite thin films from a single molecular precursor. *Inorg. Chim. Acta*, *376*, 189-194

the metal atoms. The two asymmetric units related by the two fold rotation are connected with each other through four doubly bridging oxygen atoms [O(11), O(12), O(13) and O(14)]. Each asymmetric part of precursor (**1**) is based on a triangular $FeTi_2$ fragment with a μ_3-O at the center of the triangle and with metal-metal non bond distances of Fe2…Ti1A = 3.467 (2) Å, Fe2…Ti2A = 3.515 (2) Å, and Ti1A…Ti2A = 3.361(2) Å. Both the iron and titanium metal atoms in precursor (**1**) have distorted octahedral geometries and all coordination sites are occupied by oxygen atoms as shown in Figure 4.1.

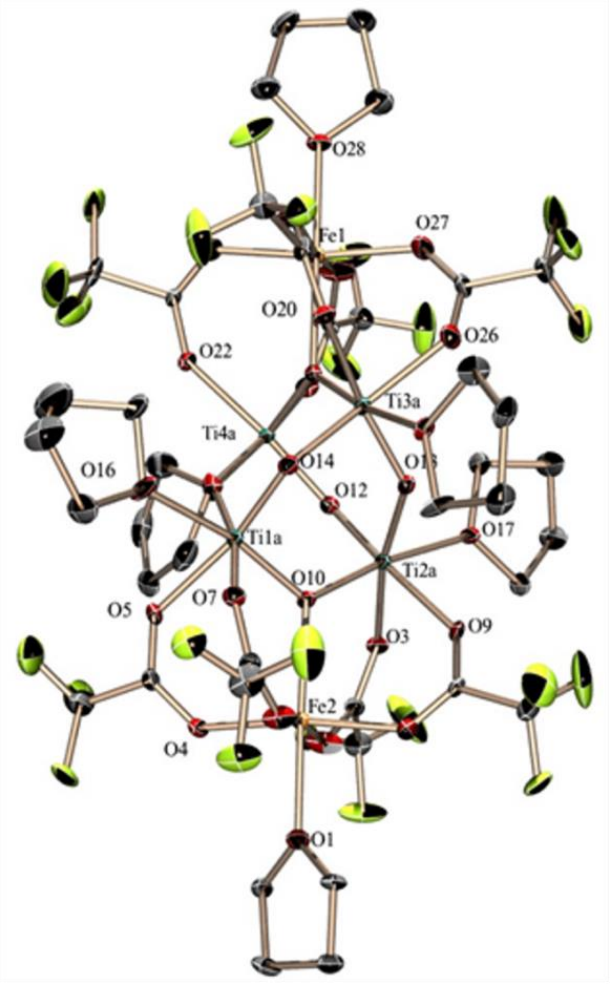

Figure 4.1: ORTEP diagram of precursor $[Fe_2Ti_4(\mu\text{-}O)_6(TFA)_8(THF)_6]$ (**1**). Only the major molecule occupying the site of the complex is shown, and only metal ions and coordinating oxygen atoms are labeled for clarity. Displacement ellipsoids are shown at the 50 % probability level.

Each titanium atom has octahedral geometry severely distorted due to the strain caused by the formation of cage involving both μ_2 and μ_3 bridged oxygen atoms with O-Ti-O angles in the range from 70.9(5) to 173.7(5). All Ti−O distances observed are closely related to those reported previously for similar heterobimetallic compounds (Hamid, 2007b).

Table 4.1: Crystal data and structure refinement for precursor $[Fe_2Ti_4(\mu\text{-}O)_6(TFA)_8(THF)_6]$ (**1**)

Identification code	$[Fe_2Ti_4(\mu\text{-}O)_6(TFA)_8(THF)_6]$ (**1**)
Empirical formula	$C_{44}H_{56}F_{24}Fe_2O_{29}Ti_4$
Formula weight	1808.19
Solvent	THF
Temperature	100(2) K
Crystal system	Orthorhombic
Space group	*P*ca2_1
Unit cell dimensions	a = 19.2114(14) Å, b =20.4804(15) Å, c = 17.2504(12) Å $\alpha = \beta = \gamma = 90^{\circ}$
Volume	6787.3(8) $Å^3$
Z	4
Density (calculated)	1.770 mg/M^3
Reflections collected	76783
Independent reflections	20026 [Rint = 0.040]
Goodness-of-fit on F^2	1.077
Final R indices [I>2σ (I)]	R1 = 0.0941, wR2 = 0.1610,
R indices (all data)	R1 = 0.0615, wR2 = 0.1407

Table 4.2: Selected bond distances [Å] and bond angels [°] for $[Fe_2Ti_4(\mu\text{-}O)_6(TFA)_8(THF)_6]$ (**1**) (major moiety only)

Bond Distances (Å)			
Fe1−O21	2.029 (5)	Fe2−O1	2.103 (4)
Fe1−O23	2.069 (5)	Fe2−O2	2.065 (5)
Fe1−O25	2.039 (5)	Fe2−O4	2.059 (9)
Fe1−O27	2.049 (13)	Fe2−O6	2.033 (5)
Fe1−O28	2.106 (4)	Fe2−O8	2.046 (5)
Fe1−O15	2.174 (4)	Fe2−O10	2.160 (4)
Ti1A −O5	2.094 (7)	Ti2A− O3	2.086 (7)
Ti1A −O7	2.075 (6)	Ti2A− O9	2.096 (6)
Ti1A− O10	1.871 (4)	Ti2A− O10	1.943 (4)
Ti1A− O11	1.785 (4)	Ti2A− O12	1.804 (4)
Ti1A− O14	1.802 (4)	Ti2A− O13	1.847 (4)
Ti1A− O16	2.120 (6)	Ti2A− O17	2.171 (7)
Ti3A− O13	1.766 (4)	Ti4A− O11	1.866 (5)
Ti3A− O14	1.871 (4)	Ti4A− O12	1.781 (4)
Ti3A− O15	1.874 (4)	Ti4A− O15	1.904 (4)
Ti3A− O18	2.147 (6)	Ti4A− O19	2.172 (9)
Ti3A− O20	2.112 (6)	Ti4A− O22	2.092 (5)
Ti3A− O26	2.095 (7)	Ti4A− O24	2.101 (7)
Ti1A−Ti2A	3.361 (2)	Ti2A−Ti3A	3.354 (2)
Ti2A−Ti4A	3.3326 (19)	Ti3A−Ti4A	3.348 (2)
Bond Angels [°]			
O8−Fe2−O4	170.3 (3)	O11−Ti1A−Ti3A	79.92 (14)
O6−Fe2−O2	170.11 (19)	O14−Ti1A−Ti3A	25.23 (13)
O8−Fe2−O2	89.1 (3)	O10−Ti1A−Ti3A	84.47 (13)
O4−Fe2−O2	83.8 (3)	O7−Ti1A−Ti3A	107.9 (2)
O6−Fe2−O1	85.87 (17)	O5−Ti1A−Ti3A	166.6 (2)
O8−Fe2−O1	85.87 (17)	O16−Ti1A−Ti3A	105.4 (2)
O4−Fe2−O1	86.9 (3)	O11−Ti1A−Ti4A	24.05 (13)
O2−Fe2−O1	84.49 (17)	O14−Ti1A−Ti4A	81.38 (14)
Ti1A−O10−Fe2	118.50 (19)	O10−Ti1A−Ti4A	83.88 (13)
Ti2A−O10−Fe2	117.84 (17)	O7−Ti1A−Ti4A	167.8 (2)
Ti1A−O11−Ti4A	133.0 (2)	O5−Ti1A−Ti4A	106.5 (2)
Ti4A−O12−Ti2A	136.7 (3)	O16−Ti1A−Ti4A	105.8 (2)
Ti3A−O13−Ti2A	136.3 (2)	O7−Ti1A−Ti4A	167.8 (2)
Ti1A−O14−Ti3A	130.5 (2)	O5−Ti1A−Ti4A	106.5 (2)
Ti3A−O15−Ti4A	124.7 (2)	O16−Ti1A−Ti4A	105.8 (2)
Ti3A−O15−Fe1	117.16 (18)	O11−Ti1A−Ti2A	80.29 (14)
Ti4A−O15−Fe1	118.05 (18)	O10−Ti1A−Ti2A	81.62 (13)
Ti1A−O10−Ti2A	123.6 (2)	O10−Ti1A−Ti2A	28.76 (12)
O13−Ti2A−Ti3A	21.31 (11)	O16−Ti1A−Ti2A	162.6 (2)
O3−Ti2A−Ti3A	168.3 (2)	O13−Ti3A−O14	93.88 (18)
O9−Ti2A−Ti3A	107.5 (2)	O13−Ti3A−O15	100.17 (18)
O17−Ti2A−Ti3A	103.74 (16)	O14−Ti3A−O15	97.74 (18)
O12−Ti2A−Ti1A	77.83 (15)	O14−Ti3A−O26	166.2 (3)
O13−Ti2A−Ti1A	76.18 (13)	O15−Ti3A−O26	93.8 (2)

O10−Ti2A−Ti1A	27.60 (11)	O13−Ti3A−O20	166.1 (2)

4.1.2 Thermal Decomposition and Thin Film Characterization

Thermogravimetric analysis (TGA) provides information about the thermal decomposition processes and the volatility of precursor under investigation. The thermal behavior of precursor (**1**) has been examined by thermogravimetric analysis performed under an atmosphere of flowing argon gas (25 mL/min) with a heating rate of 10 °C/min. The TGA of precursor (**1**) shows three stages of weight loss (Figure 4.2).

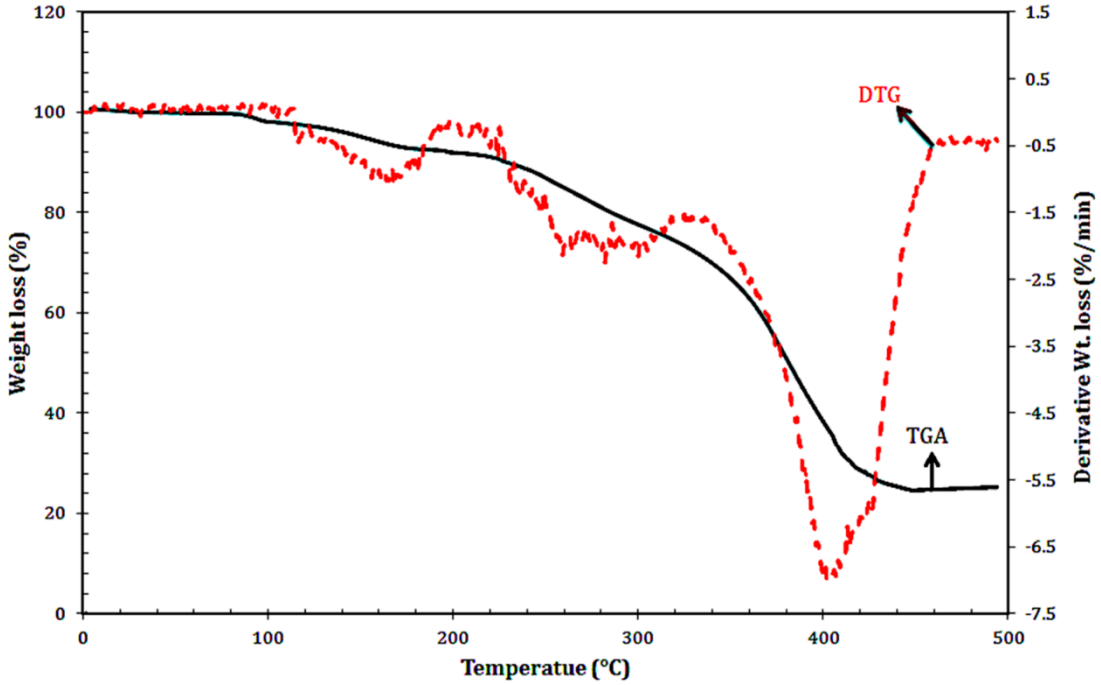

Figure 4.2: Thermogravimetric plot showing loss in weight with temperature increase for precursor $[Fe_2Ti_4(\mu\text{-}O)_6(TFA)_8(THF)_6]$ (**1**).

The first step of slow decomposition begins at 110 °C and completes at 200 °C with an approximate weight loss of 7%. The second step starts at 256 °C and is completed at 384 °C accompanied by a weight loss of 21.6%. The third step begins in continuation at 384 °C and is completed at 480 °C giving a maximum weight loss of 42.92% resulting in a residue amounting to 26.69% of the initial weight. The residual weight is close to

the expected composition for Fe_2TiO_5/TiO_2 (26.76%) indicating that the precursor decomposed quantitatively to composite oxides.

The IR spectra of the TGA residue also prove the removal of carbonaceous matter from the organic groups leaving a final residue corresponding to composite oxides. The absorption bands at 675 cm^{-1} are in good agreement with reported data for Fe_2TiO_5. Low region bands between 420 and 530 cm^{-1} along with a peak at 812cm^{1-} can be attributed to the rutile phase of TiO_2 (Navío, 1999). In the precursor (**1**), each metal center is coordinately saturated by the oxygen atoms of chelating TFA ligands, which eliminates the need of additional oxygen to form oxides. Thus, the new precursor is suitable for the deposition of thin films of an Fe_2TiO_5-TiO_2 composite at the relatively low temperature of 500 °C.

The X-ray diffractogram of the thin films deposited from precursor (**1**) (Figure 4.3) also indicates the formation of a composite of two different types of crystalline oxide phases, Fe_2TiO_5 and TiO_2. The fingerprints of the powder X-ray diffractograms of the composite oxide film obtained by AACVD of precursor (**1**) are in good agreement with the reported data of both Fe_2TiO_5 and TiO_2 in their pseudo-brookite and rutile forms. This observation suggests that the decomposition of the precursor proceeds according to the following equation.

$$[Fe_2Ti_4(\mu\text{–}O)_6(TFA)_8(THF)_6] \xrightarrow[500\ ^oC]{AACVD} Fe_2TiO_5 + 3\ TiO_2 + \text{Volatiles}$$

The TiO_2 (Swanson, 1950) is found in the form of rutile having the tetragonal space group $P4_2/mnm$, with cell parameters of a = b = 4.5940 and c = 2.9580 Å, while the Fe_2TiO_5 ((Karkhanavala, 1958) has a pseudo-brookite structure with the orthorhombic space group (*Bbmm*) and lattice dimensions of a = 9.8100, b = 9.9500 and c = 3.7300 Å. Figure 4.3 shows the diffractogram of the decomposition product with the peaks corresponding to TiO_2 (ICDD = 00-004-0551) marked as “Y” and all peaks correspond

to Fe_2TiO_5 (ICDD = 00-009-0182) labeled as "X". In the XRD pattern, the peaks at a 2θ value of 27.41°, 36.07°, 41.12°, 54.28°, and 56.32° correspond to both Fe_2TiO_5 and TiO_2. The XRD pattern of the composite thin film deposited at 500 °C showed no evidence for the formation of any iron oxide or any other form of iron titanates indicating that the precursor (**1**) is a potential candidate for the deposition of pure Fe_2TiO_5-TiO_2 composite thin films.

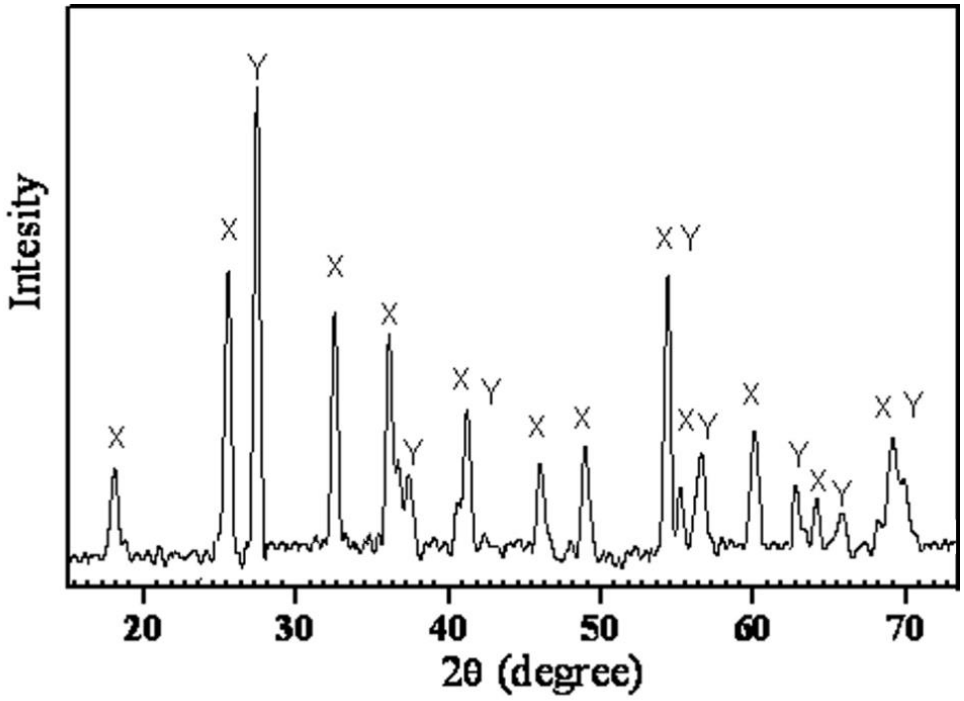

Figure 4.3: X-Ray diffractogram of oxides obtained from precursor $[Fe_2Ti_4(\mu\text{-}O)_6(TFA)_8(THF)_6]$ (**1**): X indicates the peaks originated from Fe_2TiO_5 (00-009-0183), while the TiO_2 (00-004-0551) phase peaks labeled as Y.

It is well known from the previous literature that the composition of iron titanates depends on the fabrication conditions, the Fe-Ti contents and the temperature (Khaleel, 2009) . The formation of an Fe_2TiO_5 phase along with TiO_2 at 500 °C was reported by a sol-gel method when iron contents are low (Fe:Ti 25:75). It has been reported that reaction of Fe_2O_3 with TiO_2 at 1100 °C yields a range of solid solutions Fe_{1+x} $TiO_{2-x}O_5$ $0 \leq x \leq 1$ in which both Fe^{2+} and Fe^{3+} can coexist (Phani, 2008). Mössbauer studies of

these solid solutions reveal presence of Fe^{2+} in $FeTi_2O_5$ and Fe^{3+} in Fe_2TiO_5 phases. The proportions of Fe^{2+} to Fe^{3+} in the solid solutions determine the unit cell parameters which become smaller with increase in Fe^{3+} contents indicating a dependence of the cell parameters on the effective atomic radius of iron(III). The formation of Fe_2TiO_5 from precursor (**1**) rather than an iron oxide and TiO_2 at lower temperatures may be governed by a different reaction mechanism that may involve the formation of a titania lattice followed by diffusion of already present Fe^{3+} ions into the titania lattice before any formation of iron oxide sets on. The isomorphous replacement of Ti^{4+} ions by Fe^{3+} ions in the formation of Fe_2TiO_5 is facilitated by similar effective atomic radii of both the metals, which are 0.65 Å for low spin Fe^{3+}, and 0.61 Å for Ti^{4+} respectively. Under AACVD conditions at 500 °C substitution of iron Fe^{3+} for Ti^{4+} may take place during the nucleation process in the aerosol prior to adsorption of Fe_2TiO_5 on the substrate.

The Fe_2TiO_5-TiO_2 composite film exhibits good adhesion to the substrate as verified by the "Scotch Tape Test" and is stable towards air and moisture. Thin films reflect multicolored fringes when observed at different angles.

Scanning electron microscopic (SEM) images (Figure 4.4) of composite thin films deposited from precursor (**1**) show a smooth and compact film morphology with homogenously dispersed particles. The high-resolution image (Figure 4.4b) shows that the films have a compact morphology with rectangular and pyramidal particles tightly attached to each other. These films show a large particle size distribution, with the length ranging from approximately 0.2 to 0.8μm and with a thickness varying between 0.05 and 0.150μm. The particles have well defined clear grain boundaries.

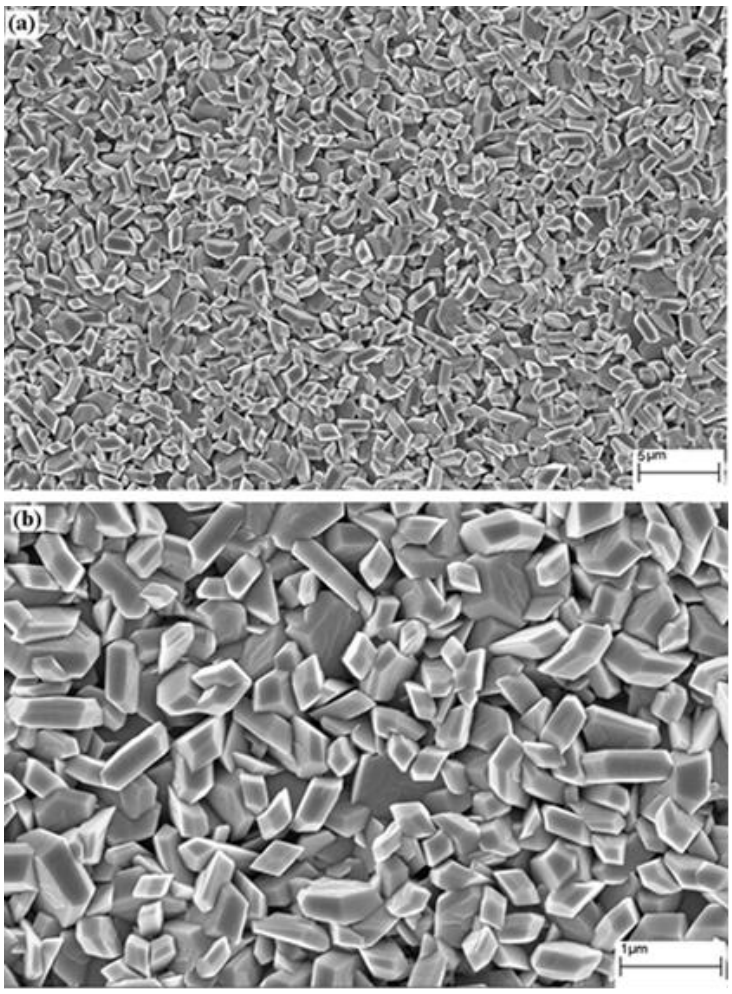

Figure 4.4: SEM images of thin film deposited from precursor (**1**) at 500 °C (a) at low and (b) at high resolution.

4.2 Cobalt Titanium Bimetallic Oxide Complex $[Co_2Ti(\mu_3\text{-}O)(TFA)_6(THF)_3]$ (2)

The precursor $[Co_2Ti(\mu_3\text{-}O)(TFA)_6(THF)_3]$ (TFA = trifloroacetate, THF = tetrahydrofuran) (**2**) was prepared by stoichiometric reaction of $Co(OAc)_2{\cdot}4H_2O$ with $Ti(^{i}PrO)_4$ and trifluoroacetic acid (TFAH) in THF at room temperature under mild conditions as shown in the following equation. The reaction seems to proceed through the hydrated starting material accompanied by the loss of acetate and iso-propanol resulting in the formation of oxo bridged complex.

$$2\ Co(OAc)_2 \cdot 4H_2O + Ti(^iPrO)_4 + 6TFAH$$

$$\downarrow \text{THF}$$

$$[Co_2Ti(\mu_3\text{-}O)(TFA)_6(THF)_3] + 4AcOH + 3H_2O + 4^iPrOH$$

The precursor (**2**) as crystallized from THF has cobalt: titanium ratio of 2:1 is stable in air and soluble in organic solvents such as toluene and THF. Melting point, elemental analysis, FT-IR, TGA (data presented in Chapter 3, section 3.2 at page 64) and single crystal X-ray analysis were conducted to characterize precursor (**2**). Two characteristic bands that appear at 1679 and 1468 cm^{-1} in the IR spectrum can be attributed to COO- ν_{asym} and COO- ν_{sym} vibrations, respectively. The difference between $\nu(COO\text{-})_{asym}$ and $\nu(COO\text{-})_{sym}$ is approximately 200 cm^{-1} suggests the presence of bridging TFA groups. Strong absorptions due to C–F and C–O stretching vibrations observed at 1198 and 1146 cm^{-1}, respectively, correspond to the TFA group (Hamid, 2008). Low intensity absorptions at 522 and 461 cm^{-1} can be assigned to νM–O vibration (Nawar, 2000).

4.2.1 Single Crystal X-ray Structure of $[Co_2Ti(\mu_3\text{-}O)(TFA)_6(THF)_3]$ (2)[2]

Molecular structure of precursor (**2**) is depicted in Figure 4.5. Main crystallographic parameters and structure refinement details are summarized in Table 4.3 and selected bond distances and angles are given in Table 4.4 respectively. The the geometry of (**2**) is based on an isosceles triangular Co_2Ti fragment, made up from two Co(II) atoms and one Ti(IV) atom with one oxygen (μ_3-O7) at the centre of the triangle. This structure is analogue to those of similar compounds reported in the literature (Gavrilenko, 2002). Six bridging trifluoroacetate anions arranged along the rim join the metal atoms through

[2] Published: **Ehsan, M.A**.; Mansoor, M.A.; Mazhar, M.; Tahir, A.A.; Hamid, M.; Upul Wijayantha, K. (2012). Cobalt titanate–cobalt oxide composite thin films deposited from heterobimetallic precursor. *Appl. Organometal. Chem., 26*, 493.

carboxylate oxygen atoms, reinforcing the triangular framework: the carboxylate groups display a bridging O, O^{i} coordination (symmetry operator (i): *x*, −*y*+1/2, *z*). The oxygen donor atoms of the THF molecules complete the coordination of each 3d-metal to six, so that each Co^{2+} and Ti^{4+} ion exhibits a distorted octahedral environment of oxygen atoms shown in Figure 4.6. The co-planarity of the μ_3-O7 atom with the metal triangle shows that it is an sp^2–hybridized oxide ion, removing the ambiguity associated with a possible μ_3–OH^- bridge (no electron density indicating the presence of a hydrogen atom was found in difference density maps). The μ_3–O–Co distance [2.1069(11) Å] is greater than the μ_3–O−Ti value [1.755(2) Å] due to the larger ionic radius of Co^{2+} (Shannon, 1976). The Ti–O7–Co bond angles [123.31(5)° and 123.32(5)°] are slightly larger than the Co–O7–Co angle [113.35(9)°].

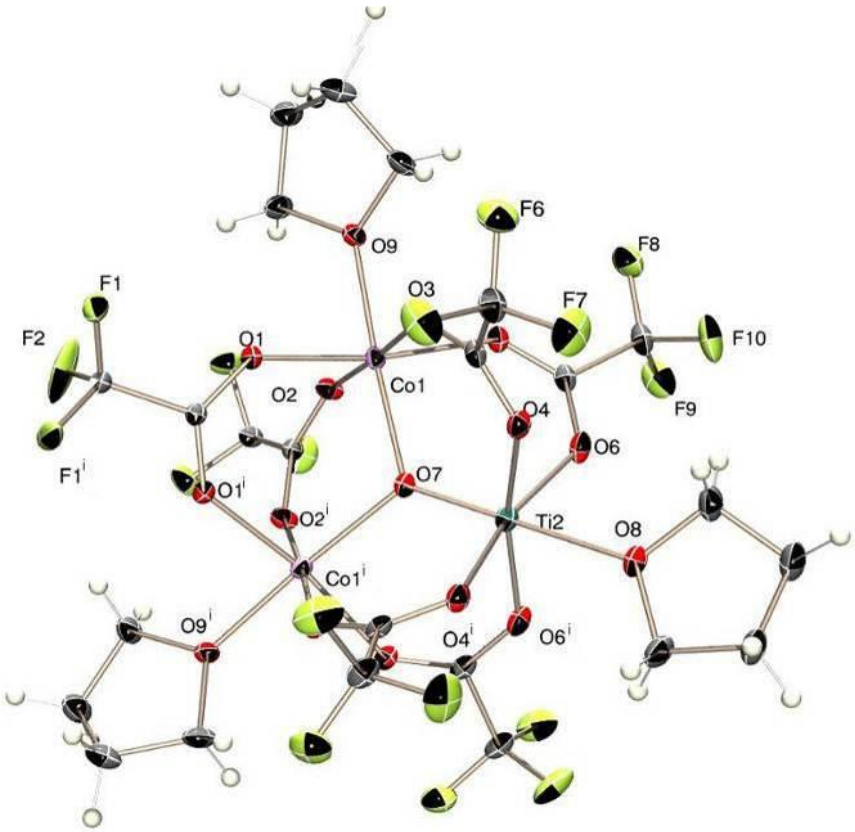

Figure 4.5: ORTEP diagram of precursor $[Co_2Ti(\mu_3\text{-}O)(TFA)_6(THF)_3]$ (**2**) with atom labels for metal, oxygen and fluorine atoms. Displacement ellipsoids are shown at the 50 % probability level.

For the Ti^{4+} ion, three sets of values of the Ti−O bond lengths are found: short μ_3-O7−Ti distances (1.755(2) Å), two intermediate Ti−O distances (one 2.0027(16) Å for Ti−O6 and Ti−$O6^{i}$ and a second for Ti−O4 and Ti−$O4^{i}$(2.0185(16) Å), where O4 and O6 are oxygen atoms of the carboxylate bridges), and longer Ti−O_{THF} bonds (2.180(2) Å). The bond distances Ti−O7 and Co−O7 are comparable to previously reported bond lengths (Gavrilenko, 2002). For the Co^{2+} ions, the Co−O_{COO} bond lengths [2.0402(15) Å, 2.0618(15) Å, 2.0965(15) Å and 2.0791(14) Å] are in good agreement with the bond lengths in analogous trinuclear acetate complexes (Gavrilenko, 2002). The Co−O_{THF} bond length (2.0611(15) Å) is shorter than the Ti−O_{THF} bond length (2.180(2) Å) and similar to such bond lengths in $Co_4(THF)_4(TFA)_8(\mu\text{-}OH)_2Cu_2(dmae)_2$ (Hamid, 2008).

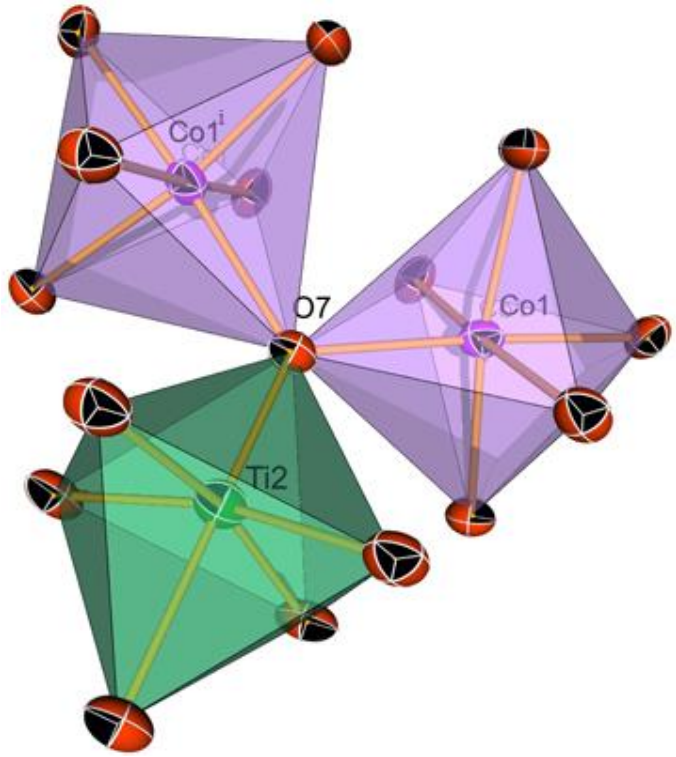

Figure 4.6: Oxygen coordinated octahedral spheres of Co1, and Ti2 in the core unit of the precursor (**2**) Displacement ellipsoids are shown at the 50 % probability level..

Table 4.3: Crystal data and structure refinement for precursor [$Co_2Ti(\mu_3$-O)$(TFA)_6(THF)_3$] (**2**)

Identification code	[$Co_2Ti(\mu_3$-O)$(TFA)_6(THF)_3$] (**2**)
Empirical formula	$C_{24}H_{24}Co_2F_{18}O_{16}Ti$
Formula weight	1076.19
Solvent	THF
Temperature	100(2) K
Crystal system	Monoclinic
Space group	$P2_1/m$
Unit cell dimensions	a = 8.6429(6)Å, b = 17.7715(13)Å, c = 12.5427(9)Å, β = 99.4220(10)°
Volume	1900.5(2) $Å^3$
Z	2
Density (calculated)	1.881 mg/M^3
Reflections collected	15004
Independent reflections	4795
Goodness-of-fit on F^2	1.054
Final R indices [I>2σ (I)]	R1 = 0.0341, wR2 = 0.0826,
R indices (all data)	R1 = 0.0432, wR2 = 0.0882

Table 4.4: Selected bond lengths [Å] and angles [°] for precursor [$Co_2Ti(\mu_3$-O)$(TFA)_6(THF)_3$] (**2**).

Bond distances(Å)			
Co1—O1	2.0402(15)	Ti2—O6	2.0028(16)
Co1—O2	2.0618(15)	Ti2—O7	1.755(2)
Co1—O3	2.0965(15)	Ti2—O8	2.180(2)
Co1—O5	2.0791(14)	Ti2—$O6^i$	2.0027(16)
Co1—O7	2.1069(11)	Ti2—$O4^i$	2.0185(16)
Bond Angles (°)			
O9—Co1—O7	176.75(7)	O5—Co1—O3	87.64(6)
O2—Co1—O7	93.15(7)	O1—Co1—O7	96.89(7)
O5—Co1—O7	91.19(7)	Co1—O7—Co^i	113.35(9)
O3—Co1—O7	89.48(7)	O7—Ti2—O6	98.09(6)
Ti2—O7—Co1	123.32(5)	$O6^i$—Ti2—O6	93.62(10)
O1—Co1—O9	86.34(6)	O7—Ti2—O4	95.83(6)
O9—Co1—O2	87.15(6)	$O6^i$—Ti2—O4	165.58(7)
O1—Co1—O5	171.23(6)	O6—Ti2—O4	88.13(7)
O9—Co1—O5	85.56(6)	$O4^i$—Ti2—O4	86.71(9)
O2—Co1—O5	93.33(6)	O7—Ti2—O8	177.71(9)
O1—Co1—O3	89.04(7)	O6—Ti2—O8	83.46(6)
O9—Co1—O3	90.27(6)	$O4^i$—Ti2—O4	86.71(9)
O2—Co1—O3	177.17(6)	Co1—O7—Co1	123.32(5)

4.2.2 Thermal Decomposition and Thin Film Characterization

Thermogravimetric analysis (TGA) gives an idea about the decomposition and volatility of complexes. The TGA curve (Figure 4.7) shows a rapid mass loss at temperatures above 129 °C and there appear to be three stages of weight loss. The first stage begins at 129 °C and is completed at 246 °C with a weight loss of 28.58%. The second step starts at 259 °C and is completed at 363 °C with a maximum weight loss of 46.16%. Directly following is the third and last stage ranging from 363 °C to 480 °C, resulting in a stable residual amount of 21.76% of the initial weight of precursor (**2**). Further heating above 480 °C to up to 900 °C did not cause any additional change in weight indicating thermal stability of the decomposition product. The residual mass is in good agreement with the expected composition for $CoTiO_3$-CoO (21.76%) indicating that the precursor has decomposed quantitatively into a composite oxide phase. DTG

curves confirm the occurrence of three major steps of decomposition of the precursor and indicate temperatures of maximum heat flow at 233, 337 and 415 °C in each degradation step, respectively.

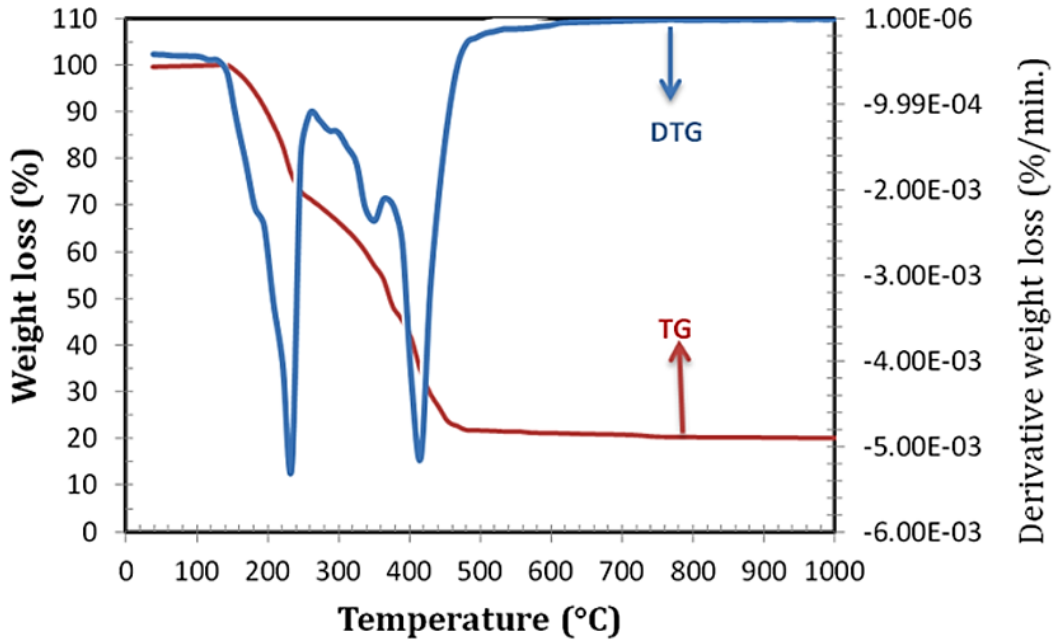

Figure 4.7: Thermogravimetric plot showing loss in weight with increase in temperature for precursor $[Co_2Ti(\mu_3\text{-}O)(TFA)_6(THF)_3]$ (**2**).

An X-ray diffractogram of the thin films deposited from precursor (**2**) at 500 °C indicates the formation of a composite of two different types of crystalline oxide phases: $CoTiO_3$ and CoO (Figure 4.8). Peaks indexed by 'X' at 2θ = 24.10, 33.17, 35.68, 40.93, 49.39, 53.56, 57.02, 57.14, 63.91, 65.53, 71.11, 78.99, 87.70 correspond to reflections (012), (104), $(2\bar{1}0)$, $(2\bar{1}3)$, (024), (116), (018), (122), (030), (125) (1010), $(4\bar{3}1)$ and $(4\bar{2}6)$, respectively, are in good agreement with reported crystallographic values for hexagonal $CoTiO_3$ (Newnham, 1964) with the space group $R\bar{3}$ and lattice dimensions of $a = b$ = 5.065 Å and c = 13.920 Å, [Inorganic Crystal Structure Database (ICSD): 98-001-6548]. The reflections (111) and (113) produced at 2θ = 37.29 and 73.99 marked by "Y" relate to CoO phase, (Tomaszewski, 1992) which has a cubic structure with the space group $Fm\bar{3}m$, and cubic axis length of 4.263 Å [ICCD: 98-000-9865]. The lines at

2θ = 43.34, 62.58, 73.99, corresponds to both hexagonal $CoTiO_3$ (202), (214), (4-20) planes and cubic CoO (002), (022) (113) planes.

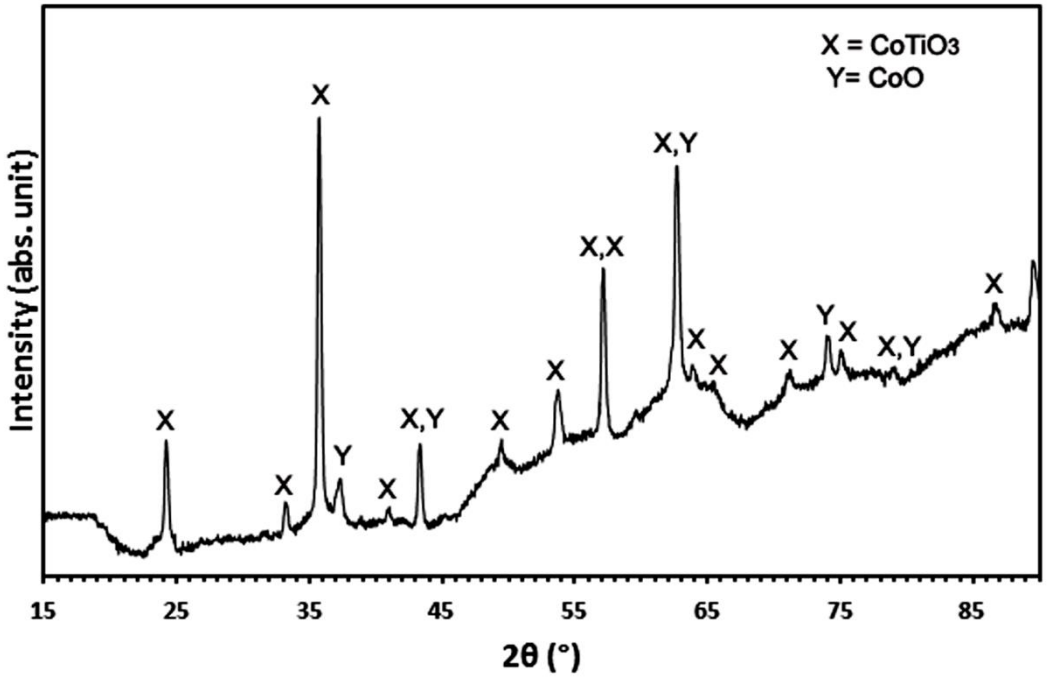

Figure 4.8: X-Ray diffractogram of the composite oxide obtained from precursor $[Co_2Ti(\mu_3\text{-}O)(TFA)_6(THF)_3]$ (**2**), X indicates peaks corresponding to $CoTiO_3$ and Y indicates peaks corresponding to CoO.

The XRD peak patterns of the thin films deposited from precursor (**2**) at 500 °C indicate its clean decomposition as it did not show any impurities such as TiO_2, Co_2O_3, Co_3O_4, Co_2TiO_4 or $CoTi_2O_4$ which were frequently observed in earlier studied cobalt titanium oxide preparative methods involving heating to 600 °C and above.

It is inferred that impurity free $CoTiO_3$-CoO composite thin films can be deposited directly on soda glass substrate from precursor (**2**) at 500 °C, as indicated in following equation

$$[Co_2Ti(\mu 3\text{-}O)(TFA)_6(THF)_3](\mathbf{2}) \xrightarrow[\text{AACVD}]{500\ ^oC} CoTiO_3 + CoO + \text{Volatiles}$$

The resulting greenish coloured thin films reflect light in multicoloured fringes when observed at different angles. Good adhesion properties were confirmed when the films were subjected to the Scotch tape test.

Generally, fabrication of thin films of titanium based composites from pre-synthesised powders for industrial applications requires temperatures of 1300 °C or higher. It has been reported (Nomura, 1983; Popov, 1981) that during fabrication of such films part of the Ti^{+4} ions are reduced to Ti^{+3} and other low valent titanium species, which negatively affects the dielectric properties and quality of these films. Since precursor (**2**) cleanly decomposes at a relatively low temperature (~500 °C), reduction of Ti^{+4} is avoided, resulting in thin films containing stoichiometric composite oxides while preserving the dielectric properties of the targeted Ti(IV) materials. Precursor (**2**) also has the potential to be used for the growth of high melting ceramic composite films on low melting substrates such as soda glass with some control over particle size and morphology in the film, thereby meeting the substrate requirements as well as microstructural requirements in certain applications (Dharmadasa, 2011; Dharmadasa, 2010).

The SEM image of the $CoTiO_3$-CoO composite thin film fabricated at 500 ºC indicates the formation flower petal-like morphology with well-defined grain boundaries and with feature sizes ranging between 2-6 μm as shown in Figure 4.9.

EDX spectra (Appendix 1) determined the stoichiometric composition of the $CoTiO_3$-CoO composite thin films indicating that the molar ratio of Co/Ti obtained from the peak areas of the EDX spectra is 15.61/7.51 and thus agrees well to the expected 2:1 ratio of $CoTiO_3$-CoO composite thin films.

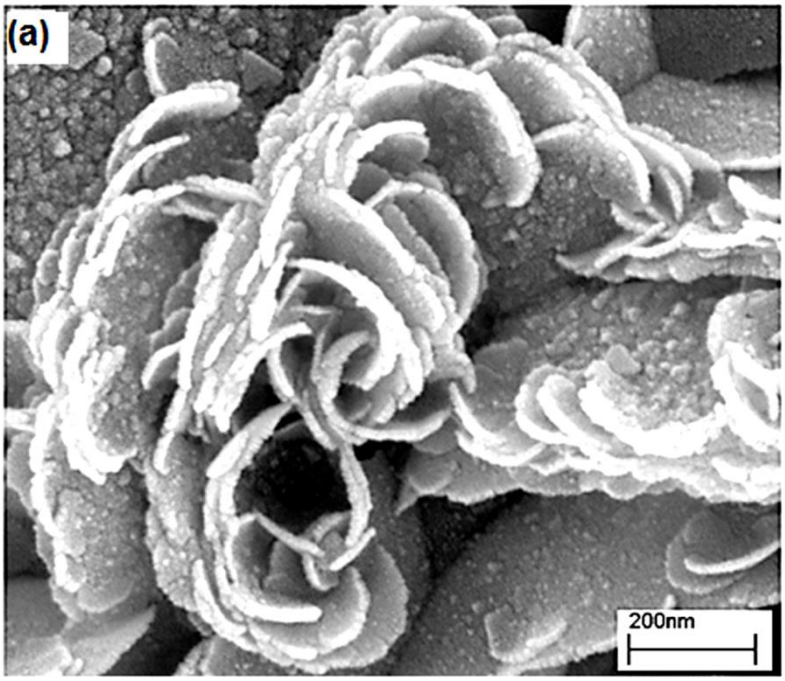

Figure 4.9: High resolution SEM microgarph of $CoTiO_3$-CoO composite thin films deposited on soda glass substrate at 500 ºC from precursor $[Co_2Ti(\mu_3\text{-}O)(TFA)_6(THF)_3]$ (**2**).

We believe that the development of suitable precursors, selection of an appropriate CVD technique to grow thin films, and mastering of deposition conditions is of crucial importance for further advancements of new technologies and applications. A recent example emphasizing this is the report by Wijayantha and co-workers who used the AACVD route to deposit SnO_2/ZnO composite films for novel photovoltaic cells and optoelectronic devices (Dharmadasa, 2011; Dharmadasa, 2010).

4.3 Tris-(*N,N'*-diethyldithiocarbamato)bismuth(III)Complex, $Bi_2[(S_2CNEt_2)_3]_2$ (3)[3]

The precursor $Bi_2[(S_2CN(C_2H_5)_2)_3]_2$ (**3**) was synthesized according to the literature procedure (Raston, 1976) by metathesis reaction of potassium dithiocarbamate with $Bi(NO_3)_3 \cdot 5H_2O$ in acetone, and was obtained as a yellow solid. Precursor (**3**) was characterized by melting point, elemental analysis, ^{1}H-NMR, IR, TGA (data presented in Chapter 3, section 3.2 at page 65) and single crystal X-ray diffraction. The precursor (**3**) is highly soluble in chloroform and dichloromethane (20g/100 mL) while the solubility decreases to 12g/100 mL in a 1:1 mixture of chloroform with toluene.

4.3.1 Single Crystal X-ray Structure of $Bi_2[(S_2CN(C_2H_5)_2)_3]_2$ (3)

The compound crystallizes in dimeric form $Bi_2[(S_2CN(C_2H_5)_2)_3]_2$ as shown in Figure 4.10 and crystal data of precursor (**3**) agree with the reported data (Raston, 1976).

4.3.2 Thermal Decomposition and Thin Film Characterization

The thermal decomposition behavior (Figure 4.10) of precursor (**3**) shows that the pyrolysis is a one stage process which begins at ca. 232 °C and ends at about 332 °C resulting in a residue amounting to 40.83% of the initial weight of the precursor which matches closely the expected composition for Bi_2S_3 (39.28%) as shown below in equation . The small weight gain around 340 °C may be due to the crystallization of Bi_2S_3. The residual weight from TGA also indicates the removal of carboneous matter from the organic groups. TGA also proves that the precursor is suitable for deposition of Bi_2S_3 at a relatively low temperature of 350 °C.

$$Bi_2[(S_2CN(C_2H_5)_2)_3]_2 \xrightarrow{350\ ^oC} Bi_2S_3 + \text{volatile by-products}$$

[3] Published: **Ehsan, M.A.;** Tahir, A.A.; Mazhar, M.; Wijayantha, K.U.; Zeller, M.; Hunter, A. (2010). Photoelectrochemical and photoresponsive properties of Bi_2S_3 nanotube and nanoparticle thin films. *Chem. Mater., 22*, 5084-5092

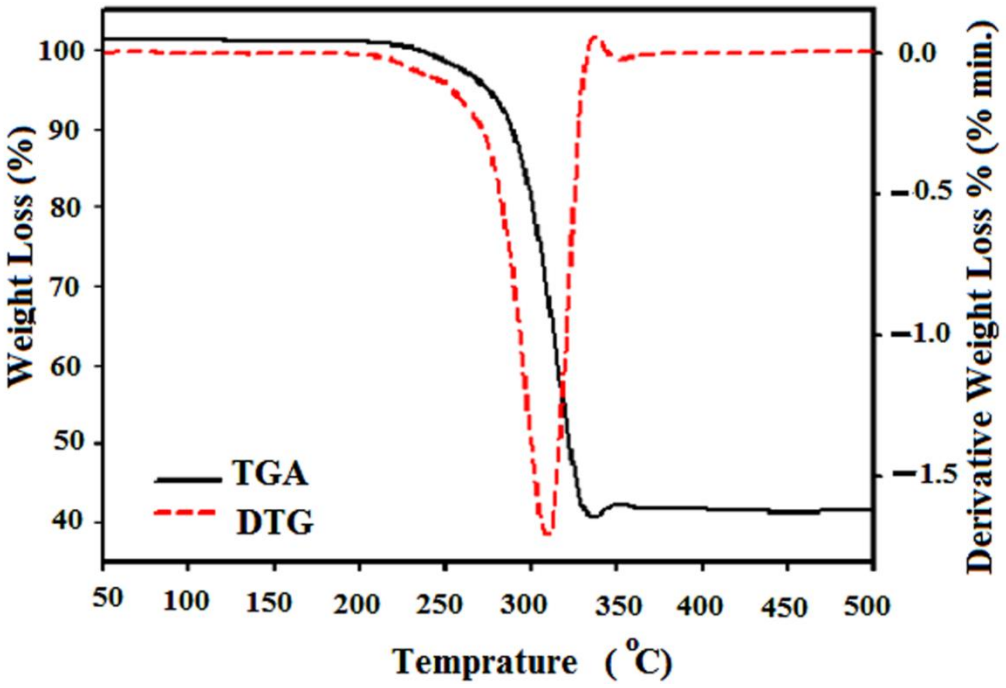

Figure 4.10: TGA/DTG plot showing loss in weight with increase in temperature for precursor (**3**).

In AACVD process solvent plays a vital role by controlling the viscosity of the deposition solution which directly affects the droplet size of the aerosol. The polarity and specific heat capacity of the solvent is also important and play a significant role during the decomposition process in the CVD reactor. In this work, we selected both nonpolar and polar solvents to investigate their effect on the texture, morphology and photoelectrochemical performance of the films. The effect of solvent and deposition temperature on the deposited thin films from precursor (**3**) was investigated using different solvents such as chloroform, dichloromethane, and a (1:1) mixture of chloroform and toluene at different deposition temperatures. The thin films deposited using CH_2Cl_2 as the solvent have very similar morphology as to the films deposited from $CHCl_3$ as to the deposition solution. The results presented here will focus on the structural, photoelectrochemical and photoresponsive properties of films made from chloroform and the chloroform/toluene mixtures as the solvents at different deposition

temperatures. All films deposited exhibit excellent adhesion properties on the substrate FTO as verified by the "Scotch tape test" and are stable in air and atmospheric moisture. Films deposited for more than 30 minutes with a thickness above 5μm lose adhesion and tend to fail the scotch tape test. Deposited films were characterized by XRD, FEGSEM, EDX and studied for their optical, photoelectrochemical and photorsponsive properties.

4.3.3 Structural Characterization

XRD was used to study the crystallinity of the deposited films and representative XRD peak patterns are shown in Figure 4.11. To eliminate the interference of SnO_2 from the FTO substrate, the films were also deposited on plane glass under similar deposition conditions as for the FTO substrates. XRD diffractogram for FTO is also shown in Figure 4.12 to recognize the FTO peaks. Comparison of the XRD pattern of the deposited thin films with the standard for Bi_2S_3 [00-017-0320] revealed that the crystalline product formed is pure Bi_2S_3 in its orthorhombic stibnite type modification, crystallizing in the *Pbnm* space group (Hofman, 1933). The XRD patterns of the nanotubes (Figure 4.12) show no significant deviation in relative peak intensities from that of bulk bismuthinite. However, the diffraction patterns for the nanoparticles (Figure 4.12) exhibit some preferred orientation with higher (310) peak intensity as compared to the nanotube films deposited from chloroform as solvent.

The XRD peak patterns show no signs of any chemically or pyrolytically driven phases other than Bi_2S_3 in the film. The XRD results agree well with reported data of Bi_2S_3 nanostructures deposited from bismuth dithiocarbamate precursor using other techniques (Koh, 2003; Monteiro, 2001; Monteiro, 2000). In contrast, Waters *et al*.(Waters, 2004) showed that the film composition deposited by AACVD using $Bi[(SPR_2)_2N]_3$ (R = ^{i}Pr or Ph) precursors are highly dependent on carrier gas flow and

temperature. Notably, the Bi/S ratio in the films changes with the change in carrier gas flow and deposition temperature. The films also contain traces of phosphorous as an impurity. Similarly, Koh *et al.*(Koh, 2003) had only been able to deposit pure Bi_2S_3 thin films for short deposition times from bismuth xanthate precursors. At increased deposition times they observed crystalline phases corresponding to elemental monoclinic sulphur forming on the surface of the resulting thicker Bi_2S_3 films. Interestingly, no such phases were detected in the present study for the films deposited by AACVD even after prolonged deposition times when the films were grown up to 30µm as shown by SEM cross-sectioning (Appendix 2). Energy dispersive X-ray spectra (EDX) were also obtained to determine the stoichiometric composition of the thin films, indicating that the thin films are composed of pure Bi_2S_3. The molar ratio of Bi/S obtained from the peak areas of the EDX graph is 39.45:60.55 and thus close to the expected 2:3 ratio of Bi_2S_3. The XRD and EDX results also prove the advantage of precursor (**3**) over the other bismuth precursors used for the deposition of Bi_2S_3 thin films.

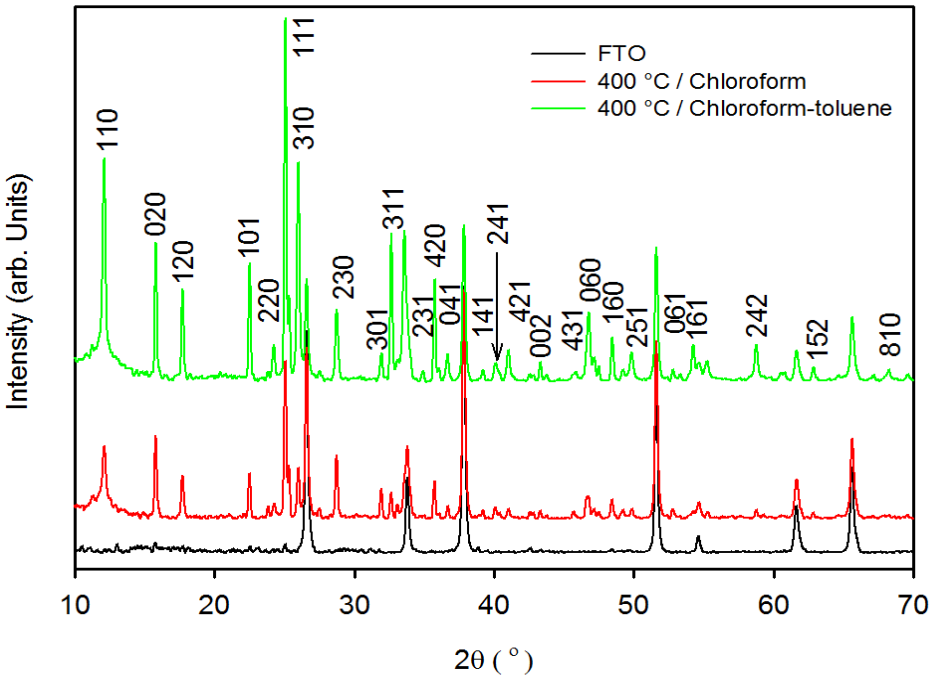

Figure 4.11: XRD patterns of Bi_2S_3 thin films deposited from precursor (1) at 400˚C on FTO substrate.

4.3.4 Surface Characterization

The morphology and structure of the Bi_2S_3 films were investigated by field-emission gun scanning electron microscopy (FEGSEM). Typical SEM images of the thin films prepared using chloroform as a deposition solvent at three different deposition temperatures (350, 400 and 450 ºC) are presented in Figure 4.12. The results illustrate that the films have complex nanostructures composed of nanotubes grown vertical on the FTO substrate as illustrated by the cross-sectional SEM image in Figure 4.12(d). The topographical SEM image of the film deposited at 350 ºC (Figure 4.12(a)) shows that the film consists of randomly oriented nanorods with a length of 200-400 nm. The image also indicates that some of the tubes started growing upwards.

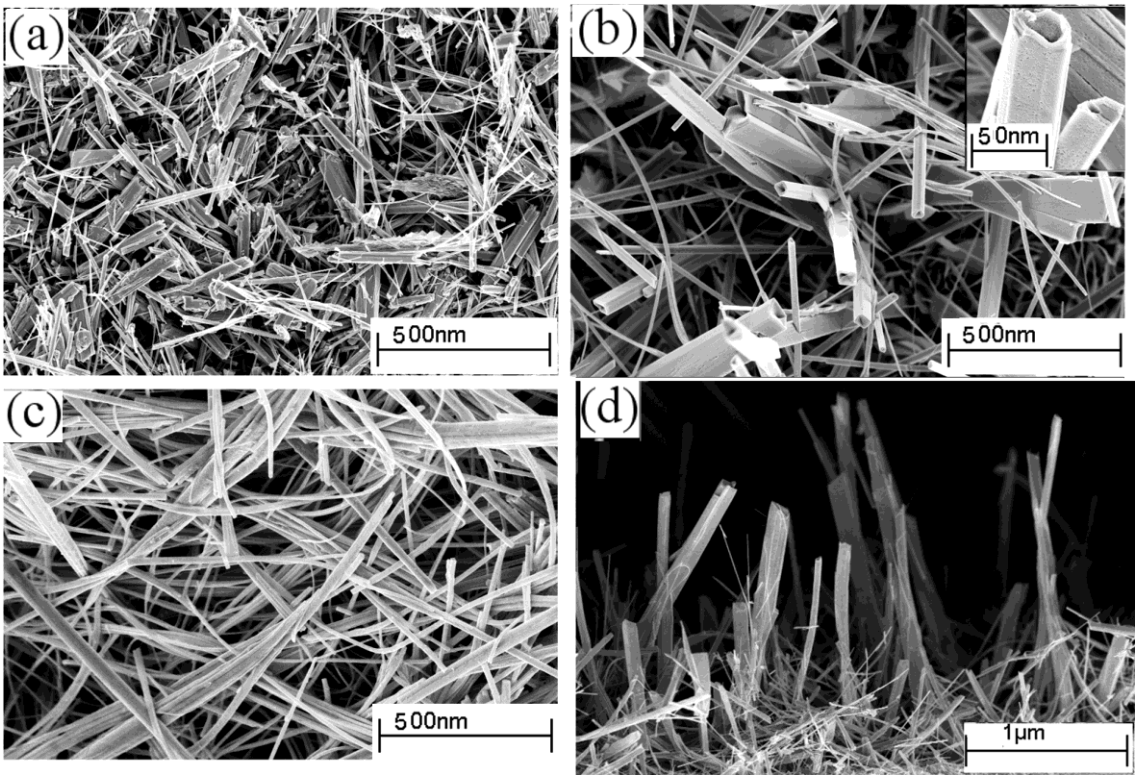

Figure 4.12: Surface topography of Bi_2S_3 thin films deposited on FTO substrate using chloroform as a solvent at (a) 350 ºC, (b) 400 ºC, (c) 450 ºC and (d) Cross-section of film deposited at 400 ºC; Inset of (b) shows a high resolution image of a nanotube.

The films deposited at 400 ºC (Figure 4.12(b)) indicate formation of much larger and hollow nanotubes growing upwards from the FTO surface. Remarkably the nanotubes grew more than a micron in length without any signs of fractures or breaking. The tubes have an internal diameter of 40 nm as shown in the high resolution image in the inset of Figure 4.12(d). The films deposited at 450 ºC are composed of radially oriented nano-wires/tubes with a diameter of 50–70 nm and an ultralong length of tens of micrometers (Figure 4.12(c)). The image also shows that the nano-wires/tubes are coiled together yielding a random and highly porous structure at the surface of the thin film. Bao *et al.* (Bao, 2008) showed that such types of nanowires can be used in back-to-back Schottky diodes. They have also shown that I–V characteristics of nanowires exhibit a unique rectifying behaviour, indicating potential applications in electronic nanodevices. Such locally ordered nanowire structures can also be used for fabricating nanosize optoelectronic and thermoelectric devices and may serve as nanoreactors and hosts (Shen, 2006).

The films deposited by using a mixture of chloroform and toluene (1:1) exhibit a completely different morphology as shown in Figure 4.13. The films deposited at 350 ºC and 400 ºC are very compact nanostructured with a particle size ranging from 25 to 45 nm as shown in Figure 4.13(a) and have an excellent adhesion to the FTO substrate surface. A cross-section (Figure 4.13(c)) shows the thickness of the film to be about 600 nm. (Differentiation between the FTO substrate and the Bi_2S_3 layer is difficult due to the compact nature of the film). Films deposited at 450 ºC show a porous structure and are composed of spherically shaped well-defined grains of 30-50 nm size (Figure 4.13(b) and 4.13(d)).

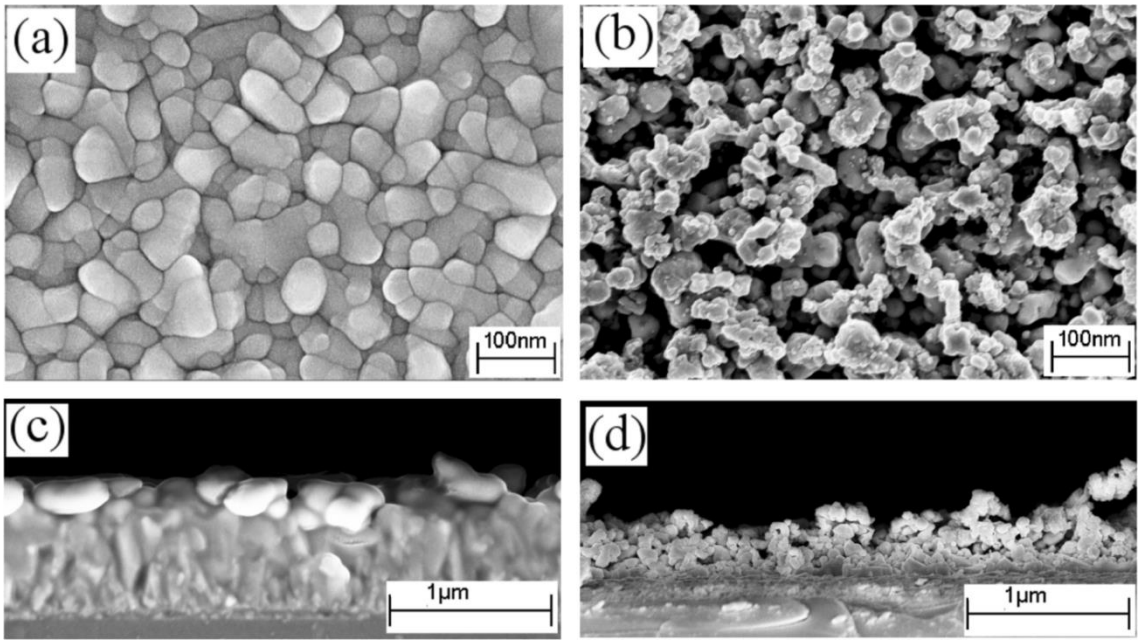

Figure 4.13: SEM images of the Bi_2S_3 surface topography of thin films deposited on the FTO substrate using chloroform/toluene (1:1) as the solvent at (a) 400 ºC and (b) 450 ºC, (c) and (d) show the cross-sections of films deposited at 400 ºC and 450 ºC, respectively.

The formation of films with different morphology and structure with the change of deposition solvent can be explained on the basis of homogeneous and heterogeneous chemical reactions and nucleation that constitute the CVD process (Hou, 2006). The main processes commonly occurring in AACVD are schematically described in Figure 2.15 (Chapter 2, page no. 28). In the first step the aerosol is delivered into the heated zone, where the solvent evaporates and vaporization of the precursor starts. The vaporized precursors then undergo subsequent decomposition in the gas phase (homogeneous) or on the heated substrate (heterogeneous) to deposit the desired film. The formation of thin films in the AACVD process is the result of homogeneous or heterogeneous reaction or a combination of both homogeneous nucleation in the gas phase and heterogeneous growth on the substrates. The type and ratio between the homogeneous and heterogeneous processes are directly responsible for the morphology, structure and composition of the thin films (Kodas, 1994). The balance between homogeneous and heterogeneous reaction in the AACVD process can be adjusted by

tuning the deposition parameters, such as the preheating temperature, the substrate temperature, the carrier gas flow rate, the type of solvent and also the concentration of precursor solution. These parameters determine the type of chemical reaction by controlling the chemical kinetics and thermodynamics of the deposition process which directly influence the structure, morphology and composition of the resulting thin films (Choy, 2003). Keeping all other parameters constant, composition, morphology and nanostructure of the thin films can be controlled by selecting solvents with a different specific heat capacity. The change in the solvent composition influences the nature of the deposition reaction by changing the size and thermodynamics of the aerosol droplets. In the current work, the concept of homogeneous and heterogeneous deposition reaction is maintained to deposit Bi_2S_3 thin films with different morphology and nanostructure by tuning the solvent of the deposition solution. Chloroform, a low specific heat capacity solvent, facilitates homogeneous reaction during deposition by evaporating and leaving the precursor molecules to vaporize much earlier in the heated zone. In a homogeneous reaction, the vaporization and decomposition of the precursor starts in the gaseous phase followed by the nucleation to form Bi_2S_3 particles. These particles are then adsorbed on the substrate surface and a ripening/growing process leads to the formation of nanotubes. Addition of toluene (a high specific heat capacity solvent), on the other hand, increases the vaporization temperature of the aerosol droplets and promotes the heterogeneous reaction. In a heterogeneous reaction, the vaporized precursor and its gaseous intermediate species are adsorbed onto the surface of the heated substrates, where they undergo substantial decomposition and chemical reactions to produce compact dense Bi_2S_3 thin films. At relatively higher deposition temperatures (~ 450 ºC), the formation of porous Bi_2S_3 films is a result of a combined contribution of homogeneous nucleation in the gas phase and heterogeneous growth on the substrates. We assume that the solvent only contributes to change the enthalpy of the

system and not the decomposition pathway of the precursor. The absence of halide contaminations in the EDX analysis of thin films indicates that the solvent is not taking part in the decomposition process and completely evaporates before the precursor decomposition starts.

4.3.5 Optical Properties of Bi_2S_3 Thin Films

The optoelectronic properties of semiconducting materials are crucial for a large number of applications as many unique electronic properties result from the band energy structures of semiconducting materials. In the band theory approach the band structure of solids is a function of a three-dimensional wave vector (*k*) within the Brillouin zone. The latter depends on the crystal structure and corresponds to the unit cell of the reciprocal lattice. The simplest method for probing the band structure of a semiconducting material is to measure its optical absorption spectrum. Figure 4.14 shows the absorption spectra recorded at room temperature using SnO_2 as reference to eliminate the contribution of the FTO substrate. The recorded optical spectrum was used to calculate the bandgap energy of bismuth(III) sulphide. Fermi's golden rule for fundamental interband electronic transitions was used for the relation between absorption coefficient and photon energy (Marder., 2000) (which is a quite reasonable approximation for values of *k* near the absorption edge):

$$\alpha h\nu = A_0(h\nu - E_g)^n$$

where E_g is the bandgap, $h\nu$ is the incident photon energy, and *n* depends on the nature of transitions and has the values 1/2 and 2 for allowed direct and indirect transitions, respectively.

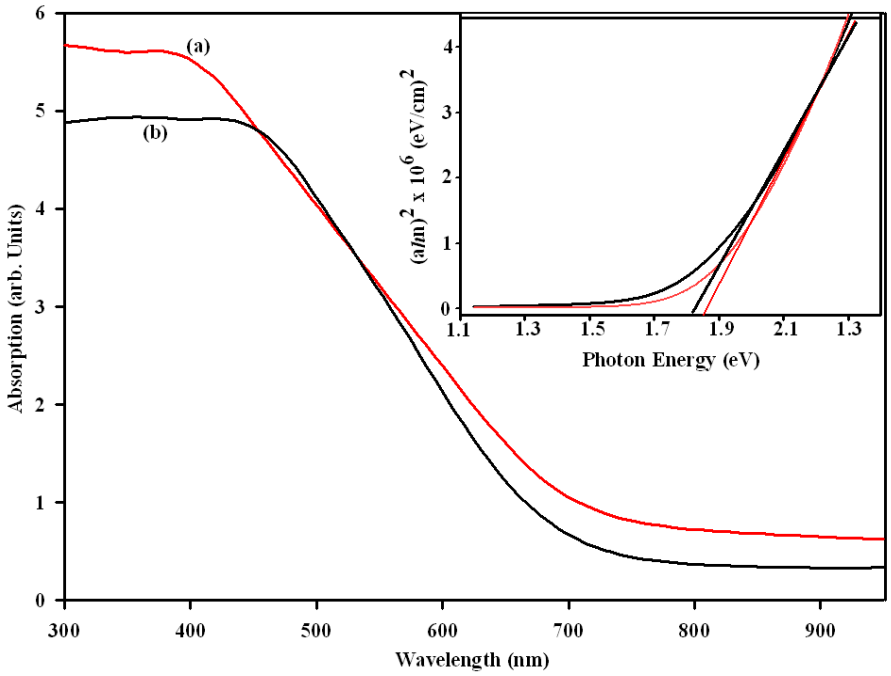

Figure 4.14: Optical absorption spectrum of Bi_2S_3 films deposited from precursor (**3**) by using chloroform (a) and choloroform/toluene (b) as solvents at 400 ºC. Inset: Tauc plot showing the estimated optical bandgap of 1.85 and 1.8 eV, respectively.

It is possible to determine the nature of transitions involved by plotting the graphs of $(\alpha h\nu)^n$ versus $h\nu$ for different values of 'n' as described above. The bandgap is estimated from the intercept of the extrapolated linear fit to the experimental data of the Tauc plot. A bandgap of 1.85 and 1.8 eV was estimated by extrapolating the linear part of the graph as shown in Figure 4.14 (inset) for the films deposited at 400 ºC from chloroform and choloroform/toluene, respectively. The estimated bandgaps were found to be very close to reported values for Bi_2S_3 thin films (Han, 2007; Mane, 2007). The higher value of the bandgap energy when compared with the corresponding bulk value (1.7 eV) can be attributed to the nanocrystalline nature of the thin films (Pejova, 2006).

4.3.6 Photoelectrochemical Properties of Bi_2S_3 Thin Films

The photoelectrochemical properties of Bi_2S_3 nanotube and nanoparticle thin film electrodes were studied in a three electrode mode using 1M Na_2SO_3 as the hole

scavenger. Electrodes were illuminated from the electrode side. The *J*-V plots of thin films deposited from chloroform and chloroform/ toluene at different temperatures are shown in Figure 4.15 and 4.16 respectively. For electrodes deposited from both solvents the anodic photocurrent steeply increases with the increase of applied potential and doesn't reach saturation which is typical for many nanoparticle electrodes. This was thought to be a result of high recombination of photogenerated charges. Similar PEC behaviour was reported for colloidal Bi_2S_3 nanoparticles (Riley, 2004) and for electrodeposited Bi_2S_3 thin films. The observation that the photocurrent falls to zero at potentials positive to the recorded flat band potential indicates that electron accumulation decreases the photogenerated charge separation as a result of back reaction of electron the conduction band (CB) with holes in the valance band (VB). For the electrodes deposited using chloroform at a deposition temperature of 400 °C the maximum photocurrent density of 1.9 mA/cm^2 was recorded (at 0.23V vs Ag/AgCl/3M KCl). The photocurrent slightly decreases with increase of deposition temperature which may be due to increased recombination with the increase of thickness in the film as revealed by cross-sectional SEM image (Figure 4.12). The Bi_2S_3 electrodes deposited from chloroform/toluene at 450 °C show a maximum photocurrent density of 1.0 mA/cm^2 (at 0.23V vs Ag/AgCl/3M KCl) which is significantly lower than the recorded value for the nanotube electrodes.

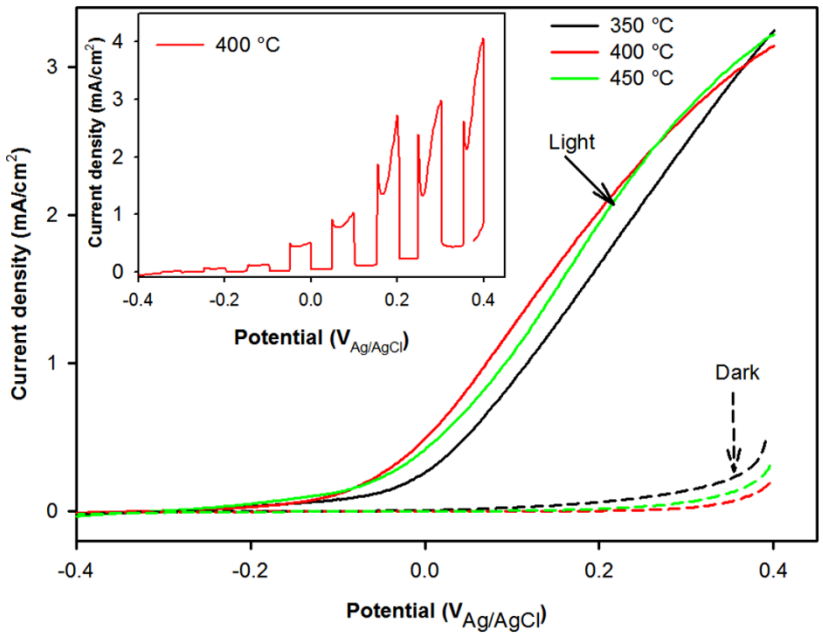

Figure 4.15: Current-voltage characteristics for the Bi_2S_3 thin films deposited from chloroform at deposition temperatures between 350 - 450 °C and measured in 1M Na_2SO_3 electrolyte. The inset shows the photocurrent transits for the film deposited at 400 °C.

The photocurrent recorded for the photoelectrodes deposited from precursor (**3**) is among the highest reported to date for Bi_2S_3 electrodes (Mane, 1999; Riley, 2004). We tentatively attribute this to the high surface area of the nanotube electrodes. The dark current characteristics for both types of electrodes are similar. Photocurrent transients are shown in the inset of Figure 4.15 and 4.16. Strong photocurrent spikes are observed in the depletion region for electrodes deposited from chloroform indicating recombination properties of nanotube electrodes presumably due to surface states related to the high surface area. However, it shows the potential of Bi_2S_3 nanotube electrodes in PEC applications compared to nanoparticle electrodes provided that the surface recombination can be minimized.

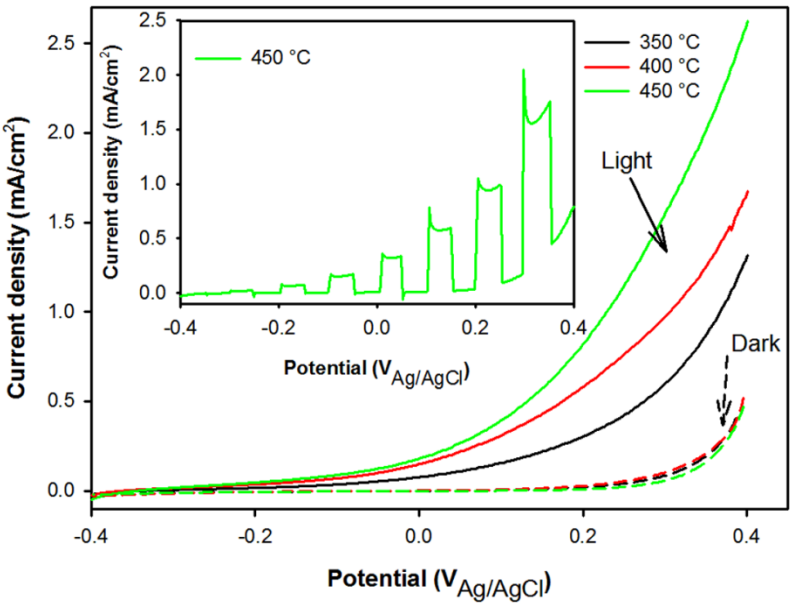

Figure 4.16: Current-voltage characteristics for the Bi_2S_3 thin films deposited from chloroform/toluene at a deposition temperature between 350- 450 °C and recorded in 1M Na_2SO_3 electrolyte. The inset shows the photocurrent transits for the film deposited at 450 °C.

Similarly, Mohapatra *et al.* has shown the advantage of use of nanotubes based electrodes in PEC applications. They found that Fe_2O_3 nanotubes are better catalysts for the photooxidation of water to H_2 and O_2 compared to other Fe_2O_3 architectures and charge transport properties of the nanotubes are 40−50 times higher than those of the nanoparticles, which led to better photocurrent of nanotubes based electrodes compared to that of nanoparticles electrodes (Yu, 2008).

4.3.7 Photoresponsive Characterization of Bi_2S_3 Films

Other important applications of photoresponsive semiconductor materials are photodetectors and optical switches. They are vital elements in light wave communications, optoelectronic circuits and imaging techniques (Yu, 2008). Studies were extended in this direction in the present work to explore the applicability of Bi_2S_3 nanotube and nanoparticle thin film electrodes in photodetectors. Figure 4.17 shows the photoresponse of FTO/Bi_2S_3/FTO devices as a function of time. Regular chopping of

the illuminated light (halogen lamp) produced a reproducible photoresponse of the device thus indicating that the Bi_2S_3 nanotube based device can be reversibly switched on and off between low and high conductivity. The on/off sensing cycles could be repeated over a period of 2 hours without any noticeable deterioration. The photocurrent produced for the Bi_2S_3 nanotube based photodetector is higher than that of the Bi_2S_3 nanoparticle based device (Figure 4.17(a),(b)), indicating that the conductivity of the nanotube based thin films is more sensitive to the light exposure than the nanoparticle based films.

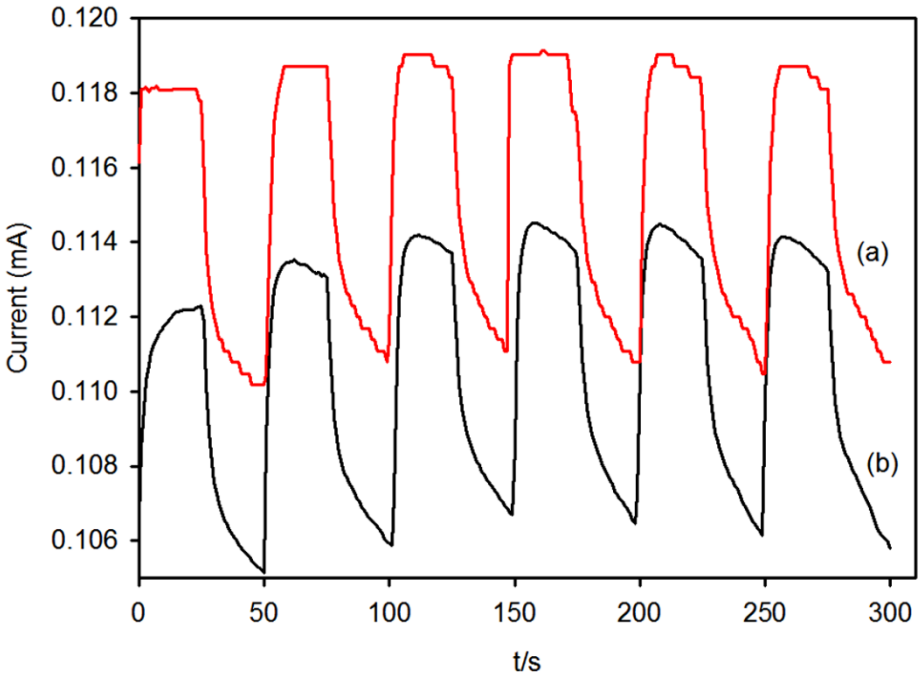

Figure 4.17: Sensitivity of the photoresponse at a bias of 20 mV for Bi_2S_3 thin films deposited by using chloroform (a) and chloroform / toluene (b) at 400 ºC.

The energy from the light promotes electrons from the valence band Bi_2S_3 into the conduction band, increasing the charge carrier concentration via direct electron-hole pair creation and thus enhancing the conductivity (Li, 2009). The rise and decay time of the Bi_2S_3 switches are less than 2 ms, suggesting that the Bi_2S_3 nanotubes/particles network thin films can be used in optoelectronic switches. It is worth noting that the repeatable measurements were recorded under open-air conditions, suggesting that

Bi_2S_3 thin films prepared in this work have a higher photostability than that of previously reported Bi_2S_3 nanowires which needed to be tested for photoconductivity under vacuum (Wang, 2002) or in a nitrogen atmosphere (Peng, 2001). The photoconductivity characteristics suggest that Bi_2S_3 nanowires are good candidates for optoelectronic switches (Kind, 2002).

The *I-V* curves of the FTO/Bi_2S_3/FTO devices measured for a 0.5V bias range under light and dark conditions are shown in Figure 4.18.

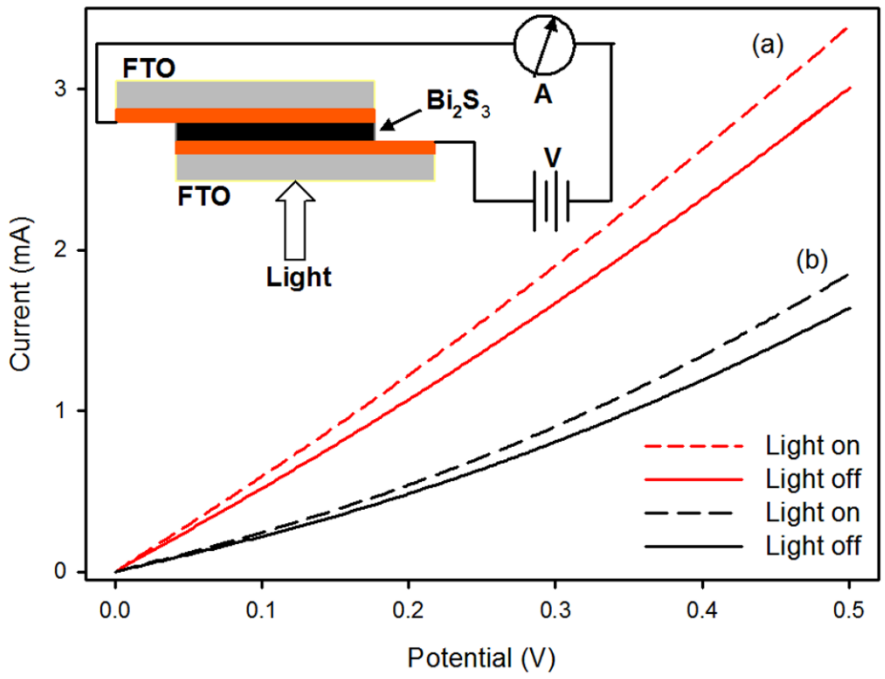

Figure 4.18: *I-V* curves for Bi_2S_3 thin films deposited by using chloroform (a) and chloroform / toluene (b) at 400 ºC. Inset: experimental setup for measurements of photoresponsive properties of Bi_2S_3 thin films.

The current-voltage curve for the FTO/Bi_2S_3 nanotubes based films shows that under light conditions the slope of the *I-V* curve is higher than under dark conditions (Figure 4.18(a)), indicating an enhanced conductivity upon irradiation. A similar increase of the slope of the *I-V* curve was also seen for the FTO/Bi_2S_3 nanoparticles based films (Figure 4.18(b)) but with a less significant response when compared with that of the nanotube based films. These results confirm that the conductivity of the nanotubes is

more sensitive than that of the nanoparticles. Interestingly, the *I–V* curves for both dark current and photocurrent exhibit an approximately linear shape with a bias from 0 to 0.5 V that displays ohmic behaviour. These phenomena are different from the observed for individual Bi_2S_3 nanowires across two Au electrodes (Bao, 2007). These results further suggest that the prepared Bi_2S_3 thin films are good candidates for applications in high-sensitivity photodetectors and photoelectronic switches. It is important to note that the Bi_2S_3 nanotube array was spontaneously formed via a facile AACVD approach and that this approach did not require any template or surfactant to control the orientation of the nanotubes, which may offer the potential for monolithic low-cost large-scale integration with CMOS electronics (Konstantatos, 2008).

4.4 Tris-(*N,N'*-dialkyldithiocarbamato)indium(III)n-pyridine Complexes, $[In(S_2CNRR')_3]\bullet n(py)$ (4)-(7)[4]

The indium dithiocarbamates with general formula $[In(S_2CNRR')_3]\bullet n(py)$ [where py = pyridine; R,R' = Cy, n = 2 (**4**); R,R' = ^{i}Pr, n = 1.5 (**5**); NRR' = Pip, n = 0.5 (**6**) and R= Bz, R' = Me, n = 0 (**7**)] are conveniently prepared via metathetical reaction of the indium trichloride and sodium dithiocarbamate in methanol-pyridine solutions as shown in chemical reaction.

$$InCl_3 + 3Na(S_2CNRR') \xrightarrow[MeOH]{Pyridine} [In(S_2CNRR')_3]\cdot n(py) + 3NaCl$$

RR' = Cy, n = 2 (**4**); RR' = ^{i}Pr, n = 1.5 (**5**)

NRR' = Pip, n = 0.5 (**6**); RR' = BzMe, n = 0 (**7**)

The synthesized complexes were characterized by microanalysis, IR, ^{1}H-NMR, (data presented in Chapter 3, section 3.2 at pages 65-67) TGA and single crystal X-ray techniques. These complexes are produced in high yield and are stable in air and moisture, highly soluble in common organic solvents such as THF, chloroform and pyridine. This makes them promising precursors for application in the deposition of indium sulphide thin films by AACVD. The CHN microanalysis found for complexes (**4**), (**5**), (**6**) and (**7**) agrees with the stoichiometry of the complex as calculated from the crystal data.

The ^{1}H-NMR studies of complexes (**4**), (**6**) and (**7**) reveal usual splitting patterns for the corresponding R groups, however an unusual splitting behaviour has been detected in the ^{1}H-NMR spectra of complex (**5**) where isopropyl ($CH(CH_3)_2$) group display three broad signals. Two equally intense broad singlets appeared at 3.95 and 5.10 ppm

[4] Published: **Ehsan, M.A**.; Peiris, T.N.; Wijayantha, K.U.; Olmstead, M.M.; Arifin, Z.; Mazhar, M., . . . McKee, V. (2013). Development of molecular precursors for deposition of indium sulphide thin film electrodes for photoelectrochemical applications. *Dalton Tran.*, *42*, 10919-10928.

are assigned to methine protons of ($NC\mathit{H}(CH_3)_2$), originating from the different positions (syn or anti) with respect to the dithiocarbamate group. The doublet signal of unequal intensities appeared at 1.48 and 1.68 ppm have been assigned to methyl protons of the isopropyl group and has been interpreted in terms of coordination and barrier rotation about C— N which makes the nitrogen substituents magnetically non-equivalent (Lindmark, 1983; Oliveira, 1999).

In the IR spectra ν(C—N) stretching vibrations for complexes (**4**)-(**7**) were detected in the range of 1471-1491 cm^{-1}. This fact implies that the dialkyldithiocarbamate is coordinated to the metal as a bidentate ligand and indicates the partial double bond character in the C ---- N bond (Clark, 2000; Dutta, 2002).

4.4.1 Single Crystal X-ray Structure of tris(*N*,*N'*-dicyclohexyldithiocarbamato) indium(III)dipyridine Complex, [In($S_2CNCy_2)_3$]•2py (4)

The four tris-dithiocarbamate complexes have similar geometric features but the structures differ in the number of pyridine solvate molecules. The In-S distances of the bidentate dithiocarbamate ligands fall within a narrow range, as do the C-S distances, indicating full delocalization. Furthermore, the C=N distances are short, as is typical for these ligands (Clark, 2000; Dutta, 2002). To illustrate these similarities, the average complex geometry is given in Table 4.6, together with the average deviations from the mean.

The crystal structure of [In($S_2CNCy_2)_3$]•2py (**4**) is shown in Figure. 4.19. The complex (**4**) has non-crystallographic three-fold symmetry as viewed down the plane of C1/C14/C27 and without inclusion of the cyclohexyl conformations. All the cyclohexyl rings are connected equatorially to their parent nitrogen atoms. The two molecules of pyridine were disordered over two orientations. The two sets of atoms comprising the pyridine molecules were refined as rigid idealized hexagonal groups with occupancies

that were initially refined and then fixed at {0.50/0.50} and {0.30/0.70} for the sets involving N4 and N5, respectively. With two pyridine molecules removed from the refinement, the solvent accessible void is 1256 $Å^3$. In the structure, one pyridine occupies a channel perpendicular to the *bc* plane. The second pyridine is sandwiched between cyclohexyl rings in an alternating fashion

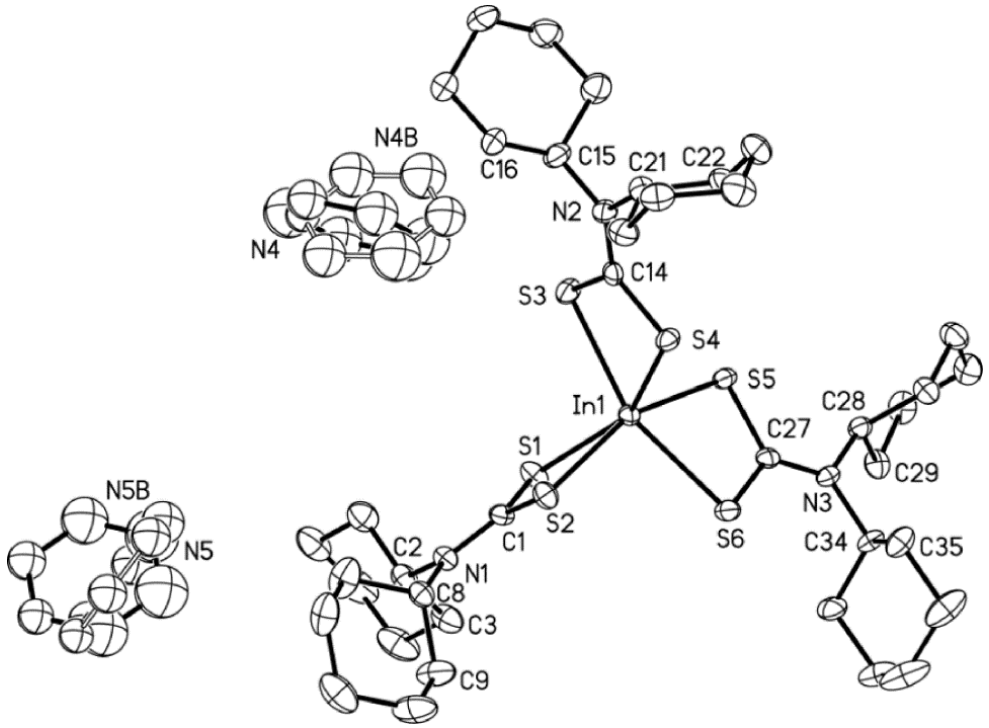

Figure 4.19: Molecular structure of complex $[In(S_2CNCy_2)_3]$•2py (**4**). Displacement ellipsoids are shown at the 50 % probability level.

4.4.2 Single Crystal X-ray Structure of tris(*N*,*N'*-di-iso-propyldithiocarbamato) indium(III) one and half pyridine Complex, $[In(S_2CN(^iPr)_2)_3]$•1.5py (5)

In the structure of $[In(S_2CN(^iPr)_2)_3]$•1.5py (**5**), shown in Figure. 4.20, there is one pyridine solvent molecule in a general position and a second pyridine at half-occupancy disordered about a centre of inversion. There is also small orientational disorder (83:17) in one of the isopropyl groups (not shown). With pyridine molecules removed from the refinement, the accessible solvent volume is 438 $Å^3$. In the structure, the 1.5 pyridine solvate molecules are encaged by isopropyl groups.

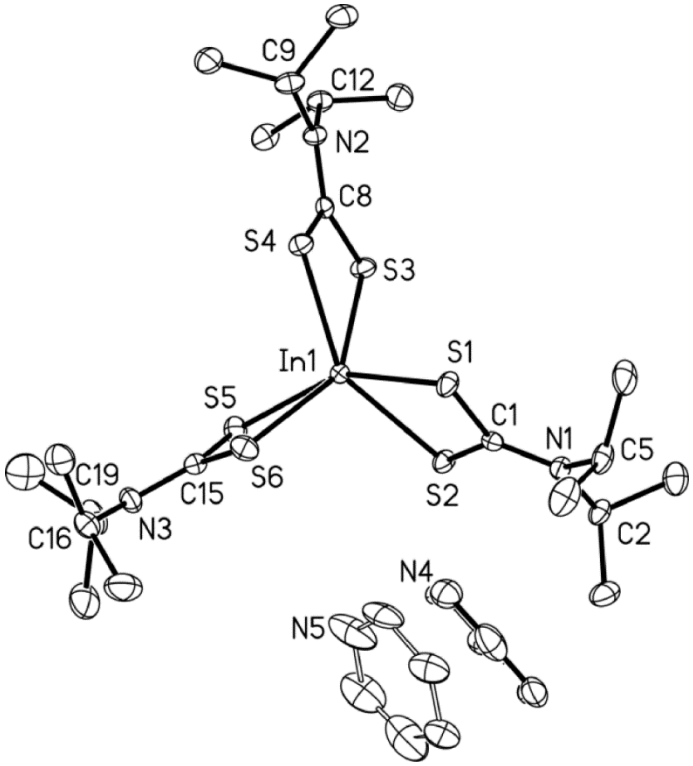

Figure 4.20: Structure of $[In(S_2CN(^iPr)_2)_3]$•1.5py (**5**). Displacement ellipsoids are shown at the 50 % probability level.

4.4.3 Single Crystal X-ray Structure of tris(piperidinedithiocarbamato)indium(III) half pyridine Complex, $[In(S_2CPip)_3]$•0.5py (6)

In this complex the dithiocarbamate has a smaller footprint, as the NRR' has been replaced by piperidine (Figure 4.21). There is one pyridine site, which is both rotationally disordered and disordered with respect to a crystallographic center of symmetry. With pyridine removed from the refinement, the solvent accessible void is 167 $Å^3$. In the structure the pyridine molecules occupy a channel perpendicular to the *bc* plane.

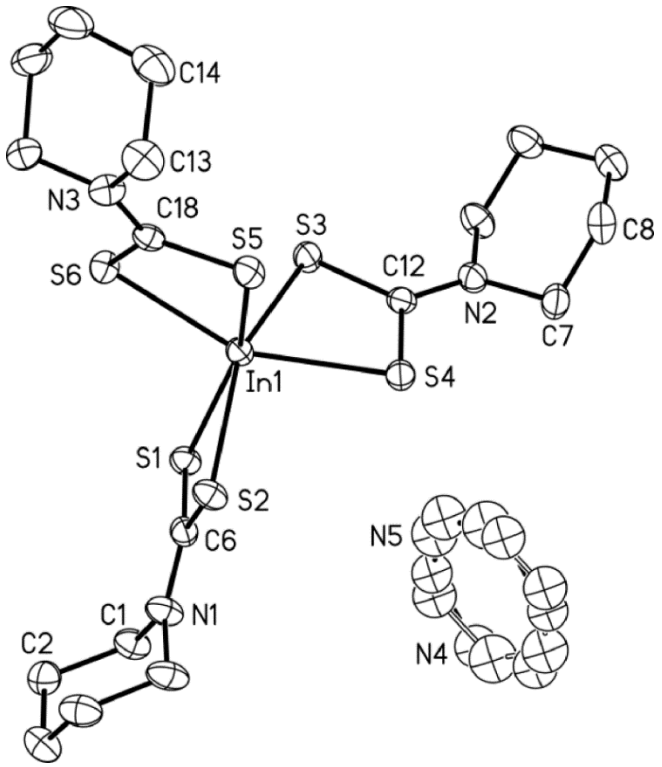

Figure 4.21**:** Structure of $[In(S_2C(Pip))_3]$•0.5py (**6**). Displacement ellipsoids are shown at the 50 % probability level.

4.4.4 Single Crystal X-ray Structure of tris(*N*-benzyl-*N'*-methyldithiocarbamato) indium(III) Complex $[In(S_2CNBzMe)_3]$ (7)

Complex (**7**), shown in Figure 4.22, has no solvate molecules in the structure. There is a non-classical hydrogen bond between S4 and a methyl H atom of a neighbouring molecule. The S···H distance is 2.81 Å. In this solvate-free structure the packing index is 68.4%, and there is no solvent accessible void.

The average In-S bond lengths 2.590[4], 2.594[9], 2.592[11] and 2.594[11] Å observed in complexes (**4**)-(**7**), respectively, are similar to those reported analogues of these compounds. The average C-S distances are close to 1.72 Å indicating delocalization in the CS_2 skeleton. The average C=N bond distances which are approximately 1.33 Å are significantly shorter than the normal single bond, suggesting considerable double bond character, as expected for metal dithiocarbamates (Clark, 2000; Dutta, 2002).

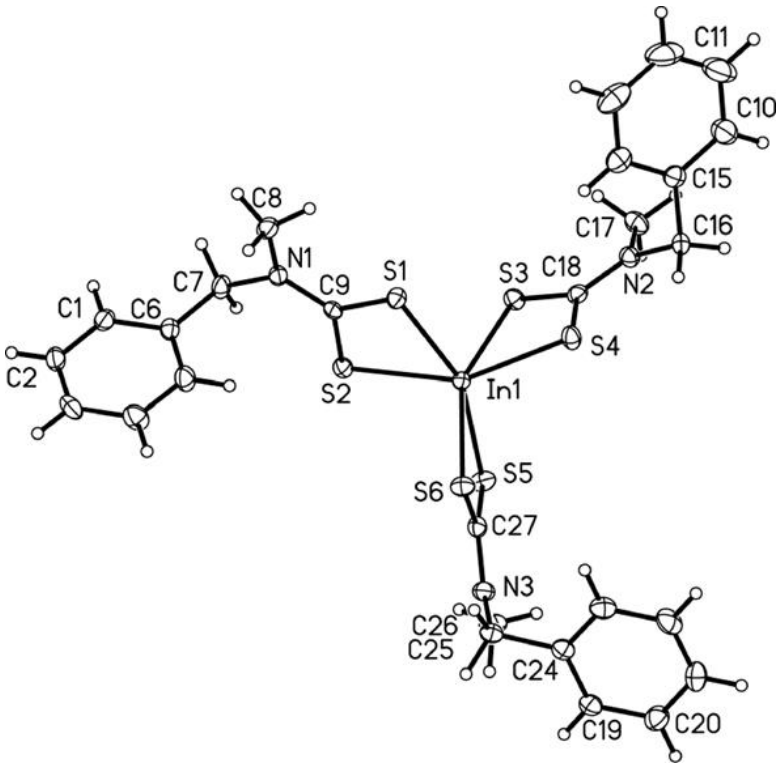

Figure 4.22: Structure of $[In(S_2CNBzMe)_3]$ (**7**). Displacement ellipsoids are shown at the 50 % probability level.

Table 4.5: Crystal data and refinement parameters for the complexes $[In(S_2CNCy_2)_3]$•2py (**4**), $[In(S_2CN(^iPr)_2)_3]$•1.5py (**5**), $[In(S_2CPip)_3]$•0.5py (**6**) and $[In(S_2CNBzMe)_3]$ (**7**).

	(1)	**(2)**	**(3)**	**(4)**
Empirical formula	$C_{49}H_{76}InN_5S_6$	$C_{28}H_{48}InN_5S_6$	$C_{20.5}H_{32.5}InN_{3.5}S_6$	$C_{27}H_{30}InN_3S_6$
Formula weight	1042.33	762.90	635.18	703.72
Temperature, K	100(2)	100(2)	100(2)	100(2)
Wavelength, Å	0.71073	0.71073	0.71073	0.71073
Crystal system	monoclinic	triclinic	triclinic	triclinic
Space group	$P2_1/c$ (No. 14)	*P-1*(No. 2)	*P-1*(No. 2)	*P-1*(No. 2)
Unit cell dimension	a = 10.5733(2) Å, b = 22.1491(6) Å, c = 22.3726(6) Å, β = 91.804(2)°	*a* = 11.6384(4) Å, *b* = 11.9426(4) Å, *c* = 14.4945(3) Å, *α* = 92.781(2)°, *β* = 102.078(2)° *γ* = 111.637(3)°	*a* = 9.4396(2) Å, *b* = 10.7753(3) Å, *c* = 14.0452(3) Å, *α* = 93.148(2)°, *β* = 91.655(2)° *γ* = 107.443(3)°	a = 9.7966(4) Å, b = 12.2791(8) Å, c = 12.7790(8) Å, α = 96.142(4)°, β = 92.353(4)°, γ = 100.383(5)°

Volume, $Å^3$	5236.8(2)	1813.63(9)	1359.31(6)	1500.51(15) $Å^3$
Z	4	2	2	2
F(000)	2200	794	650	716
Reflections collected	49516	12748	13467	13669
Independent reflections	12019 (R_{int} = 0.0679)	6324 (R_{int} = 0.0152)	6491 (R_{int} = 0.0114)	6504 unique (R_{int} = 0.0177)
R_1 ($I > 2\sigma$ (I)	0.0476	0.0608	0.0162	0.0228
$wR(F^2)$ (all data)	0.1055	0.0608	0.0403	0.0514

Table 4.6: Selected bond distances (Å) and angles (°) for the complexes $[In(S_2CNCy_2)_3]$ •2py (**4**), $[In(S_2CN(^iPr)_2)_3]$•1.5py (**5**), $[In(S_2CPip)_3]$•0.5py (**6**) and $[In(S_2CNBzMe)_3]$ (**7**) with average deviations from the mean given in square brackets

	(4)	**(5)**	**(6)**	**(7)**
In-S	2.590[4]	2.594[9]	2.592[11]	2.594[11]
S-In-S bite angle	69.26[3]	69.0[2]	69.7[3]	69.70[13]
C-S	1.732[6]	1.730[2]	1.730[2]	1.726[3]
C=N	1.335[3]	1.331[2]	1.325[1]	1.332[1]

4.4.5 Thermal Decomposition Studies of Complexes (4)-(7)

The efficacy of complexes (**4**)-(**7**) as SSPs for the deposition of indium sulphide thin films was probed by thermogravimetric experiments and their TG and DTG curves are presented in Figure 4.24 and appendix 3-6. The TG profiles of pyridine solvated (**4**), (**5**) and (**6**) exhibit two-steps while non-solvated precursor (**7**) shows a one-step pyrolysis towards the end product. The initial weight loss at temperature range of 55-115 °C from (**4**) and (**5**) and at 45-110 °C for (**6**) is attributed to the loss of pyridine molecules. The observed weight losses of 11.60 (**4**), 15.50 (**5**) and 6.84% (**6**) show some agreement with the calculated values of 11.37, 15.54 and 6.21% for the loss of 1.5 and 0.5 molecule of pyridine from (**4**), (**5**) and (**6**), respectively. The TG experiment on solvent free (**7**) did not show any weight loss in the temperature range of 55-120 °C confirming that the initial weight loss in (**4**), (**5**) and (**6**) is essentially due to the loss of pyridine. The TG and DTG data reveal that the precursors (**4**)-(**7**) decompose in the temperature range 230-400 °C in a single step to produce stable residue masses of 15.19, 20.09, 23.85 and 25.40%, respectively. These mass losses agree well with the theoretical values 15.62, 21.36, 25.64 and 23.15% for the formation of β-In_2S_3 from (**4**)-(**7**). The DTG curves of pyridine solvated complexes (**4**)-(**6**) indicate two maxima of heat intake.

The first heat intake occurs at 94 °C for (**4**) and (**6**) and at 84 °C for (**5**), indicating the removal of pyridine, while the second maxima appeared at 340 °C for (**4**), 290 °C for (**5**) and 330 °C for (**6**). The DTG curve of non-solvated (**7**) shows maximum heat intake at 340 °C and confirms its one step decomposition (Appendix 3-6). The observed final residues upon heating to 600 °C did not undergo any change in their weight suggesting that complexes (**4**)-(**7**) decompose quantitatively to furnish β-In_2S_3 as a stable end product:

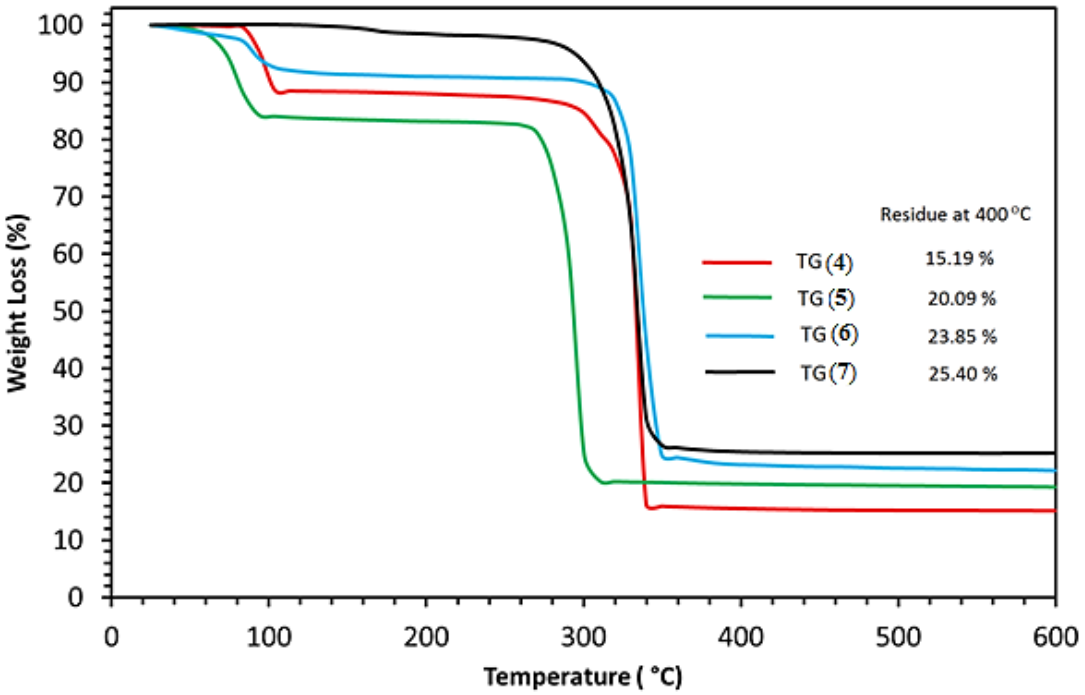

Figure 4.23**:** TG curves presenting losses in weight against temperature for precursors (**4**)-(**7**).

4.4.6 Phase and Crystalline Structure Identification of Indium Sulphide Thin Films

Indium sulphide thin films were deposited from precursors (**4**)-(**7**) on FTO substrate, at temperatures of 300, 350 and 400 °C by AACVD. The crystalline patterns obtained for indium sulphide thin films as a function of substrate temperature were investigated by powder X-ray diffraction (PXRD) and are displayed in Figure 4.24. Interestingly,

similar PXRD patterns were observed for all indium sulphide thin films prepared from precursors (**4**)-(**7**) that agree well with standard Inorganic Crystal Structure Database ICSD = [98-002-3844] (King, 1962) file in terms of their 2θ, d- spacing and reflection planes and identify the deposited product as the β-In_2S_3 crystallizing in the tetragonal crystal system with a = b = 7.632, c = 32.36 Å. The peaks indexed by (*) correspond to the SnO_2 layer of the FTO substrate. The intensity of the peaks is significantly strong, which indicates that the product is well-crystallized in all cases. All the spectra are dominated by diffraction peak (123) located at 2θ = 27.7° (d= 3.21Å) and there is no evidence of significant grain orientation. However diffraction peak intensities displayed a remarkable increase with the rise in deposition temperature, probably due to improved crystallinity of the films when the substrate temperature was raised from 350 to 400 °C. These PXRD peak patterns show no characteristic peaks arising from possible impurities such as InS, In_2SO_3 and other phases of In_2S_3. This clearly indicates that precursors (**4**)-(**7**) are capable of producing pure crystalline tetragonal phase β-In_2S_3 at 350 and 400 °C.

Previous studies have shown that deposition temperature, indium sulphur contents and molecular design of precursors are major parameters in determining the nature of deposited indium sulphide phase *i.e.* InS, In_6S_7, α-In_2S_3 and β-In_2S_3 (Lazell, 2000). For example the compound [In^{n}Bu(S^{i}Pr)$_2$] yielded tetragonal β-In_2S_3 at 400 °C, however the sulphur deficient phase, In_6S_7, was also grown with the rise in temperature to 450 °C (Nomura, 1989). This is because of the dissociation of thiolate moiety from the precursor, resulting in deposition of In_6S_7 at a high temperature of 450 °C. In a comparative growth studies of two different alkyl thiolate precursors [InMe$_2$(S^{t}Bu)]$_2$ and [In^{t}Bu$_2$(S^{t}Bu)]$_2$, the methyl derivative produced a mixture of In_6S_7 and In_2S_3 while butyl analogue generated only the tetragonal InS phase (MacInnes, 1993). This behaviour was explained in terms of the stronger In-C bond in the methyl substituted

complex that results in fragmentation of the precursor upon decomposition to give a mixture of In_6S_7 and In_2S_3 phases, whereas the tert-butyl derivative exhibits a clean ligand loss to furnish InS. The bis-thiolate precursor $[InMe(S^tBu)_2]_2$, generates an amorphous phase at 400 °C that needs further annealing to yield crystalline β-In_2S_3 (MacInnes, 1993).

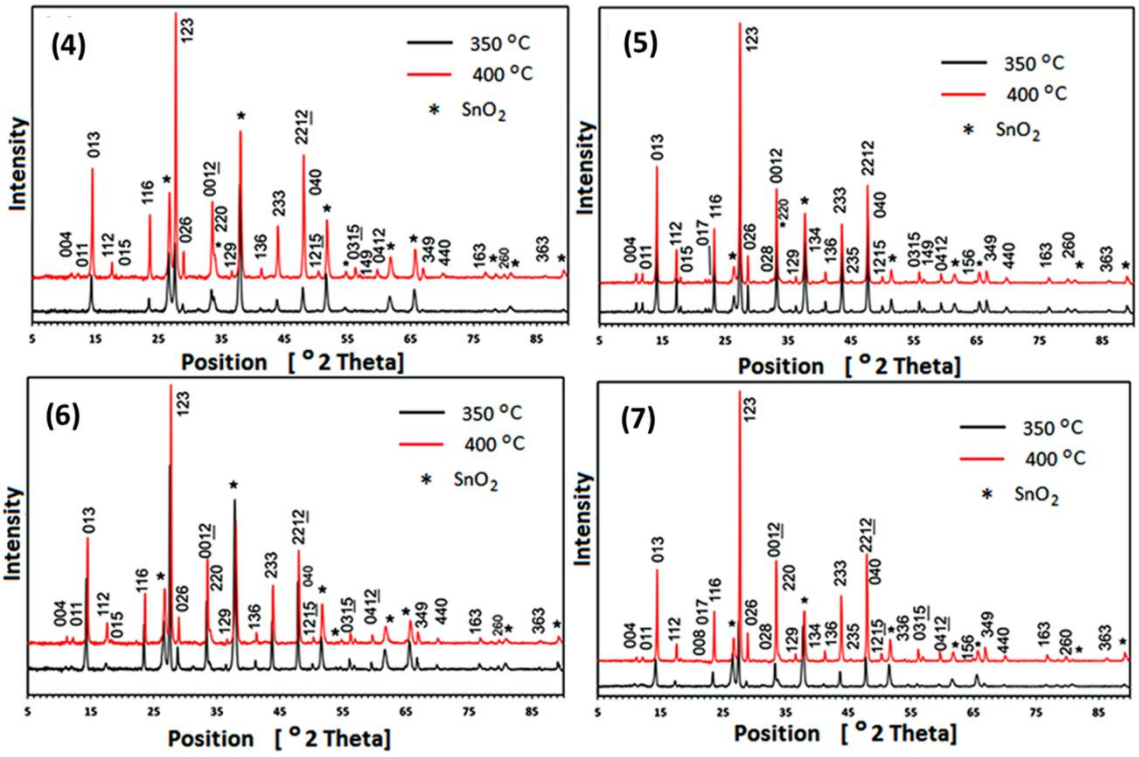

Figure 4.24: PXRD patterns of β-In_2S_3 deposited from precursor $[In(S_2CNCy_2)_3]$•2py **(4),** $[In(S_2CN(^iPr)_2)_3]$•1.5py (**5**), $[In(S_2CPip)_3]$•0.5py (**6**) and $[In(S_2CNBzMe)_3]$ (**7**) at 350 (black) and 400 °C (red) on FTO glass substrate. All of the diffraction peaks can be matched with ICSD = [98-002-3844].

When indium tris-(dialkyldithiocarbamates) complexes were investigated as SSPs by LPCVD technique, their unsymmetrical forms successfully yielded cubic α-In_2S_3 thin films at 500 °C while the symmetrical derivative proved in-volatile and no deposition occurred (O'Brien, 1998a). A comparison of the films deposited by LPCVD at 350 °C using two different indium tris(monothiocarbamates) $[In(SOCNEt_2)_3]$ and $[In(SOCN^iPr_2)_3]$ precursors, reveals that the former complex produced thin films with

poor morphology while the diisopropyl derivative deposited good quality β-In_2S_3 thin films (Horley, 1999; Horley, 1998). The forgoing discussion summarizes that steric demand and coordinative flexibility of the ligand have a great influence on the aggregation, stability and volatility of the resulting complexes and therefore the choice of appropriate deposition technique is required for the growth of good quality thin films.

4.4.7 Surface Characterization of β-In_2S_3 Thin Films

The morphology and architectures of β-In_2S_3 thin films fabricated from precursor (**4**)-(**7**) were investigated by scanning electron microscopy (SEM). SEM images of the thin films prepared using THF solutions of the precursors (**4**)-(**7**) on FTO glass substrates at temperatures 300, 350 and 400 °C are presented in Figure 4.25. These indicate that shape and design of β-In_2S_3 films vary with the rise in substrate temperature. Thin films grown from (**4**)-(**7**) at 300 °C were too thin and were not detected by PXRD and SEM micrographs. Figure 4.26((a), (d), (g) and (j)), show indistinguishable designs and crystallites stacked together with poor coverage of substrate. These observations suggest that none of the four precursors is completely decomposed and the slow growth rate of the films at 300 °C is due to low deposition temperature. This observation is also confirmed by TGA where decomposition of all the complexes occurs in the temperature range 340-375 °C. With the increase in deposition temperature to 350 °C, thin films growth rates from all (**4**)-(**7**) become better and the substrate surface is fully covered with different morphologies of β- In_2S_3 *i.e.* (**4**) granules crystallites with clear boundaries, Figure 4.25(b) (**5**) lumps, Figure 4.25(e), (**6**) agglomerates of particles along with some buds, Figure 4.25(h) and (**7**) multi-shaped (triangular, square and hexagonal based pyramidal) interconnected crystallites, Figure 4.25(k). Further increase in deposition temperature to 400 °C, (**4**) showed a similar kind of morphology, Figure 4.25(c), as were observed from (**7**) at 350 °C. However (**5**), (**6**)

and (**7**) developed large, small and flake like architectures, Figure. 4.25(f),(i),(l) respectively.

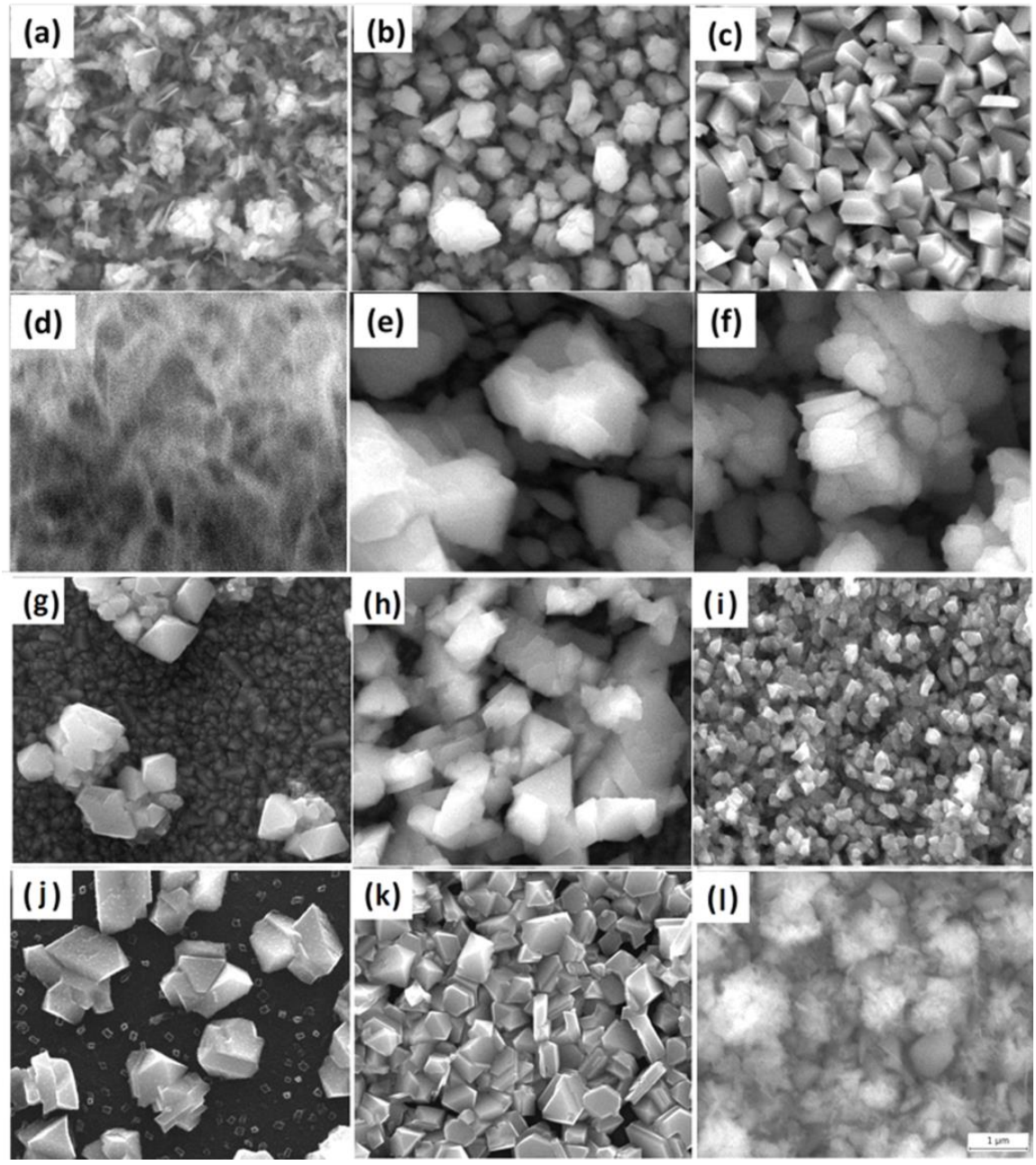

Figure 4.25**:** SEM images of β-In_2S_3 films deposited using precursors $[In(S_2CNCy_2)_3]$•2py (**4**) at (a) 300 °C (b) 350 °C (c) 400 °C; $[In(S_2CN(^iPr)_2)_3]$•1.5py (**5**) at (d) 300 °C (e) 350 °C and (f) 400 °C; $[In(S_2CNPip_2)_3]$•0.5py (**6**) at (g) 300 °C (h) 350 °C (i) 400 °C and $[In(S_2CNBzMe)_3]$ (**7**) at (j) 300 °C (k) 350 °C and (l) 400 °C.

All the indium sulphide films produced from precursors (**4**)-(**7**) were well adhered to FTO substrate and qualified the scotch tape test. Visual inspection of the films revealed that dark yellow films were made at 300 and 350 °C while their colour turned to orange red at 400 °C. The film surface composition was determined by energy dispersive X-ray analysis (EDX). Table 4.7 and appendix 7 show that the In/S atomic ratio existing in all the films prepared from precursors (**4**)-(**7**) are close to the expected ratio of 1:1.5, indicating the formation of β-In_2S_3.

Table 4.7**:** Description of morphologies (Figure 4.25) and In/S ratio in thin films fabricated from precursors (**4**)-(**7**) at 300, 350 and 400 °C.

Type of precursor	Deposition temperature, °C, morphology and In/S ratio		
	300	350	400
(**4**)	(a) Flakes 1:1.68	(b) Irregular shaped crystallites 1:1.49	(c) Multi-shaped crystallites 1:1.48
(**5**)	(d)Unstructured deposit 1:1.61	(e) Lumps 1:1.66	(f) Agglomerates 1:1.64
(**6**)	(g) Unstructured deposit with poor coverage of substrate 1:1.52	(h) lumps 1: 1.84	(i) Deteriorated crystallites 1:1.57
(**7**)	(x) Unstructured deposit with poor coverage of substrate 1:1.88	(y) multi-shaped crystallites 1:1.40	(z) flakes 1:1.47

4.4.8 Optical Properties of β-In_2S_3 Thin Films

The optical band gap energies of β-In_2S_3 thin films fabricated from precursor (**4**) at 400 °C and (**7**) at 350 °C were studied by spectrophotometry and are presented in Figure 4.26. The UV-Vis spectra of these films recorded in the wavelength range between 350-1000 nm indicate significant absorption in the ultraviolet and the early visible regions, Figure 4.27(a).

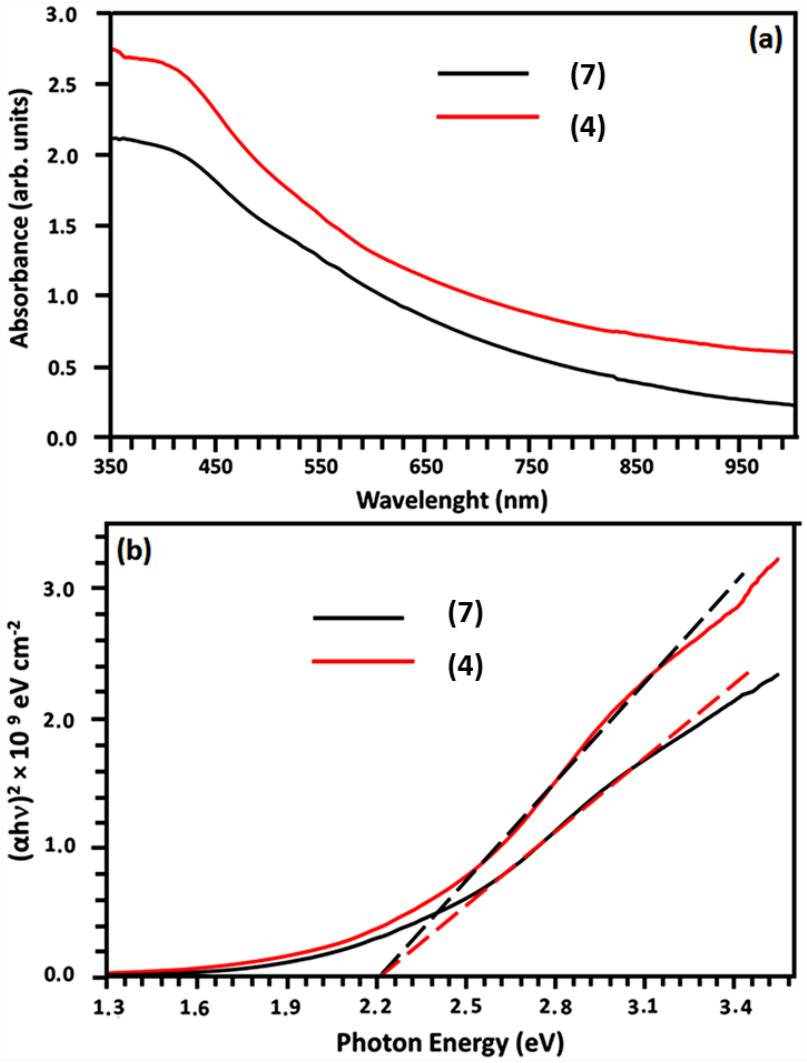

Figure 4.26**:** (a) UV-vis spectra of β-In_2S_3 thin films deposited using precursor (**4**) at 400 °C and (**7**) at 350 °C on the FTO substrate. (b) shows the direct band gaps of 2.2 eV for β-In_2S_3 films.

Optical band gaps were calculated from the absorbance data by plotting $(\alpha h\nu)^2$ versus photonic energy ($h\nu$) and extrapolating the linear part of the curve on the energy axis and were found to be 2.2 eV (Figure 4.26(b)). The thickness of the β-In_2S_3 films used for the optical experiments was estimated by profilometer to be 395 and 358 nm respectively. Our band gap value is in agreement with the band gap energies of β-In_2S_3 thin films made through other synthetic routes and with the bulk material (Allsop, 2006). The band structure indicates that charge transfer upon photo excitation occurs from the sulphur 3p orbital to the indium 5p empty orbital.

4.4.9 Photoelectrochemical Properties of β-In_2S_3 Thin Films

Photoelectrochemical (PEC) characteristics obtained from the electrical and optical studies of an electrode-electrolyte interface are an important tool for identifying the stability of the deposited films for electrochemical photovoltaic applications. The PEC performance of such deposited electrodes can be improved by using desirable precursors, composition, concentration, deposition temperature, deposition time *etc*. The PEC characteristics of as-prepared β-In_2S_3 films from precursors (**4**) and (**7**) by AACVD at 400 and 350 °C under the alternative dark and illumination conditions are shown in Figure 4.27 and 4.28 respectively. The plots indicated that under illumination, a β-In_2S_3 electrode exhibits an anodic photocurrent, which increases with increasing anodic bias (Sirimanne, 2000). The rectified I-V plot (Figure 4.27) of β-In_2S_3 from precursor (**4**) at 400 ^oC shows 1.25 mA cm^{-2} of photocurrent density at 0.23 V vs. Ag/AgCl and rises steeply up to 1.5 mA cm^{-2} as the applied voltage further increased without reaching the saturation. The β-In_2S_3 films prepared using precursor (**4**) at 400 °C displayed higher photocurrent response compared to the other depositions which is attributed to the well interconnected and uniform structure of the multi-shaped β-In_2S_3 crystallites in the film. As evident from the SEM images and XRD patterns, the film

deposited using precursor (**4**) at 400 °C is superior to films deposited at 300 and 350 °C. For better performance of an electrode, the structural uniformity and crystallinity are highly important in acquiring a better charge transport. Films fabricated from precursor (**4**) at 400 °C have structural uniformity and crystallinity resulting in better PEC performance. As is evident from the SEM images, the electrodes fully covered with sharp-edged crystallites of β-In_2S_3 films deposited at 400 °C from precursor (**4**) benefit in terms of improved charge transfer by avoiding electron-hole recombination. The I-V plots confirmed that precursors (**4**) and (**7**) are suited for the fabrication of β-In_2S_3 thin films by AACVD technique. The deposited β-In_2S_3 films display a reasonable photosensitivity, which indicates their potential for application in optoelectronic devices.

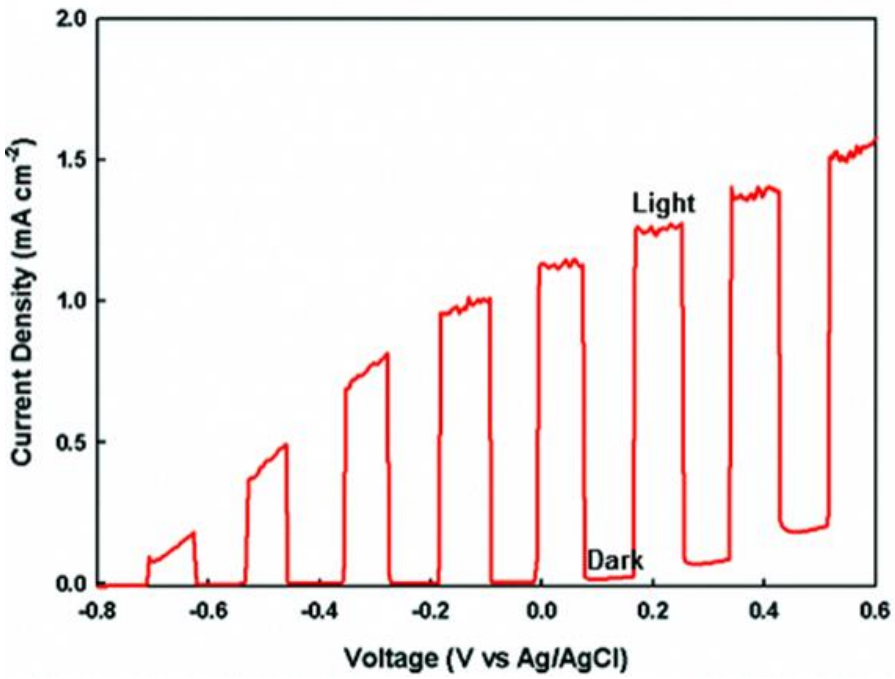

Figure 4.27: J-V plot of β-In_2S_3 films obtained from precursor (**4**) by AACVD at 400 °C.

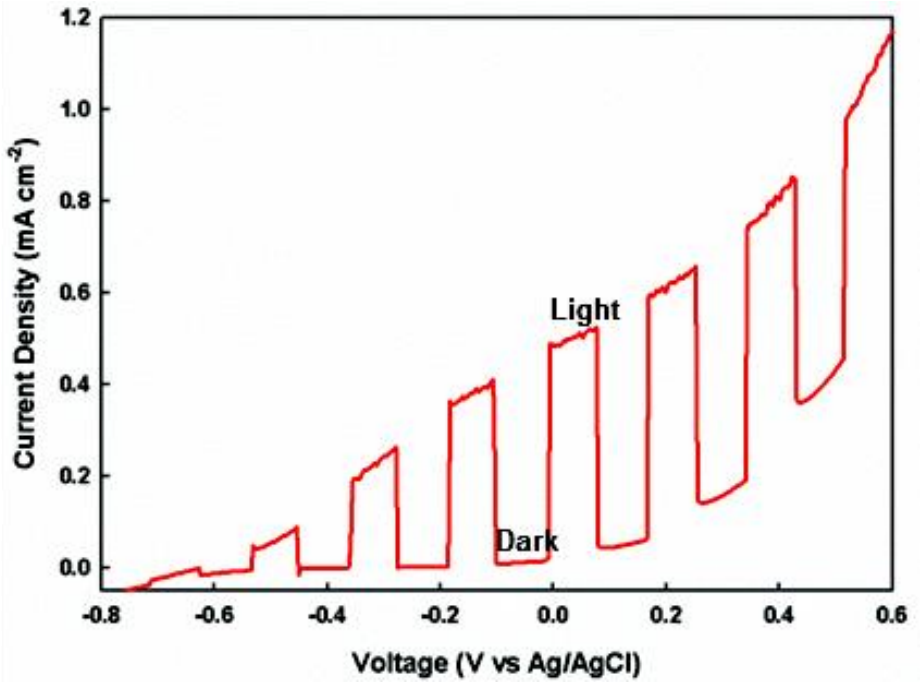

Figure 4.28**:** J-V plot of β-In_2S_3 films obtained from precursor (**7**) by AACVD at 350 °C.

4.5 n-tris(*N,N′* diethyldithiocarbamato)-bis(pyridine)argentate(+n)n-nitrate di-n-hydrate Cluster, $[Ag_4(S_2CNEt_2)_3(py)_2]_n{\cdot}nNO_3{\cdot}2nH_2O$ (8)

The cluster $[Ag_4(S_2CNEt_2)_3(py)_2]_n{\cdot}nNO_3{\cdot}2nH_2O$ (**8**) was readily prepared as a light yellow solid by metathesis reaction of sodium diethyl dithiocarbamate with silver (I) nitrate in a mixture of acetone and pyridine as shown in chemical equation

$$4nAgNO_3 + 3nNa(S_2CNEt_2) \xrightarrow[\text{Acetone}]{\text{Pyridine}} [Ag_4(SCNEt_2)_3(py)_2]_n{\cdot}nNO_3{\cdot}2nH_2O$$

The composition of (**8)** has been determined by CHNS, FT-IR, TG (data presented in Chapter 3, section 3.2 at page 67) and single crystal X-ray diffraction analyses. FT-IR spectrum in the range of 4000-500 cm^{-1} depicts the presence of various functional groups in (**8**). A broad absorption band around 3400cm^{-1} corresponds to the ν-(O—H) vibration suggests the presence of hydrogen bonding among the uncoordinated water molecules in (**8**) (Silverstein, 1963)**.** The presence of NO_3^{1-} ion has been detected by the splitting of absorption bands at 1339 (antisymmetric stretching modes for NO_3^{1-}) and absorption band at 1632 cm^{-1} (water bending mode). Comparison of the peak positions

and features with reported literature (Goebbert, 2009) reveals the presence of nitrate ion is not as free NO_3^{1-} but exist as hydrated nitrate ion $NO_3^{1-}(H_2O)_2$. Strong absorption bands at about 1496 cm^{-1} can be attributed to the ν(C⋯N) stretching vibrations. This value lie between the ranges reported for C—N single bonds at 1250–1360 cm^{-1} and C═N double bonds at 1640–1690 cm^{-1} and are an indication of partial double bond character of the C⋯N bonds (Criado, 1992). The emergence of two bands at 1033($\nu_{asymmetric}$ CSS) and 973 cm^{-1} ($\nu_{symmetric}$ CSS) suggest that the dithiocarbamate ligand is unsymmetrically coordinated to the metal ions (Bernal, 2001).

4.5.1 SingleCrystal X-ray Structure of$Ag_4(S_2CNEt_2)_3(py)_2]_n \cdot nNO_3 \cdot 2nH_2O$ (8)[5]

The single crystal X-ray structure of cation $[Ag_4(S_2CNEt_2)_3(py)_2]^{n+}$ of (**8**) is shown in Figure 4.29. The crystal data and structural refinement parameters are given in Table 4.8 and selected bond distances and angles are provided in Table 4.9.

As the structure reveals, the three unique diethyldithiocarbamate act as quadruply bridging ligands and each sulphur (S) atom being doubly bridging connects the Ag centers into a polymeric chain along the crystallographic *a* axis. There are four different Ag centers in the structure. Two of them [Ag(1) and Ag(3)] have trigonal AgS3 environments with Ag centers being deviated from the S3 planes by 0.3118(6)Å for Ag(1) and 0.2835(6)Å for Ag(3). The other two metal centers [Ag(2) and Ag(4)], each being coordinated by three S atoms from three diethyldithiocarbamate ligands and one pyridine N atom, are in distorted tetrahedral environments with the bond angles ranging from 96.35(8)° to 133.90(3)° for Ag(2) and 96.55(8)° to 132.73(3)° for Ag(4). The Ag—S bond distances lie in the range 2.4757(9)-2.6246(9) Å which are comparable with the values observed for similar structures (Su, 2002). The Ag—$N_{pyridine}$ bond

[5] Published: **Ehsan, M.A**.; Khaledi, H.; Tahir, A.A.; Ming, H.N.; Wijayantha, K.; Mazhar, M. (2013). Synthesis and characterization of silver diethyldithiocarbamate cluster for the deposition of acanthite (Ag_2S) thin films for photoelectrochemical applications. *Thin Solid Films, 536*, 124-129

lengths of 2.388(3) and 2.408(3) Å are normal for a pyridine-dithiolate Ag(I) complex (Schuerman, 1989). There are five Ag…Ag contacts in the range 2.9014(5) to 3.1027(4) Å which are shorter than the sum of the Van Der Waals radii of two silver atoms (3.44 Å), thus signifying the existence of Ag—Ag metallophilic bonds (Bondi, 1964) These interactions form a centrosymmetric Ag8 cluster with inversion center being located at the mid-point of Ag(1) —Ag(1'). The neighboring Ag8 clusters in the coordination polymer chain are separated by an Ag(3) —Ag(4') distance of 3.7903(4) Å.

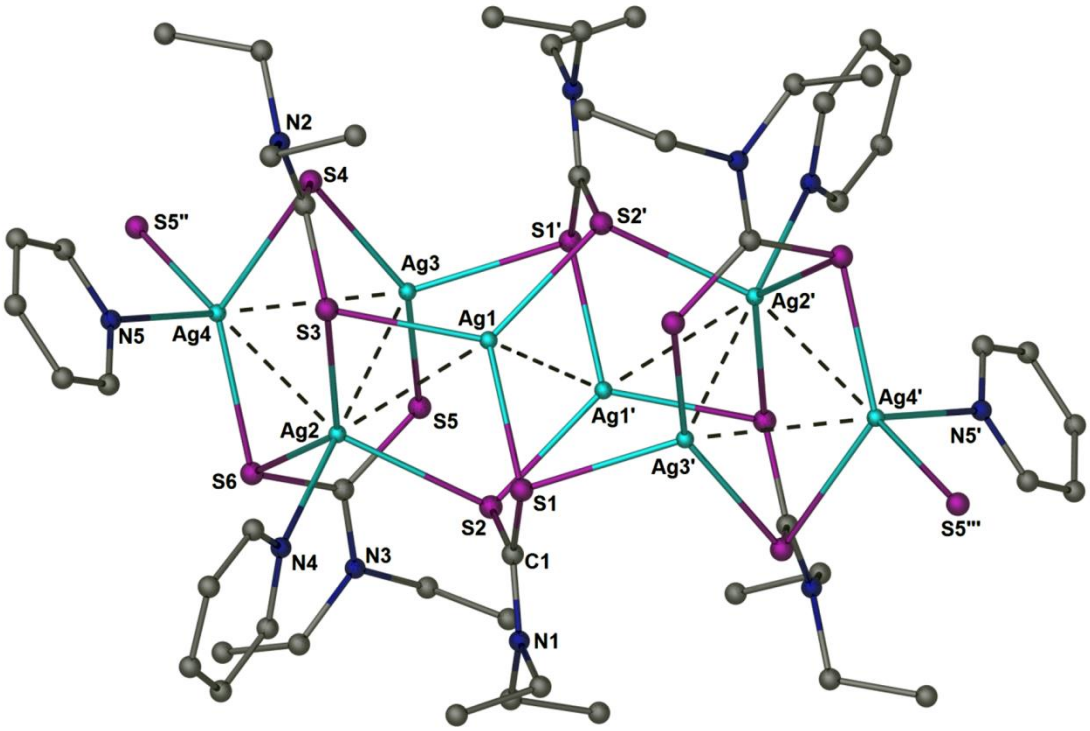

Figure 4.29**:** Crystal structure of the cation $[Ag_4(S_2CNEt_2)_3(py)_2]_n^{n+}$ of (**8**). Hydrogen atoms have been omitted for clarity. Ag…Ag contacts are represented as dashed (…) lines. Hydrogen atoms have been omitted for clarity. Ag…Ag contacts are represented as dashed (…) lines. Symmetry codes: ' = –*x*+1, –*y*+1, –*z*+1; " = -*x*+2, –*y*+1, –*z*+1; "' = *x*-1, *y*, *z*.

Table 4.8: Crystal data and refinement parameters for cation of cluster $[Ag_4(S_2CNEt_2)_3(py)_2]_n^{n+}$ (**8**)

Identification code	$[Ag_4(S_2CNEt_2)_3(py)_2]_n \cdot nNO_3 \cdot 2nH_2O$ (**8**)
Empirical formula	$C_{25}H_{44}Ag_4N_6O_5S_6$
Formula weight	1132.50
Solvent	Pyridine
Temperature	296(2) K
Crystal system	Triclinic
Space group	*P -1*
Unit cell dimensions	*a* = 11.4372(3)Å, α = 105.817(3)° *b* = 11.6768(3)Å, β = 97.891(3)° *c* = 16.3672(4)Å, γ = 93.274(3)°
Volume	2072.89(9)Å^3
Z	2
Density (calculated)	1.814mg/M^3
Reflections collected	11284
Goodness-of-fit on F^2	1.016
Final R indices [I>2σ (I)]	R_1= 0.0272, wR_2 = 0.0697
R indices (all data)	R1 = 0.0346, wR_2 = 0.0730

Table 4.9**:** Selected bond lengths [Å] and angles [°] of cation of cluster $[Ag_4(S_2CNEt_2)_3(py)_2]_n^{n+}$ (**8**)

Bond Lengths [Å]			
Ag(1)-S(2)#1	2.4783(9)	Ag(2)-Ag(4)	3.1027(4)
Ag(1)-S(3)	2.5085(10)	Ag(3)-S(4)	2.4757(9)
Ag(1)-S(1)	2.5464(9)	Ag(3)-S(5)	2.4851(10)
Ag(1)-Ag(1)#1	2.9014(5)	Ag(3)-S(1)#1	2.5994(9)
Ag(1)-Ag(2)	3.0880(4)	Ag(3)-Ag(4)	2.9189(4)
Ag(2)-N(4)	2.408(3)	Ag(4)-N(5)	2.388(3)
Ag(2)-S(3)	2.5341(10)	Ag(4)-S(6)	2.5314(10)
Ag(2)-S(6)	2.5811(10)	Ag(4)-S(5)#2	2.5909(10)
Ag(2)-S(2)	2.6246(9)	Ag(4)-S(4)	2.6590(10)
Bond Angles [°]			
S(2)#1-Ag(1)-S(3)	123.55(3)	S(4)-Ag(3)-S(5)	145.82(3)
S(2)#1-Ag(1)-S(1)	122.71(3)	S(4)-Ag(3)-S(1)#1	111.55(3)
S(3)-Ag(1)-S(1)	109.12(3)	S(5)-Ag(3)-S(1)#1	98.16(3)
N(4)-Ag(2)-S(3)	96.35(8)	N(5)-Ag(4)-S(6)	103.01(9)
N(4)-Ag(2)-S(6)	98.85(8)	N(5)-Ag(4)-S(5)#2	103.21(8)
S(3)-Ag(2)-S(6)	133.90(3)	S(6)-Ag(4)-S(5)#2	117.31(3)
N(4)-Ag(2)-S(2)	96.75(8)	N(5)-Ag(4)-S(4)	96.55(8)
S(3)-Ag(2)-S(2)	118.86(3)	S(6)-Ag(4)-S(4)	132.73(3)
S(6)-Ag(2)-S(2)	102.20(3)	S(5)#2-Ag(4)-S(4)	98.90(3)

4.5.2 Thermal Decomposition Studies of Complex (8)

The TG/DTG curves show a seven step pyrolysis modes of (**8**) (Figure 4.30). The initial two steps occurring in the temperature range of 40-90 °C indicate the loss of water from (**8**). The observed weight loss 3.12% precisely matches with the calculated value of 3.17% for the elimination of two water molecules. The next four steps of

degradation that take place successively in the temperature range of 90-210 °C are complex in nature causing a weight loss of 22.96% which might be due to the loss of two pyridine and one nitrate ion (20.17%). The final and major weight loss of 29.40% occurs in the temperature domain of 210-400 °C to yield a solid residue of 44.52% of the initial weight of the sample. The weight of the residue matches closely with the expected weight of Ag_2S (43.76%) from decomposition of (**8**). Further heating the sample to 600 °C did not bring any further change the residual weight indicating its thermal stability. DTG also confirms occurrence of seven step**s** of decomposition of (**8**) and indicates temperatures of maximum heat flow at 64, 85, 114, 164, 187, 200 and 241 °C in each degradation step respectively.

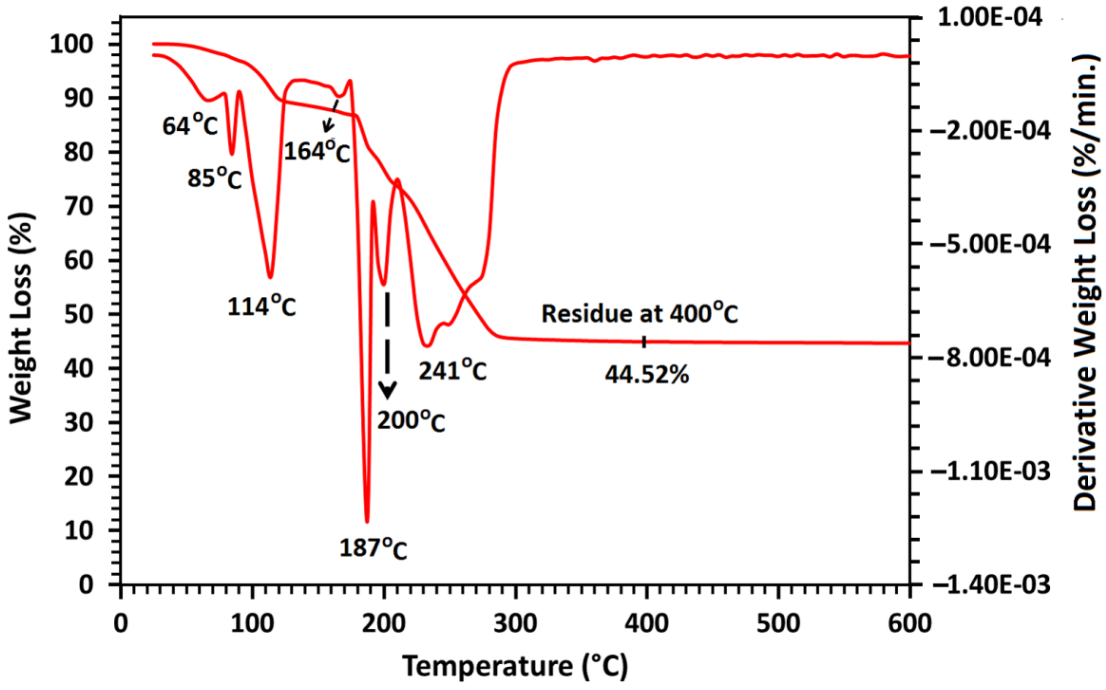

Figure 4.30: Thermogravimetric curves showing the loss in weight as function of temperature for $[Ag_4(S_2CNEt_2)_3(py)_2]_n \cdot nNO_3 \cdot 2nH_2O$ (**8**).

4.5.3 Phase and Crystalline Structure Identification of Silver Sulphide Thin Films

Following the results from TG, the AACVD experiments for the deposition of silver sulphide thin films were carried at 350 and 400 °C on FTO substrate using argon as the carrier gas. The crystalline pattern obtained for silver sulphide thin films deposited at 400 °C was investigated by XRD and is shown in Figure 4.31.

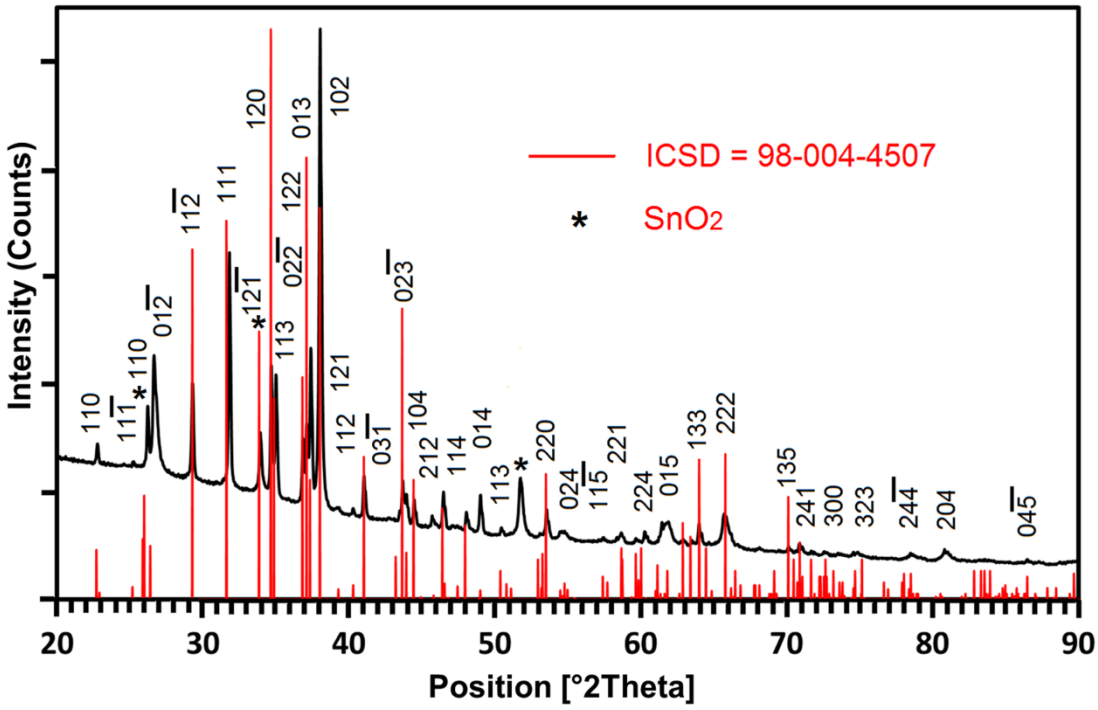

Figure 4.31**:** XRD patterns of acanthite (Ag_2S) thin films deposited from (**8**) at 400 °C on a FTO substrate. Bars represent the standard library pattern (98-004-4507) of Ag_2S. "*" indicates the peak originated from crystalline SnO_2.

A careful comparison reveals that the observed diffraction pattern matches well with standard Inorganic Crystal Structure Database ICSD [98-004-4507] in terms of their peak positions and d- spacing and identifies the crystalline product as "Acanthite" Ag_2S in monoclinic form and space group *P21/c* with cell parameters a = 4.23, b = 6.91, c = 8.29 Å, β = 110.62°. All the peaks in the pattern have been indexed with a reflection plane according to the matching with standard "Acanthite" Ag_2S library card. However

the relative diffraction intensity of (102) plane is unusually higher than the corresponding conventional values ICSD [98-004-4507]. This observation reveals that the resultant acanthite nanorods are grown preferentially along the (102) direction. The XRD pattern does not show any noticeable impurity peaks from metallic silver or other phases of silver sulphide. This observation is different from the previous findings where, using the precursor $[Ag_3\{(SP^iPr_2)_6N_3)\}]$ $((NSP^iPr_2)_2$ = dithioimidodiphosphinate) a high contamination of metallic silver was observed upon deposition by AACVD(Panneerselvam, 2008).

4.5.4 Surface Characterization of Acanthite (Ag_2S) Thin Films

The FESEM images of acanthite thin films prepared from (**8**) using pyridine as a deposition solvent at 350 and 400 °C are presented in Figure 4.32. The surface morphology of the films deposited at 350 °C (Figure 4.32(a)) show the growth of randomly oriented nanorods and these rods grew slightly in width(100-150 nm) and extensively in length(>1000 nm) with rise in deposition temperature to 400 °C (Figure 4.32(b)). These multi shaped (zigzag, coil or curled) nanorods did not exhibit any signs of fractures or cracks and were developed in unspecific directions and orientations on the substrate surface.

Visual inspection of the films obtained at 350 and 400 °C were dark brown in color and showed strong adhesion with FTO substrate and qualify the scotch tape test. The EDX analysis (Appendix 10) identifies Ag/S ratio in these acanthite nanorods as 49.29: 25.50 which closely agrees with the expected 2: 1 ratio for Ag_2S.

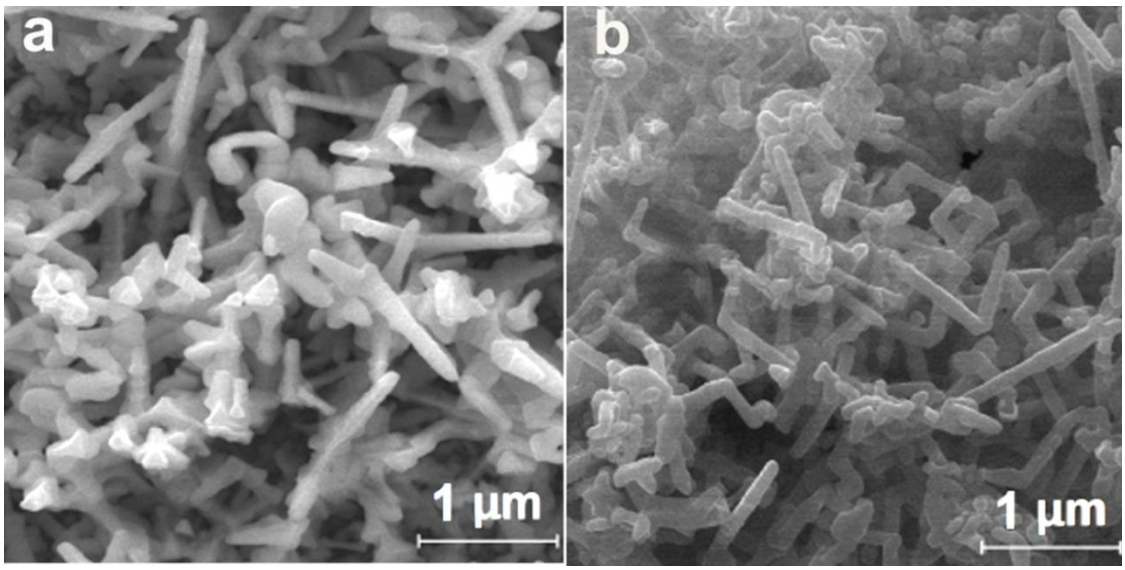

Figure 4.32**:** SEM images of acanthite (Ag_2S) thin films deposited from (**8**) on FTO substrates at 350 °C (a) and at 400 °C (b).

4.5.5 Optical Properties of Acanthite (Ag_2S) Thin Films

The optical band gap of the acanthite thin film deposited at 400 °C on FTO was evaluated from their UV-Vis spectra recorded in the wavelength range of 350–1700 nm using FTO coated glass substrate as a reference to eliminate the contribution from the substrate (Figure 4.33(a)). It has been observed that the UV-Vis data of acanthite thin films fits very well for n = 1/2, approving the direct band gap nature of the films. Thus, by extrapolating the linear part of the Tauc plot $(\alpha h\nu)^2$ vs E_g $(h\nu)$ (Figure 4.33(b)) on the energy axis gives a band gap value of 1.05 eV. The estimated band gap is found to be close to the reported values (1.10eV) for Ag_2S thin films (Prabhune, 2008).

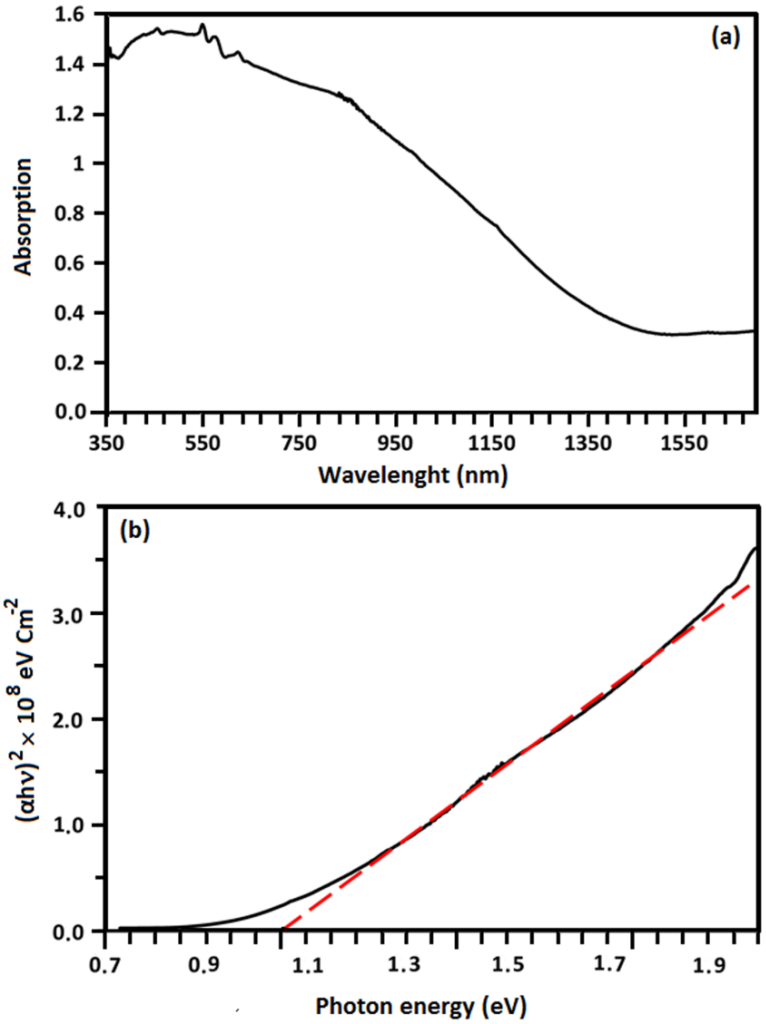

Figure 4.33: (a) UV-Vis spectra of acanthite (Ag_2S) thin films deposited from (**8**) on FTO substrates at 400 °C (b) Tauc plot showing direct band gap of 1.05 eV.

4.5.6 Photoelectrochemical Properties of Acanthite (Ag_2S) Thin Films

The PEC properties of the acanthite electrodes were studied in a three electrode mode using aqueous 0.05 M Na_2S + 0.05M Na_2SO_3 + 0.1M $NaClO_4$ solution as the electrolyte. The J−V plots of acanthite nanorods thin films deposited at 400 °C are shown in Figure 4.34. The acanthite electrode was illuminated using a 1.5AM solar simulator and light was manually chopped at regular intervals to reveal the light and dark current simultaneously. The anodic photocurrent steeply increases with the increase of applied potential and does not reach saturation which is typical for many sulphide electrodes.

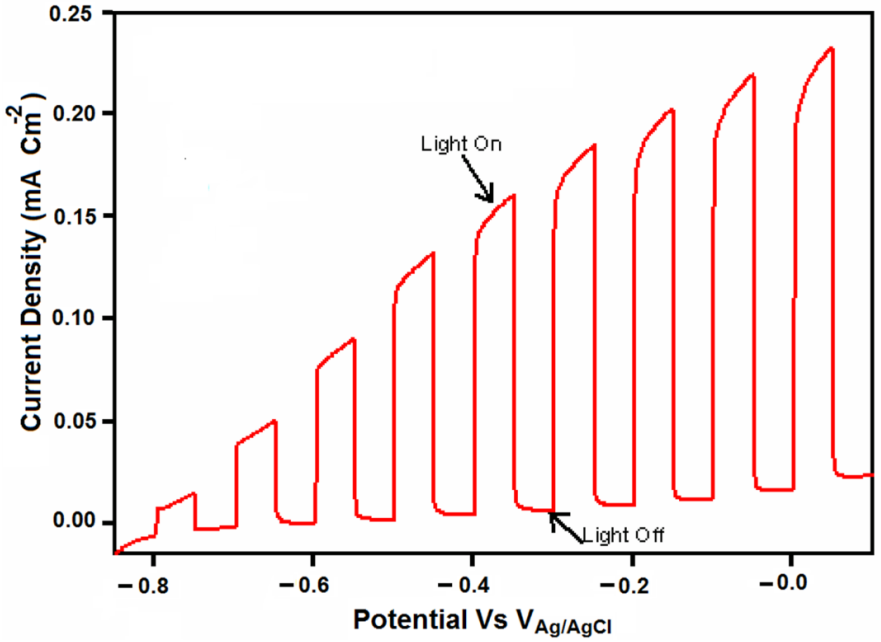

Figure 4.34**:** The transient photocurrent potential curves for the acanthite (Ag_2S) thin film electrode deposited from (**8)** at 400 °C measured under simulated AM 1.5 sunlight in aqueous 0.05 M Na_2S + 0.05 M Na_2SO_3 + 0.1 M $NaClO_4$ solution as electrolyte.

Similar n-type behavior for Ag_2S nanoparticles and quantum dots was observed previously (Nagasuna, 2011). The maximum photocurrent density of 220 μA/cm^2 was recorded (at 0.0 V vs Ag/AgCl/3 M KCl). The rectangle shaped photocurrent pulses without any sharp spikes indicate a low electron hole recombination of nanorod acanthite electrodes, the electrons generated are transported to the underlying FTO in competition with the back reaction with S_2^{2-} ions. SO_3^{2-} ions in the electrode prevent the back reaction by reducing S_2^{2-} ions back to S^{2-} ions (Reber, 1986) . This also indicates that S^{2-} ions operate as good hole (Ag_2S) scavengers to restrict its photocorrosion (Tachibana, 2007). The electrons transferred to the Pt counter electrode via the external circuit reduce H^+ to H_2. The nanorod photoelectrodes deposited from (**8**) shows a better PEC performance both in terms of photocurrent and dark current than the Ag_2S electrode deposited by electrodeposition and the SILAR method (Omeiri, 2011; Pathan, 2001). We attribute this to the high surface area of the electrodes and better electron transport properties of nanorods as it is well known that the charge transport

properties of nanorods and nanotubes are much better than those of other nanoparticle electrodes (Mohapatra, 2009).

4.6 Bis(*N,N'*-dicyclohexyldithiocarbamato)(pyridine)cadmium(II) Adduct, $[Cd(S_2CNCy_2)_2(py)]$ (9)[6]

The precursor $[Cd(S_2CNCy_2)_2(py)]$ (**9**) was isolated in 85% yield as a colourless solid from the metathetical reaction of sodium dicyclohexyldithiocarbamate and cadmium(II) nitrate trihydrate from a chloroform-pyridine solution as shown in the chemical equation.

$$Cd(NO_3)_2{\cdot}3H_2O + 2Na(S_2CNCy_2) \xrightarrow[\text{Pyridine}]{\text{chloroform}} [Cd(S_2CNCy_2)(py)] + 2NaNO_3 + 3H_2O$$

Precursor (**9**) has been characterized by elemental analysis, IR, thermogravimetry (data presented in Chapter 3, section 3.2 at page 68) and single crystal X-ray diffraction analysis. The IR spectra of dithiocarbamate complexes contain three main regions of interest. The 1580–1450 cm^{-1} region is mainly related with the stretching of the C—N bond of NCS_2^-; the 1060–940 cm^{-1} region, associated with ν(—CS_2); and the 420–250 cm^{-1} region, associated with ν(M—S). The strong absorption bands at about 1473 and 1441 cm^{-1} in the IR spectrum of (**9**) are attributed to the ν(C—N) stretching vibrations. These values lie between the range reported for C—N single bond (1250–1360 cm^{-1}) and C=N double bond (1640–1690 cm^{-1}), indicating the partial double bond character in C⋯N bond (Criado, 1992). The $\nu(CS_2)_{asym}$ and $\nu(CS_2)_{sym}$ vibrations that appear at 1055 cm^{-1} and 961 cm^{-1} in the dithiocarbamate ligand are substituted by a strong singlet at about 997 cm^{-1} in (**9**), indicating that the dithiocarbamate moiety is symmetrically coordinated to the metal ions (Johnson, 1969).

[6] Published: **Ehsan, M.A.**; Ming, H.N.; Misran, M.; Arifin, Z.; Tiekink, E.R.; Safwan, A.P., . . . Mazhar, M. (2012). Effect of AACVD Processing Parameters on the Growth of Greenockite (CdS) Thin Films using a Single-Source Cadmium Precursor. *Chem. Vap. Deposition, 18*, 191-200.

4.6.1 Single Crystal X-ray Structure of $[Cd(S_2CNCy_2)_2(py)]$ (9)

The binary metal dithiocarbamate of the zinc-triad elements, as well their 1,1-dithiolate analogues, e.g. xanthate and dithiophosphate, are well known to aggregate in the solid-state via M...S secondary interactions to form higher dimensional aggregates (Tiekink, 2003). Directly relevant to the present study is the centrosymmetric dinuclear structural motif of $\{Cd(S_2CNR_2)\}_2$, uniformly adopted by structures of this formulation (Tiekink, 2003). In this motif, one sulphur atom of one of the two chelating dithiocarbamate ligands bridges a cadmium atom so that each cadmium is five coordinate. It is also well known that the addition of a Lewis base disrupts the structural motif of the original binary species giving rise to structures of lower dimensionality and/or nuclearity (Haiduc, 1995; Hogarth, 2005; Tiekink, 2005). In the case of $Cd[S_2CNCy_2]_2$, the addition of pyridine results in the formation of the 1:1 adduct, $[Cd(S_2CNCy_2)_2(py)]$ (**9**). The molecular structure is shown in Figure 4.35 and cell parameters and selected material data are collected in Table 4.10 and 4.11 respectively. Figure 4.36 shows that the cadmium atom is in a five-coordinate NS_4 coordination geometry defined by chelating dithiocarbamate ligands and the pyridine-N atom. It is noted that the dithiocarbamate ligands form slightly asymmetric bonds, as reflected in the values of Δ(Cd—S) = 0.065 and 0.058 Å for the S1- and S3-containing ligands, respectively; the range of Cd–S bond distances is 2.5683(7) to 2.6518(6) Å. The dihedral angle between the chelate rings is 45.28(6)°, and the dihedral angles between these and the pyridine ring are 62.42(9) and 76.07(9)°, indicating a twist in the relative orientation of the pyridine ring to the chelate rings.

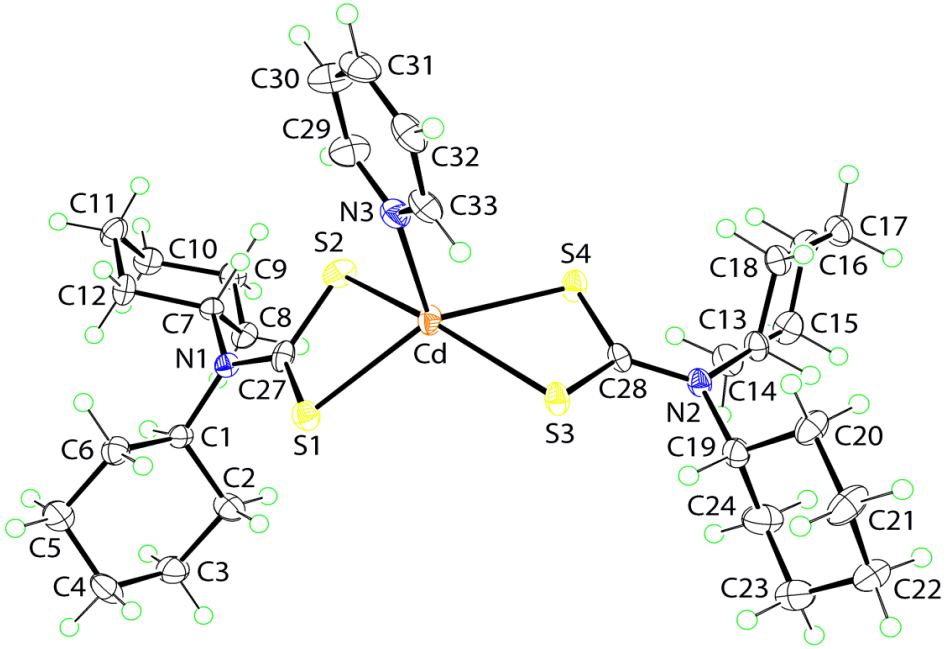

Figure 4.35: Molecular structure of [Cd(S_2CNCy_2)$_2$(py)] (**9**). Displacement ellipsoids are drawn at the 50 % probability level. Only one orientation of the disordered NCy_2 residue is shown for reasons of clarity.

The geometry of (**9**) is distorted with a tendency towards square pyramidal. This is quantified by the value of τ (Addison, 1984) of 0.28, which is nearer to an ideal square pyramidal geometry (τ = 0) than to an ideal trigonal bipyramidal geometry with τ = 1.0. Not surprisingly, given the steric bulk of the cyclohexyl rings in (**9**), there is limited supramolecular aggregation in the crystal structure, Figure 4.36. Centrosymmetrically related molecules are connected into dimeric aggregates via S...S interactions involving S3 atoms. Supramolecular chains are formed along the *a*-axis whereby the dimeric aggregates thus formed are connected via C–H...π interactions, where the π--system is a chelate ring. Such interactions are recognised as being important contributors to the stabilisation of the crystal structures of metal dithiocarbamates (Tiekink, 2011).

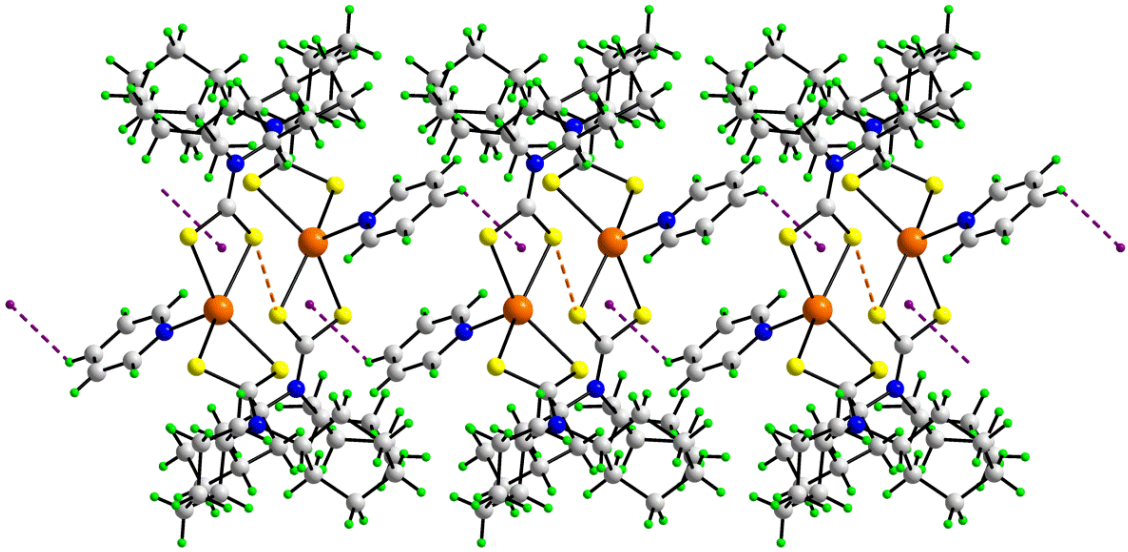

Figure 4.36: A view of the supramolecular chain in the crystal structure of (**9**). The chains are sustained by S...S and C–H...π (chelate) interactions, shown as orange and purple dashed lines, respectively.

Table 4.10: Crystal data and structure refinement for precursor $[Cd(S_2CNCy_2)_2(py)]$ (**9**).

Identification code	$[Cd(S_2CNCy_2)_2(py)]$ (**9**)
Empirical formula	$C_{31}H_{49}CdN_3S_4$
Formula weight	704.37
Solvent	Pyridine
Temperature	100(2) K
Crystal system	Triclinic
Space group	$P\bar{1}$
Unit cell dimensions	a = 8.9806(4)Å, α = 76.977(3)° b = 13.2878(5)Å, β = 85.652(4)° c = 14.5560(6)Å, γ = 82.914(4)°
Volume	1677.33(12)Å^3
Z	2
Density (calculated)	1.395mg/M^3
Reflections collected	11925

Goodness-of-fit on F^2	1.019
R (obs. data)	0.033
R_w (all data)	0.078

Table 4.11: Selected bond lengths [Å] and angles [°] for precursor [$Cd(S_2CNCy_2)_2(py)$] (**9**).

Bond distances(Å)	
Cd—S1	2.5683(7)
Cd—S2	2.6333(6)
Cd—S3	2.5941(6)
Cd—S4	2.6518(6)
Cd—N3	2.311(2)
Bond Angles (°)	
S1—Cd—S2	69.14(2)
S3—Cd—S4	68.251(18)
S1—Cd—S3	109.65(2)
S1—Cd—S4	138.42(2)
S2—Cd—S3	155.43(2)
S2—Cd—S4	95.954(19)

4.6.2 Thermal Decomposition Studies of Complex (9)

TG curve (Figure 4.37) shows that the overall pyrolysis of (**9**) was accomplished in three complex phases. The first phase ranges from 80-123 °C, causing a mass loss of 9.67%, indicating partial elimination of total of 11.21% of pyridine. Following this step is the second broad and weak phase in the temperature limits of 123-275 °C, yielding a mass loss of 7.45%. The third and the last decomposition stage, that ranges from 275 to 350 °C, releases the major weight loss of 61.50%, resulting in a stable residual amount of 21.39% of the initial mass of (**9**). This residual mass is close to the expected 20.30% mass for CdS, indicating that (**9**) has decomposed quantitatively into cadmium sulphide

phase. Differential (D)TG also confirms the existence of three phases of decomposition of (**9**) and indicates temperatures of maximum heat intake at 108, 207 and 339 °C in each degradation stage, respectively.

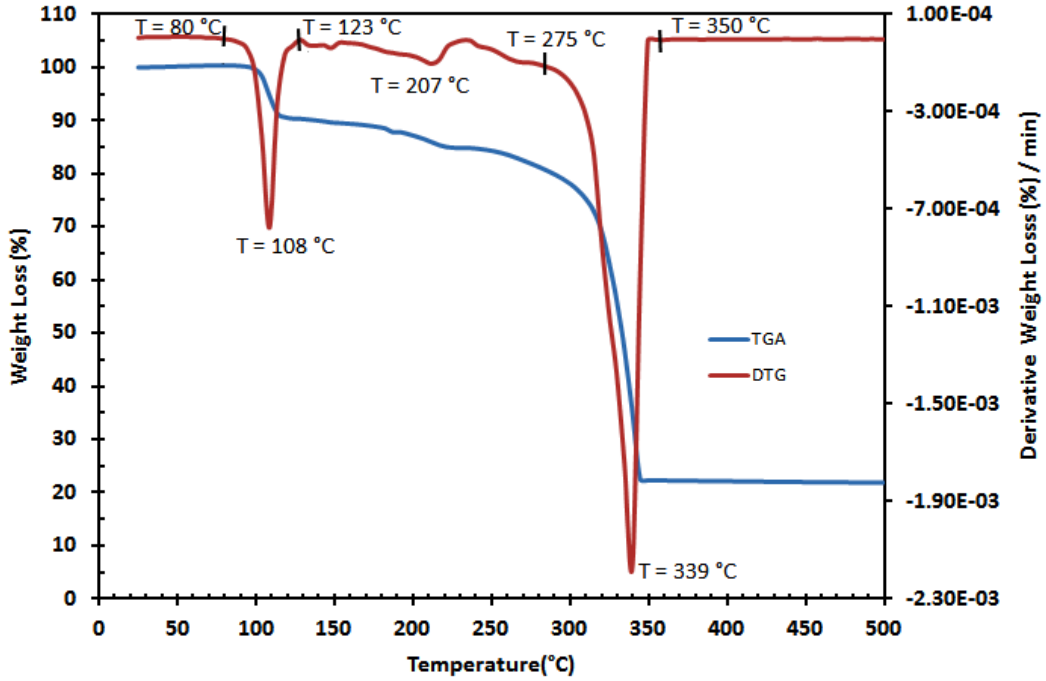

Figure 4.37: TGA/DTG plots showing losses in mass with increase in temperature for precursor (**9**).

4.6.3 Deposition and Characterization of Greenockite (CdS) Thin Films

Thin films from (**9**) were grown on crystalline FTO glass and amorphous soda glass substrates under a dynamic argon flow of 100 mL min^{-1} using pyridine, toluene and THF as solvents at deposition temperatures of 350, 400 and 450 °C. A comparison of the XRD patterns of the thin films grown in pyridine [Figure 4.38(a),(b)] and THF [Figure 4.38(c),(d)] on FTO and soda glass substrates with standard CdS [00-001-0780], revealed that the crystalline product formed is pure CdS "greenockite" in its hexagonal modification that crystallized in the *P*63*mc* space group. The calculated values of hexagonal lattice constants are found to be a = b = 4.1420 Å and c = 6.7240 Å, which agrees well with the standard values for CdS [00-001-0780].

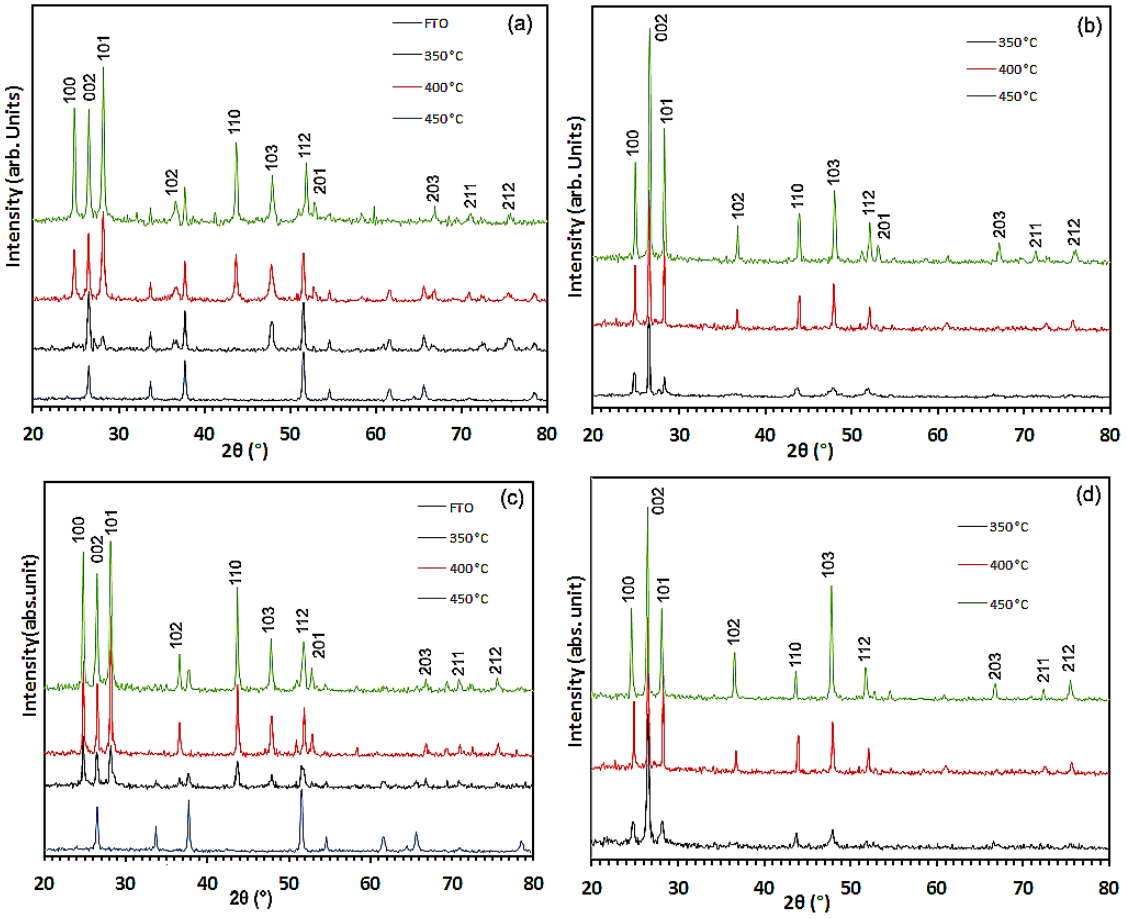

Figure 4.38: XRD patterns of greenockite CdS thin films deposited from (**9**) on substrates (a) FTO, (b) soda glass using pyridine ; (c) FTO, (d) soda glass via THF solutions at 350, 400 and 450 °C, respectively.

It is observed that as the substrate temperature increases, the intensity and sharpness of peaks also increases due to the improvement in crystallinity without affecting the hexagonal CdS phase. The diffraction patterns of CdS on soda glass (Figure 4.38(b) exhibit some preferred orientations (002) with higher peak intensity as compared to the films deposited on FTO (Figure 4.38(a)) from pyridine. These XRD peak patterns show no signs of any chemically or pyrolytically driven impurity phases of elemental cadmium, sulphur, and CdO. This observation is in contrast to an earlier study where films deposited from the precursor $Cd[\{(SP^{i}Pr_2)_2N\}_2]$ using AACVD (Oyetunde, 2011) and LPCVD (AfzaalCrouch, 2004) were highly dependent on temperature and were

contaminated with traces of phosphorous. Interestingly, the use of (**9**) in the deposition of thin films from different solvents and temperatures consistently produced the hexagonal phase of deposited CdS. In another report, CdS thin films deposited through fluid deposition techniques from the precursor [$Cd(S_2CN(Hexyl)_2)_2$] yielded sulphur deficient CdS thin films, and some extra sulphur source was employed to balance the stoichiometry (Yang, 2009).

4.6.4 Surface Characterization of Greenockite (CdS) Thin Films

The architecture of thin films deposited by AACVD process depends on gas phase nucleation of homogeneous and heterogeneous reactions, and is influenced by the deposition conditions such as physical properties of solvent (boiling point, heat of combustion, viscosity, specific heat capacity and coordination ability), as well as the growth temperature and nature of substrate. By tuning these parameters, greenockite thin films with a variety of morphologies, mutable particle size, and composition have been engineered and these features are summarized in Table 4.12. FESEM images of the films deposited from (**9**) on FTO and soda glass substrates at 350, 400 and 450 °C using pyridine, toluene, and THF as solvents are shown in Figures 4.39, 4.40 and 4.41, When films were deposited in the temperature range 350-450 °C using pyridine solution, different morphologies were detected on FTO and soda glass substrates. At 350 °C, regular-shaped hexagons of size 250 nm, tightly coupled with each other, manifested clear boundaries and edges on the FTO glass. Similar hexagonal CdS nanocrystals have been prepared earlier by solution methods (Cheng, 2006). On increasing the temperature to 400 °C, the hexagonal geometry starts to deteriorate to small-sized 180 nm particles (Figure 4.39(b)) and, at 450 °C, completely converted to isolated corn grains having particle size of 220 nm (Figure 4.39(c)).

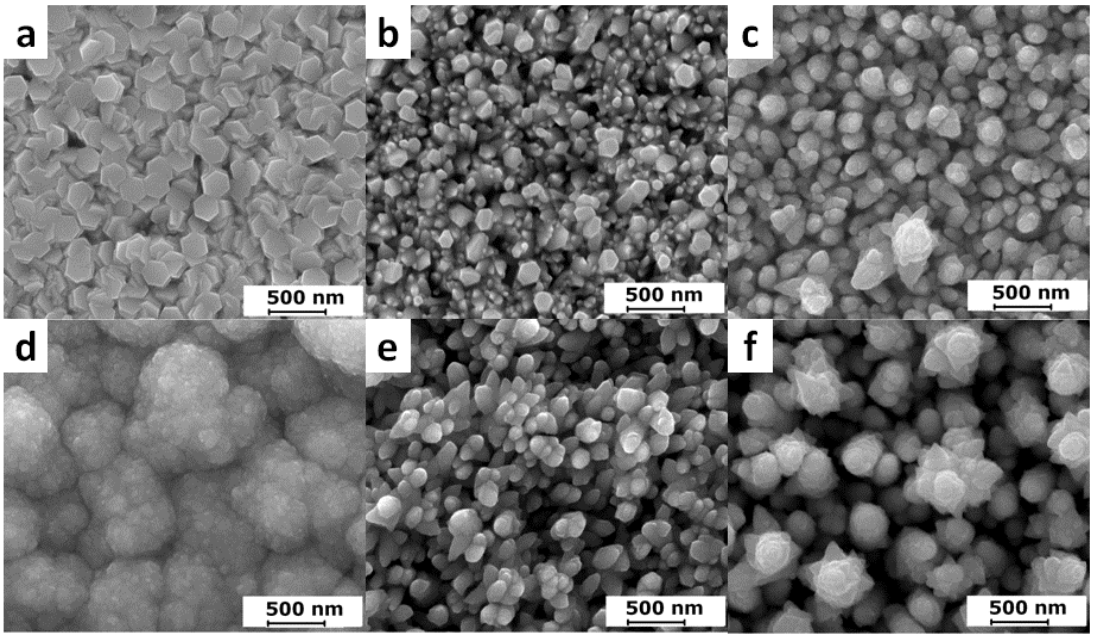

Figure 4.39: SEM images of greenockite (CdS) thin films deposited from (**9**) on FTO (a-c) and soda glass (d-f) at 350, 400, and 450°C in pyridine solution, respectively

Various greenockite nanostructures were obtained when FTO glass was replaced by soda glass substrate (Figure 4.39(d)-(f)). At 350 °C, tightly bound, spherical, cauliflower like architectures of size > 1μm (Figure 4.39(d)), made from a combination of several small particles of size 30-50 nm, were formed. On further increasing the temperature to 400 °C, round-shaped particles of size range 150-200 nm, growing in a perpendicular direction, were obtained. At 450 °C, the growth direction along the perpendicular axis continued to produce large, intergrown white flakes of size 250-300 nm (Figure 4.39(f)).

Thin films deposited from a toluene solution of (**9**) indicate some growth of hexagonal crystallite of average size 300 nm on FTO glass at 350 °C (Figure 4.40(a)). At 400 °C, randomly oriented but interconnected hexagonal plates of average size 350 nm became visible. With a further increase in temperature to 450 °C, a morphology shift was apparent in that small and large- sized flakes, ranging from 180 to 540 nm were noted.

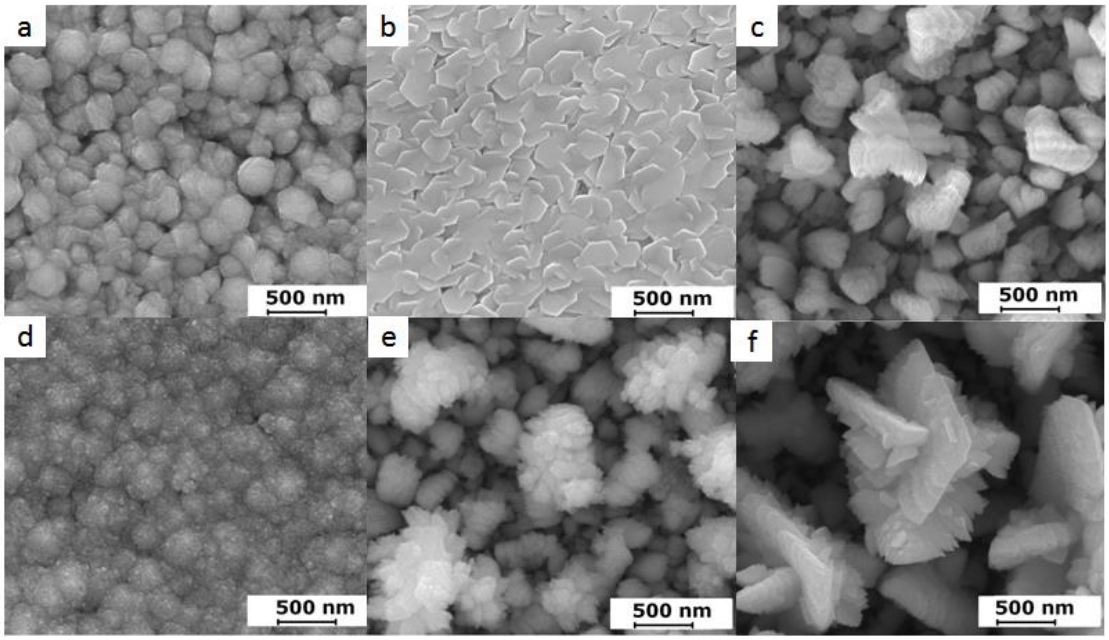

Figure 4.40: SEM images of greenockite (CdS) thin films deposited from (**9**) on FTO (a-c) and soda glass (d-f) at 350, 400, and 450 °C in toluene solution, respectively.

When deposition experiments under similar conditions were carried out on soda glass substrate, irregular-shaped small heaps appeared at 350 °C (Figure 4.40(d)). On further increase in temperature to 400 °C, flake-like objects of size range 540-720 nm started growing; these later converted to large, intergrown flakes in the size range >1μm at 450 °C (Figure 4.40(f)).

The effect of solvent on greenockite nanostructures, morphology and composition in THF was also studied on FTO (Figure 4.41(a)-(c)) and soda glass substrates (Figure 4.41(d)-(f)). At 350 °C, growths of strip-like objects of varying length and breadth with clear texture and boundaries were bred without any directional preferences. At 400 °C, these strips started caving down to small objects of sizes ca. 100 nm as shown in Figure 4.41(b), and at 450 °C agglomeration of small particles (50 nm) took place to furnish large heaps of sizes 200-400 nm. The fabrication of thin films on soda glass, as shown in Figure 4.41(d)-(f), under similar conditions except for temperature variation, also revealed changes in morphology. At 350 °C, irregular grains of size 300-400 nm with distinct boundaries appeared, and these changed into heaps of large sizes > 2μm at 400

°C. At 450 °C, considerably interconnected flakes of different sizes appeared (Figure 4.41(f)).

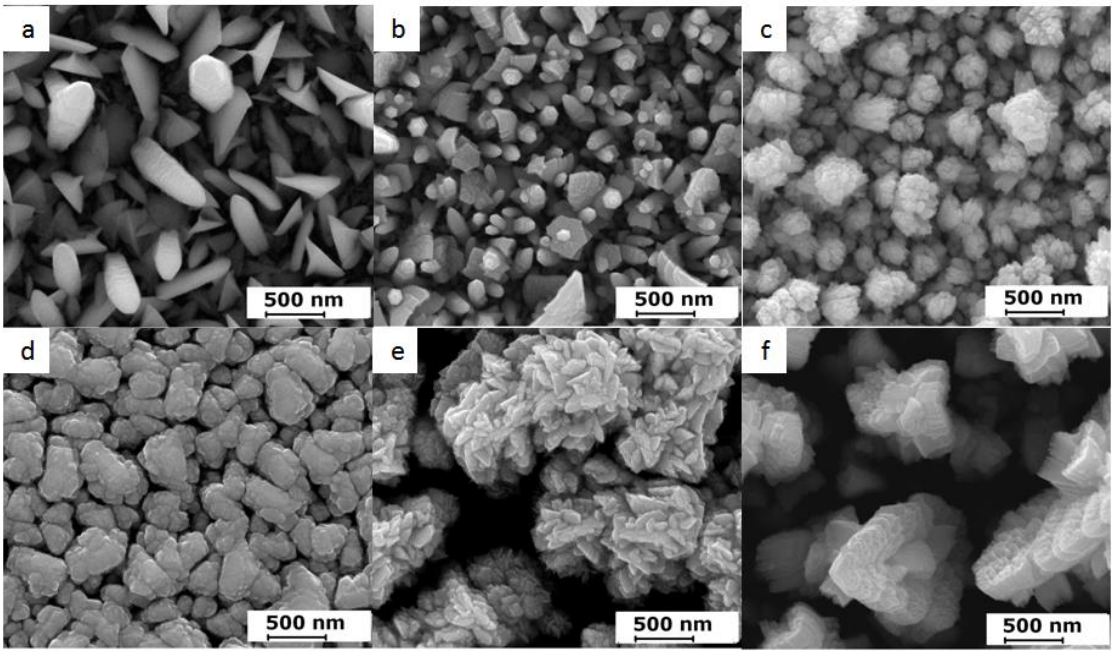

Figure 4.41: SEM images of greenockite (CdS) thin films deposited from (**9**) on FTO (a-c) and soda glass (d-f) at 350, 400, and 450°C from THF solution, respectively.

Depending on the temperature of the deposition chamber, the aerosol droplets undergo evaporation, vaporization, precipitation, and thermolysis before or after reaching to the substrate surface. We believe that, at relatively low temperatures, the heterogeneous process is dominant and the precursor molecule adsorbed on the substrate surface, and subsequent evaporation, vaporization, and decomposition tends to produce high-quality, designed films with good adhesive strength (Figure 4.39(a), 4.40(b), 4.41(a)). With the increase in temperature up to 400 ºC, the aerosol absorbs more heat in the delivery tube causing solvent evaporation, while vaporization of precursor molecules starts before adsorbing on the substrate surface, which results in the deposition of films with a distorted structure (Figure 4.39(b), 4.40(b)). With a further increase in temperatures up to 450 ºC, the temperature gradient inside the delivery tube

reached the flash point of the solvent. This leads to the burning and decomposition of the solvent causing evaporation, vaporization, precipitation and thermolysis of aerosol droplets in a single-step in the gas phase. This process is brought about by the mechanism of heat and mass transfer inside the droplets, and between the droplets and surrounding gas, resulting in the formation of thin films governed by the homogeneous deposition process. Such a mechanism enables high decomposition as well as segregation suppression to the droplet scale, resulting in the formation of nanometer-scale particles in gas phase. These nanometer-scale particles adsorb on the substrate surface, and act as nuclei for the further growth of porous thin film with irregular texture and poor adhesion to the substrate (Figure 4.39(c), 4.40(c), 4.41(c)).

The role of solvent in the building of robust nanostructures (Figure 4.39(a), 4.40(b), 4.41(a)) can be described on the basis of heat of combustion (Tahir, 2010) and the coordinating ability of the solvent. Pyridine, having moderate heat of combustion (2782 kJ/mol) and high coordinating ability, favours heterogeneous nucleation mode at 350 ºC, while toluene, with much higher heat of combustion (3910.3KJ/mol) and having no coordinating ability, facilitates both the homogeneous and heterogeneous nucleation at 400 ºC. In contrast, THF with much less heat of combustion (2501.2 kJ/mol) when compared to both pyridine and toluene, evaporates faster causing homogeneous nucleation at 350 ºC.

It is noteworthy that selective nanostructures were only produced by conducting FTO substrate where the landing of charged aerosol cluster is a function of electrical and electrochemical nature of the conducting substrate which is more favourable to nucleation than insulating soda glass. When a charged aerosol droplet undergoes evaporation, the electric charge density increases with the shrinking of the droplet, and the conducting substrate offers intense repulsion which split the particle apart until the solvent completely evaporates (Hou, 2006). As a result, multiple fine particles are

selectively formed and adsorbed on the conducting substrate, where a specific ripening and growing process yields the selective structures (Figure 4.39(a), 4.40(b), 4.41(a)).

All deposition experiments carried out in the solvents pyridine, toluene and THF led to the fabrication of yellow greenockite CdS thin films at 350 and 400 °C that adhered well to the both FTO and soda glass substrates and qualified “scotch tape test”. While the films deposited at 450°C show a change in colour from bright-yellow to dark-yellow-brown and became less adherent to the substrates and failed scotch tape test

Table 4.12: Effect of nature of substrate, solvent and temperature on morphology particle size and elemental ratio of greenockite (CdS) thin films deposited from (**9**).

Figure No.	Solvent Type	Substrate	Substrate Temperature (°C)	Crystallite Morphology	Particle size (nm)	Elemental Ratio (Cd : S)
5(a)	Pyridine	FTO	350	hexagon	250	0.98 : 1.02
(b)	Pyridine	FTO	400	distorted hexagon	180	0.99 : 1.01
(c)	Pyridine	FTO	450	corn grain	220	1.04 : 0.96
(d)	Pyridine	Soda Glass	350	cauliflower	>1000	0.99 : 1.01
(e)	Pyridine	Soda Glass	400	round grain	150—200	1.00 : 1.00
(f)	Pyridine	Soda Glass	450	snowflake	250—300	1.04 : 0.96
6(a)	Toluene	FTO	350	rough hexagon	300	0.9 : 1.1
(b)	Toluene	FTO	400	hexagonal sheet	350	0.88 : 1.12
(c)	Toluene	FTO	450	flake	180—540	0.94 : 1.06
(d)	Toluene	Soda glass	350	Agglomerate heap	250—500	0.97 : 1.03
(e)	Toluene	Soda glass	400	flake	540—720	0.90 : 1.10
(f)	Toluene	Soda glass	450	flake	>1000	1.04 : 0.96
7(a)	THF	FTO	350	stripe	55	0.98 : 1.02
(b)	THF	FTO	400	crumbled particle	100	0.95 : 1.05
(c)	THF	FTO	450	flake	200—400	1.07 : 0.93
(d)	THF	Soda glass	350	irregular grain	300—400	1.02 : 0.98
(e)	THF	Soda glass	400	heap	>1000	1.04 : 0.96
(f)	THF	Soda glass	450	flake	>1000	1.01 : 0.99

4.6.5 Optical Properties of Greenockite (CdS) Thin Films

The UV-Vis spectra of the greenockite thin films in the wavelength range of 350-900 nm, using SnO_2 as a reference, were recorded to calculate the band gap (E_g) from the Tauc plot as given by the formula $\alpha h\nu = A_0(h\nu - E_g)^n$ (where A is a constant, and *n* is the power of the exponent) which takes a value of 1/2 for directly allowed and 2 for indirectly allowed transitions; E_g is the band gap and hν is the incident photon energy. It is possible to determine the nature of the transitions by plotting graphs of $(\alpha h\nu)^{1/n}$ versus hν for different values of "*n*".

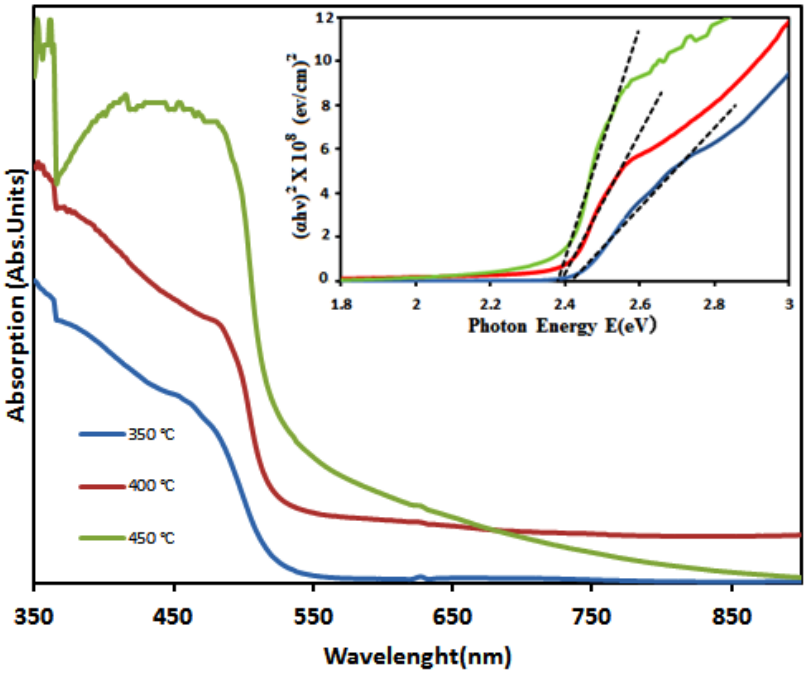

Figure 4.42: Optical absorption spectrum of greenockite (CdS) thin films deposited from precursor (**9**). Inset: Tauc plot showing the estimated optical band gap of 2.4eV.

It has been observed that the UV-vis data of greenockite thin films prepared in pyridine, in the temperature range of 350-450 °C, fitted very well to n = 1/2 (Figure 4.42). The band gap is estimated from the intercept of the extrapolated linear fit to the experimental data of the Tauc plot. A band gap of 2.4 eV was estimated by this

procedure as shown in Figure 4.42 (inset). It has been observed that the E_g of CdS was not significantly affected by deposition temperature and that the estimated band gaps were found to be very close to reported values for other CdS thin films (Vanalakar, 2011).

4.6.6 Photoelectrochemical Studies of Greenockite (CdS) Thin Films

Based on nanostructure, morphology, and compactness, greenockite thin film electrodes prepared from pyridine solution at 350, 400, and 450 °C were tested for their PEC studied in a three electrode mode using an aqueous 0.1 M Na_2SO_3 solution as an electrolyte. The *J*−*V* plots of all the three thin film electrodes are shown in Figure 4.43. The nanocrystalline greenockite photoelectrodes prepared at 350, 400, and 450 °C showed photocurrent densities at 0.4 V of 1.30, 1.0 and 0.6 mA cm^{-2}, respectively, vs. Ag/AgCl/ 3M KCl. It is noted that the photocurrent density significantly depends on the nanostructure and architecture of the photoelectrode that, in turn, alters with the deposition temperature. At 350 °C, tightly interconnected hexagons (Figure 4.39(a)) increase light residence time, reduce reflectivity, and increase charge mobility to provide a good path for the excitation of electron-holes, correlating nicely with the observed maximum photocurrent density. With the increase in the substrate deposition temperature, the ordered hexagonal structure partly deteriorates into small particles resulting in defects and voids in the nanocrystalline structure that may act as recombination centres for the photo-generated electron-hole pairs and consequently show poor PEC performance. Similarly, at 450 °C the premature precursor decomposition and nucleation produces loosely bonded films, thereby influencing the morphology and texture, and thus diminishing the photocurrent density.

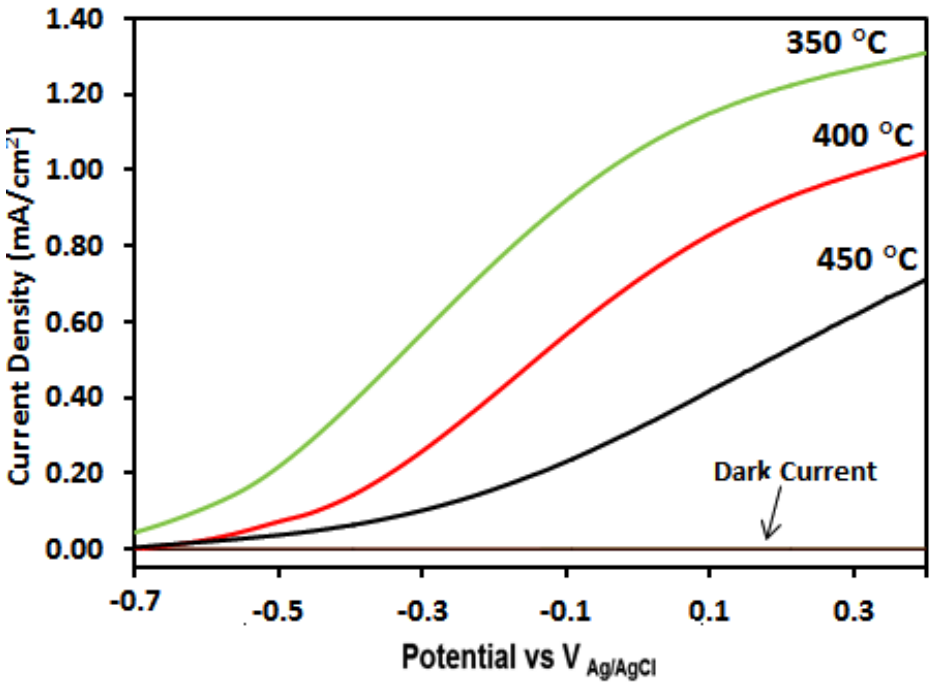

Figure 4.43: *J*−*V* curves for the greenockite (CdS) thin film electrodes deposited from (**9**) in pyridine measured under simulated AM 1.5 sunlight in aqueous 0.1M Na_2SO_3 solution as an electrolyte.

4.7 Bis(*N,N'*-dialkyldithiocarbamato)(pyridine)zinc(II) Adducts, $[Zn(S_2CNR_2)_2(py)]$ (10)-(11)[7]

Bis(*N,N'*-dialkyldithiocarbamto)(pyridine)zinc(II) adducts $[Zn(S_2CNR_2)_2(py)]$ (R = Cy (**10**); R = BzMe (**11**)) were synthesized by the double displacement reactions of zinc (II) chloride and sodium dicyclohexyldithiocarbamate in chloroform-pyridine solution for (**10**) and sodium bezylmethydithiocarbamate in acetone-pyridine solution for (**11**), respectively. The general chemical reaction is illustrated in the equation.

$$ZnCl_2 + 2NaS_2CNR \xrightarrow[\text{Pyridine}]{} [Zn(S_2CNR_2)_2(py)] + 2NaCl$$

R = Cy_2(**10**) / Bz, Me (**11**)

Chloroform (**10**) /Acetone (**11**)

Both zinc pyridine adducts (**10**) and (**11**) are air and moisture stable and are soluble in organic solvents such as pyridine, toluene and chloroform. The compounds were fully characterized by elemental analysis, infrared (IR) spectroscopy, proton nuclear magnetic resonance spectroscopy (^{1}H-NMR) (data presented in Chapter 3, section 3.2 at page 68-69) and thermogravimetric and derivative (TG/DTG) analysis. The single crystal X-ray analysis proved the stoichiometry of the complexes obeys the reaction given in the above chemical equation.

The IR spectra of complexes (**10**) and (**11**) show strong absorption bands at 1473, 1441 and 1482, 1428 cm^{-1} , respectively, showing the ν(C—N) stretching vibrations. As these values appears between the region of C— N single bond (1250–1360 cm^{-1}) and C ═N double bond (1640–1690 cm^{-1}), indicating the partial double bond character in the C ----N bond (Bereman, 1979). The $\nu(CSS)_{asym}$ and $\nu(CSS)_{sym}$ absorption bands appear at 1029, 997 cm^{-1} for (**10**) and 1041, 995 cm^{-1} for (**11**) support the bidentate coordination of the S atoms of dithiocarbamate moieties with a metal centre (Parish,

[7] Published: **Ehsan, M.A**.; Peiris, T.; Wijayantha, K.; Khaledi, H.; Ming, H.N.; Misran, M., . . . Mazhar, M. (2013). Surface morphological and photoelectrochemical studies of ZnS thin films developed from single source precursors by aerosol assisted chemical vapour deposition. *Thin Solid Films, 540*, 1-9.

1996; Tiekink, 1999). The ^{1}H-NMR spectra of (**10**) comprises a complex pattern in the region 3.14–1.14 ppm ascribed to Cy_2 group directly attached with N atoms in dithiocarbamate. The multiple signals observed in the region δ = 8.70–7.31 ppm are attributed to the protons of pyridine ring. The ^{1}H-NMR spectra of (**11**) show a sharp singlet at 3.40 ppm, which corresponds to three protons of the methyl group in dithiocarbamate. The multiple signals observed in the region δ = 7.52–7.17 ppm indicate the protons of phenyl rings while the multiple signals mounted in the region δ = 9.03–7.86 are assigned to pyridine ring.

4.7.1 Single Crystal X-ray Structure of Bis(*N,N'*-dicyclohexyldithiocarbamato) (pyridine)zinc(II) Adduct, [Zn(S_2CNCy_2)$_2$(py)] (10)

The molecular structure of [Zn(S_2CNCy_2)$_2$(py)] (**10)** is shown in Figure 4.44 and crystal data and structure refinement details and geometric parameters are summarized in Tables 4.13 and 4.14 respectively. Crystal structure of (**10**) indicates that the Zn atom is five- coordinated by four S atoms from two dithiocarbamate ligands and a pyridine N atom. The dithiocarbamate ligands form slightly asymmetric Zn–S bond distances, Δ Zn–S ($Zn–S_{long}$ – $Zn–S_{short}$) being 0.103 and 0.066 Å for the S1- and S3-containing ligands, respectively. The Zn–S bond lengths are somewhat longer than the distances observed in a tetrahedral bis-chelated zinc complex of the same dithiocarbamate ligand (Cox, 1999). The value of Addison index (τ = (β-α)/60) indicates the coordination geometry for five-coordinate structures, where β is the largest angle and α is the second one around the metal center. In the present structure τ computes to 0.29, which is closer to an ideal square pyramidal geometry (τ = 0) than to a perfect trigonal bipyramidal geometry with τ = 1. All the cyclohexyl rings adopt the chair conformation. The N-CS2 bond lengths of 1.342(8) and 1.328(8) Å indicate their significant double bond

characters and are comparable to the values observed in similar structures, as are the C-S bond lengths of 1.701(7)-1.722(7) (Srinivasan, 2009).

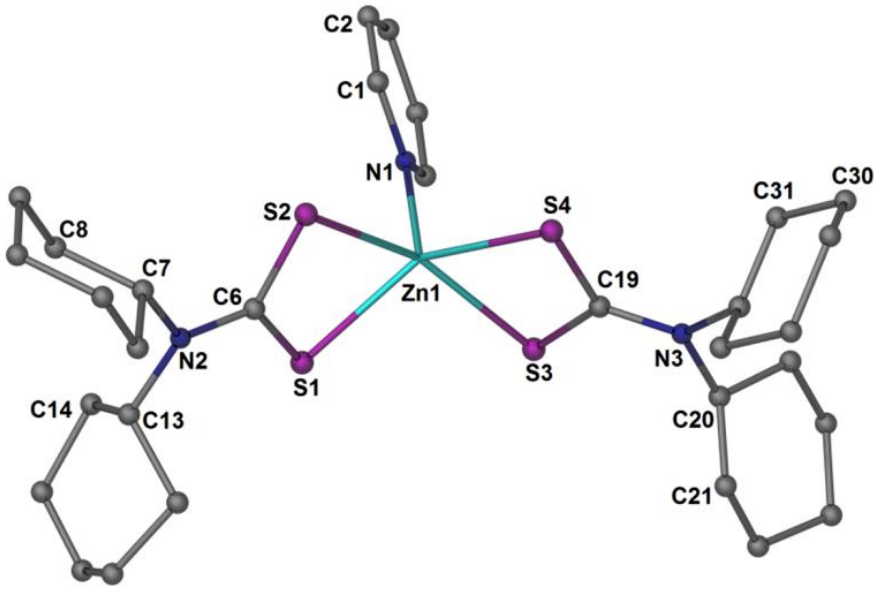

Figure 4.44: Molecular structure and atom labelling scheme for $[Zn(S_2CNCy_2)_2(py)]$ (**10**). Hydrogen atoms have been omitted for clarity.

In the crystal, pairs of the molecules are double C1-H…S2 bonded around centres of inversion. The resultant dimers are linked through long range C4–H...S4 (Table 4.14) to form infinite chains along *a* axis (Figure 4.45).

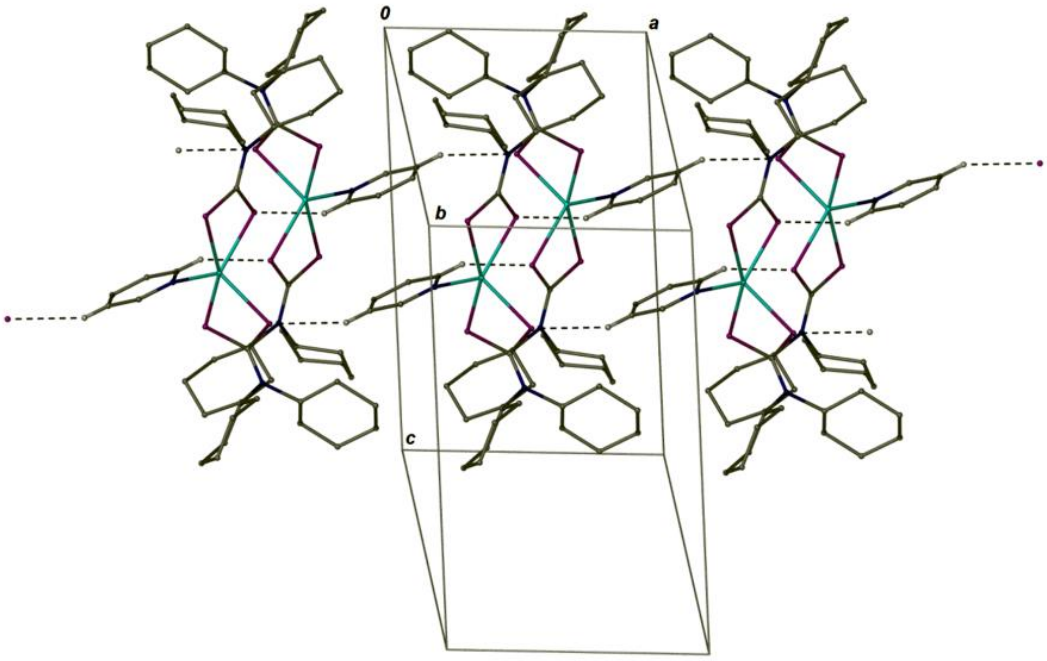

Figure 4.45: A view of the infinite chain of molecules of [Zn(S_2CNCy_2)$_2$(py)] (**10**) along the *a* axis formed by C-H…S interactions. The H atoms, except for those involved in the H-bonding interactions, are omitted.

4.7.2 Single crystal X-ray structure of Bis-(*N*-benzyl-*N′*-methyldithiocarbamato) (pyridine)zinc(II) Adduct, [Zn(S_2CN(BzMe)$_2$)$_2$(py)] (11)

The coordination environment of the Zn centre in [Zn(S_2CNBzMe)$_2$(py)] (**11**) mimics that of [Zn(S_2CNCy_2)$_2$(py)] (**10**). The metal centre is five coordinated by two chelating dithiocarbamate ligands and one pyridine N atom in a distorted square-pyramidal geometry (τ = 0.39). The Δ (Zn–S) values equal to 0.1837 and 0.1593 Å for the S1- and S3-containing ligands respectively. The selected bond lengths and angles are compiled in Table 4.14. The Zn–S bond distances are comparable to those in [Zn(S_2CNCy_2)$_2$(py)] (**10**), as are the N-CS2 and C-S bond lengths (Figure 4.46).

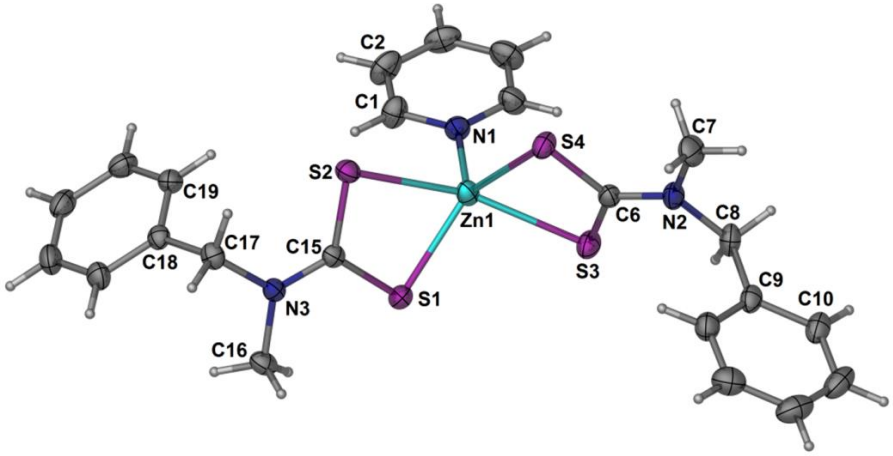

Figure 4.46: Molecular structure of [Zn(S_2CN(BzMe)$_2$)$_2$(py)] (**11**) with thermal ellipsoids drawn at the 30% probability level.

In the crystal packing structure, as represented in Figure 4.47, the adjacent molecules are linked through C-H… π interactions to form infinite chains along the *c* axis and these are further connected into layers parallel to the *bc* plane by long range C-H…S interactions (Table 4.15).

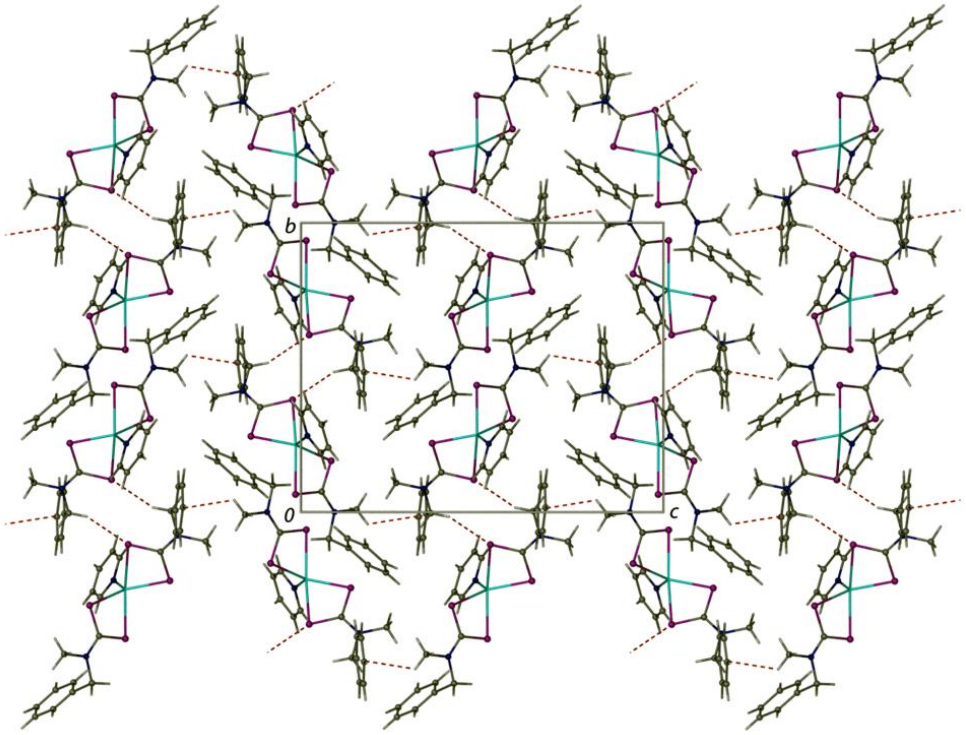

Figure 4.47: The 2-D array of [Zn(S_2CN(BzMe)$_2$)$_2$(py)] (**11**) in the *bc* plane formed by C–H...π and C–H...S interactions, shown as red dashed lines.

Table 4.13**:** Crystallographic parameters and refinement details for $[Zn(S_2CNCy_2)_2(py)]$ (**10**) and $[Zn(S_2CN(BzMe)_2)_2(py)]$ (**11**)

Identification code	(**10**)	(**11**)
Empirical formula	$C_{31}H_{49}N_3S_4Zn$	$C_{23}H_{25}N_3S_4Zn$
Formula weight	657.34	537.07
Temperature, K	296(2)	296(2)
Wavelength, Å	0.71073	0.71073
Crystal system	triclinic	monoclinic
Space group	$P\bar{1}$	$P2_1/n$
a, Å	8.689(12)	8.9306(4)
b, Å	13.74(2)	14.9418(7)
c, Å	14.63(2)	19.3063(8)
α, °	77.99(3)	90
β, °	86.42(2)	103.887(2)
γ, °	84.18(3)	90
Volume, $Å^3$	1698(4)	2500.92(19)
Z	2	4
No obs. reflns with I > 2σ(I)	3453	4292
No. of Independent reflections	5951	5713
R_1 ($I > 2\sigma(I)$)	0.0588	0.0322
$wR(F^2)$ (all data)	0.1136	0.0490

Table 4.14: Bond lengths [Å] and Bond angles [°] for for $[Zn(S_2CNCy_2)_2(py)]$ (**10**) and $[Zn(S_2CN(BzMe)_2)_2(py)]$ (**11**)

(**10**)		(**11**)	
Bond lengths[Å]			
Zn(1)-S(1)	2.401(4)	Zn(1)-S(1)	2.3779(6)
Zn(1)-S(2)	2.504(3)	Zn(1)-S(2)	2.5616(6)
Zn(1)-S(3)	2.454(3)	Zn(1)-S(3)	2.5455(6)
Zn(1)-S(4)	2.388(3)	Zn(1)-S(4)	2.3862(6)
Zn(1)-N(1)	2.070(6)	Zn(1)-N(1)	2.0668(17)
S(1)-C(6)	1.702(7)	S(1)-C(15)	1.724(2)
S(2)-C(6)	1.711(6)	S(2)-C(15)	1.714(2)
S(3)-C(19)	1.722(7)	S(3)-C(6)	1.714(2)
S(4)-C(19)	1.701(7)	S(4)-C(6)	1.718(2)
N(2)-C(6)	1.342(8)	N(2)-C(6)	1.330(3)
N(3)-C(19)	1.328(8)	N(3)-C(15)	1.326(2)
Bond angles[°]			
N(1)-Zn(1)-S(4)	108.92(16)	N(1)-Zn(1)-S(1)	110.55(5)
N(1)-Zn(1)-S(1)	110.94(15)	N(1)-Zn(1)-S(4)	112.59(5)
S(4)-Zn(1)-S(1)	140.11(9)	S(1)-Zn(1)-S(4)	136.85(2)
N(1)-Zn(1)-S(3)	100.44(18)	N(1)-Zn(1)-S(3)	100.74(5)
S(4)-Zn(1)-S(3)	73.49(9)	S(1)-Zn(1)-S(3)	98.60(2)
S(1)-Zn(1)-S(3)	97.75(10)	S(4)-Zn(1)-S(3)	72.90(2)
N(1)-Zn(1)-S(2)	102.23(18)	N(1)-Zn(1)-S(2)	98.69(5)
S(4)-Zn(1)-S(2)	100.94(11)	S(1)-Zn(1)-S(2)	72.719(19)
S(1)-Zn(1)-S(2)	72.05(10)	S(4)-Zn(1)-S(2)	101.14(2)
S(3)-Zn(1)-S(2)	157.23(8)	S(3)-Zn(1)-S(2)	160.50(2)
S(1)-C(6)-S(2)	115.5(4)	S(3)-C(6)-S(4)	117.41(12)
S(4)-C(19)-S(3)	115.6(4)	S(2)-C(15)-S(1)	117.04(12)

Table 4.15: Hydrogen-bond geometry for (**10)** and (**11)**. *Cg* is the centroid of the C9-C14 ring

	D-H...A	H…A (Å)	D...A (Å)	D-H…A (°)
(10)				
	C(1)-H(1)...S(2)#1	2.68	3.533(8)	152.1
	C(4)-H(4)...S(4)#2	2.89	3.750(10)	154.5
(11)				
	C(8)-H(8B)...S(3)#1	2.89	3.656(3)	136.4
	C(16)-H(16B)...Cg#3	2.94	3.468(2)	116

Symmetry operations used to generate equivalent atoms: #1 -x+1, -y, -z+1; #2 x-1, y, z; #3 x, -y+1/2, z+1/2.

4.7.3 Thermogravimetric Decomposition of Complexes (10) and (11)

The TGA/DTG plots (Figure 4.48) of complexes (**10**) and (**11**) indicate that the complexes are suitable to be employed as AACVD precursors to fabricate ZnS thin films at about 375 °C. The TGA of complex (**10**) reveals a two-step decomposition. In the first step, a weight loss of 11.60% in the temperature range of 75-115 °C is observed, which is attributed with the loss of pyridine (12.03%). The second step of pyrolysis commences between 270 °C and 375 °C with a rapid weight loss of 73.26% to yield a stable residue of 15.14%. The decomposition of complex (**11**) involves five steps, where the first three steps occur consecutively in the temperature range of 70-210 °C with a weight loss of 16.90% indicating the loss of pyridine (14.72%). The fourth and fifth steps collectively yield a rapid weight loss of 63.68% between 210 °C and 375 °C. The solid residues amounting to 15.14% for (**10**) and 19.42% for (**11**) at 375 °C are in close agreement with the calculated values of 14.83% and 18.15% for ZnS from complexes (**10**) and (**11**), respectively. Further heating these residues up to 550 °C did not generate any change in their weight indicating that the both complexes degrade

quantitatively to furnish ZnS as a stable end product.

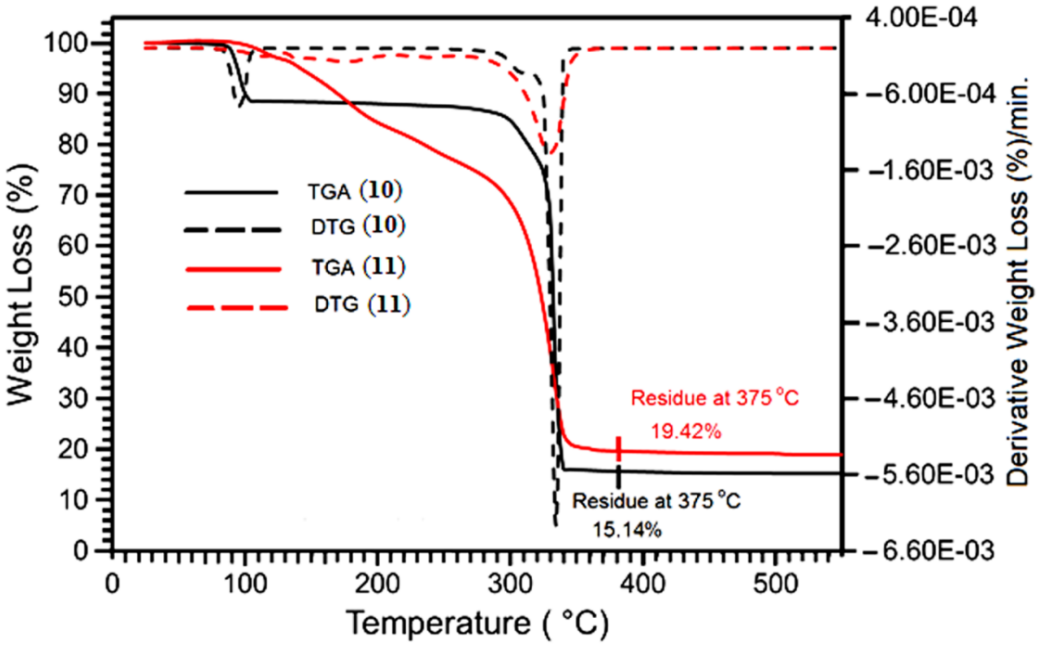

Figure 4.48: TGA/DTG plots which show the percentage weight losses and derivative weight losses with the increase of temperature for (**10**) and (**11**) Zn complexes.

It is worth noticing that the removal of pyridine in complex (**11**) takes place at a relatively higher temperature than in complex (**10**). This is due to the formation of different molecular packing structures in these complexes. In complex (**11**), due to presence of lighter alkyl (benzyl and methyl) groups, adjacent molecules extensively interact with each other and develop infinite molecular chain, Figure 4.47. These molecular aggregations provide thermal stability to pyridine and cause its elimination at high temperature. While in complex (**10**) adjacent molecular interactions are blocked by the presence bulky alky (dicyclohexyl) groups and molecular chains exist as dimers, Figure 4.46, therefore, elimination of pyridine occurs at relatively low temperature than complex (**11**).

4.7.4 Phase and Crystalline Structure Identification of Zinc Sulphide Thin Films

Generally, ZnS crystallizes into two structural polymorphs known as sphalerite (cubic) and wurtzite (hexagonal). The phase selectivity (cubic/hexagonal) is influenced by the deposition technique, processing parameters, type of substrate and precursor metal ligand design (Pike, 1993). ZnS films grown by Elidrissi et al. through spray pyrolysis exhibited a mixture of cubic and hexagonal phases(Elidrissi, 2001) . Studies conducted via chemical bath deposition by Johnston et al. (Johnston, 2002) and Cheng et al. (Cheng, 2003) described the deposition of hexagonal ZnS phase while Saratale et al. (Sartale, 2005) and Lee et al. (Lee, 2003) deposited the cubic ZnS. In a recent study, O'Brien et al. (Frigo, 1989b) deposited pure hexagonal ZnS films using [Zn(N-$SCNEt_2)_2)_2$] precursor while a mixture of cubic and hexagonal ZnS were produced when the [$Zn(SON(CN^iPr_2)_2)_2$] precursor was used. The co-occurrence of cubic and hexagonal phases at relatively low temperatures and the transition of cubic to hexagonal phase with the increase of the substrate temperature have been reported by many workers in the literature (El Hichou, 2004; Scott, 1972). However, thin films with only hexagonal phase can only be produced by changing the metal ligand design, deposition parameters and nature of the substrate. With regards to the present study, the metal ligand frames and sulphur fugacity of both (**10**) and (**11**) precursors are alike, producing the traditional patterns of ZnS phases.

The X-ray diffraction (XRD) patterns of ZnS thin films deposited from precursors (**10**) and (**11**) on FTO glass substrate at temperatures 375, 425 and 475 °C by AACVD are shown in Figure 4.49. The peaks indexed by (*) correspond to the SnO_2 layer of the FTO substrate. For the 375 °C deposited film, the strong reflection produced at 2θ = 28.6° is shared by both hexagonal (002) (ICSD: 98-004-3597) and cubic (111) (ICSD: 98-065-1457) forms of ZnS, respectively.

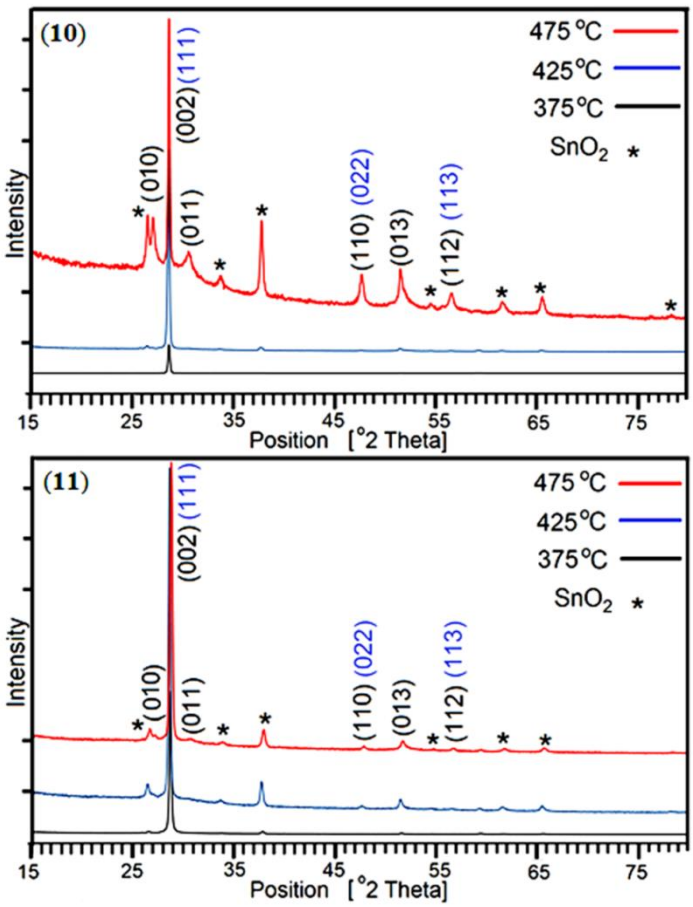

Figure 4.49: XRD patterns of ZnS thin films deposited from precursors (**10**) and (**11**) at 375, 425 and 475 °C on the FTO substrate.

When the substrate temperature is increased to 475 °C the peaks produced by the planes (010), (011) and (013) at 2θ = 26.9°, 30.6° and 51.6° respectively are discreetly assigned to the hexagonal phase (ICSD:98-004-3597). However, for the same film still the peaks at 2θ = 28.6, 47.6, 56.5° can be observed which are characteristics of hexagonal (002), (110), (112) and cubic (111), (022) and (113) planes, respectively. Hence, we conclude that at 375 °C cubic phase is dominating with co-existence of hexagonal phase as a minority phase. While at high temperature 475 °C hexagonal phase is observed as major phase with the contamination of cubic phase. All ZnS spectra are dominated by the diffraction peak located at 2θ = 28.6°. It is worth noting that the diffraction peak intensities displayed a remarkable increase due to the growth of

the film thickness when the substrate temperature was gradually raised from 375 to 475 °C. Generally, the ZnS film prepared using the precursor (**10**) shows better crystallinity.

4.7.5 Surface Characterization of ZnS films

SEM images of ZnS films deposited from precursors (**10**) and (**11**) by AACVD at 375, 425 and 475 °C on FTO substrates are presented in Figure 4.50.

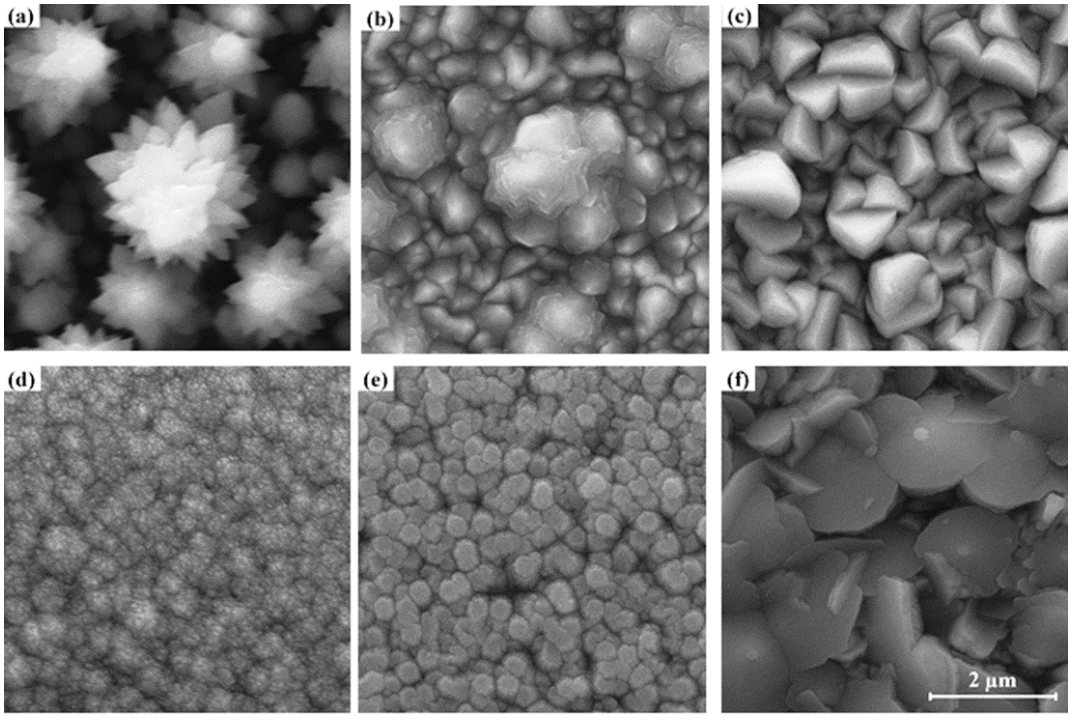

Figure 4.50: SEM images of ZnS films deposited using precursor (**10**) at (a) 375 °C (b) 425 °C (c) 475 °C , and precursor (**11**) at (d) 375 °C (e) 425 °C and (f) 475 °C.

Figure 4.50(a) shows that the ZnS film deposited at 375 °C using precursor (**10**) consists of well-oriented cauliflower-like structure that diminishes when the deposition temperature is increased to 425 °C. This has resulted in densely packed globules making the film more compact and uniform [Figure 4.50(b)]. As the deposition temperature is further increased to 475 °C, a complete morphological shift is observed yielding a granular compact and uniform film of ZnS [Figure 4.50(c)].

Figure 4.50(d) indicates the formation of unstructured particles emerging from the

compact structure at 375 °C that become visible in the form of spherical features as the deposition temperature is increased to 425 °C [Figure 4.50(e)]. A further increase of the deposition temperature to 475 °C resulted in a morphology of ZnS consisting of irregular inter-penetrating crystallites with a large feature size [Figure 4.50(f)].

EDX spectra (Appendix 12) illustrate the stoichiometric composition of the ZnS films. They show the expected stoichiometric ratio, indicating that the composition of film is in fact ZnS. The molar ratio of Zn/S obtained from the peak areas of the EDX spectra is shown in the Table 4.16 and thus close to the expected 1:1 ratio of ZnS.

Table 4.16: Zn/S molar ratio of ZnS films made using (**10**) and (**11**) precursors at different deposition temperatures.

Zn/S molar ratio	375 °C	425 °C	475 °C
For precursor (**10**)	0.84	0.88	0.93
For precursor (**11**)	0.90	0.92	0.90

4.7.6 Optical Properties of ZnS films

The optical properties of ZnS films deposited on FTO substrate from precursor (**10**) and (**11**) at 475 °C are determined from absorbance spectra as shown in Figure 4.51. The spectra of ZnS films reveal that no absorbance occurs beyond 500 nm. The steep optical absorption features starting from 380 nm indicate better crystallinity and lower defects density near the band edge and are analogous to the reported hexagonal ZnS spectra (Biswas, 2008). The optical band gap (E_g) was estimated from the $(\alpha h\nu)^2$ versus (E_g) plot according to the equation:

$$\alpha h\nu = A_0(h\nu - E_g)^n$$

where A is a constant and n is an integer, the value of which depends on the mode of electronic transitions. In the present case, the best fit to the experimental data of the above formula was obtained with n = 1/2, corresponding to direct allowed transitions.

The extrapolations of the curves to the energy axis for zero absorption provide the optical band gap value. The observed band gap for ZnS films deposited from precursors (**10**) and (**11**) are 3.36 and 3.40 eV respectively. These values are comparable to the literature value for hexagonal ZnS (Fan, 2007; Tran, 1999).

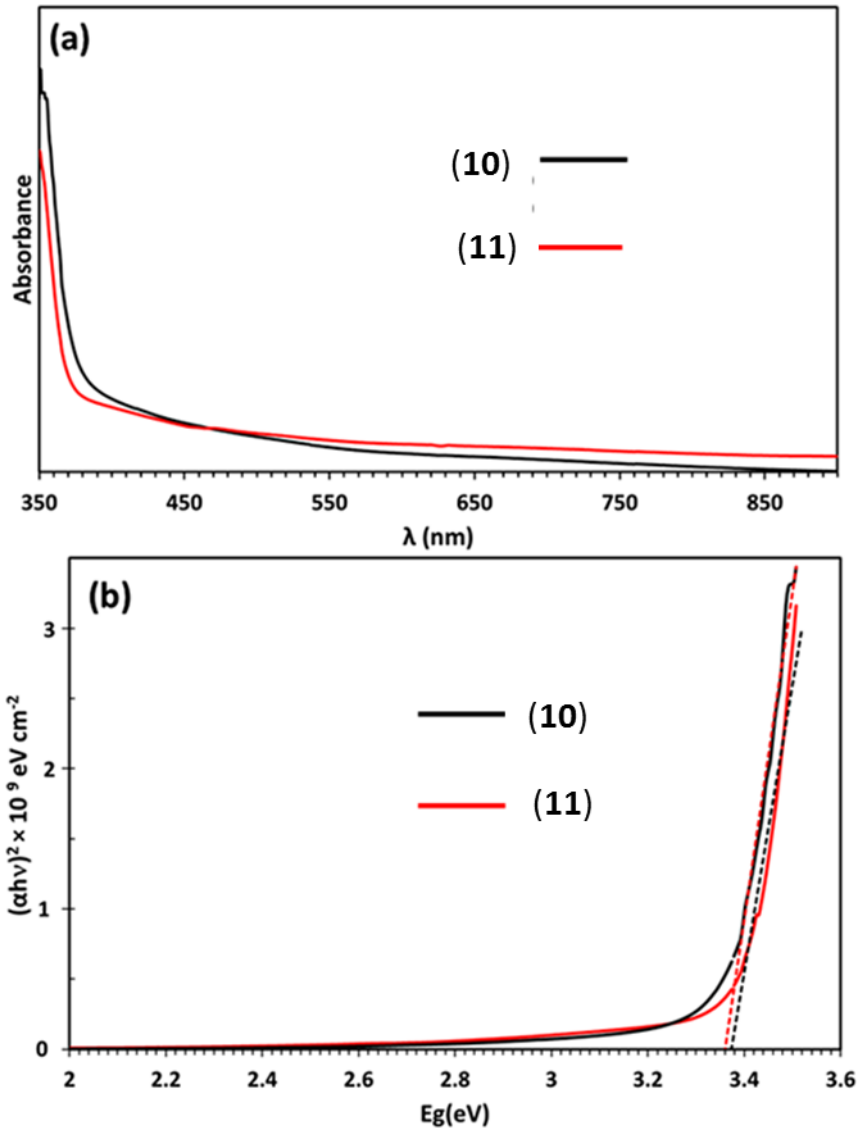

Figure 4.51: (a) UV- visible spectra of ZnS thin films deposited from precursor (**10**) and (**11**) at 475 °C on the FTO substrate. (b) Shows the corresponding Tauc plots.

4.7.7 Photoelectrochemical Properties of ZnS films

The current–voltage (I–V) measurements were conducted (while the 1 sun illumination was regularly interrupted by chopping) in conventional three-electrode electrochemical set-up employing an Ag/AgCl/3 M KCl as the reference electrode and a platinum mesh as the counter electrode. An aqueous electrolyte of Na_2SO_3 (0.25 M) and Na_2S (0.35 M) was used for all PEC measurements. Figures 4.52 and 4.53 show the photocurrent response of ZnS electrodes prepared using precursor (**10**) and (**11**) at 475 °C, respectively. The illuminated light was manually chopped over the potential range in order to distinguish the photocurrent of the electrodes from the dark current. The anodic photocurrent recorded under positive bias confirms that our ZnS films are anodic in nature and the minority carriers are holes. This observation agrees well with the previously reported work on ZnS (Fathy, 2005) . This behaviour can be explained in terms of the energetics at the ZnS semiconductor/electrolyte interface (Zheng, 2010). Upon illumination of the ZnS electrode, the electron-hole pairs are generated. The photogenerated minority carriers (holes) generated within the space charge region diffuse to the surface to undergo the electrochemical reaction at the interface (Tennakone, 1997). This phenomenon was observed under anodic biasing for the both ZnS electrodes deposited using precursor (**10**) as well as precursor (**11**). The electrode prepared from precursor (**10**) shows dark current within the entire potential window. In contrast, the ZnS electrode prepared from the precursor (**11**) shows no dark current between -1.0 and 0.2 V vs Ag/AgCl/3M KCl. Clearly, the PEC properties of ZnS electrode prepared by the precursor (**2**) are superior to that of the ZnS electrode prepared by precursor (**10**). This could be due to the difference in crystalline orientation in these electrodes. However, the PEC data indicate that the precursors (**10**) and (**11**) are suitable to deposit photoelectrochemically active ZnS electrodes using the AACVD

technique. Furthermore, the ZnS thin films reported in this study are very promising for optical, PEC and optoelectronic applications.

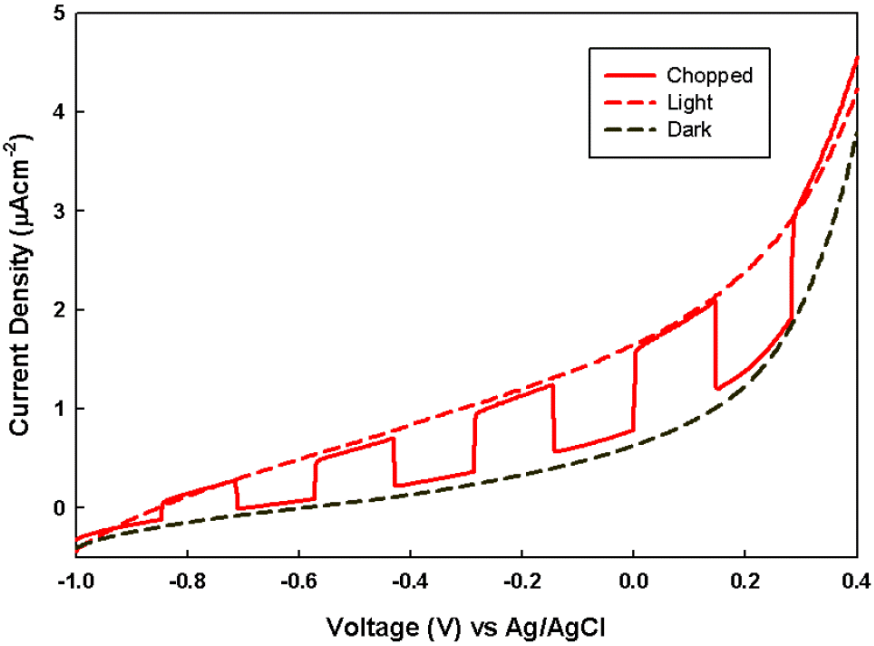

Figure 4.52: Current–voltage plot for ZnS thin film deposited from precursor (**10**) at 475 °C under chopped AM 1.5 illumination.

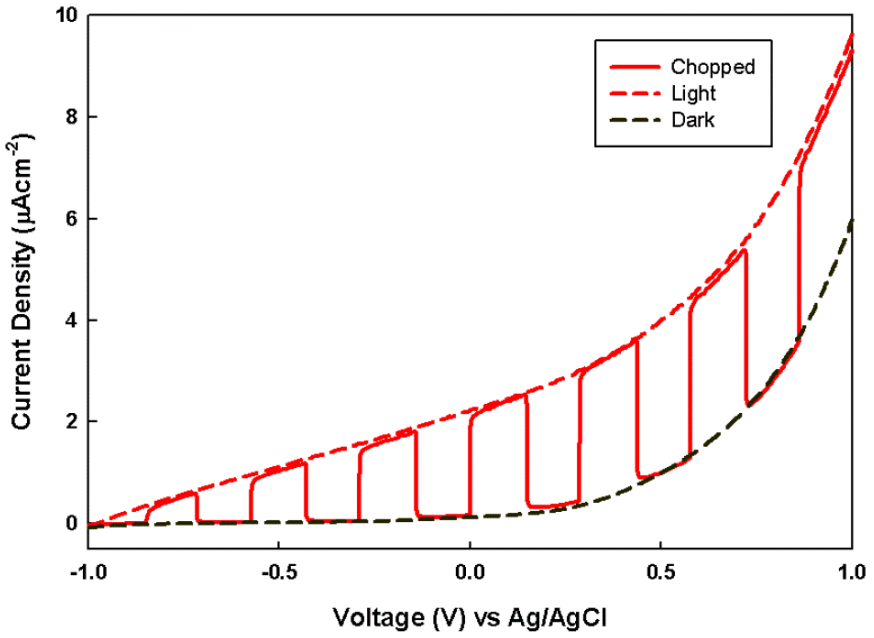

Figure 4.53: Current–voltage plot for ZnS thin film deposited from precursor (**11**) at 475 °C under chopped AM 1.5 illumination.

4.8 Bis(*N*,*N'*-dialkyldithiocarbamato)palladium(II)n-pyridine Complexes $[Pd(S_2CNRR')_3]\bullet n(py)$ (12)-(15)

The palladium (II) nitrate dihydrate reacts with sodium dithiocarbamate in stoichiometric 1: 2 in acetone pyridine solution to yield mononuclear complexes $[Pd(S_2CNRR')_2]\bullet n(py)$ [where py = pyridine; RR' = Bz, n = 1 (**12**); Cy, n = 1 (**13**); ^{n}Hex, n = 0 (**14**) and MeCy n = 0 (**15**)] as shown in chemical reaction below.

$$PdNO_3\cdot 2H_2O + 2Na(S_2CNRR') \xrightarrow[\text{Acetone}]{\text{Pyridine}} [Pd(S_2CNRR')_3]\cdot n(py) + 2NaNO_3$$

The reaction proceeds through metathetical reaction with the elimination of sodium nitrate and the complexes were isolated as dry crystalline solids, varying in appearance from yellow (**12**)-(**14**) to dark brown (**15**) and readily soluble in common organic solvents, THF, pyridine and chloroform. An earlier method reported for the preparation of such SSPs involves the *in situ* synthesis of dithiocarbamates followed by reaction with $Na_2[PdCl_4]$ aqueous solutions (Malik, 2002). Thus the prepared complexes needed to be dried in vacuum for several days and subsequently needed sublimation to obtain pure products. This synthetic strategy enabled us to obtain pure crystalline product from acetone-pyridine mixture.

The stoichiometry of the complexes (**12**)-(**15**) has been formulated on the basis of elemental analysis, IR, ^{1}H-NMR (data presented in chapter 3, page 69-71) and single crystal X-ray analyses. The microanalysis (CHN) of all complexes match well with their compositions calculated from the crystal data. The IR spectrum of all complexes (**12)-(15)** shows typical absorptions between 1427-1510 cm^{-1} due to ν(C⁼⁼⁼⁼N) stretching vibrations. The absorption bands in the region of 966 cm^{-1} and 1030 cm^{-1} are characteristic of the stretching vibrations of the $\nu(CSS)_{sym}$ and $\nu(CSS)_{asym}$ respectively and support the bidentate coordination of the S atoms of dithiocarbamate moieties with a metal centre (Alverdi, 2004; Torres-Huerta, 2013). The ^{1}H-NMR spectra of complexes

(**12**)-(**15**) reveal the usual splitting patterns for protons attached to the corresponding R groups. The ^{1}H-NMR spectra of complexes (**12**)-(**13**) show multiple peaks centred between δ 7.31 and 8.70 ppm due to the protons of pyridine ring. However such peaks are not observed in the spectra of complexes (**14**)-(**15**) which suggests the absence of pyridine in their molecular structures. Further evidences in this regard have been provided by thermogravimetric/derivative thermogravimetric and single crystal X-ray analysis of these complexes.

4.8.1 Single Crystal X-ray Structure of Complexes (12)-(15)

Perspective views of the four [$Pd(S_2CNRR')_2$] [where py = pyridine; RR' = Bz, n = 1 (**12**); Cy, n = 1 (**13**); ^{n}Hex, n = 0 (**14**) and MeCy n = 0 (**15**)] molecules are shown in Figures 4.54-4.57, respectively. Crystal data, data collection and structure refinement details are summarized in Table 4.17. The coordination environment of the metal ion is very similar in each complex (Table 4.18). The palladium ion lies on a centre of symmetry in [$Pd(S_2CNBz_2)_2$]•py (**12**) [$Pd(S_2CNCy_2)_2$]•py (**13**) and [$Pd(S_2CNCyMe)_2$] (**15**), but there is no crystallographically imposed symmetry in [$Pd(S_2CN^{n}Hex_2)_2$] (**14**). In each complex the palladium is coordinated to two deprotonated dithiocarbamate groups and the PdS_4 moiety is planar. The S–Pd–S bite angle for each ligand is approximately 75° (Table 4.18), so preventing adoption of regular square planar coordination geometry. The unit cell packing is different in each case, controlled by the substituents on the dithiocarbamate ligands (and incorporated solvate molecules).

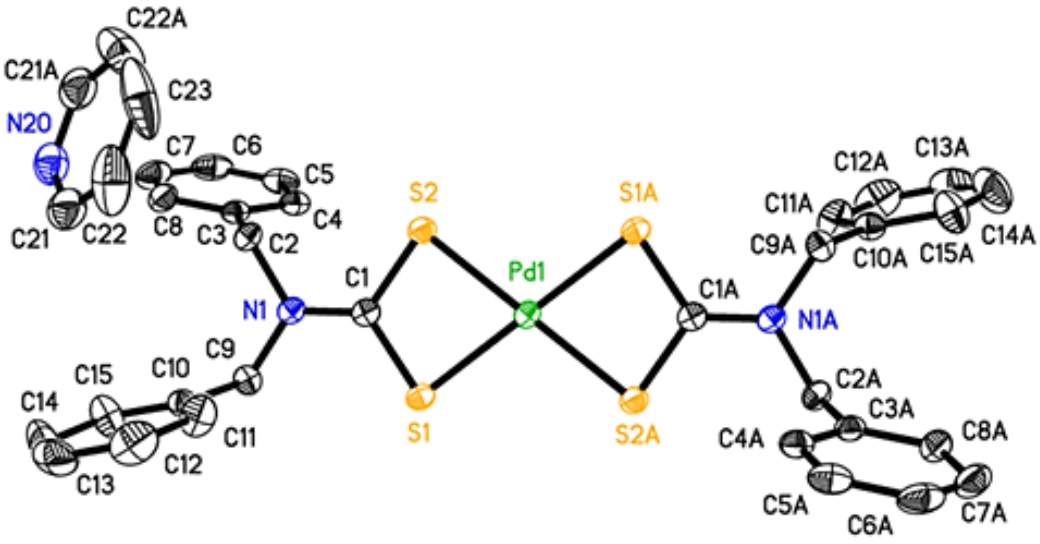

Figure 4.54: Perspective view of $[Pd(S_2CNBz_2)_2]$•py (**12**) showing 50% ellipsoids, hydrogen atoms have been omitted for clarity and the disorder of the pyridine solvate is not shown. Atoms with label suffix A have been generated by inversion (symmetry operations 1½-x, 2½-y, 1-z (for the complex and by a 2-fold rotation (under 1-x, 1-y, ½-z) for the pyridine).

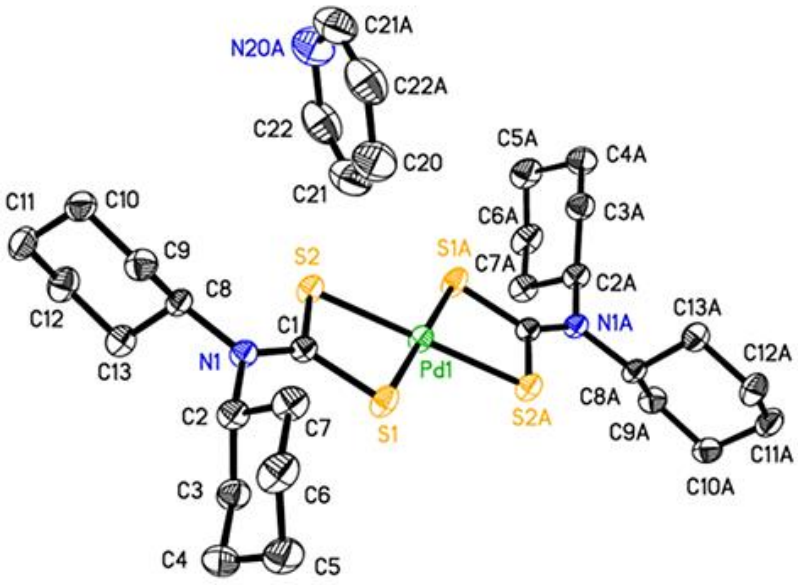

Figure 4.55: Perspective view of $[Pd(S_2CNCy_2)_2]$•py (**13**) showing 50% ellipsoids. Hydrogen atoms have been omitted for clarity and the disorder of the pyridine solvate is not shown. Atoms with label suffix A have been generated by inversion (symmetry operations 1-x, 1-y, 1-z for the complex and 1-x, 1-y, -z for the pyridine).

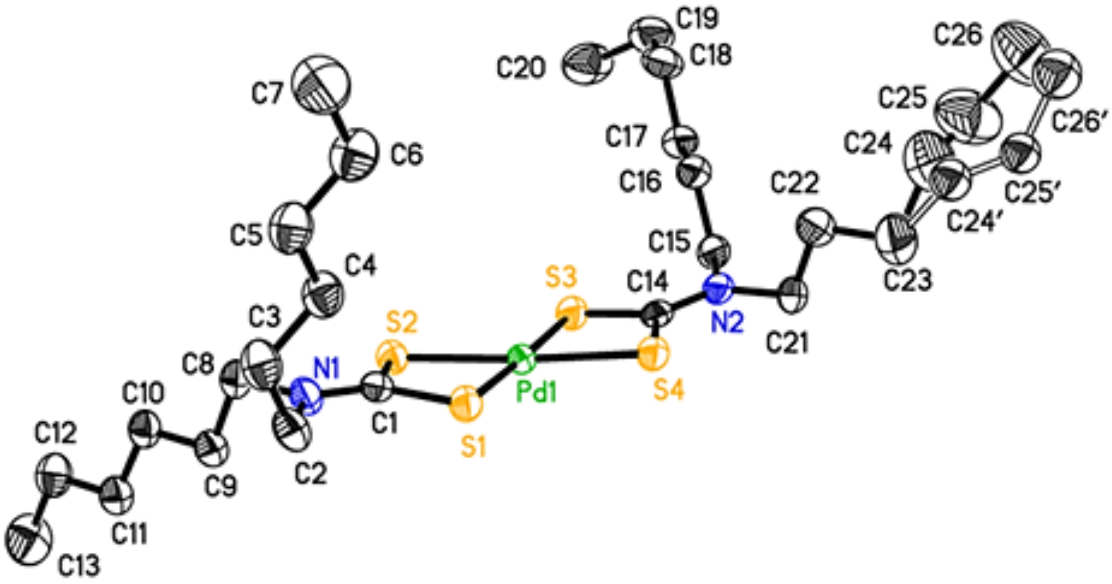

Figure 4.56: Perspective view of [Pd($S_2CN^nHex_2)_2$] (**14**) showing 50% ellipsoids. Hydrogen atoms have been omitted for clarity. Atoms with label suffix (') represent the minor component of a disorder modelled with 74:26% occupancy of the two sites shown.

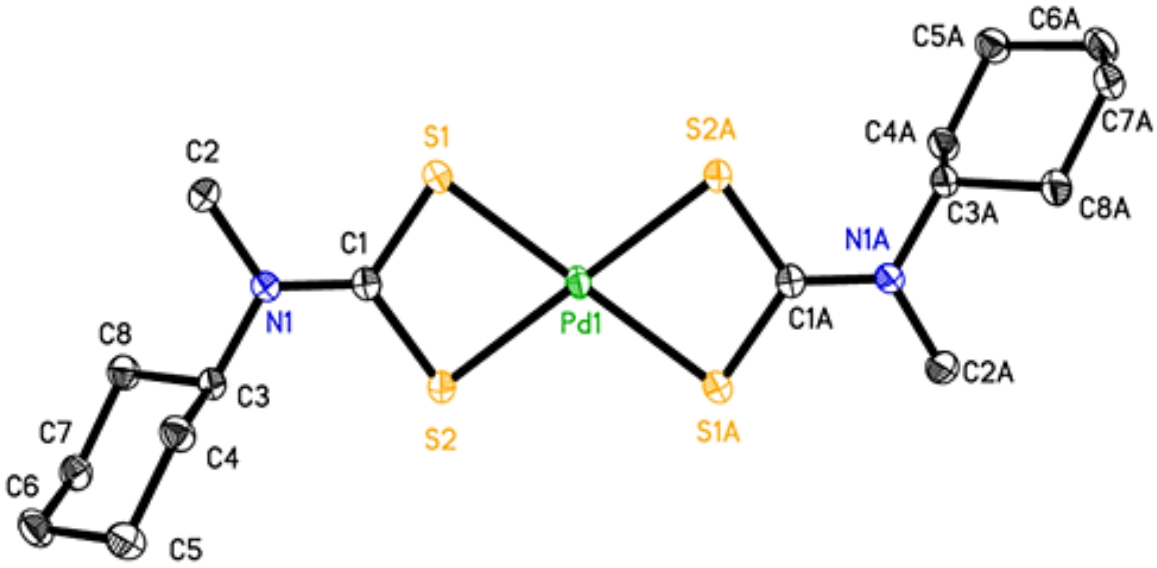

Figure 4.57: Perspective view of [Pd($S_2CNCyMe)_2$] (**15**) showing 50% ellipsoids. Hydrogen atoms have been omitted for clarity. Atoms with label suffix A have been generated by inversion (symmetry operation 2-x, -y, 2-z).

In structure of $[Pd(S_2CNBz_2)_2]$•py (**12**), the benzyl substituents are arranged with one on each side of the PdS_4 plane; the phenyl rings are close to coplanar (interplanar angle 21.0(1)°). This structure also contains a solvate pyridine making a weak H-bond interaction, this time with itself C23-H23···N20 is 3.613(5) Å (under symmetry operation x, 1+y, z). There is an indication of π-π stacking involving C1 and S1 of neighbouring molecules (under 1½-x, 1½-y, 1-z), and the π-system of the ring containing C3– C8 is arranged directly above S2 (under x, 1+y, z). These intermolecular interactions are all shown in Figure 4.58.

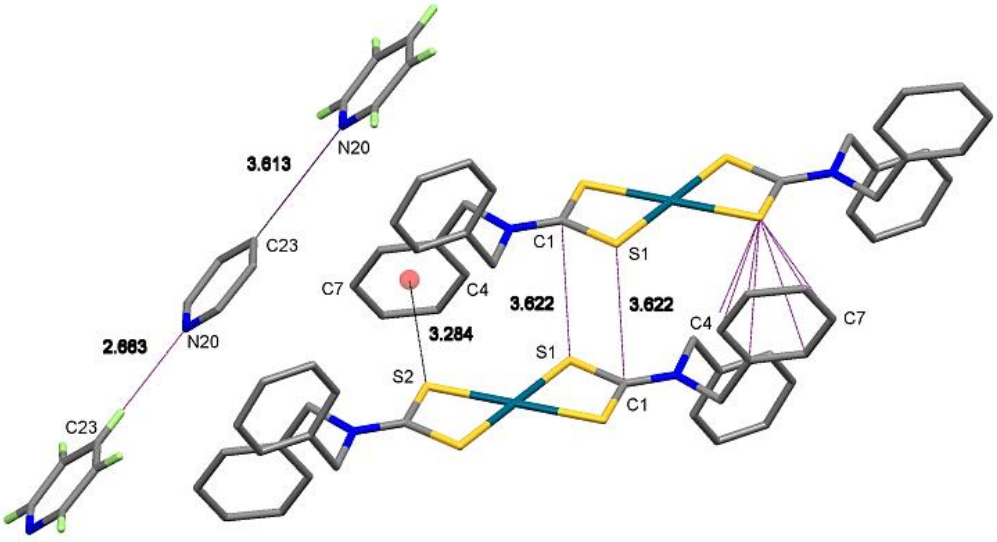

Figure 4.58: Weak interactions in the lattice of $[Pd(S_2CNBz_2)_2]$•py (**12**). Hydrogen atoms not involved have been omitted for clarity.

$[Pd(S_2CNCy_2)_2]$•py (**13**) contains one pyridine solvate molecule for each complex. The pyridine molecules are aligned between adjacent $[PdS_2CNCy_2]$ units, suggesting a hydrogen-bond interaction with the delocalised dithiocarbamate (Figure 4.60). At best this is a weak interaction since the C21-H21···C1 distance is 3.667(4) Å, but it would account for the location and orientation of the pyridine molecules. There are no other striking interactions in the lattice.

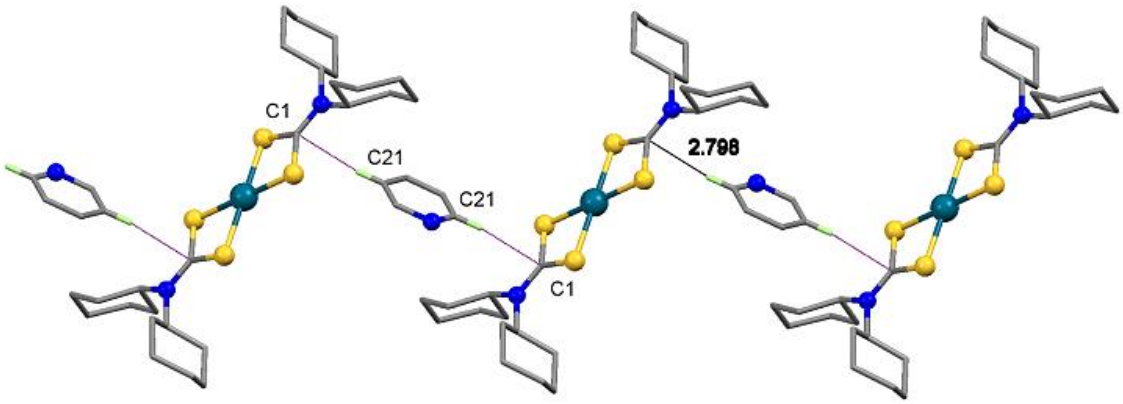

Figure 4.59: The long interaction between the solvate pyridine and the dithiocatbamate groups in $[Pd(S_2CNCy_2)_2]$•py (**13**). Distance C21–C1 is 3.667(4) Å.

Three of the four independent alkyl chains in $[Pd(S_2CN^nHex_2)_2]$ (**14**) lie on the same side of the PdS_4 plane and one of these shows some disorder. The PdS_4 unit is not strictly planar, the palladium ion is displaced by 0.0565(4) Å from the mean plane of the sulphur donors on the opposite side to the three alkyl chains. Again there is some long C-H···S interactions (Figure 4.60) but no single reason for the slightly strained geometry.

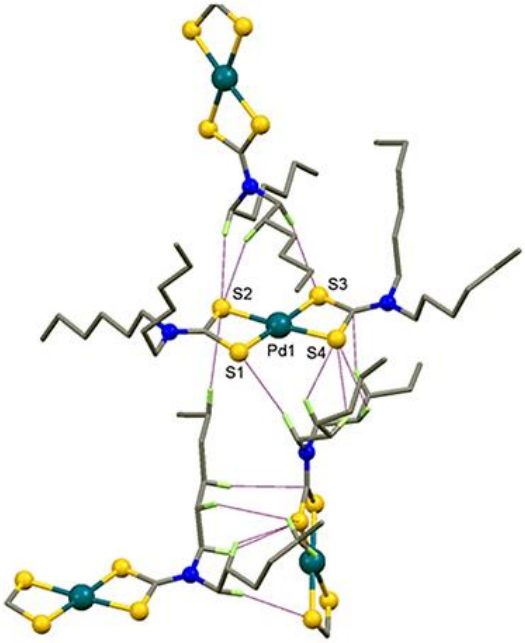

Figure 4.60: Weak interactions in the lattice of $[Pd(S_2CN^nHex_2)_2]$ (**14**). Some hydrogen atoms and some sections of the molecules have been omitted for clarity.

The most striking feature in the unit cell packing of complex [Pd(S_2CNCyMe)$_2$] (**15**) is the possible axial agostic interaction of two hydrogen atoms with the Pd ion (Pd1 – H2C 2.787 Å under 1½-x, 1½+y, 1½-z and 1½-x, -½+y, 1½-z). Additional long C-H···S interactions are also shown in the Figure 4.61.

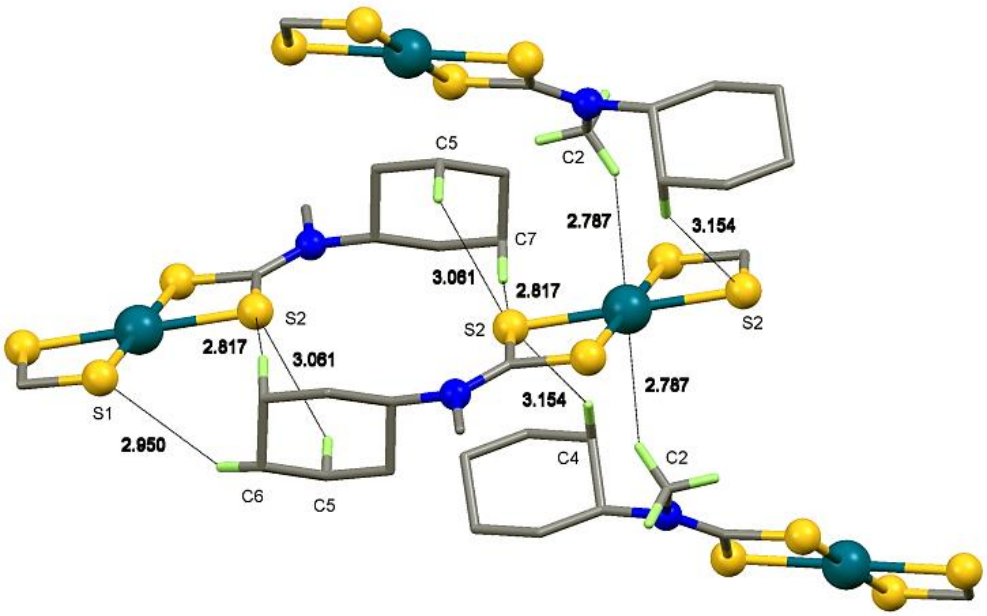

Figure 4.61: Weak interactions in the lattice of [Pd(S_2CNMeCy)$_2$] (**15**). Some hydrogen atoms and some sections of the molecules have been omitted for clarity.

Table 4.17: Crystal data and refinement parameters for the complexes $[Pd(S_2CNBz_2)_2]$•py (**12**), $[Pd(S_2CNCy_2)_2]$•py (**13**), $[Pd(S_2CN^nHex_2)_2]$ (**14**) and $[Pd(S_2CNCyMe)_2]$ (**15**)

Identification code	(**12**)	(**13**)	(**14**)	(**15**)
Empirical formula	$C_{35}H_{33}N_3PdS_4$	$C_{31}H_{49}N_3PdS_4$	$C_{26}H_{52}N_2PdS_4$	$C_{16}H_{28}N_2PdS_4$
Formula weight	730.28	698.37	627.33	483.04
Crystal system	monoclinic	monoclinic	orthorhombic	monoclinic
Space group	C 2/*c*	P 2_1/*n*	P *b c a*	P 2_1/*n*
Unit cell a(Å)	20.803(3)	9.9610(13)	12.3351(11)	9.9199(7)
b (Å)	6.3637(8)	14.0277(19)	20.5728(19)	11.0292(7)
c (Å)	25.240(3)	12.1552(16)	25.918(2)	10.1444(7)
β (°)	99.136(2)	104.023(2)	90	114.6960(10)
Volume ($Å^3$)	3299.0(7)	1647.8(4)	6577.2(10)	1008.37(12)
Z	4	2	8	2
D (calc) (Mg/m^3)	1.470	1.408	1.267	1.591
Abs coeff. (mm^{-1})	0.845	0.842	0.834	1.335
F(000)	1496	732	2656	496

Crystal size (mm^3)	0.40x0.24x0.07	0.20x0.16x0.16	0.34x0.24x0.15	0.28x0.22x0.20
Crystal description	yellow lath	yellow block	yellow block	yellow block
q range (°)	1.634 - 28.325	2.256 - 28.347	1.571 - 28.315	2.412 - 31.804
Reflections collected	16346	16333	64543	11825
Ind. refl [R_{int}]	4121 [0.0385]	4109 [0.0478]	8186 [0.0704]	3217 [0.0298]
Data /restraints/param	4121 / 0 / 197	4109 / 0 / 178	8186 / 20 / 311	3217 / 0 / 107
Goof on F^2	1.049	0.999	1.010	1.063
R1, wR2 [I>2s(I)]	0.0283, 0.0606	0.0348, 0.0773	0.0375, 0.0817	0.0262, 0.0623
R1, wR2 [all data]	0.0378, 0.0640	0.0519, 0.0832	0.0731, 0.0955	0.0327, 0.0651
± Residuals (e $Å^{-3}$)	0.406, -0.467	0.479, -0.758	0.375, -0.864	0.651, -0.600

Table 4.18: Selected bond lengths (Å) and angles (°) for complexes (**12**)-(**15**)

	(**12**)	(**13**)	(**14**) [a]	(**15**)
Pd1 – S1	2.3315(5)	2.3141(6)	2.3272(8), 2.3241(8)	2.3319(4)
Pd1 – S2	2.3172(5)	2.3237(6)	2.3143(7), 2.3236(8)	2.3261(5)
C1 - S1	1.7220(19)	1.730(2)	1.725(3), 1.720(3)	1.7201(16)
C1 – S2	1.718(2)	1.738(2)	1.724(3), 1.724(3)	1.7223(16)
N1 - C1	1.323(2)	1.326(3)	1.315(3), 1.317(3)	1.3273(19)
S1 – Pd1 – S2	75.329(17)	75.15(2)	75.68(3), 75.62(3)	75.080(14)
S1 – Pd1 – S2'	104.671(17)	104.85(2)	104.51(3), 104.06(3)	104.919(14)
S1 – C1 – S2	111.32(11)	109.29(13)	111.27(16), 111.66(16)	111.08(9)

[a] (**3**) has no internal symmetry; second entries are bonds or angles involving S3, S4, C14 and N2 (matching S1, S2, C1 and N1, respectively

4.8.2 Thermogravimetric Decomposition of Complexes (12)-(15)

The suitability of palladium dithiocarbamate complexes (**12**)-(**15**) for use as SSP for the deposition of PdS thin films was studied by TG/DTG (Appendix 13-16). It was revealed that the pyridine solvated complexes (**12**) and (**13**) display four-steps while the non-solvated (**14**) and (**15**) show a three-step decomposition to leave a residue of palladium sulphide. The initial mass losses from (**12**) and (**13**) occur in the temperature ranges of 66-139 and 75-163 °C with maximum heat intake steps at 197 and 124 °C, respectively, and is associated with the loss of pyridine molecules (Appendix 13 and 14). The observed weight losses of 6.02 and 8.38% show some consistency with the calculated values of 5.41 and 11.31% for the loss of 0.5 and 1 molecule of pyridine from (**12**) and (**13**), respectively.

The TG profiles of the non-solvated (**14**) and (**15**) did not show any weight loss in the temperature range of 70-170 °C suggesting that the initial weight losses in (**12**) and (**13**) are essentially due to the loss of solvated pyridine molecule (Appendix 15 and 16). The TG and DTG data reveal that the precursors (**12**),(**13**) and (**14**),(**15**) show major

weight losses in the temperature range 240-500 and 200-500 °C with maximum heat intake steps at 380, 385, 338 and 333 °C to produce stable residue amounting to 17.70, 19.20, 21.78 and 27.40% respectively. These residue masses are consistent with the theoretical values of 18.90, 19.77, 22.00 and 28.57% for the formation of PdS from (**12**)-(**15**). Continued heating of the observed final residues up to 600 °C gives no further change in weight suggesting that the complexes (**12**)-(**15**) have decomposed quantitatively to furnish PdS as a stable end product.

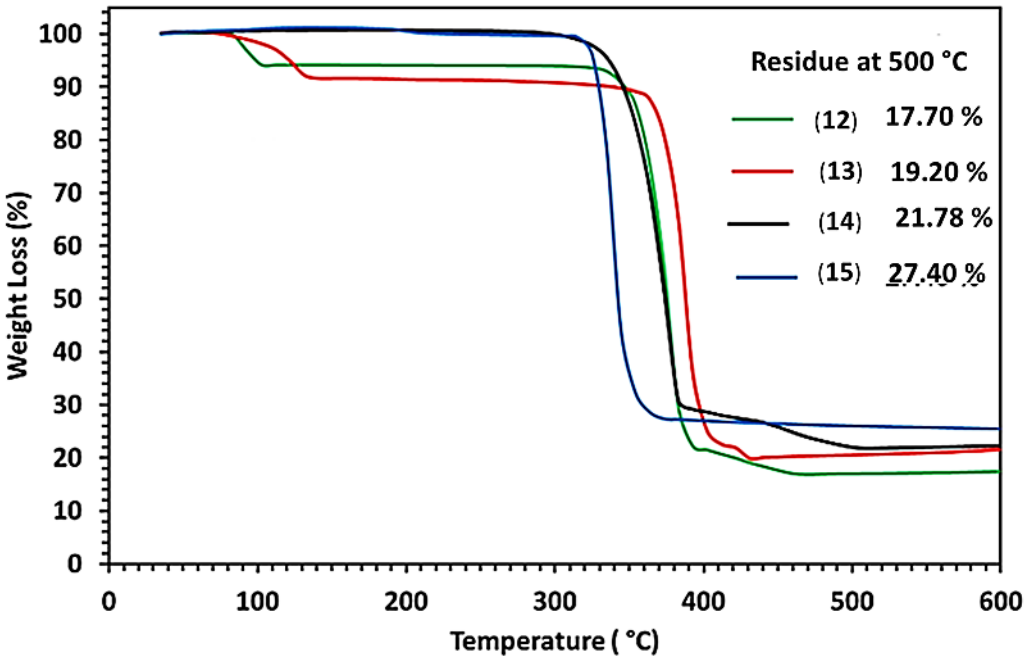

Figure 4.62: Thermograms for precursors (**12**)-(**15**), showing (%) weight losses against temperature.

4.8.3 Phase and Crystalline Structure Identification of Palladium Sulphide Thin Films

Three different temperatures of 400, 450 and 500 °C were applied for the deposition of palladium sulphide thin films from pyridine solution of precursors (**12**)-(**15**) by AACVD. It was found that 450 °C is the most appropriate temperature for the

deposition of palladium sulphide reflective thin films adherent to the substrate which appears dark gray in colour.

While the films deposited at 400 and 500 °C from these precursors appear dark black in colour and were non-adherent to the substrate, they were too thin to be investigated by XRPD. The XRPD patterns of the films deposited on FTO glass substrate at 450 °C from pyridine solution of precursors (**12**)-(**15**) are displayed in Figure 4.63.

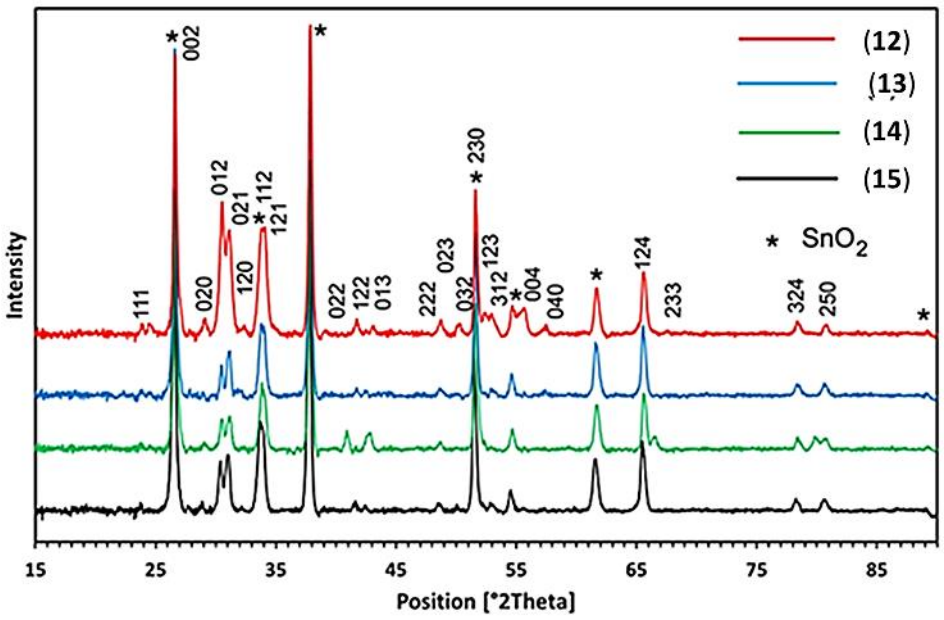

Figure 4.63: PXRD patterns of tetragonal-PdS films deposited from precursor $[Pd(S_2CNBz_2)_2]$•py (**12**) (red line), $[Pd(S_2CNCy_2)_2]$•py (**13**) (blue line), $[Pd(S_2CN^nHex_2)_2]$ (**14**) (green line) and $[Pd(S_2CNMeCy)_2]$ (**15**) (black line) at 450 °C on FTO glass substrate.

A careful inspection of the recorded XRPD patterns was made against palladium sulphide materials including Pd_4S, Pd_3S, $Pd_{2.8}S$, PdS, PdS_2 held in the database. It was found that similar XRPD patterns were observed for all palladium sulphide thin films prepared from precursors (**12**)-(**15**) at 450 °C while diffraction peaks were indexed to standard Inorganic Crystal Structure Database ICSD = [98-064-8749] to identify the deposited product as the "Vysotskite PdS" crystallizing in the tetragonal structure

(P42/*m*) with crystal parameters a = b = 6.4290, and c = 6.6080 Å. The diffraction peaks originating from crystalline layers of SnO_2 are indicated by (*). The strong reflections produced at 2θ = 26.60°, 33.84° 51.60° are shared by both crystalline PdS and SnO_2. No possible crystalline impurities such as $Pd_{2.8}S$ Pd_3S, Pd_4S, $Pd_{2.2}S$ and $Pd_{2.5}S$ were detected from these XRPD patterns. This clearly indicates that all the precursors (**12**)-(**15**) decompose cleanly at 450 °C to yield pure crystalline tetragonal phase PdS.

Recently, palladium sulphide thin films deposited from complexes $[Pd(S_2CNRR')_2]$ (RR' = Et_2, MeEt, Me^{n}Bu) showed widely differing results depending on the type of precursor and growth temperature (O'Brien, 2006). Poorly crystalline films of tetrahedral Pd_4S were deposited from $Pd(S_2CNEt_2)_2$ and mixtures of tetragonal PdS and cubic $Pd_{16}S_7$ were deposited from $Pd(S_2CNMeEt)_2$ at 450 °C. The deposition from $Pd(S_2CNMe^nBu)_2$ at temperatures of 475, 500 and 525 °C resulted in $Pd_{16}S_7$, mixtures of $Pd_{16}S_7$ and tetrahedral Pd_4S and cubic Pd respectively (O'Brien, 2006). The formation of stoichiometric tetragonal PdS thin films in our AACVD experiments coincides with previous investigations for low pressure and photochemical CVD experiments using dithiocarbamate $[Pd(S_2CNMeHex)_2]$ and xanthate $[Pd(S_2COCHMe_2)_2]$ precursors, respectively (CheonTalaga, 1997a; Malik, 2002). These observations suggest that the molecular design of precursors, deposition technique and temperature play a vital role in determining the nature of palladium sulphide deposit. Furthermore, thermal decomposition of allyl palladium dithiocarbamate/xanthate SSPs for the generation of palladium sulphide (PdS, Pd_4S, Pd_xS) powders have been widely studied and explored in the past. For example, the thermal decomposition of allyl palladium dithiocarbamates $[(\eta^3\text{-}C_3H_5)Pd(S_2CNC_5H_{10})]$ and $[(\eta^3\text{-}C_4H_7)Pd(S_2CNPr_2)]$ having similar Pd:S (2:1) ratio decomposed to PdS and PdS/Pd composite respectively (Birri, 2007). The thermal decomposition of allyl palladium xanthae $[(\eta^3\text{-}CH_2C(CH_3)CH_2)Pd(S_2X)]$ (X = COMe; COEt; CO^{i}Pr), $[(\eta^3\text{-}CH_2C(CH_3)CH_2)Pd(S_2COMe)]$ and palladium xanthate

{$Pd(S_2COMe)_2$] having different alkyl groups and same Pd:S (2:1) ratio result in the formation of single phase PdS as end product (Singhal, 2007). Furthermore, the thermal decomposition of allyl palladium dithiophosphinate complex, [$(\eta^3\text{-}C_4H_7)Pd(S_2PPh_2)$] and organosulphur-bridged dimeric 2-methylallaylpalladium complex [$Pd_2(\mu\text{-}SBu^t)_2(\eta^3\text{-}C_4H_7)_2$] having different Pd:S ratio yielded the same metal-rich palladium sulphide (Pd_4S) material (Singhal, 2007). The forgoing discussion summarizes that during thermal treatments at certain higher temperatures the precursor molecules absorb specific thermal energies that allow simultaneous and multiple bond breakings of the precursor molecules sometimes causing non-selective bond dissociation of the precursor molecule to yield variable products. Moreover the ratio of palladium:sulphur in the precursor may play an important role in deciding the nature of the end product.

4.8.4 Surface Characterization of PdS Thin Films

The influence of solvents on the morphologies of films deposited by AACVD can be significant and is dependent upon the materials being deposited and the precursors used. Although the complexes (**12**)-(**15**) are highly soluble in common organic solvents chloroform, methanol and pyridine, the selection of deposition solvent (pyridine) is made on the basis of its physical properties i.e. boiling point, heat of combustion and coordinating ability. Based on our recent investigations, pyridine having coordinating ability with high boiling point (115 °C) and heat of combustion (2782 kJ/mol) facilitates both the homogeneous and heterogeneous nucleation and helps in building novel design and morphologies. In contrast, methanol and chloroform have low boiling points of 64.7 and 61.2 °C and have much lower heat of combustions of 725 and 473 kJ/mol respectively, which when compared to pyridine, evaporate faster causing unwanted homogenous nucleation to generate ultrafine particles that are embedded into the thin film and cause deterioration to the film properties such as crystallinity, microstructure

and uniformity (Hou, 2006; MarchandHassan, 2013). SEM images of the thin films prepared using pyridine solutions of the precursors (**12**)-(**15**) on FTO glass substrates at temperatures 400, 450 and 500 °C are presented in Figure 4.65, that indicates that shape, design and morphology of PdS films developed from precursor (**12**)-(**14**) vary with the rise in deposition temperature while precursor (**15**) builds similar PdS architectures at all temperatures from 400 to 500 °C.

SEM images of all the films grown from (**12**)-(**15**) at 400, 450 and 500 °C are shown in Figure 4.64(**a**)-(**l**) and description of their morphologies and Pd:S ratio in the thin films are given in Table 4.19 and Appendix 17-20.

It can be seen that with the increase in deposition temperature from 400 to 450 °C, thin film growth rates from all precursors (**12**)-(**15**) become better and the substrate surface is covered with different directional morphologies of PdS (Table 4.19). A further increase in deposition temperature to 500 °C, (**12**) developed acacia thorn tree, (**13**) produced deteriorated nano wires, (**14**) produced thorn design and (**15**) remained almost unchanged. The elemental composition as determined by EDX analysis shows stoichiometric Pd:S at 1:1 indicating formation of Vysotskite-structured PdS that is further verified by the PXPD results.

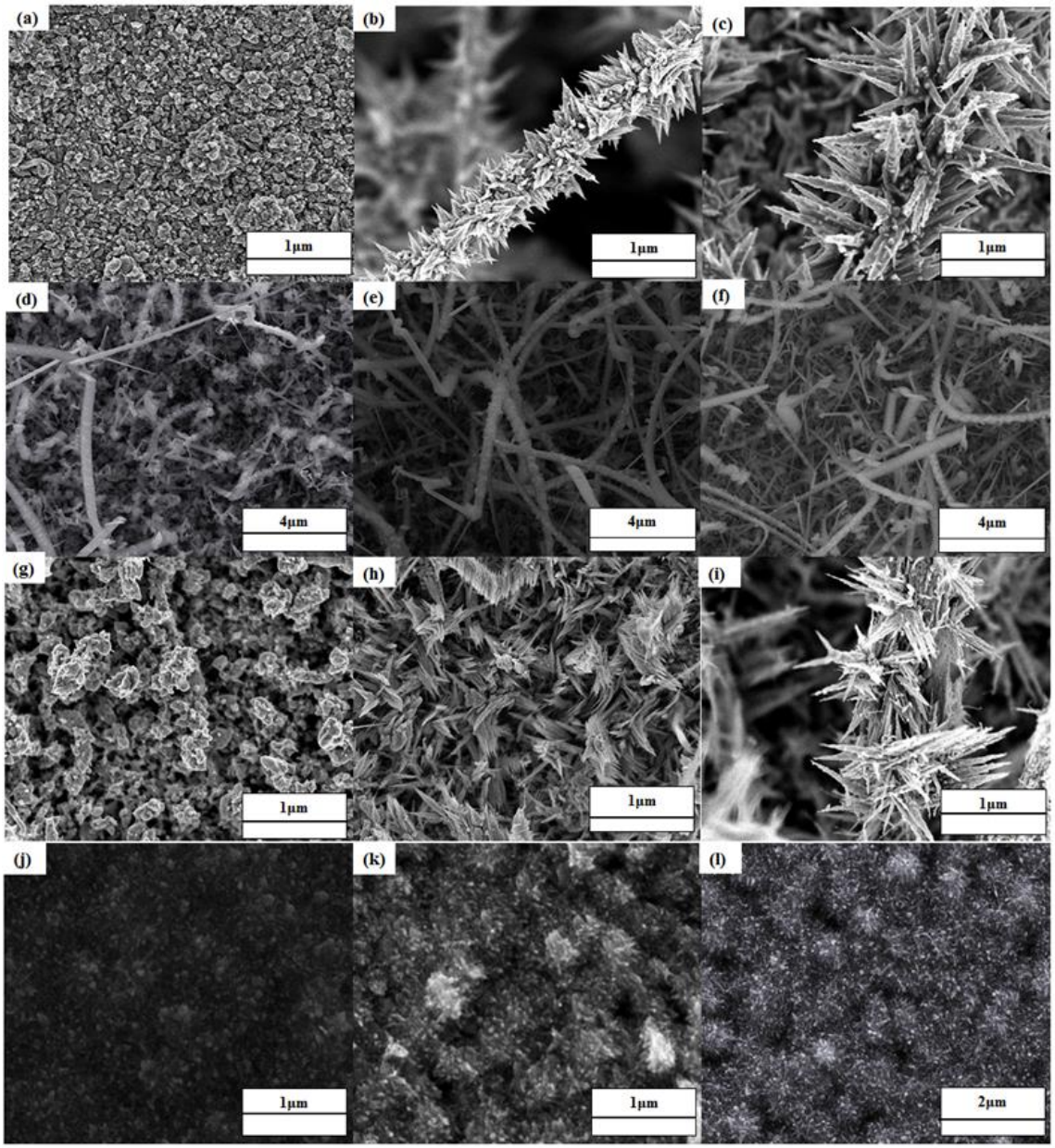

Figure 4.64: SEM images of PdS films deposited using precursors $[Pd(S_2CNBz_2)_2]$•py (**12**) at (a) 400 °C (b) 450 °C (c) 500 °C; $[Pd(S_2CNCy_2)_2]$•py (**13**) at (d) 400 °C (e) 450 °C and (f) 500 °C; $[Pd(S_2CN^nHex_2)]$ (**14**) at (g) 400 °C (h) 450 °C (i) 500 °C and $[Pd(S_2CNCyMe)_2]$ (**15**) at (j) 400 °C (k) 450 °C and (l) 500 °C.

Table 4.19: Description of morphologies [Figure 4.64 (a)-(l)] and Pd:S elemental ratio as determined by EDX in thin films fabricated from precursors (**12**)-(**15**) at 400, 450 and 500 °C.

Type of Precursor	Deposition temperatures (°C), Morphology, Pd/S ratio		
	400	450	500
(**12**)	(a) densely packed grains (37.14): (34.23)	(b) cactus branch (31.41): (29.98)	(c) acacia thorn (21.34): (20.13)
(**13**)	(d) featureless texture (32.56): (35.45)	(e) randomly oriented nanowires (25.57): (29.00)	(f) deteriorated nano wires (23.00): (26.13)
(**14**)	(g) irregular shape crystallites (39.19): (35.71)	(h) featureless pattern (20.33): (20.29)	(i) thorn design (25.36): (23:89)
(**15**)	(j) heap of crystallites (12.23): (11.69)	(k) heap of crystallites (28.25): (31.19)	(l) heap of crystallites (20.53): (23.40)

4.8.5 Optical Properties of PdS Thin Films

The optical band gap energy (E_g) of PdS thin films deposited from precursor (**13**) at 450 °C was determined by spectrophotometry and is shown in Figure 4.65. The UV-Vis spectra of the film recorded in the wavelength range between 350-900 nm shows that the PdS films absorb light over the full range in the visible region, Figure 4.65(a).

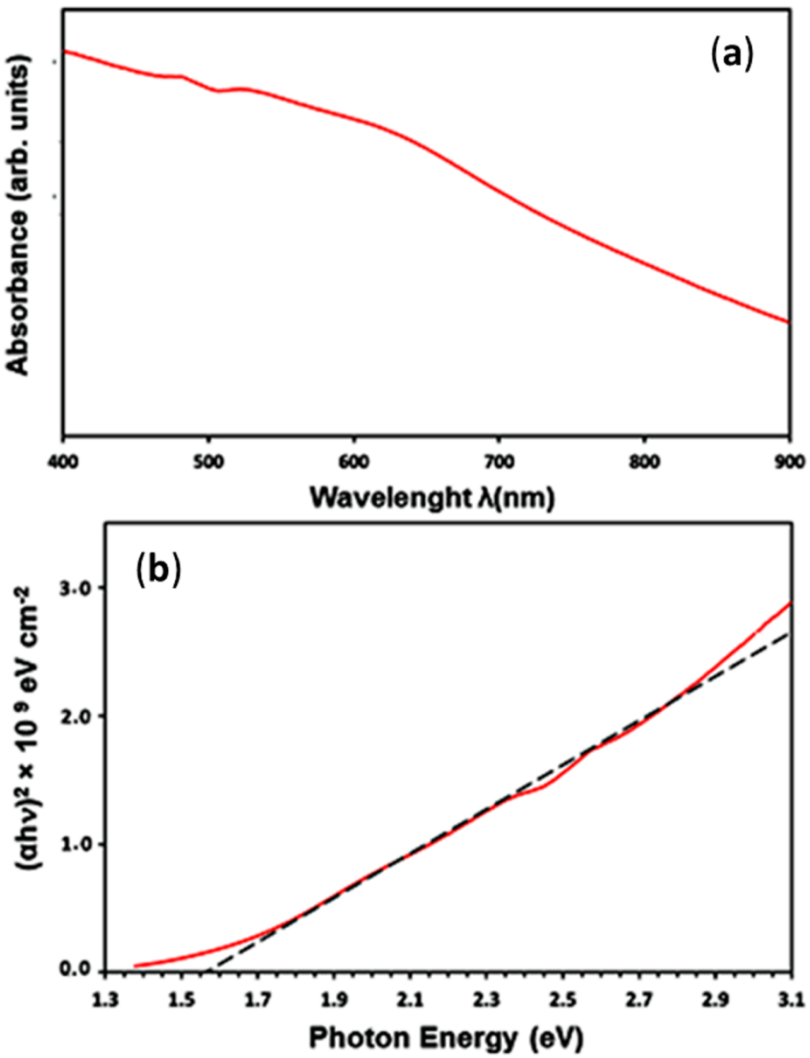

Figure 4.65: (a) UV-Vis spectra of PdS thin films deposited using precursor (**13**) at 450 °C (b) shows the direct band gaps of 1.56 eV for PdS films.

The optical band gap (E_g) value was derived from the following equation:

$$(\alpha h\nu) = A(h\nu - Eg)^n$$

where α is absorption coefficient, A is a constant, $h\nu$ the photon energy and n is an exponent which differentiate between direct allowed (n = 1/2), direct forbidden (n = 3/2), indirect allowed (n = 2), and indirect forbidden (n = 3) transitions. The optical band gap was estimated from the absorbance data by plotting $(\alpha h\nu)^2$ versus photonic energy ($h\nu$) and extending the linear part of the curve on the energy axis and were measured to be 1.56 eV (Figure 4.65(b)). The thickness of the PdS films used for the optical experiments was measured by profilometer to be 210 nm. Our band gap value

shows a good match with the band gap energy of PdS thin films reported through other preparative methods (Ferrer, 2007).

4.8.6 Photoelectrochemical Properties of PdS Thin Films

The steady-state current-voltage measurements, in the dark and under illumination, were measured in a conventional three-electrode electrochemical set-up with Ag/AgCl as a reference electrode and a platinum mesh as a counter electrode. An aqueous electrolyte of 1 M Na_2SO_3 was used for the measurements. Figure 4.66 shows the photocurrent response in the PEC measurements of PdS electrodes fabricated using precursor (**13**) at 450 °C with a photocurrent onset of -0.3 V. The plot indicated that the PdS electrode exhibited an anodic photocurrent which increases with increasing applied bias. The film showed a reasonable photocurrent response compared to the film obtained from the other precursor solutions at 450 ^{o}C. This could be due to the higher internal surface acquired from the randomly oriented nanowire structure of the film (Fig. 4.64e). The film showed a maximum net photocurrent density of 4 $\mu A/cm^2$ at 0 V vs (Ag/AgCl/3 M KCl). However, the dark current of the films are intense with applied bias which is probably representing oxidation of the electrode surface. To the best of our knowledge this is the first demonstration of PEC studies of PdS thin films that reveals the photoactivity of PdS thin films fabricated by AACVD technique using palladium(II) dithiocarbamate complexes as precursors. The reasonable photoactivity of the PdS films indicates their potential to be used in large number of applications in photoelectrochemical devices

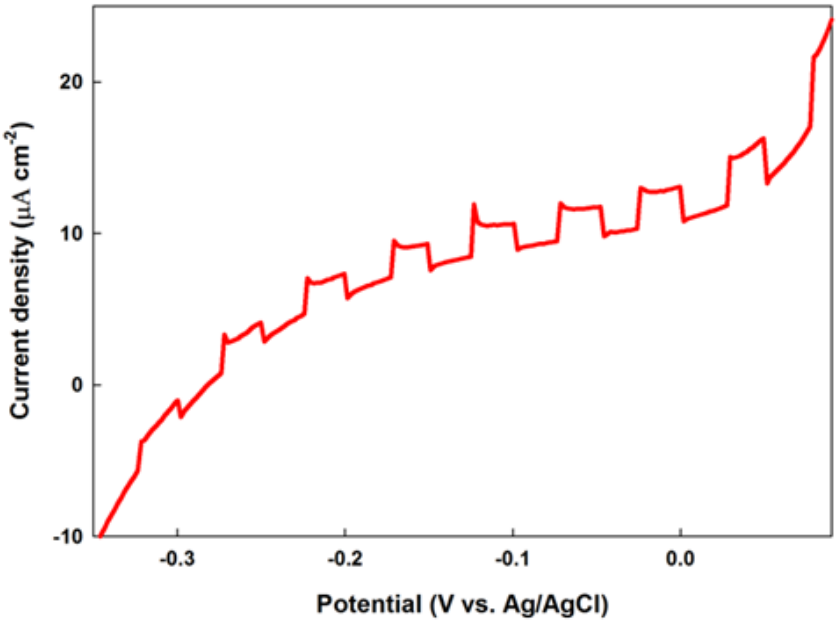

Figure 4.66: Chopped current-voltage curve for PdS thin film deposited using precursor (**13**) at 450 °C on the FTO substrate.

CHAPTER 5

CONCLUSION

In this research work, two heterobimetallic oxides $[Fe_2Ti_4(\mu\text{-}O)_6(TFA)_8(THF)_6]$ (**1**), $[Co_2Ti(\mu_3\text{-}O)(TFA)_6(THF)_3]$ (**2**) and several monometallic dithiocarbamate $[Bi(S_2CNEt_2)_3]_2$ (**3**), $[In(S_2CNCy_2)_3]\bullet 2py$ (**4**), $[In(S_2CN(^{i}Pr)_2)_3]\bullet 1.5py$ (**5**), $[In(S_2CPip)_3]\bullet 0.5py$ (**6**) and $[In(S_2CNBzMe)_3]$ (**7**), $[Ag_4\{S_2CNEt_2\}_3(py)_2]_n\cdot nNO_3\cdot 2nH_2O$ (**8**), $[Cd(S_2CNCy_2)_2(py)]$ (**9**), $[Zn(S_2CNCy_2)_2(py)]$ (**10**), $[Zn(S_2CNBzMe)_2(py)]$ (**11**), $[Pd(S_2CNBz_2)_2]\bullet py$ (**12**) $[Pd(S_2CNCy_2)_2]\bullet py$ (**13**), $[Pd(S_2CN^{n}Hex)_2]$ (**14**) and $[Pd(S_2CNCyMe)_2]$ (**15**) complexes were synthesized under mild conditions and characterized by their melting point, elemental analysis, infrared (IR), proton nuclear magnetic resonance (^{1}H-NMR) spectroscopies, and their molecular structures were established by single crystal X-ray analysis. Thermal stability of these complexes were analysed by thermogravimetric and derivative thermogravimetric (TG/DTG) analysis. These compounds were found to possess versatile physical and chemical properties including air and moisture stability, ease of synthesis at room temperature, high solubility in common organic solvents, enhanced volatility and facile thermal decomposition at relatively low temperature, which made them elegant precursors for aerosol assisted chemical vapour (AACVD) to deposit mixed metal composite oxides and metal sulphide thin films.

The heterobimetallic oxide complexes (**1**) and (**2**) were synthesized by routine chemical reaction of $[Fe_3O(OAc)_6(H_2O)_3]NO_3\cdot 4H_2O$ with tetrakis(2-ethoxyethanalato)titanium(IV) and $Co(OAc)_2\cdot 4H_2O$ with $Ti(^{i}PrO)_4$ respectively in the presence of trifluoroacetic acid in THF under ordinary reaction conditions and were used for the growth of Fe_2TiO_5/TiO_2 and $CoTiO_3/CoO$ composite oxide ceramic thin films by AACVD on soda glass substrate. Thin films were found to exhibit good adhesion with substrate, crystalline in nature with well-defined grain boundaries and

their metallic composition is similar to that exist in the relevant complex indicating the formation of impurity free films.

Metal dithiocarbamate precursors (**3**)-(**15**) were conveniently prepared via salt elimination reactions of stoichiometric amount of metal nitrates or chlorides with sodium dialkyldithiocarbamate ligands in a mixture of acetone and pyridine solutions and metal sulphide thin films were deposited on FTO glass substrates at different temperatures between 300 to 500 °C. The crystallinity, size, shape and design of metal sulphide deposit strongly depend upon the nature of precursor, substrate temperature and deposition solvent.

UV-Vis measurements of good quality nanophase Bi_2S_3, β-In_2S_3, Ag_2S, CdS, ZnS and PdS films deposited from precursors (**3**), (**4**), (**8**) (**9**), (**11**) and (**13**) at temperature of 400 and 475 °C showed direct band gap energies (E_g) of 1.8, 2.2, 1.05, 2.4, 3.5 and 1.7eV respectively and were further investigated for solar energy harvesting applications.

The photoelectrochemical performances of nanostructured metal sulphide thin films showed n-type behaviour and photocurrent density at 0.23 and 0.0 V vs. RHE is about 1.90, 1.25, 1.20, 8.0×10^{-3} and 4.0×10^{-3}, 0.22 mA/cm^2 for Bi_2S_3, β-In_2S_3, CdS, ZnS and Ag_2S, PdS electrodes made from precursors (**3**), (**4**), (**9**) (**11**) and (**8**), (**13**), respectively. The photocurrent onset for β-In_2S_3, CdS, ZnS, Ag_2S and Bi_2S_3 electrodes is at about -0.7V and -0.2 V respectively while photocurrent density rises steeply without reaching saturation under 1 sun illumination and no dark current was observed for Bi_2S_3, β-In_2S_3, CdS, ZnS and Ag_2S photoelectrodes up to about 0.3 and -0.2 V vs RHE respectively. The PEC efficiencies suggest that metal sulphide photoelectrodes are very auspicious for solar energy conversion and optoelectronic applications.

Thus the whole research work can be summarized that by designing and developing single source precursors with suitable physico-chemical properties and by manipulating

the deposition conditions of AACVD, functional material thin films of diverse nanostructures and architectures can be fabricated for solar energy conversion and optoelectronic applications.

Future Work Plan

Further research work is being carried out towards synthesis of single source molecular precursors for fabrication of transition metal sulphide, oxides and mixed metal composite oxides thin films. Single source precursors and films developed from them will be characterized and tested for their electrical and photoelectrochemical applications.

REFERENCES

Abbasi, T.; Abbasi, S. (2011). 'Renewable'hydrogen: Prospects and challenges. *Renew. Sust. Energ. Rev.,* 15, 3034-3040.

Abdelhady, A.L.; Ramasamy, K.; Malik, M.A.; O'Brien, P.; Haigh, S.J.; Raftery, J. (2011). New routes to copper sulfide nanostructures and thin films. *J. Mater. Chem. A,* 21, 17888-17895.

Addison, A.W.; Rao, T.N.; Reedijk, J.; van Rijn, J.; Verschoor, G.C. (1984). Synthesis, structure, and spectroscopic properties of copper (II) compounds containing nitrogen–sulphur donor ligands; the crystal and molecular structure of aqua [1, 7-bis (N-methylbenzimidazol-2′-yl)-2, 6-dithiaheptane] copper (II) perchlorate. *J. Chem. Soc., Dalton Trans.,* 1349-1356.

Adeogun, R.A.; O'Brien, P. (2007). *Deposition of Semiconductor Thin Films Using Single-source Metal-organic Precursors by AACVD Technique*: University of Manchester.

Afsal, M.; Wang, C.-Y.; Chu, L.-W.; Ouyang, H.; Chen, L.-J. (2012). Highly sensitive metal–insulator–semiconductor UV photodetectors based on ZnO/SiO2 core–shell nanowires. *J. Mater. Chem.,* 22, 8420-8425.

Afzaal, M.; Crouch, D.; Malik, M.A.; Motevalli, M.; O'Brien, P.; Park, J.H.; Woollins, J.D. (2004). Deposition of II-VI Thin Films by LP-MOCVD Using Novel Single-Source Precursors. *Eur. J. Inorg. Chem.,* 2004, 171-177.

Afzaal, M.; Ellwood, K.; Pickett, N.L.; O'Brien, P.; Raftery, J.; Waters, J. (2004). Growth of lead chalcogenide thin films using single-source precursors. *J. Mater. Chem.,* 14, 1310-1315.

Afzaal, M.; Malik, M.A.; O'Brien, P. (2010). Chemical routes to chalcogenide materials as thin films or particles with critical dimensions with the order of nanometres. *J. Mater. Chem.,* 20, 4031-4040.

Akhtar, J.; Malik, M.A.; O'Brien, P.; Helliwell, M. (2010). Controlled synthesis of PbS nanoparticles and the deposition of thin films by Aerosol-Assisted Chemical Vapour Deposition (AACVD). *J. Mater. Chem.,* 20, 6116-6124.

Alam, N.; Hill, M.S.; Kociok-Köhn, G.; Zeller, M.; Mazhar, M.; Molloy, K.C. (2008). Pyridine Adducts of Nickel (II) Xanthates as Single-Source Precursors for the

Aerosol-Assisted Chemical Vapor Deposition of Nickel Sulfide. *Chem. Mater.,* 20, 6157-6162.

Alessio, E. (2011). *Bioinorganic medicinal chemistry*: John Wiley & Sons.

Allsop, N.; Schönmann, A.; Belaidi, A.; Muffler, H.-J.; Mertesacker, B.; Bohne, W., . . . Fischer, C.-H. (2006). Indium sulfide thin films deposited by the spray ion layer gas reaction technique. *Thin Solid Films,* 513, 52-56.

Alverdi, V.; Giovagnini, L.; Marzano, C.; Seraglia, R.; Bettio, F.; Sitran, S., . . . Fregona, D. (2004). Characterization studies and cytotoxicity assays of Pt (II) and Pd (II) dithiocarbamate complexes by means of FT-IR, NMR spectroscopy and mass spectrometry. *J. Inorg. Biochem.,* 98, 1117-1128.

Asamoto, M.; Miyake, S.; Sugihara, K.; Yahiro, H. (2009). Improvement of Ni/SDC anode by alkaline earth metal oxide addition for direct methane–solid oxide fuel cells. *Electrochem. Commun.,* 11, 1508-1511.

Bakar, S.A.; Hussain, S.T.; Mazhar, M. (2012). $CdTiO_3$ thin films from an octa-nuclear bimetallic single source precursor by aerosol assisted chemical vapor deposition (AACVD). *New J. Chem.*, 36, 1844-1851.

Bao, H.; Cui, X.; Li, C.M.; Gan, Y.; Zhang, J.; Guo, J. (2007). Photoswitchable Semiconductor Bismuth Sulfide (Bi_2S_3) Nanowires and Their Self-Supported Nanowire Arrays. *J. Phys. Chem. C*, 111, 12279-12283.

Bao, H.; Li, C.M.; Cui, X.; Gan, Y.; Song, Q.; Guo, J. (2008). Synthesis of a Highly Ordered Single-Crystalline Bi_2S_3 Nanowire Array and its Metal/Semiconductor/Metal Back-to-Back Schottky Diode. *Small,* 4, 1125-1129.

Barbour, L.J. (2001). X-Seed—A software tool for supramolecular crystallography. *Supramol. Chem.,* 1, 189-191.

Barreca, D.; Gasparotto, A.; Maragno, C.; Tondello, E. (2004). CVD of nanosized ZnS and CdS thin films from single-source precursors. *J. Electrochem. Soc.,* 151, G428-G435.

Barreca, D.; Tondello, E.; Lydon, D.; Spalding, T.R.; Fabrizio, M. (2003). Single-Source Chemical Vapor Deposition of Zinc Sulfide-Based Thin Films from Zinc bis(O-ethylxanthate). *Chem. Vap. Deposition,* 9, 93-98.

Beckers, N.; Taschuk, M.; Brett, M. (2013). Selective room temperature nanostructured thin film alcohol sensor as a virtual sensor array. *Sen. Actuators B-Chem.*, 176, 1096-1102.

Bereman, R.D.; Churchill, M.R.; Nalewajek, D. (1979). Coordination chemistry of new sulfur-containing ligands. 16. Crystal and molecular structure of tris(pyrrole-n-carbodithioato)iron(III)-hemikis(dichloromethane), $Fe(S_2CNC_4H_4)_3.0.5CH_2Cl_2$, a low-spin dithiocarbamate complex of iron(III). *Inorg. Chem.*, 18, 3112-3117.

Bernal, C.; Neves, E.A.; Cavalheiro, É.T.G. (2001). Differences in thermal decomposition of Ag(I), Mn(II), Fe(II) and Fe(III) complexes of cyclic dithiocarbamates. *Thermochim. Acta*, 370, 49-55.

Binions, R.; Parkin, I.P. (2011). Novel Chemical Vapour Deposition Routes to Nanocomposite Thin Films.

Birri, A.; Harvey, B.; Hogarth, G.; Subasi, E.; Uğur, F. (2007). Allyl palladium dithiocarbamates and related dithiolate complexes as precursors to palladium sulfides. *J. Org. Chem.*, 692, 2448-2455.

Biswas, S.; Kar, S. (2008). Fabrication of ZnS nanoparticles and nanorods with cubic and hexagonal crystal structures: a simple solvothermal approach. *Nanotechnology*, 19, 045710.

Bloor, L.G.; Carmalt, C.J.; Pugh, D. (2011). Single-source precursors to gallium and indium oxide thin films. *Coord. Chem. Rev.*, 255, 1293-1318.

Bochmann, M. (1996). Metal Chalcogenide Materials: Chalcogenolato complexes as "single-source" precursors. *Chem. Vap. Deposition*, 2, 85-96.

Bonamico, M.; Mazzone, G.; Vaciago, A.; Zambonelli, L. (1965). Structural studies of metal dithiocarbamates. III. The crystal and molecular structure of zinc diethyldithiocarbamate. *Acta Cryst.*, 19, 898-909.

Bondi, A. (1964). van der Waals Volumes and Radii. *J. Phys. Chem.*, 68, 441-451.

Boudjouk, P.; Seidler, D.J.; Grier, D.; McCarthy, G.J. (1996). Benzyl-Substituted Tin Chalcogenides. Efficient Single-Source Precursors for Tin Sulfide, Tin Selenide, and Sn (S_xSe_{1-x}) Solid Solutions. *Chem. Mater.*, 8, 1189-1196.

Bradley, D.C., Mehrotra, R.C., Gaur, D.P. (1978). *Metal Alkoxides*: Academic Press, London,.

Brewer, M.; Khasnis, D.; Buretea, M.; Berardini, M.; Emge, T.; Brennan, J. (1994). Pyridine Coordination Complexes of the Divalent Ytterbium Chalcogenolates Yb (EPh) $_2$ (E= S, Se, Te). *Inorg. Chem.*, 33, 2743-2747.

Bruker, A. (1997-2003). Inc. smart apex (Version 5.628), saint+(Version 6.45) and shelxtl-nt (Version 6.12). *Bruker AXS Inc., Madison, WI, USA*.

Bruker, A. (2003). SHELXTL (Version 6.14). *Bruker Advanced X-ray Solutions, Madison, Wisconsin, USA*, 97-92.

Bruker, A. (2007). APEX2, SAINT, SADABS: Bruker AXS Inc., Madison, WI.

Byrom, C.; Malik, M.; O'Brien, P.; White, A.; Williams, D. (2000). Synthesis and X-ray single crystal structures of bis (diisobutyldithiophosphinato) cadmium (II) or zinc (II): Potential single-source precursors for II/VI materials. *Polyhedron*, 19, 211-215.

Callister, W.D.; Rethwisch, D.G. (2012). *Fundamentals of materials science and engineering: an integrated approach*: John Wiley & Sons.

Carmalt, C.J.; O'Neill, S.A.; Parkin, I.P.; Peters, E.S. (2004). Titanium sulfide thin films from the aerosol-assisted chemical vapour deposition of [Ti(SBut)$_4$]. *J. Mater. Chem.*, 14, 830-834.

Carter, C.B.; Norton, M.G. (2013). *Ceramic Materials: Science and Engineering*: Springer.

Castro, J.R.; Molloy, K.C.; Liu, Y.; Lai, C.S.; Dong, Z.; White, T.J.; Tiekink, E.R. (2008). Formation of antimony sulfide powders and thin films from single-source antimony precursors. *J. Mater. Chem.*, 18, 5399-5405.

Chambouleyron, I.; Martınez, J. (2001). Optical properties of dielectric and semiconductor thin films. *Handbook of Thin Film Materials*, 3, 593-622.

Chen, D.; Yin, L.; Ge, L.; Fan, B.; Zhang, R.; Sun, J.; Shao, G. (2013). Low-temperature and highly selective NO-sensing performance of WO nanoplates decorated with silver nanoparticles. *Sens. Actuators B-Chem.*, 185, 445-455.

Chen, X.; Li, C.; Grätzel, M.; Kostecki, R.; Mao, S.S. (2012). Nanomaterials for renewable energy production and storage. *Chem. Soc. Rev.*, 41, 7909-7937.

Chen, X.; Shen, S.; Guo, L.; Mao, S.S. (2010). Semiconductor-based photocatalytic hydrogen generation. *Chem. Rev.*, 110, 6503-6570.

Chen, Y.; Huang, G.-F.; Huang, W.-Q.; Zou, B.; Pan, A. (2012). Enhanced visible-light photoactivity of La-doped ZnS thin films. *Appl. Phys. A*, 108, 895-900.

Cheng, J.; Fan, D.; Wang, H.; Liu, B.; Zhang, Y.; Yan, H. (2003). Chemical bath deposition of crystalline ZnS thin films. *Semicond. Sci. Technol.*, 18, 676.

Cheng, Y.; Wang, Y.; Bao, F.; Chen, D. (2006). Shape control of monodisperse CdS nanocrystals: hexagon and pyramid. *J. Phys. Chem. B*, 110, 9448-9451.

Cheon, J.; Gozum, J.E.; Girolami, G.S. (1997). Chemical Vapor Deposition of MoS_2 and TiS_2 Films From the Metal-Organic Precursors $Mo(S^tBu)_4$ and $Ti(S^tBu)_4$. *Chem. Mater.*, 9, 1847-1853.

Cheon, J.; Talaga, D.S.; Zink, J.I. (1997a). Laser and thermal vapor deposition of metal sulfide (NiS, PdS) films and in situ gas-phase luminescence of photofragments from M $(S_2COCHMe_2)_2$. *Chem. Mater.*, 9, 1208-1212.

Cheon, J.; Talaga, D.S.; Zink, J.I. (1997b). Photochemical deposition of ZnS from the gas phase and simultaneous luminescence detection of photofragments from a single-source precursor, Zn $(S_2COCHMe_2)_2$. *J. Am. Ceram. Soc.*, 119, 163-168.

Chilla, J.; Shu, Q.-Z.; Zhou, H.; Weiss, E.; Reed, M.; Spinelli, L. (2007). *Recent advances in optically pumped semiconductor lasers.* Paper presented at the Lasers and Applications in Science and Engineering.

Cho, I.S.; Chen, Z.; Forman, A.J.; Kim, D.R.; Rao, P.M.; Jaramillo, T.F.; Zheng, X. (2011). Branched TiO_2 nanorods for photoelectrochemical hydrogen production. *Nano Lett.*, 11, 4978-4984.

Choudhary, S.; Upadhyay, S.; Kumar, P.; Singh, N.; Satsangi, V.R.; Shrivastav, R.; Dass, S. (2012). Nanostructured bilayered thin films in photoelectrochemical water splitting–A review. *Int. J. Hydrogen Energy*, 37, 18713-18730.

Choujaa, H.; Johnson, A.L.; Kociok-Köhn, G.; Molloy, K.C. (2013). Synthesis of heterobimetallic tungsten acetylacetonate/alkoxide complexes and their application as molecular precursors to metal tungstates. *Polyhedron*, 59, 85-90.

Choy, K. (2000). Vapor Processing of nanostructured materials (Vol. 533): Academic Press.

Choy, K.L. (2003). Chemical vapour deposition of coatings. *Prog. Mater Sci.*, 48, 57-170.

Clark, E.B.; Breen, M.L.; Fanwick, P.E.; Hepp, A.F.; Duraj, S.A. (2000). Synthesis and Characterization of Tris(dimethyldithiocarbamte)indium(III), $In[S_2CN(CH_3)_2]_3$. *J. Coord. Chem.,* 52, 111-117.

Coates, J. (2000). Interpretation of infrared spectra, a practical approach. *Encyclopedia of analytical chemistry*.

Colodrero, S.; Mihi, A.; Häggman, L.; Ocana, M.; Boschloo, G.; Hagfeldt, A.; Miguez, H. (2009). Porous One-Dimensional Photonic Crystals Improve the Power-Conversion Efficiency of Dye-Sensitized Solar Cells. *Adv. Mater.,* 21, 764-770.

Cong, C.; Hong, J.; Zhang, K. (2009). Effect of atmosphere on the magnetic properties of the Co-doped ZnO magnetic semiconductors. *Mater. Chem. Phys.,* 113, 435-440.

Corriu, Robert J.P. (2001). The Control of Nanostructured Solids: A Challenge for Molecular Chemistry. *Eur. J. Inorg. Chem.,* 2001, 1109-1121.

Cox, M.; Tiekink, E.R.T. (1999). Structural features of zinc (II) bis (O-alkyldithiocarbonate) and zinc (II) bis (N, N-dialkyldithiocarbamate) compounds. *Z. Kristallogr.,* 214, 184-190.

Criado, J.J.; Lopez-Arias, J.A.; Macias, B.; Fernandez-Lago, L.R.; Salas, J.M. (1992). Au (III) complexes of tris-dithiocarbamate derivatives of α-amino acids: spectroscopic studies, thermal behaviour and antibacterial activity. *Inorg. Chim. Acta,* 193, 229-235.

De Melo, J.V.S.; Trichês, G. (2012). Evaluation of the influence of environmental conditions on the efficiency of photocatalytic coatings in the degradation of nitrogen oxides (NO_x). *Build. Environ.,* 49, 117-123.

Deacon, G.B.; Huber, F.; Phillips, R.J. (1985). Diagnosis of the nature of carboxylate coordination from the direction of shifts of carbon-oxygen stretching frequencies. *Inorg. Chim. Acta,* 104, 41-45.

Dharmadasa, R.; Tahir, A.A.; Wijayantha, K. (2011). Single Step Growth and Characterization of Zinc Oxide, Tin Oxide, and Composite ($Zn_xSn_{1-x}O_y$) Nanoplate and Nanocolumn Electrodes. *J. Am. Ceram. Soc.,* 94, 3540-3546.

Dharmadasa, R.; Wijayantha, K.G.U.; Tahir, A.A. (2010). ZnO–SnO_2 composite anodes in extremely thin absorber layer (ETA) solar cells. *J. Electroanal. Chem.,* 646, 124-132.

Dikarev, E.V.; Zhang, H.; Li, B. (2005). Heterometallic bismuth-transition metal homoleptic β-diketonates. *J. Amer. Chem. Soc.,* 127, 6156-6157.

Dillon, A.; Mahan, A.; Deshpande, R.; Parilla, P.; Jones, K.; Lee, S. (2008). Metal oxide nano-particles for improved electrochromic and lithium-ion battery technologies. *Thin Solid Films,* 516, 794-797.

Dischler, B.; Bubenzer, A.; Koidl, P. (1983). Bonding in hydrogenated hard carbon studied by optical spectroscopy. *Solid State Commun.,* 48, 105-108.

Dobkin, D.M.; Zuraw, M.K. (2003). *Principles of chemical vapor deposition*: Springer.

Domenicano, A.; Torelli, L.; Vaciago, A.; Zambonelli, L. (1968). Structural studies of metal dithiocarbamates. Part IV. The crystal and molecular structure of cadmium (II) NN-diethyldithiocarbamate. *Dalton Trans.*, 1351-1361.

Dorey, R.; Rocks, S.; Dauchy, F.; Wang, D.; Bortolani, F.; Hugo, E. (2008). Integrating functional ceramics into microsystems. *J. Eur. Ceram. Soc.,* 28, 1397-1403.

Dutta, D.P.; Jain, V.K.; Knoedler, A.; Kaim, W. (2002). Dithiocarbamates of gallium (III) and indium (III): syntheses, spectroscopy, and structures. *Polyhedron,* 21, 239-246.

Eason, R. (2007). *Pulsed laser deposition of thin films: applications-led growth of functional materials*: John Wiley & Sons.

El Hichou, A.; Addou, M.; Bubendorff, J.; Ebothe, J.; El Idrissi, B.; Troyon, M. (2004). Microstructure and cathodoluminescence study of sprayed Al and Sn doped ZnS thin films. *Semicond. Sci. Technol.,* 19, 230.

Elidrissi, B.; Addou, M.; Regragui, M.; Bougrine, A.; Kachouane, A.; Bernède, J.C. (2001). Structure, composition and optical properties of ZnS thin films prepared by spray pyrolysis. *Mater. Chem. Phys.,* 68, 175-179.

Fabian, J.; Matos-Abiague, A.; Ertler, C.; Stano, P.; Žutić, I. (2007). Semiconductor spintronics. *Acta Phys. Slovaca,* 57, 565-907.

Fainer, N.; Kosinova, M.; Rumyantsev, Y.M.; Salman, E.; Kuznetsov, F. (1996). Growth of PbS and CdS thin films by low-pressure chemical vapour deposition using dithiocarbamates. *Thin Solid Films,* 280, 16-19.

Fan, D.; Afzaal, M.; Mallik, M.A.; Nguyen, C.Q.; O'Brien, P.; Thomas, P.J. (2007). Using coordination chemistry to develop new routes to semiconductor and other materials. *Coord. Chem. Rev.,* 251, 1878-1888.

Fang, X.; Bando, Y.; Liao, M.; Zhai, T.; Gautam, U.K.; Li, L., . . . Golberg, D. (2010). An Efficient Way to Assemble ZnS Nanobelts as Ultraviolet-Light Sensors with Enhanced Photocurrent and Stability. *Adv. Funct. Mater.,* 20, 500-508.

Farrer, N.J.; Sadler, P.J. (2011). Medicinal inorganic chemistry: state of the art, new trends, and a vision of the future (pp. 1-47): Wiley-VCH: Weinheim, Germany.

Farrugia, L.J. (1999). WinGX suite for small-molecule single-crystal crystallography. *J. Appl. Crystallogr.,* 32, 837-838.

Fathy, N.; Ichimura, M. (2005). Photoelectrical properties of ZnS thin films deposited from aqueous solution using pulsed electrochemical deposition. *Sol. Energy Mater. Sol. Cells,* 87, 747-756.

Ferrer, I.; Díaz-Chao, P.; Pascual, A.; Sánchez, C. (2007). An investigation on palladium sulphide (PdS) thin films as a photovoltaic material. *Thin Solid Films,* 515, 5783-5786.

Frigo, D.M.; Khan, O.F.; O'Brien, P. (1989a). Growth of epitaxial and highly oriented thin films of cadmium and cadmium zinc sulfide by low-pressure metalorganic chemical vapour deposition using diethyldithiocarbamates. *Journal of Crystal Growth,* 96, 989-992.

Frigo, D.M.; Khan, O.F.; O'Brien, P. (1989b). Growth of epitaxial and highly oriented thin films of cadmium and cadmium zinc sulfide by low-pressure metalorganic chemical vapour deposition using diethyldithiocarbamates. *J. Cryst. Growth,* 96, 989-992.

Gang, S.-R.; Kim, D.; Kim, S.-M.; Hwang, N.; Lee, K.-C. (2012). Improvement in the moisture stability of CaS: Eu phosphor applied in light-emitting diodes by titania surface coating. *Microelectron. Reliab.,* 52, 2174-2179.

Gao, M.-R.; Xu, Y.-F.; Jiang, J.; Yu, S.-H. (2013). Nanostructured metal chalcogenides: synthesis, modification, and applications in energy conversion and storage devices. *Chem. Soc. Rev.,* 42, 2986-3017.

Gavrilenko, K.S.; Vértes, A.; Vanko, G.; Kiss, L.F.; Addison, A.W.; Weyhermüller, T.; Pavlishchuk, V.V. (2002). Synthesis, Magnetochemistry, and Spectroscopy of

Heterometallic Trinuclear Basic Trifluoroacetates [$Fe_2M(\mu_3$-$O)(CF_3COO)_6(H_2O)_3]\cdot H_2O$ (M= Mn, Co, Ni). *Eur. J. Inorg. Chem.,* 2002, 3347-3355.

Ghadwal, R.S.; Singh, A. (2005). Synthesis and characterisation of heterobimetallic N-substituted diethanolaminate-alkoxides of niobium (V). *Indian J. Chem., Sect A,* 44, 2439.

Glerup, M.; Kanzow, H.; Almairac, R.; Castignolles, M.; Bernier, P. (2003). Synthesis of multi-walled carbon nanotubes and nano-fibres using the aerosol method with metal-ions as the catalyst precursors. *Chem. Phys. Lett.*, 377, 293-298.

Goebbert, D.J.; Garand, E.; Wende, T.; Bergmann, R.; Meijer, G.; Asmis, K.R.; Neumark, D.M. (2009). Infrared Spectroscopy of the Microhydrated Nitrate Ions $NO_3^-(H_2O)_{1-6}$. *J. Phys. Chem. A,* 113, 7584-7592.

Goel, M. (2004). Recent developments in electroceramics: MEMS applications for energy and environment. *Ceram. Int.,* 30, 1147-1154.

Gong, S.; Liu, J.; Quan, L.; Fu, Q.; Zhou, D. (2011). Preparation of Tin Oxide Thin Films on Silicon Substrates via SolGel Routes and the Prospects for the H_2S Gas Sensor. *Sensor Lett.,* 9, 625-628.

Grgicak, C.M.; Giorgi, J.B. (2007). Improved performance of Ni-and Co-YSZ anodes via sulfidation to NiS-and CoS-YSZ. Effects of temperature on electrokinetic parameters. *J. Phys. Chem. C,* 111, 15446-15455.

Haiduc, I.; Sowerby, D.B.; Lu, S.-F. (1995). Stereochemical aspects of phosphor-1,1-dithiolato metal complexes (dithiophosphates, dithiophosphinates): Coordination patterns, molecular structures and supramolecular associations. *Polyhedron*, 14, 3389-3472.

Hamid, M.; Tahir, A.A.; Mazhar, M.; Molloy, K.C.; Kociok-Köhn, G. (2008). Copper–cobalt heterobimetallic ceramic oxide thin film deposition: Synthesis, characterization and application of precursor. *Inorg. Chem. Commun.,* 11, 1159-1161.

Hamid, M.; Tahir, A.A.; Mazhar, M.; Zeller, M.; Hunter, A.D. (2007a). Heterobimetallic molecular cages for the deposition of Cu/Ti and Cu/Zn mixed-metal oxides. *Inorganic chemistry*, 46, 4120-4127.

Hamid, M.; Tahir, A.A.; Mazhar, M.; Zeller, M.; Hunter, A.D. (2007b). Heterobimetallic molecular cages for the deposition of Cu/Ti and Cu/Zn mixed-metal oxides. *Inorg. Chem.,* 46, 4120-4127.

Hamid, M.; Tahir, A.A.; Mazhar, M.; Zeller, M.; Molloy, K.C.; Hunter, A.D. (2006). Synthesis of isostructural cage complexes of copper with cobalt and nickel for deposition of mixed ceramic oxide materials. *Inorg. Chem.,* 45, 10457-10466.

Han, Q.; Chen, J.; Yang, X.; Lu, L.; Wang, X. (2007). Preparation of uniform Bi_2S_3 nanorods using xanthate complexes of bismuth (III). *J. Phys. Chem. C,* 111, 14072-14077.

Han, W.; Zhou, Y.; Zhang, Y.; Chen, C.-Y.; Lin, L.; Wang, X., . . . Wang, Z.L. (2012). Strain-gated piezotronic transistors based on vertical zinc oxide nanowires. *ACS nano,* 6, 3760-3766.

Hassan, I.A.; Ratnasothy, A.; Bhachu, D.S.; Sathasivam, S.; Carmalt, C.J. (2013). The Effect of Solvent on the Morphology of Indium Oxide Deposited by Aerosol-assisted Chemical Vapour Deposition. *Aust. J. Chem.,* 66, 1274-1280.

Hehemann, D.G.; Lau, J.E.; Harris, J.D.; Hoops, M.D.; Duffy, N.V.; Fanwick, P.E., . . . Hepp, A.F. (2005). Synthesis, characterization and decomposition studies of tris (N, N-dibenzyldithiocarbamato) indium (III): chemical spray deposition of polycrystalline CuInS2 on copper films. *Mater. Sci. Eng., B,* 116, 381-389.

Heimann, R.B. (2010). Introduction to Classic Ceramics. *Classic and Advanced Ceramics: From Fundamentals to Applications,* 1-10.

Hofmann, W. (1933). Strukturelle und morphologische Zusammenhänge bei Erzen vom Formeltyp ABC2. *Z. Kristallogr.,* 84, 177-178.

Hogarth, G. (2005). Transition metal dithiocarbamates: 1978–2003. *Prog. Inorg. Chem.,* 53, 71-561.

Horley, G.; White, A.P.; Williams, D. (1999). Deposition of tetragonal β-In_2S_3 thin films from tris (*N,N*-diisopropylmonothiocarbamato)indium(III), In $(SOCN^iPr_2)_3$, by low pressure metal-organic chemical vapour deposition. *J. Mater. Chem.,* 9, 1289-1292.

Horley, G.A.; Chunggaze, M.; O'Brien, P.; J. P. White, A.; J. Williams, D. (1998). The synthesis and characterisation of tris(*N,N'*-diethylmonothiocarbamato)indium(III) [$In(SOCNEt_2)_3$] and diethyl(*N,N'*-diethylmonothiocarbamato)indium(III)

[$Et_2In(SOCNEt_2)$]: potential precursors for the growth of indium sulfide by low pressure metal organic chemical vapour deposition. *J. Chem. Soc., Dalton Trans.*, 4205-4210.

Hou, X.; Choy, K.L. (2006). Processing and Applications of Aerosol-Assisted Chemical Vapor Deposition. *Chem. Vap. Deposition*, 12, 583-596.

Hubert-Pfalzgraf, L.G. (2003). Some trends in the design of homo- and heterometallic molecular precursors of high-tech oxides. *Inorg. Chem. Commun.*, 6, 102-120.

Hubert-Pfalzgraf, L.G.; Daniele, S.; Decams, J.M.; Vaissermann, J. (1997). The quest for single-source precursors for $BaTiO_3$ and $SrTiO_3$. *J. Sol-Gel Sci. Technol.*, 8, 49-53.

Hubert-Pfalzgraf, L.G.; Guillon, H. (1998). Trends in precursor design for conventional and aerosol-assisted CVD of high-T_c superconductors.

Hursthouse, M.B.; Malik, M.A.; Motevalli, M.; O'Brien, P. (1991). Mixed alkyl dialkylthiocarbamates of zinc and cadmium: potential precursors for II/VI materials. X-ray crystal structure of $[MeZnS_2CNEt_2]_2$. *Organometallics*, 10, 730-732.

Im, J.S.; Bai, B.C.; Lee, Y.-S. (2010). The effect of carbon nanotubes on drug delivery in an electro-sensitive transdermal drug delivery system. *Biomaterials*, 31, 1414-1419.

Iwashina, K.; Kudo, A. (2011). Rh-doped $SrTiO_3$ photocatalyst electrode showing cathodic photocurrent for water splitting under visible-light irradiation. *J. Am. Chem. Soc.*, 133, 13272-13275.

Jaeger, R.C. (2001). *Introduction to Microelectronic Fabrication: Volume 5 of Modular Series on Solid State Devices*.

Jiang, F.; Shen, H.; Wang, W.; Zhang, L. (2012). Preparation of SnS film by sulfurization and SnS/a-Si heterojunction solar cells. *J. Electrochem. Soc.*, 159, H235-H238.

Jo, W.-K.; Kang, H.-J. (2012). LED irradiation of a photocatalyst for benzene, toluene, ethyl benzene, and xylene decomposition. *Chinese J. Catal.*, 33, 1672-1680.

Johnson, B. (1969). K. H. Al-Obaidi, and JA McCleverty. *J. Chem. SOC.(A)*, 1668.

Johnson, B.F.G.; Klunduk, M.C.; O'Connell, T.J.; McIntosh, C.; Ridland, J. (2001). The compound $[Ti_4O_4\{OCH_2CH_2N(CH_3)_2\}_8]$ containing the new Ti_4O_4 cluster core. *J. Chem. Soc., Dalton Trans.*, 1553-1555.

Johnston, D.; Carletto, M.; Reddy, K.; Forbes, I.; Miles, R. (2002). Chemical bath deposition of zinc sulfide based buffer layers using low toxicity materials. *Thin Solid Films,* 403, 102-106.

Jones, A.C.; Hitchman, M.L. (2009). Overview of Chemical Vapour Deposition. *Chem. Vap. Deposition*, 1-36.

Kana, A.; Hibbert, T.; Mahon, M.; Molloy, K.; Parkin, I.; Price, L. (2001). Organotin unsymmetric dithiocarbamates: synthesis, formation and characterisation of tin (II) sulfide films by atmospheric pressure chemical vapour deposition. *Polyhedron,* 20, 2989-2995.

Kao, K.C. (2004). *Dielectric phenomena in solids*: Academic press.

Karami, H.; Babaei, S. (2013). Application of Tin Sulfide-Tin Dioxide Nanocomposite as Oxygen Gas-Sensing Agent. *Int. J. Electrochem. Sci.,* 8.

Karkhanavala, M. (1958). ICDD powder diffraction database file card number [00-009-0182]. Atomic Energy Establishment, Bombay, India: Private Communication.

Keppens, V. (2013). Structural transitions:'Ferroelectricity'in a metal. *Nat. Mater.,* 12, 952-953.

Kessler, V.G.; Gohil, S.; Parola, S. (2003). Interaction of some divalent metal acetylacetonates with Al, Ti, Nb and Ta isopropoxides. Factors influencing the formation and stability of heterometallic alkoxide complexes. *Dalton Trans.*, 544-550.

Kessler, V.G.; Hubert-Pfalzgraf, L.G.; Daniele, S.; Gleizes, A. (1994). Single-source Precursors for $BaTiO_3$: Synthesis and Characterization of β-Diketonato Alkoxides and Molecular Structure of $Ba_2Ti_2(thd)_4(\mu_3\text{-}OEt)_2(\mu\text{-}OEt)_4(OEt)_2(EtOH)_2$. *Chem. Mater.,* 6, 2336-2342.

Khaleel, A. (2009). Sol–gel synthesis, characterization, and catalytic activity of Fe (III) titanates. *Colloids Surf., A,* 346, 130-137.

Khalil, K.A. (2012). Advanced Sintering of Nano-Ceramic Materials. .

Kim, K.M.; Song, S.J.; Kim, G.H.; Seok, J.Y.; Lee, M.H.; Yoon, J.H., . . . Hwang, C.S. (2011). Collective motion of conducting filaments in Pt/n-type TiO2/p-type NiO/Pt stacked resistance switching memory. *Adv. Funct. Mater.*, 21, 1587-1592.

Kind, H.; Yan, H.; Messer, B.; Law, M.; Yang, P. (2002). Nanowire Ultraviolet Photodetectors and Optical Switches. *Adv. Mater.*, 14, 158-160.

King, G. (1962). The space group of-In_2S_3. *Acta Crystallog.*, 15, 512-512.

Klug, H. (1966). The crystal structure of zinc dimethyldithiocarbamate. *Acta Crystallographica*, 21, 536-546.

Knapp, C.E.; Prassides, I.D.; Sathasivam, S.; Parkin, I.P.; Carmalt, C.J. (2014). Aerosol-Assisted Chemical Vapour Deposition of a Copper Gallium Oxide Spinel. *ChemPlusChem*, 79, 122-127.

Kodas, T.T.; Hampden-Smith, M.J. (2008). *The chemistry of metal CVD*: John Wiley & Sons.

Kodas, T.T., Hampden-Smith, M. J. (1994). *The Chemistry of Metal CVD*: VCH Weinheim.

Koh, Y.W.; Lai, C.S.; Du, A.Y.; Tiekink, E.R.; Loh, K.P. (2003). Growth of bismuth sulfide nanowire using bismuth trisxanthate single source precursors. *Chem. Mater.*, 15, 4544-4554.

Konstantatos, G.; Levina, L.; Tang, J.; Sargent, E.H. (2008). Sensitive Solution-Processed Bi_2S_3 Nanocrystalline Photodetectors. *Nano Lett.*, 8, 4002-4006.

Krishna, H.; Kalyanaraman, R. (2008). Functional Nanostructured Thin Films *Functional Nanostructures* (pp. 65-106): Springer.

Krishnan, K.; Powell, J.R.; Hill, S.L. (1995). Infrared microimaging. *PRACTICAL SPECTROSCOPY SERIES*, 19, 85-85.

Kudo, A.; Miseki, Y. (2009). Heterogeneous photocatalyst materials for water splitting. *Chem. Soc. Rev.*, 38, 253-278.

Kumar, R. (2014). Synthesis, spectral, and thermoanalytical studies on the new heterobimetallic [Mg(II)-Ti(IV)]-μ-oxoisopropoxide and its β-diketonates. *Turk. J. Chem.*, 38, 41-49.

Kunze, K.; Bihry, L.; Atanasova, P.; Hampden-Smith, M.J.; Duesler, E.N. (1996). Synthesis and characterization of polyether adducts of group 2 metal thioacetates: Single-source precursors to binary metal sulfide films, MS, where M = Ca, Sr, Ba

Chem. Vap. Deposition, 2, 105-108.

Lai, C.-H.; Huang, K.-W.; Cheng, J.-H.; Lee, C.-Y.; Hwang, B.-J.; Chen, L.-J. (2010). Direct growth of high-rate capability and high capacity copper sulfide nanowire array cathodes for lithium-ion batteries. *J. Mater. Chem.*, 20, 6638-6645.

Lai, C.-H.; Huang, K.-W.; Cheng, J.-H.; Lee, C.-Y.; Lee, W.-F.; Huang, C.-T., . . . Chen, L.-J. (2009). Oriented growth of large-scale nickel sulfide nanowire arrays via a general solution route for lithium-ion battery cathode applications. *J. Mater. Chem.*, 19, 7277-7283.

Lai, C.-H.; Lu, M.-Y.; Chen, L.-J. (2012). Metal sulfide nanostructures: synthesis, properties and applications in energy conversion and storage. *J. Mater. Chem.*, 22, 19-30.

Lang, S.B. (2005). Pyroelectricity: from ancient curiosity to modern imaging tool. *Physics Today*, 58, 31-36.

Lazell, M.; O'Brien, P.; Otway, D.J.; Park, J.-H. (2000). Single source molecular precursors for the deposition of III/VI chalcogenide semiconductors by MOCVD and related techniques. *J. Chem. Soc., Dalton Trans.*, 4479-4486.

Lazell, M.R.; O'Brien, P.; Otway, D.J.; Park, J.-H. (1999). Deposition of thin films of gallium sulfide from a novel single-source precursor, $Ga(S_2CNMeHex)_3$, by low-pressure metal-organic chemical vapor deposition. *Chem. Mater.*, 11, 3430-3432.

Lee, G.-H.; Park, J.-G.; Sung, Y.-M.; Chung, K.Y.; Cho, W.I.; Kim, D.-W. (2009). Enhanced cycling performance of an Fe^0/Fe_3O_4 nanocomposite electrode for lithium-ion batteries. *Nanotechnology*, 20, 295205.

Lee, J.; Lee, S.; Cho, S.; Kim, S.; Park, I.Y.; Choi, Y.D. (2003). Role of growth parameters on structural and optical properties of ZnS nanocluster thin films grown by solution growth technique. *Mater. Chem. Phys.*, 77, 254-260.

Li, L.; Cao, R.; Wang, Z.; Li, J.; Qi, L. (2009). Template Synthesis of Hierarchical Bi_2E_3 (E = S, Se, Te) Core−Shell Microspheres and Their Electrochemical and Photoresponsive Properties. *J. Phys. Chem. C*, 113, 18075-18081.

Li, L.; Wu, P.; Fang, X.; Zhai, T.; Dai, L.; Liao, M., . . . Golberg, D. (2010). Single-Crystalline CdS Nanobelts for Excellent Field-Emitters and Ultrahigh Quantum-Efficiency Photodetectors. *Adv. Mater.*, 22, 3161-3165.

Li, Q.; Guo, B.; Yu, J.; Ran, J.; Zhang, B.; Yan, H.; Gong, J.R. (2011). Highly efficient visible-light-driven photocatalytic hydrogen production of CdS-cluster-decorated graphene nanosheets. *J. Am. Chem. Soc.*, 133, 10878-10884.

Li, X.; Shen, H.; Li, S.; Niu, J.Z.; Wang, H.; Li, L.S. (2010). Investigation on type-II Cu_2S-CdS core/shell nanocrystals: synthesis and characterization. *J. Mater. Chem.*, 20, 923-928.

Lindmark, A.F.; Fay, R.C. (1983). Kinetics of hindered rotation about carbon-nitrogen single bonds in some N, N-diisopropyldithiocarbamates. *Inorg. Chem.*, 22, 2000-2006.

Liu, J.; Guo, Z.; Zhu, K.; Wang, W.; Zhang, C.; Chen, X. (2011). Highly porous metal oxide polycrystalline nanowire films with superior performance in gas sensors. *J. Mater. Chem.*, 21, 11412-11417.

MacInnes, A.N.; Power, M.B.; Barron, A.R. (1992). Chemical vapor deposition of cubic gallium sulfide thin films: a new metastable phase. *Chem. Mater.*, 4, 11-14.

MacInnes, A.N.; Power, M.B.; Barron, A.R. (1993). Chemical vapor deposition of gallium sulfide: phase control by molecular design. *Chem. Mater.*, 5, 1344-1351.

Malik, M.A.; Afzaal, M.; O'Brien, P. (2010). Precursor chemistry for main group elements in semiconducting materials. *Chem. Rev.*, 110, 4417-4446.

Malik, M.A.; Motevalli, M.; Walsh, J.R.; O'Brien, P. (1992). Neopentyl-or tert-butylzinc complexes with diethylthio-or diethylselenocarbamates: precursors for zinc chalcogens. *Organometallics*, 11, 3136-3139.

Malik, M.A.; O'BRIEN, P.; Revaprasadu, N. (2002). Synthesis of TOPO-capped PtS and PdS nanoparticles from [Pt $(S_2CNMe\ (Hex))_2$] and [$Pd(S_2CNMe(Hex))_2$]. *J. Mater. Chem.*, 12, 92-97.

Mane, R.; Desai, J.; Joo, O.-S.; Han, S.-H. (2007). Surface Morphology and Optical Studies of Non-aqueous Bi_2S_3 Thin Films. *Int. J. Electrochem. Sci*, 2, 141-148.

Mane, R.; Lokhande, C. (2000). Chemical deposition method for metal chalcogenide thin films. *Mater. Chem. Phys.*, 65, 1-31.

Mane, R.; Sankapal, B.; Lokhande, C. (1999). Photoelectrochemical (PEC) characterization of chemically deposited Bi_2S_3 thin films from non-aqueous medium. *Mater. Chem. Phys.,* 60, 158-162.

Mansoor, M.A.; Ehsan, M.A.; McKee, V.; Huang, N.-M.; Ebadi, M.; Arifin, Z., . . . Mazhar, M. (2013). Hexagonal structured $Zn_{1-x}Cd_xO$ solid solution thin films: synthesis, characterization and applications in photoelectrochemical water splitting. *J. Mater. Chem. A,* 1, 5284-5292.

Mansoor, M.A.; Ismail, A.; Yahya, R.; Arifin, Z.; Tiekink, E.R.T.; Weng, N.S., . . . Esmaeili, A.R. (2013). Perovskite-structured $PbTiO_3$ thin films grown from a single-source precursor. *Inorg. Chem.,* 52, 5624-5626.

Marchand, P.; Carmalt, C.J. (2013). Molecular precursor approach to metal oxide and pnictide thin films. *Coord. Chem. Rev.,* 257, 3202-3221.

Marchand, P.; Hassan, I.A.; Parkin, I.P.; Carmalt, C.J. (2013). Aerosol-assisted delivery of precursors for chemical vapour deposition: expanding the scope of CVD for materials fabrication. *Dalton Trans.,* 42, 9406-9422.

Marchetti, F.; Marchetti, F.; Melai, B.; Pampaloni, G.; Zacchini, S. (2007). Synthesis and Reactivity of Haloacetato Derivatives of Iron (II) Including the Crystal and the Molecular Structure of $[Fe(CF_3COOH)_2\ (\mu\text{-}CF_3COO)_2]_n$. *Inorg. Chem.,* 46, 3378-3384.

Marder., M.P. (2000). *Condensed Matter Physics*: John Wiley & Sons New York.

Mathur, S.; Shen, H.; Altmayer, J. (2007). Nanostructured functional ceramic coatings by molecule-based chemical vapor deposition. *Rev. Adv. Mater. Sci,* 15, 16-23.

Mathur, S.; Veith, M.; Haas, M.; Shen, H.; Lecerf, N.; Huch, V., . . . Jilavi, M. (2001). Single-Source Sol-Gel Synthesis of Nanocrystalline $ZnAl_2O_4$: Structural and Optical Properties. *J. Am. Ceram. Soc.,* 84, 1921-1928.

Mathur, S.; Veith, M.; Rapalaviciute, R.; Shen, H.; Goya, G.F.; Martins Filho, W.L.; Berquo, T.S. (2004). Molecule derived synthesis of nanocrystalline $YFeO_3$ and investigations on its weak ferromagnetic behavior. *Chem. Mater.,* 16, 1906-1913.

Mattox, D.M. (2010). *Handbook of physical vapor deposition (PVD) processing*: William Andrew.

McAleese, J.; O′Brien, P.; Otway, D.J. (1998). A Novel Simple Process for the Deposition of Thin Films of $CuInSe_2$ by MOCVD. *Chem. Vap. Deposition,* 4, 94-96.

McElwee-White, L. (2006). Design of precursors for the CVD of inorganic thin films. *Dalton Trans.*, 5327, 5333.

McElwee-White, L.; Koller, J.; Kim, D.; Anderson, T.J. (2009). Mechanism-Based Design of Precursors for MOCVD. *ECS Transactions*, 25, 161-171.

Mehrotra, R.C.; Singh, A.; Sogani, S. (1994). Recent advances in the chemistry of homo-and heterometallic alkoxides of p-block metal (loid) s. *Chem. Rev.*, 94, 1643-1660.

Menezes, D.; De Lima, G.; Porto, A.; Donnici, C.; Ardisson, J.; Doriguetto, A.; Ellena, J. (2004). Synthesis, characterisation and thermal decomposition of tin (IV) dithiocarbamate derivatives–single source precursors for tin sulfide powders. *Polyhedron*, 23, 2103-2109.

Milosevic, O.; Mancic, L.; Rabanal, M.; Gomez, L.; Marinkovic, K. (2009). Aerosol route in processing of nanostructured functional materials. *KONA*, 27, 84-107.

Miyamae, H.; Ito, M.; Iwasaki, H. (1979). The structure of zinc (II) N, N-diisopropyldithiocarbamate {bis [-(N,N-diisopropyldithiocarbamato)--S, S']-bis (N, N-diisopropyldithiocarbamato) dizinc (II)}. *Acta Crystallogr. Sect. B*, 35, 1480-1482.

Mohapatra, S.K.; John, S.E.; Banerjee, S.; Misra, M. (2009). Water photooxidation by smooth and ultrathin α-Fe_2O_3 nanotube arrays. *Chem. Mater.*, 21, 3048-3055.

Monteiro, O.C.; Nogueira, H.I.; Trindade, T.; Motevalli, M. (2001). Use of dialkyldithiocarbamato complexes of bismuth (III) for the preparation of nano-and microsized Bi_2S_3 particles and the X-ray crystal structures of [Bi{$S_2CN(CH_3)(C_6H_{13})$}$_3$] and [Bi{$S_2CN(CH_3(C_6H_{13})$}$_3$($C_{12}H_8N_2$)]. *Chem. Mater.*, 13, 2103-2111.

Monteiro, O.C.; Trindade, T.; Park, J.H.; O'Brien, P. (2000). The Use of Bismuth (III) Dithiocarbamato Complexes as Precursors for the Low-Pressure MOCVD of Bi_2S_3. *Chem. Vap. Deposition*, 6, 230-232.

Moon, K.-J.; Lee, T.-I.; Choi, J.-H.; Jeon, J.; Kang, Y.H.; Kar, J.P., . . . Myoung, J.-M. (2010). One-dimensional semiconductor nanostructure based thin-film partial composite formed by transfer implantation for high-performance flexible and printable electronics at low temperature. *ACS nano*, 5, 159-164.

Morrell, R. (2011). Ceramics, Structural *Kirk-Othmer Encyclopedia of Chemical Technology*: John Wiley & Sons, Inc.

Motevalli, M.; O'Brien, P.; Walsh, J.R.; Watson, I.M. (1996). Synthesis, characterization and x-ray crystal structures of asymmetric bis (dialkyldithiocarbamates) of zinc: Potential precursors for ZnS deposition. *Polyhedron*, 15, 2801-2808.

Nagasuna, K.; Akita, T.; Fujishima, M.; Tada, H. (2011). Photodeposition of Ag_2S Quantum Dots and Application to Photoelectrochemical Cells for Hydrogen Production under Simulated Sunlight. *Langmuir*, 27, 7294-7300.

Nakamura, T.; Shan, Y.J.; Sun, P.-H.; Inaguma, Y.; Itoh, M. (1998). The cause of high-temperature quantum paraelectricity in some perovskite titanates. *Solid state ionics*, 108, 53-58.

Nalwa, H.S. (2000). *Handbook of advanced electronic and photonic materials and devices* (Vol. 1): Academic Press.

Nalwa, H.S. (2002). *Handbook of thin film materials*: Academic Press.

Navío, J.A.; Colón, G.; Macías, M.; Real, C.; Litter, M.I. (1999). Iron-doped titania semiconductor powders prepared by a sol–gel method. Part I: synthesis and characterization. *Appl. Catal., A*, 177, 111-120.

Nawar, N.; Hosny, N.M. (2000). Synthesis, spectral and antimicrobial activity studies of o-aminoacetophenone o-hydroxybenzoylhydrazone complexes. *Transition Met. Chem.*, 25, 1-8.

Newnham, R.; Fang, J.; Santoro, R. (1964). Crystal structure and magnetic properties of $CoTiO_3$. *Acta Cryst.*, 17, 240-242.

Nikitinskii, A.; Bochkarev, L.; Voronin, R.; Khorshev, S.Y.; Kurskii, Y.A.; Bochkarev, M. (2004). Synthesis of heterobimetallic zinc complexes and their catalytic properties in reactions of CO_2 with cyclohexene oxide. *Russ. J. Gen. Chem.*, 74, 1194-1196.

Nomura, R.; Inazawa, S.j.; Kanaya, K.; Matsuda, H. (1989). Thermal decomposition of butylindium thiolates and preparation of indium sulfide powders. *Appl. Organomet. Chem.*, 3, 195-197.

Nomura, R.; Konishi, K.; Matsuda, H. (1991). Single-source organometallic chemical vapour deposition process for sulphide thin films: Introduction of a new

organometallic precursor $Bu^{n}In(SPr^{i})$ and preparation of In_2S_3 thin films *Thin Solid Films,* 198, 339-345.

Nomura, R.; Miyawaki, K.; Toyosaki, T.; Matsuda, H. (1996). Preparation of copper sulfide thin layers by a single-source MOCVD process. *Chem. Vap. Deposition,* 2, 174-179.

Nomura, R.; Murai, T.; Toyosaki, T.; Matsuda, H. (1995). Single-source MOVPE growth of zinc sulfide thin films using zinc dithiocarbamate complexes. *Thin Solid Films,* 271, 4-7.

Nomura, S.; Tomaya, K.; Kaneta, K. (1983). Effect of Mn doping on the dielectric properties of $Ba_2Ti_9O_{20}$ ceramics at microwave frequency. *Jpn. J. Appl. Phys,* 22, 1125.

Nyman, M.; Hampden-Smith, M.J.; Duesler, E.N. (1996). Low temperature, aerosol-assisted chemical vapor deposition (AACVD) of CdS, ZnS, and $Cd_{1-x}Zn_xS$ using monomeric single-source precursors: $M(SOCCH_3)_2TMEDA$. *Chem. Vap. Deposition,* 2, 171-174.

Nyman, M.; Jenkins, K.; Hampden-Smith, M.; Kodas, T.; Duesler, E.; Rheingold, A.; Liable-Sands, M. (1998). Feed-Rate-Limited Aerosol-Assisted Chemical Vapor Deposition of $Cd_xZn_{1-x}S$ and ZnS: Mn with Composition Control. *Chem. Mater.,* 10, 914-921.

O'Brien, P.; Malik, M.; Chunggaze, M.; Trindade, T.; Walsh, J.; Jones, A. (1997). Precursor chemistry: remaining challenges and some novel approaches. *J. Cryst. Growth,* 170, 23-29.

O'Brien, P.; Otway, D.J.; Park, J.-H. (1999). *Iron Sulfide (FeS_2) Thin Films From Single-Source Precursors by Aerosol-Assisted Chemical Vapor Deposition (AACVD).* Paper presented at the MRS Proceedings.

O'Brien, P.; Otway, D.J.; Walsh, J.R. (1998a). Novel precursors for the growth of α-In_2S_3: trisdialkyldithiocarbamates of indium. *Thin Solid Films,* 315, 57-61.

O'Brien, P.; Otway, D.J.; Walsh, J.R. (1998b). Novel precursors for the growth of α-In_2S_3: trisdialkyldithiocarbamates of indium

Thin Solid Films, 315, 57-61.

O'Brien, P.; Walsh, J.; Watson, I.; Hart, L.; Silva, S. (1996). Properties of cadmium sulphide films grown by single-source metalorganic chemical vapour deposition with dithiocarbamate precursors. *J. Cryst. Growth,* 167, 133-142.

O'Brien, P.; Waters, J. (2006). Deposition of Ni and Pd Sulfide Thin Films via Aerosol-Assisted CVD. *Chem. Vap. Deposition,* 12, 620-626.

Oliveira, M.M.; Pessoa, G.M.; Carvalho, L.C.; Peppe, C.; Souza, A.G.; Airoldi, C. (1999). *N,N'*-Dialkyldithiocarbamate chelates of indium (III): alternative synthetic routes and thermodynamics characterization. *Thermochim. Acta*, 328, 223-230.

Omeiri, S.; Hadjarab, B.; Trari, M. (2011). Photoelectrochemical properties of anodic silver sulphide thin films. *Thin Solid Films,* 519, 4277-4281.

Osterloh, F.E. (2013). Inorganic nanostructures for photoelectrochemical and photocatalytic water splitting. *Chem. Soc. Rev.,* 42, 2294-2320.

Oyetunde, D.; Afzaal, M.; Vincent, M.A.; Hillier, I.H.; O'Brien, P. (2011). Cadmium sulfide and cadmium phosphide thin films from a single cadmium compound. *Inorg. Chem.,* 50, 2052-2054.

Panneerselvam, A.; Malik, M.A.; O'Brien, P.; Raftery, J. (2008). The CVD of silver sulfide and silver thin films from a homoleptic crystalline single-source precursor. *Journal of Materials Chemistry,* 18, 3264-3269.

Parish, R.V.; Howe, B.P.; Wright, J.P.; Mack, J.; Pritchard, R.G.; Buckley, R.G., . . . Fricker, S.P. (1996). Chemical and biological studies of dichloro (2-((dimethylamino) methyl) phenyl) gold (III). *Inorg. Chem.,* 35, 1659-1666.

Park, J.S.; Maeng, W.-J.; Kim, H.-S.; Park, J.-S. (2012). Review of recent developments in amorphous oxide semiconductor thin-film transistor devices. *Thin Solid Films,* 520, 1679-1693.

Pathan, H.; Salunkhe, P.; Sankapal, B.; Lokhande, C. (2001). Photoelectrochemical investigation of Ag_2S thin films deposited by SILAR method. *Mater. Chem. Phys.,* 72, 105-108.

Pearce, C.I.; Pattrick, R.A.; Vaughan, D.J. (2006). Electrical and magnetic properties of sulfides. *Rev. Mineral Geochem.,* 61, 127-180.

Pearton, S.; Heo, W.; Ivill, M.; Norton, D.; Steiner, T. (2004). Dilute magnetic semiconducting oxides. *Semicond. Sci. Technol.,* 19, R59.

Pejova, B.; Grozdanov, I. (2006). Structural and optical properties of chemically deposited thin films of quantum-sized bismuth (III) sulfide. *Mater. Chem. Phys.*, 99, 39-49.

Peng, X.S.; Meng, G.W.; Zhang, J.; Zhao, L.X.; Wang, X.F.; Wang, Y.W.; Zhang, L.D. (2001). Electrochemical fabrication of ordered Bi_2S_3 nanowire arrays. *J. Phys. D: Appl. Phys.*, 34, 3224.

Phani, A.R.; Ruggieri, F.; Passacantando, M.; Santucci, S. (2008). Low temperature growth of nanocrystalline Fe_2TiO_5 perovskite thin films by sol–gel process assisted by microwave irradiation. *Ceram. Int.*, 34, 205-211.

Pickett, N.L.; O'Brien, P. (2001). Syntheses of semiconductor nanoparticles using single-molecular precursors. *Chem. Rec.*, 1, 467-479.

Pike, R.; Cui, H.; Kershaw, R.; Dwight, K.; Wold, A.; Blanton, T., . . . Gysling, H. (1993). Preparation of zinc sulfide thin films by ultrasonic spray pyrolsis from bis (diethyldithiocarbamato) zinc (II). *Thin Solid Films*, 224, 221-226.

Popov, S.G.; Levitskii, V.A. (1981). Thermodynamics of double oxides. II. Study of the $CoO\text{-}TiO_2$ system by the emf method. *J. Solid State Chem.*, 38, 1-9.

Prabhune, V.; Shinde, N.; Fulari, V. (2008). Studies on electrodeposited silver sulphide thin films by double exposure holographic interferometry. *Appl. Surf. Sci.*, 255, 1819-1823.

Price, L.S.; Parkin, I.P.; Field, M.N.; Hardy, A.M.E.; Clark, R.J.H.; Hibbert, T.G.; Molloy, K.C. (2000). Atmospheric pressure chemical vapour deposition of tin(II) sulfide films on glass substrates from $^{n}Bu_3SnO_2CCF_3$ with hydrogen sulfide. *J. Mater. Chem.*, 10, 527-530.

Prime, R.B.; Bair, H.E.; Vyazovkin, S.; Gallagher, P.K.; Riga, A. (2009). Thermogravimetric analysis (TGA). *Thermal Analysis of Polymers, Fundamentals and Applications*, 241-317.

Qiu, W.; Xu, M.; Yang, X.; Chen, F.; Nan, Y.; Zhang, J., . . . Chen, H. (2011). Biomolecule-assisted hydrothermal synthesis of In_2S_3 porous films and enhanced photocatalytic properties. *J. Mater. Chem.*, 21, 13327-13333.

R.M. Silverstein, G.C.B. (1963). *Spectrometric Identification of Organic Compounds*. London-New York: John Wiley and Sons.

Rabe, K.M. (2013). Antiferroelectricity in oxides: a reexamination. *Functional Metal Oxides: New Science and Novel Applications*, 221-244.

Rahaman, M.N. (2003). *Ceramic Processing and Sintering*: CRC Press.

Rahaman, M.N. (2006). *Ceramic processing*: CRC Press.

Ramasamy, K.; Kuznetsov, V.L.; Gopal, K.; Malik, M.A.; Raftery, J.; Edwards, P.P.; O'Brien, P. (2013). Organotin Dithiocarbamates: Single-Source Precursors for Tin Sulfide Thin Films by Aerosol-Assisted Chemical Vapor Deposition (AACVD). *Chem. Mater.*, 25, 266-276.

Ramasamy, K.; Malik, M.A.; Helliwell, M.; Raftery, J.; O'Brien, P. (2011). Thio-and Dithio-Biuret Precursors for Zinc Sulfide, Cadmium Sulfide, and Zinc Cadmium Sulfide Thin Films. *Chem. Mater.*, 23, 1471-1481.

Ramasamy, K.; Malik, M.A.; Helliwell, M.; Tuna, F.; O'Brien, P. (2010). Iron thiobiurets: single-source precursors for iron sulfide thin films. *Inorg. Chem.*, 49, 8495-8503.

Ramasamy, K.; Malik, M.A.; Raftery, J.; Tuna, F.; O'Brien, P. (2010). Selective deposition of cobalt sulfide nanostructured thin films from single-source precursors. *Chemistry of materials*, 22, 4919-4930.

Ramesh, R.; Aggarwal, S.; Auciello, O. (2001). Science and technology of ferroelectric films and heterostructures for non-volatile ferroelectric memories. *Mater. Sci. Eng., R*, 32, 191-236.

Ramesh, R.; Spaldin, N.A. (2007). Multiferroics: progress and prospects in thin films. *Nature Mater.*, 6, 21-29.

Raston, C.L.; White, A.H. (1976). Crystal structures of tris(diethyldithiocarbamato)-antimony(III) and -bismuth(III). *J. Chem. Soc., Dalton Trans.*, 791-794.

Reber, J.F.; Rusek, M. (1986). Photochemical hydrogen production with platinized suspensions of cadmium sulfide and cadmium zinc sulfide modified by silver sulfide. *J. Phys. Chem.*, 90, 824-834.

Riedel, R.; Ionescu, E.; Chen, I.-W. (2011). Modern trends in advanced ceramics. *Ceramics science and technology*, 1, 3-38.

Riley, D.J.; Waggett, J.P.; Wijayantha, K.G.U. (2004). Colloidal bismuth sulfide nanoparticles: a photoelectrochemical study of the relationship between bandgap and particle size. *J. Mater. Chem.,* 14, 704-708.

Riley, F. (2009). Structural Ceramics: Cambridge Univ. Press, Cambridge.

Rohrer, G.S.; Affatigato, M.; Backhaus, M.; Bordia, R.K.; Chan, H.M.; Curtarolo, S., . . . Garay, J.E. (2012). Challenges in Ceramic Science: A Report from the Workshop on Emerging Research Areas in Ceramic Science. *J. Am. Ceram. Soc.,* 95, 3699-3712.

Rumyantsev, Y.M.; Fainer, N.; Kosinova, M.; Ayupov, B.; Sysoeva, N. (1999). RPECVD thin cadmium, copper and zinc sulphide films. *Le Journal de Physique IV,* 9, Pr8-777-Pr778-784.

Saha, S.; Das, S.; Ghorai, U.K.; Mazumder, N.; Gupta, B.K.; Chattopadhyay, K.K. (2013). Charge compensation assisted enhanced photoluminescence derived from Li-codoped $MgAl_2O_4$:Eu^{3+} nanophosphors for solid state lighting applications. *Dalton Trans.,* 42, 12965-12974.

Sahraei, R.; Shahriyar, S.; Ara, M.M.; Daneshfar, A.; Shokri, N. (2010). Preparation of Nanocrystalline CdS Thin Films by a New Chemical Bath Deposition Route for Application in Solar Cells as Antireflection Coatings. *Prog. Color Colorants Coat.*

Sartale, S.; Sankapal, B.; Lux-Steiner, M.; Ennaoui, A. (2005). Preparation of nanocrystalline ZnS by a new chemical bath deposition route. *Thin Solid Films,* 480, 168-172.

Scheldrick, G. (2008). A short history of SHELX. *Acta Cryst. A,* 64, 112-122.

Schuerman, J.A.; Fronczek, F.R.; Selbin, J. (1989). New silver cluster compounds containing dithiobenzoate ligands. *Inorg. Chim. Acta,* 160, 43-52.

Scott, S.; Barnes, H. (1972). Sphalerite-wurtzite equilibria and stoichiometry. *Geochim. Cosmochim. Acta,* 36, 1275-1295.

Sebald, G.; Lefeuvre, E.; Guyomar, D. (2008). Pyroelectric energy conversion: optimization principles. *Ultrasonics, Ferroelectrics and Frequency Control, IEEE Transactions on,* 55, 538-551.

Seisenbaeva, G.A.; Gohil, S.; Kessler, V.G. (2004). Molecular structure design approach to perspective single-source precursors of titanate materials. Synthesis, X-

ray single crystal and mass-spectrometric study of $M_2Ti_2(acac)_4(OMe)_8$, M=Mg, Co. *Inorg. Chem. Commun.*, 7, 18-20.

Sen, S.; Kanitkar, P.; Sharma, A.; Muthe, K.; Rath, A.; Deshpande, S., . . . Yakhmi, J. (2010). Growth of $SnO_2/W_{18}O_{49}$ nanowire hierarchical heterostructure and their application as chemical sensor. *Sens. Actuators B Chem.*, 147, 453-460.

Senocq, F.; Viguier, N.; Gleizes, A. (1996). Bis (η^5-cyclopentadienyl)bis(thiolato)titanium(IV) and zirconium(IV): synthesis and crystal structure of $Cp_2M(S^tBu)_2$ (M = Ti, Zr). Use of $Cp_2Ti(S^tBu)_2$ and $Cp_2Ti(SEt)_2$ as single source precursors for the chemical vapour deposition of titanium sulfides. *Eur. J. Solid State Inorg. Chem.*, 33, 1185-1197.

Setter, N.; Damjanovic, D.; Eng, L.; Fox, G.; Gevorgian, S.; Hong, S., . . . Stephenson, G. (2006). Ferroelectric thin films: Review of materials, properties, and applications. *J. Appl. Phys.*, 100, 051606.

Shahid, M.; Mazhar, M.; Hamid, M.; Zeller, M.; O'Brien, P.; Malik, M.A., . . . Hunter, A.D. (2009). Isostructural cage complexes of copper with cadmium or zinc for single source deposition of composite materials. *New J. Chem.*, 33, 2241-2247.

Shang, G.; Hampden-Smith, M.J.; Duesler, E.N. (1996). Synthesis and characterization of gallium thiocarboxylates as novel single-source precursors to gallium sulfide thin films by aerosol-assisted CVD. *Chem. Commun.*, 1733-1734.

Shang, G.; Kunze, K.; Hampden-Smith, M.J.; Duesler, E.N. (1996). Low-temperature chemical vapor deposition of indium sulfide thin films using a novel single-source indium thiocarboxylate compound as precursor. *Chem. Vap. Deposition*, 2, 242-244.

Shannon, R. (1976). Revised effective ionic radii and systematic studies of interatomic distances in halides and chalcogenides. *Acta Crystallogr. Sect. A*, 32, 751-767.

Sharma, A.K. (1986). Thermal behaviour of metal-dithiocarbamates. *Thermochim. Acta*, 104, 339-372.

Sheldrick, G. (2004). SADABS version 2004/1. *A Program for Empirical Absorption Correction, University of Göttingen, Göttingen, Germany*.

Shen, S.; Mao, S.S. (2012). Nanostructure designs for effective solar-to-hydrogen conversion. *Nanophotonics*, 1, 31-50.

Shen, S.; Shi, J.; Guo, P.; Guo, L. (2011). Visible-light-driven photocatalytic water splitting on nanostructured semiconducting materials. *Int. J. of Nanotechnol.,* 8, 523-591.

Shen, X.-P.; Yin, G.; Zhang, W.-L.; Xu, Z. (2006). Synthesis and characterization of Bi_2S_3 faceted nanotube bundles. *Solid State Commun.,* 140, 116-119.

Shi, L.; Naik, A.J.; Goodall, J.B.; Tighe, C.; Gruar, R.; Binions, R., . . . Darr, J. (2013). Highly Sensitive ZnO Nanorod-and Nanoprism-Based NO_2 Gas Sensors: Size and Shape Control Using a Continuous Hydrothermal Pilot Plant. *Langmuir,* 29, 10603-10609.

Singh, J. (2006). *Optical properties of condensed matter and applications* (Vol. 6): John Wiley & Sons.

Singhal, A.; Dutta, D.P.; Tyagi, A.K.; Mobin, S.M.; Mathur, P.; Lieberwirth, I. (2007). Palladium (II)/allylpalladium (II) complexes with xanthate ligands: Single-source precursors for the generation of palladium sulfide nanocrystals. *J. Organomet. Chem.,* 692, 5285-5294.

Sirimanne, P.M.; Shiozaki, S.; Sonoyama, N.; Sakata, T. (2000). Photoelectrochemical behavior of In_2S_3 formed on sintered In_2O_3 pellets. *Sol. Energy Mater. Sol. Cells,* 62, 247-258.

Smet, P.F.; Moreels, I.; Hens, Z.; Poelman, D. (2010). Luminescence in sulfides: a rich history and a bright future. *Materials,* 3, 2834-2883.

Spek, A. (2003). Single-crystal structure validation with the program PLATON. *J. Appl. Crystallogr.,* 36, 7-13.

Spek, A. (2010). PLATON; The University of Utrecht: Utrecht, The Netherlands, 1999. *There is no corresponding record for this reference*.

Srinivasan, N.; Thirumaran, S.; Ciattini, S. (2009). Effect of phenyl and benzyl group in heterocyclic dithiocarbamates on the ZnS_4N chromophore: Synthesis, spectral, valence-bond parameters and single crystal X-ray structural studies on (pyridine)bis(1,2,3,4-tetrahydroquinolinedithiocarbamato)zinc(II) and (pyridine)bis(1,2,3,4-tetrahydroisoquinolinedithiocarbamato)zinc(II). *J. Mol. Struct.,* 921, 63-67.

Srouji, F.; Afzaal, M.; Waters, J.; O'Brien, P. (2005). Single-Source Routes to Cobalt Sulfide and Manganese Sulfide Thin Films. *Chem. Vap. Deposition,* 11, 91-94.

Štengl, V.; Opluštil, F.; Němec, T. (2012). In^{3+}-doped TiO_2 and TiO_2/In_2S_3 Nanocomposite for Photocatalytic and Stoichiometric Degradations. *Photochem. Photobiol.,* 88, 265-276.

Su, W.; Hong, M.; Weng, J.; Liang, Y.; Zhao, Y.; Cao, R., . . . Chan, A.S.C. (2002). Tunable polymerization of silver complexes with organosulfur ligand: counterions effect, solvent- and temperature-dependence in the formation of silver(I)-thiolate(and/or thione) complexes. *Inorg. Chim. Acta*, 331, 8-15.

Sukkha, U.; Vittayakorn, N.; Bhalla, A.; Guo, R. (2014). Phase transition behavior of $Ba(Mg_{1/3}Nb_{2/3})O_3$ modified $PbZrO_3$ solid solution. *J. Mater. Chem. C.*

Swanson, T., J.C. Fel. (1950). ICDD

powder diffraction database file card number [00-004-0551]: Reports, NBS, Private Communication.

Szafert, S.; John, Ł.; Sobota, P. (2008). Well-defined polynuclear heterobimetallic complexes as precursors for ceramic and magnetic materials. *Dalton Trans.,* 6509-6520.

Sze, S.M.; Ng, K.K. (2006). *Physics of semiconductor devices*: John Wiley & Sons.

Tachibana, Y.; Akiyama, H.Y.; Ohtsuka, Y.; Torimoto, T.; Kuwabata, S. (2007). CdS quantum dots sensitized TiO_2 sandwich type photoelectrochemical solar cells. *Chem. Lett.,* 36, 88-89.

Tagantsev, A.; Vaideeswaran, K.; Vakhrushev, S.; Filimonov, A.; Burkovsky, R.; Shaganov, A., . . . Uchiyama, H. (2013). The origin of antiferroelectricity in $PbZrO_3$. *Nat. commun.,* 4.

Tahir, A.A.; Burch, H.A.; Wijayantha, K.; Pollet, B.G. (2013). A new route to control texture of materials: Nanostructured $ZnFe_2O_4$ photoelectrodes. *Int. J. Hydrogen Energy,* 38, 4315-4323.

Tahir, A.A.; Mazhar, M.; Hamid, M.; Wijayantha, K.U.; Molloy, K.C. (2009). Photooxidation of water by $NiTiO_3$ deposited from single source precursor $[Ni_2Ti_2(OEt)_2(\mu\text{-}OEt)_6(acac)_4]$ by AACVD. *Dalton Trans.,* 3674-3680.

Tahir, A.A.; Wijayantha, K. (2010). Photoelectrochemical water splitting at nanostructured $ZnFe_2O_4$ electrodes. *J. Photochem. Photobiol., A,* 216, 119-125.

Tahir, A.A.; Wijayantha, K.U.; Saremi-Yarahmadi, S.; Mazhar, M.; McKee, V. (2009). Nanostructured α-Fe_2O_3 thin films for photoelectrochemical hydrogen generation. *Chem. Mater.*, 21, 3763-3772.

Takahashi, Y.; Yuki, R.; Sugiura, M.; Motojima, S.; Sugiyama, K. (1980). Vapor deposition of thin cadmium sulfide layers using thermal decomposition of dithiolatocadmium complexes. *J. Cryst. Growth*, 50, 491-497.

Tennakone, K.; Kumara, G.; Wijayantha, K.; Kottegoda, I.; Perera, V.; Aponsu, G. (1997). A nanoporous solid-state photovoltaic cell sensitized with copper chlorophyllin. *J. Photochem. Photobiol., A*, 108, 175-177.

Thurston, J.H.; Trahan, D.; Ould-Ely, T.; Whitmire, K.H. (2004). Toward a General Strategy for the Synthesis of Heterobimetallic Coordination Complexes for Use as Precursors to Metal Oxide Materials: Synthesis, Characterization, and Thermal Decomposition of $Bi_2(Hsal)_6{\times}M(Acac)_3$ (M= Al, Co, V, Fe, Cr). *Inorg. Chem.*, 43, 3299-3305.

Thurston, J.H.; Whitmire, K.H. (2002). Heterobimetallic Bismuth-Transition Metal Salicylate Complexes as Molecular Precursors for Ferroelectric Materials. Synthesis and Structure of $Bi_2M_2(sal)_4(Hsal)_4(OR)_4$ (M= Nb, Ta; R= CH_2CH_3 , $CH(CH_3)_2$), $Bi_2Ti_3(sal)_8(Hsal)_2$, and $Bi_2Ti_4(O^iPr)(sal)_{10}(Hsal)$(sal= $O_2CC_6H_4$-2-O; Hsal = $O_2CC_6H_4$-2-OH). *Inorg. Chem.*, 41, 4194-4205.

Tiekink, E.R. (2003). Molecular architecture and supramolecular association in the zinc-triad 1, 1-dithiolates. Steric control as a design element in crystal engineering? *CrystEngComm*, 5, 101-113.

Tiekink, E.R.; Haiduc, I. (2005). Stereochemical Aspects of Metal Xanthate Complexes: Molecular Structures and Supramolecular Self-Assembly. *Prog. Inorg. Chem*, 54, 127-319.

Tiekink, E.R.; Zukerman-Schpector, J. (2011). Emerging supramolecular synthons: C–Hπ (chelate) interactions in metal bis (1, 1-dithiolates). *Chem. Commun.*, 47, 6623-6625.

Tiekink, E.R.T.; Hall, V.J.; Buntine, M.A. (1999). An examination of the influence of crystal structure on molecular structure. The crystal and molecular structures of some diorganotin-chloro-(N,N-dialkyldithiocarbamate)s, $R_2Sn(S_2CNR'_2)Cl$, R = Me, ^{t}Bu, Ph, Cy; R'_2 = $(Et)_2$, (Et, Cy) and $(Cy)_2$: a comparison between solid state and theoretical structures

Z. Kristallogr., 214, 124-134.

Tomaszewski, P.E. (1992). Structural phase transitions in crystals. I. Database. *Phase Transitions: A Multinational Journal,* 38, 127-220.

Torres-Huerta, A.; Höpfl, H.; Tlahuext, H.; Hernández-Ahuactzi, I.F.; Sánchez, M.; Reyes-Martínez, R.; Morales-Morales, D. (2013). Dinuclear Macrocyclic Palladium Dithiocarbamates Derived from the Homologous Series of Aliphatic 1, x-Diamines (x = 4–10). *Eur. J. Inorg. Chem.,* 2013, 61-69.

Tran, N.; Lamb, R.; Mar, G. (1999). Single source chemical vapour deposition of zinc sulphide thin films: film composition and structure. *Colloids Surf., A,* 155, 93-100.

Tressler, J.F.; Alkoy, S.; Newnham, R.E. (1998). Piezoelectric sensors and sensor materials. *J. Electroceram.,* 2, 257-272.

Trindade, T.; Brien, P.O. (1997). Lead (II) dithiocarbamato complexes as precursors for the LP-MOCVD of lead sulfide. *Chem. Vap. Deposition,* 3, 75-77.

Tseng, C.-J.; Wang, C.-H.; Cheng, K.-W. (2012). Photoelectrochemical performance of gallium-doped $AgInS_2$ photoelectrodes prepared by electrodeposition process. *Sol. Energy Mater. Sol. Cells,* 96, 33-42.

Tsuji, I.; Shimodaira, Y.; Kato, H.; Kobayashi, H.; Kudo, A. (2010). Novel Stannite-type Complex Sulfide Photocatalysts $A^{I}{}_{2}$-Zn-A^{IV}-S_4 (A^{I}= Cu and Ag; A^{IV}= Sn and Ge) for Hydrogen Evolution under Visible-Light Irradiation. *Chem. Mater.,* 22, 1402-1409.

Tuan, A.C.; Bryan, J.D.; Pakhomov, A.; Shutthanandan, V.; Thevuthasan, S.; McCready, D.E., . . . Krishnan, K. (2004). Epitaxial growth and properties of cobalt-doped ZnO on α-Al_2O_3 single-crystal substrates. *Phys. Rev. B,* 70, 054424.

Turte, K.; Shova, S.; Spatar, F.; Mazus, M.; Malinovskii, T. (1994). Crystal, molecular, and electronic structure of carboxylate $[Fe_3O(CH_3COO)_6\ (H_2O)_3]\ NO_3 \cdot\ 4H_2O$. *J. Struct. Chem.,* 35, 248-255.

Van den Eeckhout, K.; Smet, P.F.; Poelman, D. (2011). Luminescent afterglow behavior in the $M_2Si_5N_8$: Eu family (M= Ca, Sr, Ba). *Materials,* 4, 980-990.

Vanalakar, S.; Mali, S.; Pawar, R.; Tarwal, N.; Moholkar, A.; Kim, J.A., . . . Patil, P. (2011). Synthesis of cadmium sulfide spongy balls with nanoconduits for effective light harvesting. *Electrochim. Acta,* 56, 2762-2768.

Varghese, J.; Whatmore, R.W.; Holmes, J.D. (2013). Ferroelectric nanoparticles, wires and tubes: synthesis, characterisation and applications. *J. Mater. Chem. C,* 1, 2618-2638.

Veith, M.; Haas, M.; Huch, V. (2005). Single source precursor approach for the sol-gel synthesis of nanocrystalline $ZnFe_2O_4$ and zinc-iron oxide composites. *Chem. Mater.,* 17, 95-101.

Veith, M.; Mathur, S.; Lecerf, N.; Huch, V.; Decker, T.; Beck, H.P., . . . Haberkorn, R. (2000). Sol-gel synthesis of nano-scaled $BaTiO_3$, $BaZrO_3$ and $BaTi_{0.5}Zr_{0.5}O_3$ oxides via single-source alkoxide precursors and semi-alkoxide routes. *J. Sol-Gel Sci. Technol.,* 17, 145-158.

Veith, M.; Mathur, S.; Mathur, C.; Huch, V. (1998). Synthesis, structure, and reactivity of iodo-functionalized heterobimetallic alkoxides of tin (IV): X-ray crystal structures of $[I_2Sn\{Al(OPr^i)_4\}_2]$,$[I_2Sn\{Ti(OPr^i)_5\}_2]$,$[I_3Sn\{Zr(OPr^{i5}(Pr^iOH)\}]$, and $[I_2Sn\{Mo(C_5H_5)(CO)_3\}_2]$. *Organometallics,* 17, 1044-1051.

Veith, M.; Mathur, S.; Shen, H.; Lecerf, N.; Hüfner, S.; Jilavi, M.H. (2001). Single-step preparation of oxide-oxide nanocomposites: chemical vapor synthesis of $LnAlO_3/Al_2O_3$ (Ln= Pr, Nd) thin films. *Chem. Mater.,* 13, 4041-4052.

Version, S. (2007). 2; Bruker AXS Inc. *Madison, WI*.

Wang, H.; Zhu, J.-J.; Zhu, J.-M.; Chen, H.-Y. (2002). Sonochemical Method for the Preparation of Bismuth Sulfide Nanorods. *J. Phys. Chem. B,* 106, 3848-3854.

Wang, J.-C.; Weng, W.-T.; Tsai, M.-Y.; Lee, M.-K.; Horng, S.-F.; Perng, T.-P., . . . Meng, H.-F. (2010). Highly efficient flexible inverted organic solar cells using atomic layer deposited ZnO as electron selective layer. *J. Mater. Chem.,* 20, 862-866.

Wang, L.; Wang, W.; Shang, M.; Yin, W.; Sun, S.; Zhang, L. (2010). Enhanced photocatalytic hydrogen evolution under visible light over $Cd_{1-x}Zn_xS$ solid solution with cubic zinc blend phase. *Int. J. Hydrogen Energy,* 35, 19-25.

Waser, R.; Schneller, T.; Hoffmann-eifert, S.; Ehrhart, P. (2001). Advanced chemical deposition techniques-from research to production. *Integr. Ferroelectr.,* 36, 3-20.

Waters, J.; Crouch, D.; Raftery, J.; O'Brien, P. (2004). Deposition of bismuth chalcogenide thin films using novel single-source precursors by metal-organic chemical vapor deposition. *Chem. Mater.,* 16, 3289-3298.

Whatmore, R.W.; Watton, R. (2000). Pyroelectric ceramics and thin films for uncooled thermal imaging. *Ferroelectrics*, 236, 259-279.

Wheeler, D.A.; Wang, G.; Ling, Y.; Li, Y.; Zhang, J.Z. (2012). Nanostructured hematite: synthesis, characterization, charge carrier dynamics, and photoelectrochemical properties. *Energy Environ. Sci.*, 5, 6682-6702.

Wilson, S.A.; Jourdain, R.P.; Zhang, Q.; Dorey, R.A.; Bowen, C.R.; Willander, M., . . . Nur, O. (2007). New materials for micro-scale sensors and actuators: An engineering review. *Mater. Sci. Eng., R*, 56, 1-129.

Winter, C.H.; Lewkebandara, T.S.; Proscia, J.W.; Rheingold, A.L. (1993). A class of single-source precursors to titanium disulfide films. Synthesis, structure, and chemical vapor deposition studies of $[TiCl_4(HSR)_2]$. *Inorg. Chem.*, 32, 3807-3808.

Xu, C.; Hampden-Smith, M.J.; Kodas, T.T. (1995). Aerosol-Assisted Chemical Vapor Deposition (AACVD) of Binary Alloy (Ag_xPd_{1-x},Cu_xPd_{1-x}, Ag_xCu_{1-x}) Films and Studies of Their Compositional Variation. *Chem. Mater.*, 7, 1539-1546.

Xu, P.; Zeng, G.M.; Huang, D.L.; Feng, C.L.; Hu, S.; Zhao, M.H., . . . Xie, G.X. (2012). Use of iron oxide nanomaterials in wastewater treatment: a review. *Science of the Total Environment*, 424, 1-10.

Yang, J. (2005). *An introduction to the theory of piezoelectricity* (Vol. 9): Springer.

Yang, J.; Hyde, J.R.; Wilson, J.W.; Mallik, K.; Sazio, P.J.; O'Brien, P., . . . George, M.W. (2009). Continuous flow supercritical chemical fluid deposition of optoelectronic quality CdS. *Adv. Mater.*, 21, 4115-4119.

Yanovsky, A.I.; Yanovskaya, M.I.; Limar, V.K.; Kessler, V.G.; Turova, N.Y.; Struchkov, Y.T. (1991). Synthesis and crystal structure of the double barium-titanium isopropoxide $[Ba_4Ti_4(\mu_4\text{-}O)_4([\mu_3\text{-}OR)_2(\mu\text{-}OR)_8(OR)_6(ROH)_4][Ba_4Ti_4([\mu_4\text{-}O)_4(\mu_3\text{-}OR)_2(\mu\text{-}OR)_9(OR)_5(ROH)_3]$. *J. Chem. Soc., Chem. Commun.*, 1605-1606.

Yu, X.; Cao, C. (2008). Photoresponse and Field-Emission Properties of Bismuth Sulfide Nanoflowers. *Cryst. Growth Des.*, 8, 3951-3955.

Zearing, D.J.; Coates, V.J. (1981). *Small area measurement of multiple film thicknesses, dopant concentrations and impurity levels using a new infrared microspectrophotometer.* Paper presented at the 1981 Microlithography Conferences.

Zemskova, S.; Glinskaya, E.B.L.; Klevtsova, R.; Gromilov, S.; Larionov, V.D.S. (1996). *SOME NEW SINGLE SOURCE PRECURSORS FOR CVD OF MULTI-*

COMPONENT MATERIALS BASED ON DITHIOLATES. Paper presented at the Proceedings of the Thirteenth International Conference on Chemical Vapor Deposition.

Zhang, H.; Yang, J.-H.; Shpanchenko, R.V.; Abakumov, A.M.; Hadermann, J.; Clérac, R.; Dikarev, E.V. (2009). New Class of Single-Source Precursors for the Synthesis of Main Group− Transition Metal Oxides: Heterobimetallic Pb− Mn β-Diketonates. *Inorg. Chem.,* 48, 8480-8488.

Zhang, K.; Guo, L. (2013). Metal sulphide semiconductors for photocatalytic hydrogen production. *Catal. Sci. Tech.,* 3, 1672-1690.

Zhao, D.; Sheng, G.; Chen, C.; Wang, X. (2012). Enhanced photocatalytic degradation of methylene blue under visible irradiation on graphene@ TiO_2 dyade structure. *Appl. Catal., B,* 111, 303-308.

Zhao, J.; Wu, L.; Zhi, J. (2008). Fabrication of micropatterned ZnO/SiO_2 core/shell nanorod arrays on a nanocrystalline diamond film and their application to DNA hybridization detection. *J. Mater. Chem.,* 18, 2459-2465.

Zheng, X.J.; Chen, Y.Q.; Zhang, T.; Jiang, C.B.; Yang, B.; Yuan, B., . . . Li, W. (2010). A photoconductive semiconductor switch based on an individual ZnS nanobelt. *Scripta Mater.,* 62, 520-523.

Zhu, J.; Zäch, M. (2009). Nanostructured materials for photocatalytic hydrogen production. *Curr. Opin. Colloid Interface Sci.,* 14, 260-269.

LIST OF APPENDICES

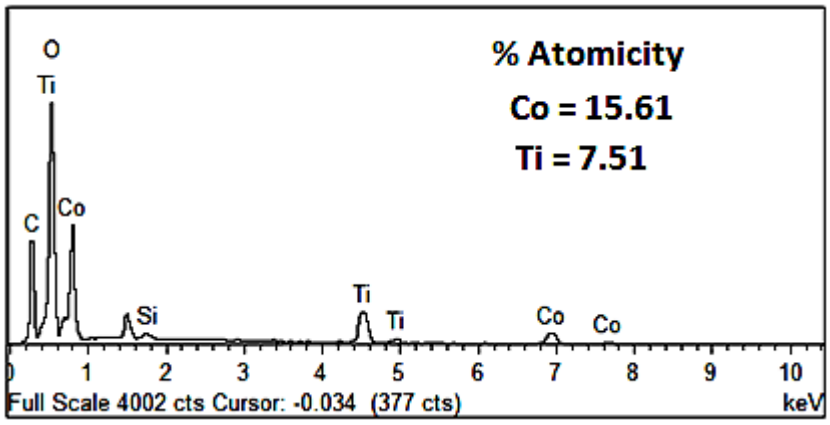

Appendix 1**:** EDX spectra of $CoTiO_3$-CoO composite thin films deposited from precursor $[Co_2Ti(\mu_3\text{-}O)(TFA)_6(THF)_3]$ (**2**).

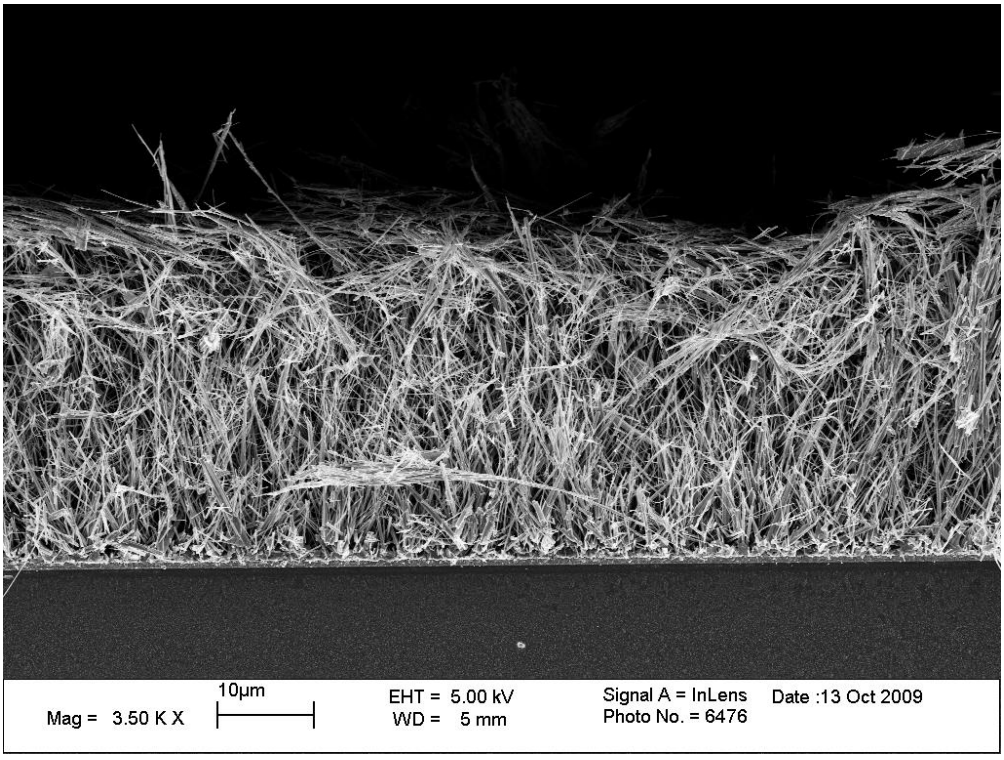

Appendix 2: Cross-section of Bi_2S_3 thin films deposited on FTO substrate using chloroform as a solvent at 400 ºC for 45 min.

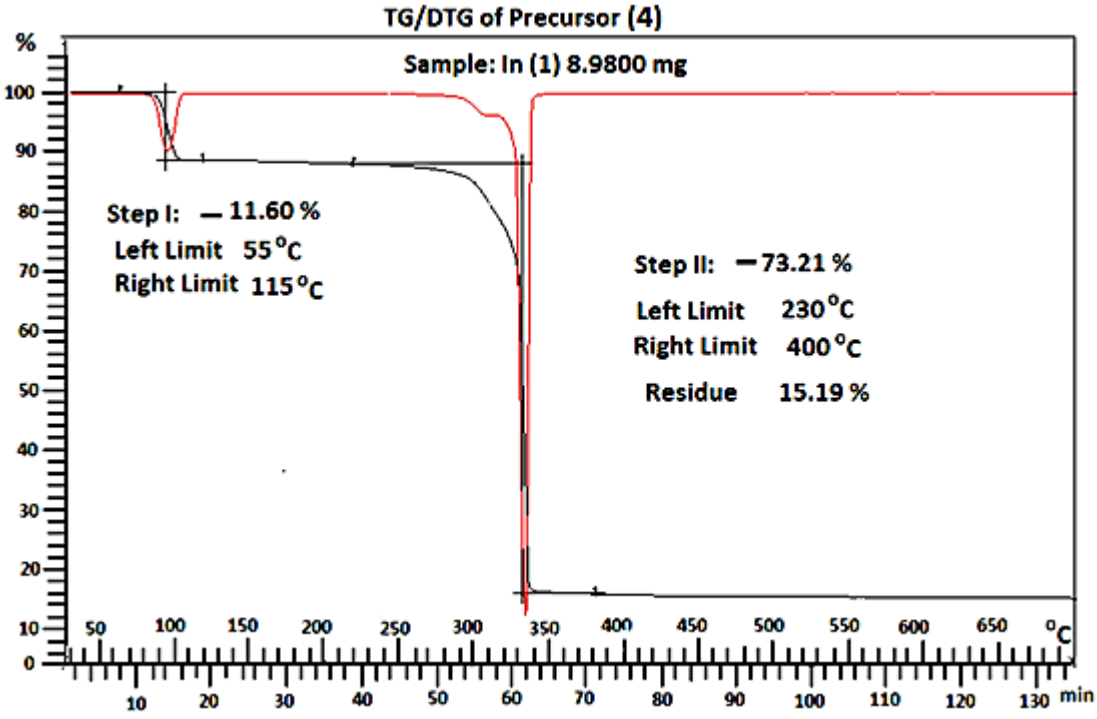

Appendix 3: TG/DTG curves presenting losses in weight against temperature for precursor $[In(S_2CNCy_2)_3]$ •2py (**4**).

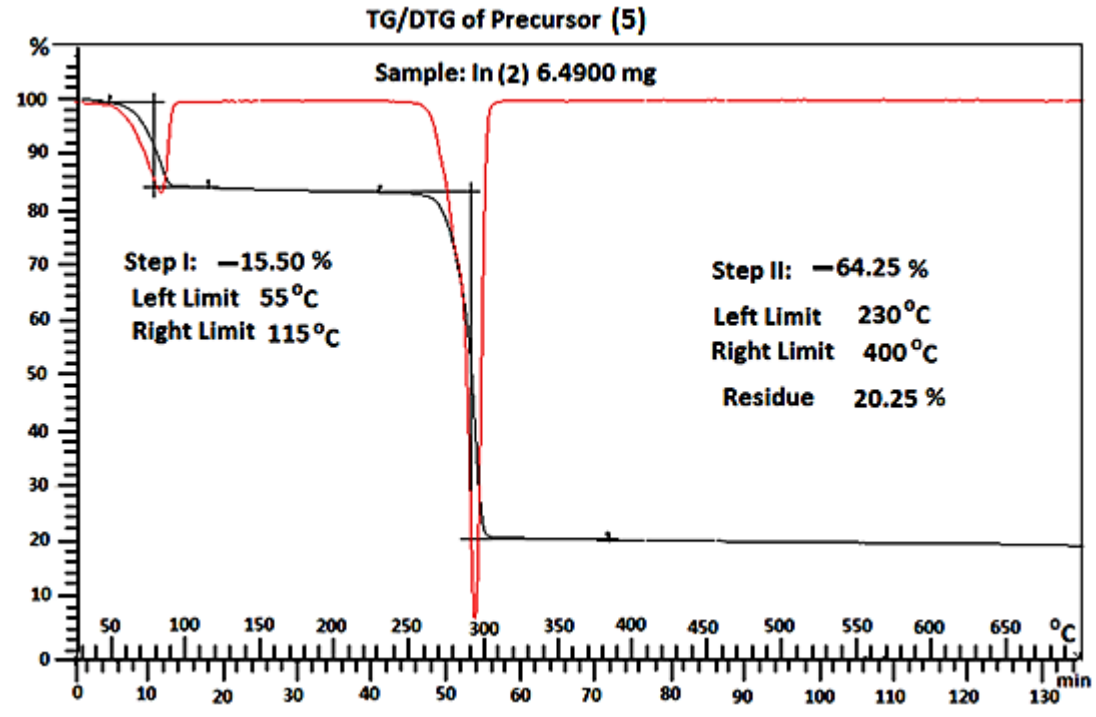

Appendix 4: TG/DTG curves presenting losses in weight against temperature for precursor $[In(S_2CN(^iPr)_2)_3]$•1.5py (**5**).

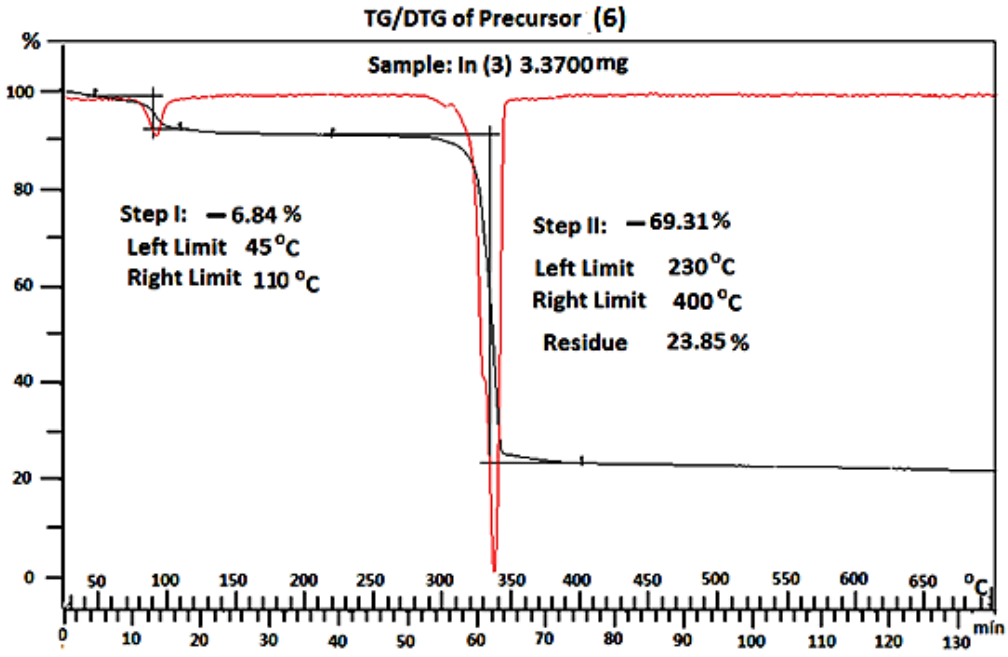

Appendix 5: TG/DTG curves presenting losses in weight against temperature for precursor $[In(S_2CPip)_3]$•0.5Py (**6**).

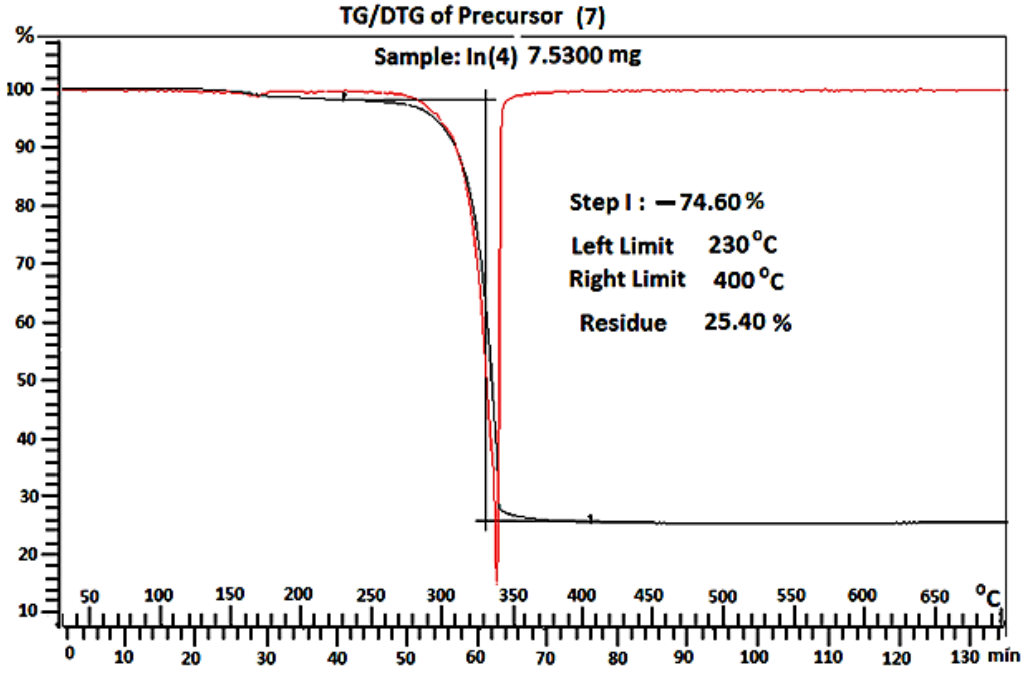

Appendix 6: TG/DTG curves presenting losses in weight against temperature for precursor $[In(S_2CNBzMe)_3]$(**7**).

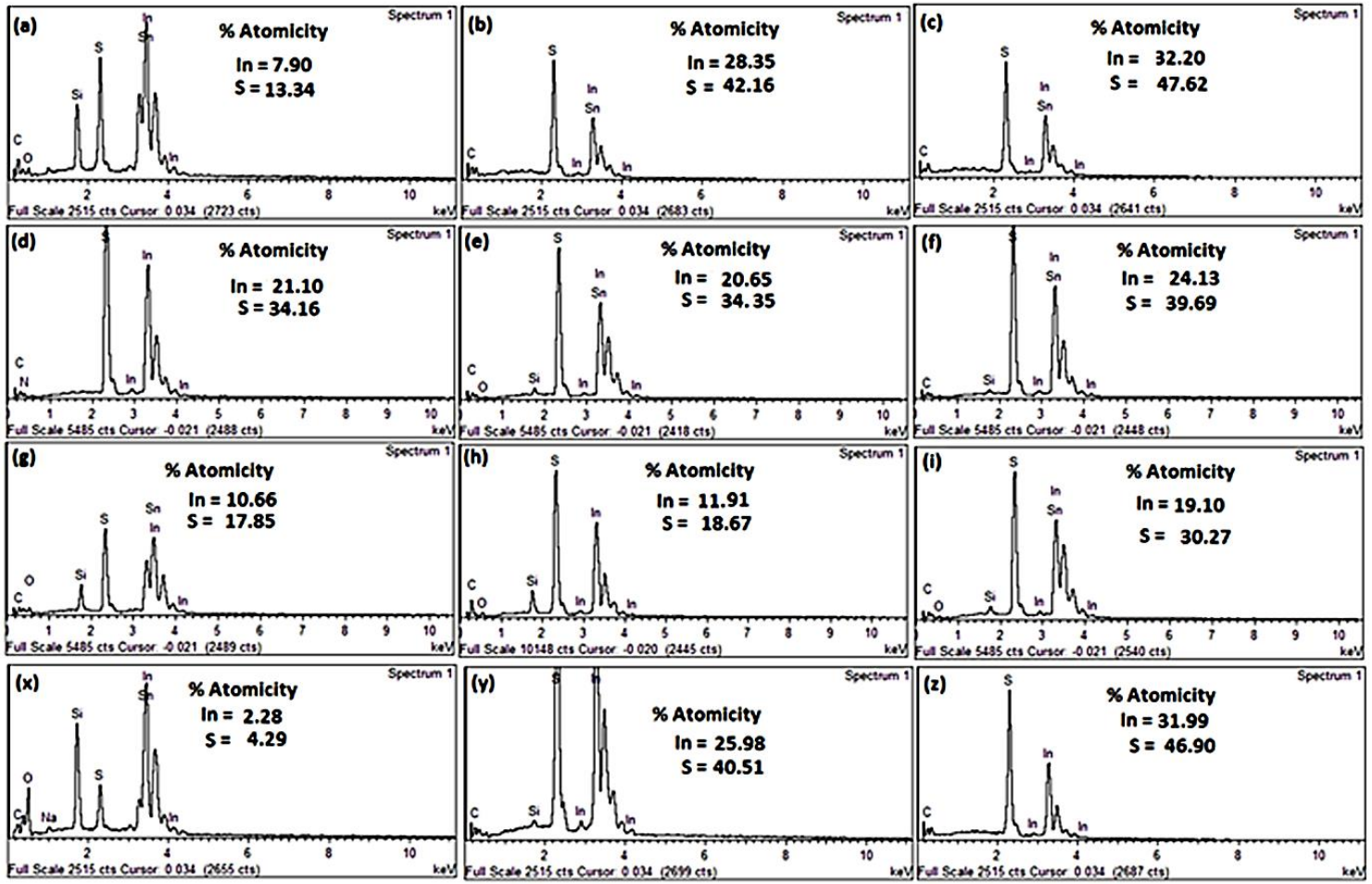

Appendix 7: EDX spectra of β-In_2S_3 thin films deposited using precursors $[In(S_2CNCy_2)_3]$•2py (**4**) at (a) 300 °C (b) 350 °C (c) 400°C $[In(S_2CN(^iPr)_2)_3]$•1.5py (**5**) at (d) 300 °C (e) 350 °C and (f) 400 °C; $[In(S_2CPip)_3]$•0.5py (**6**) at (g) 300 °C (h) 350 °C (i) 400 °C and $[In(S_2CNBzMe)_3]$ (**7**) at (x) 300 °C (y) 350 °C and (z) 400 °C.

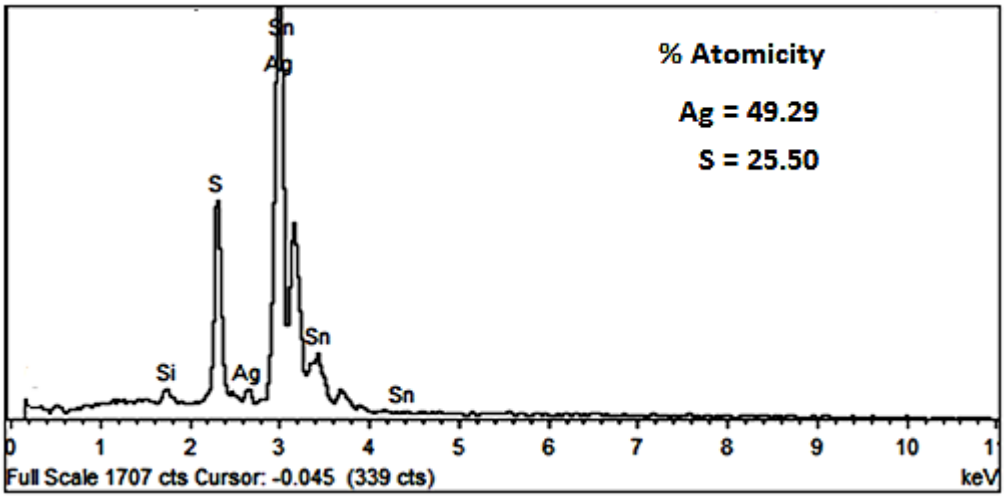

Appendix 8: EDX spectra showing Ag/S contents in acanthite (Ag_2S) thin films deposited from (**8**) on FTO substrates at 400 °C.

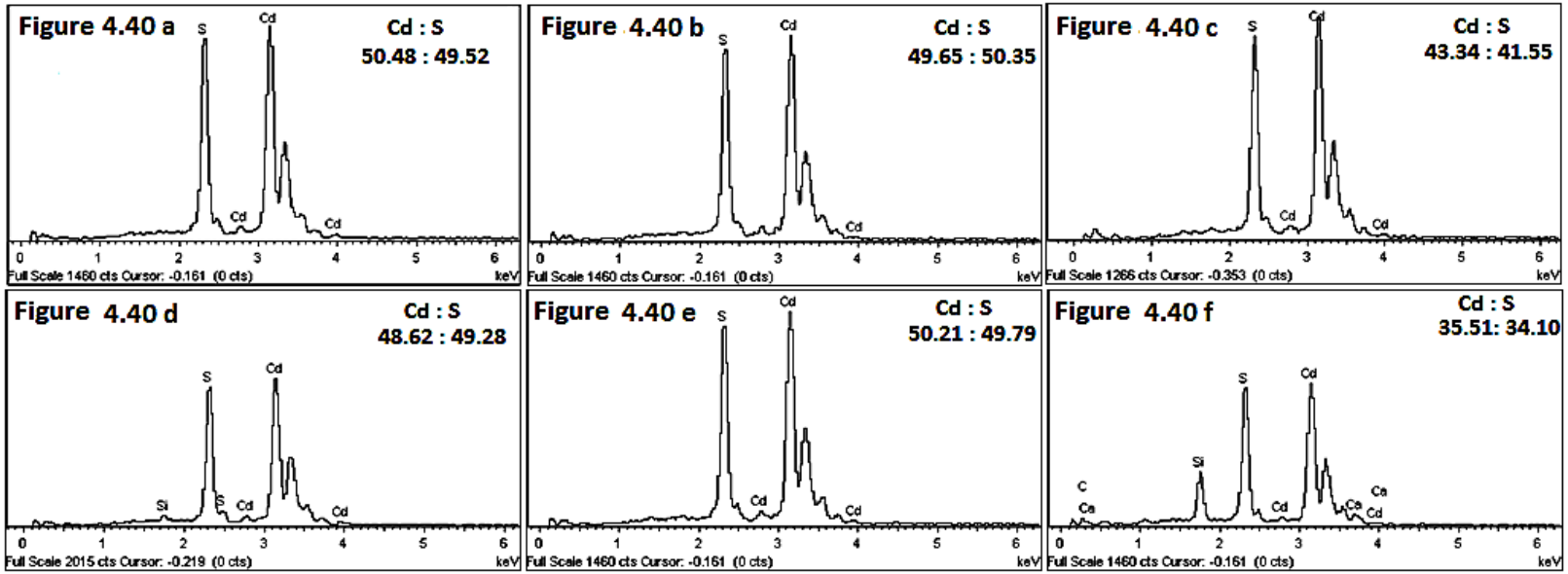

Appendix 9: EDX analysis results of CdS thin films deposited from [$Cd(S_2CNCy_2)_2(py)$] (**9**) in pyridine solution.

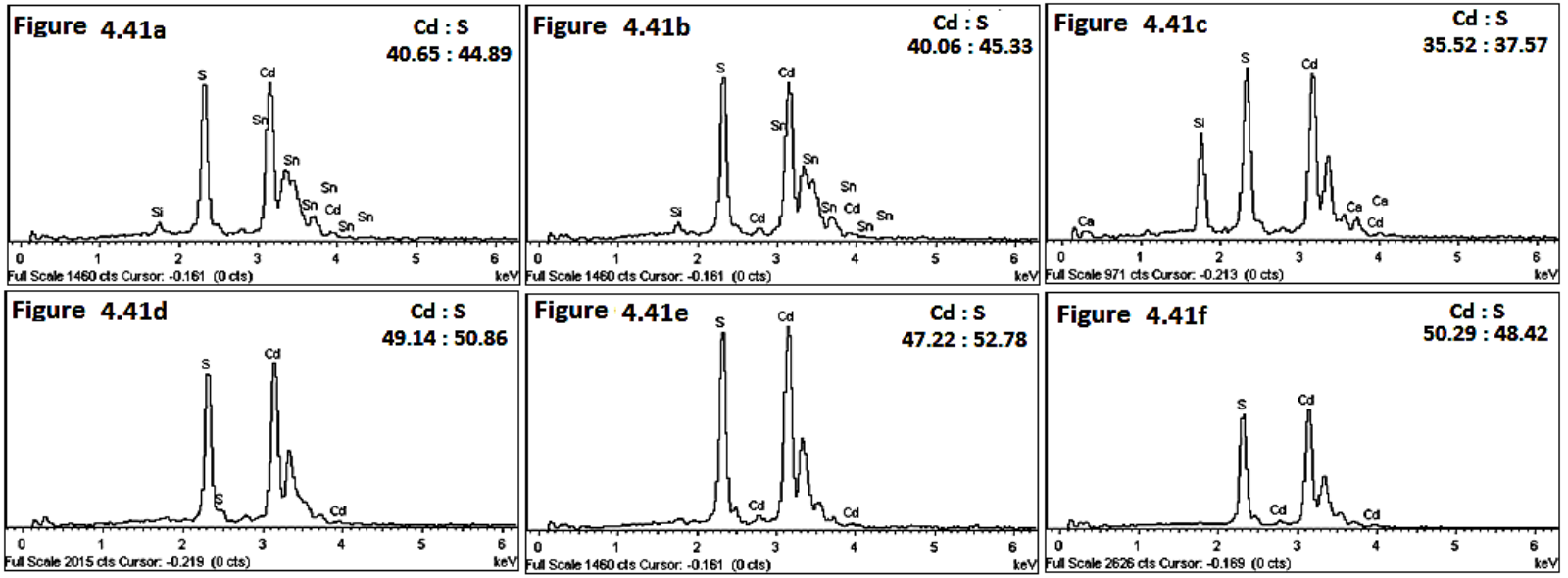

Appendix 10: EDX analysis results of CdS thin films deposited from [$Cd(S_2CNCy_2)_2(py)$] (**9**) in toluene solution.

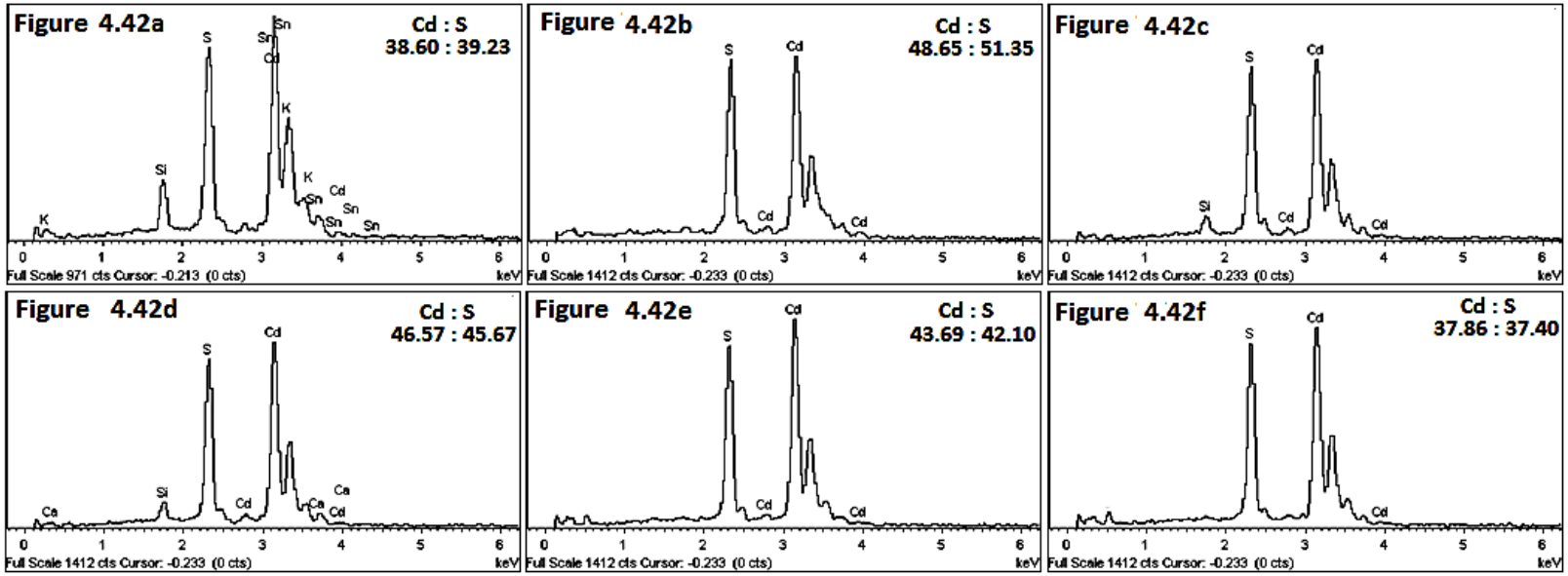

Appendix 11: EDX analysis results of CdS thin films deposited from $[Cd(S_2CNCy_2)_2(py)]$ (**9**) in THF solution.

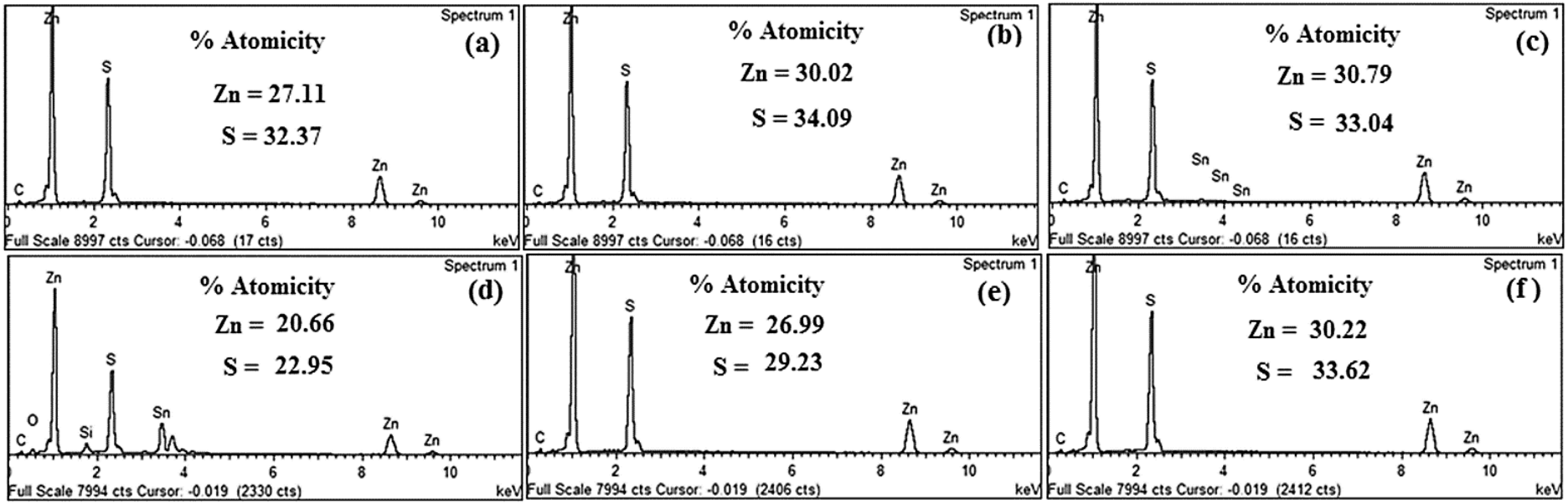

Appendix 12: EDX spectra of thin films deposited from precursor $[Zn(S_2CNCy_2)_2(py)]$ (**10**), (a-c) and precursor $[Zn(S_2CNBzMe)_2(py)]$ (**11**) (d-f).

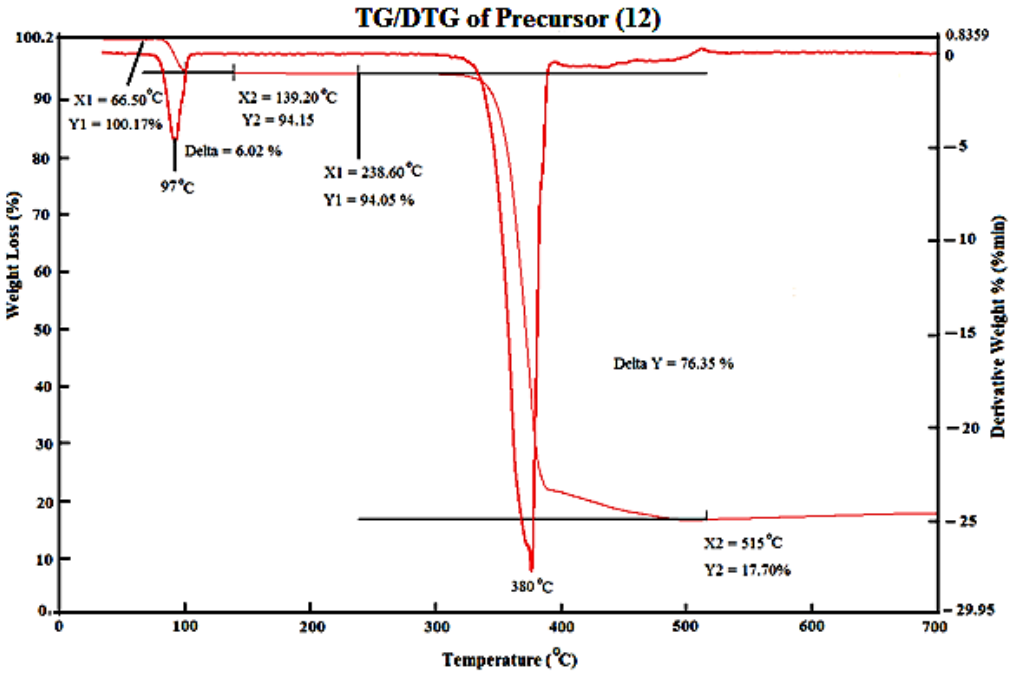

Appendix 13: TG/DTG curves presenting losses in weight against temperature for precursor $[Pd(S_2CNBz_2)_2]$•py (**12**).

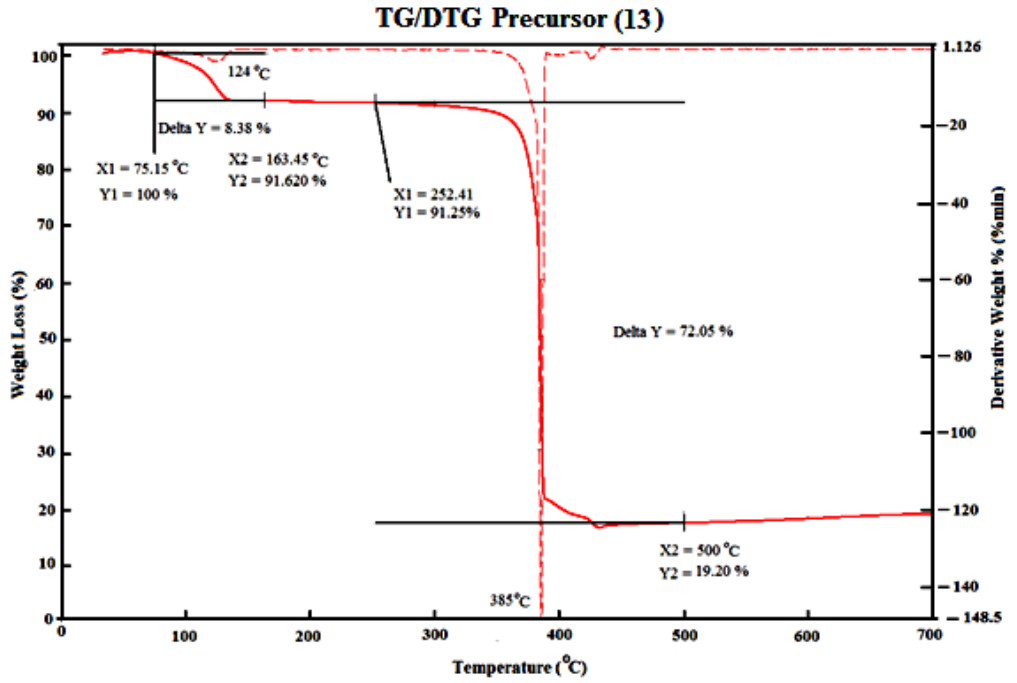

Appendix 14: TG/DTG curves presenting losses in weight against temperature for precursor $[Pd(S_2CNCy_2)_2]$•py (**13**).

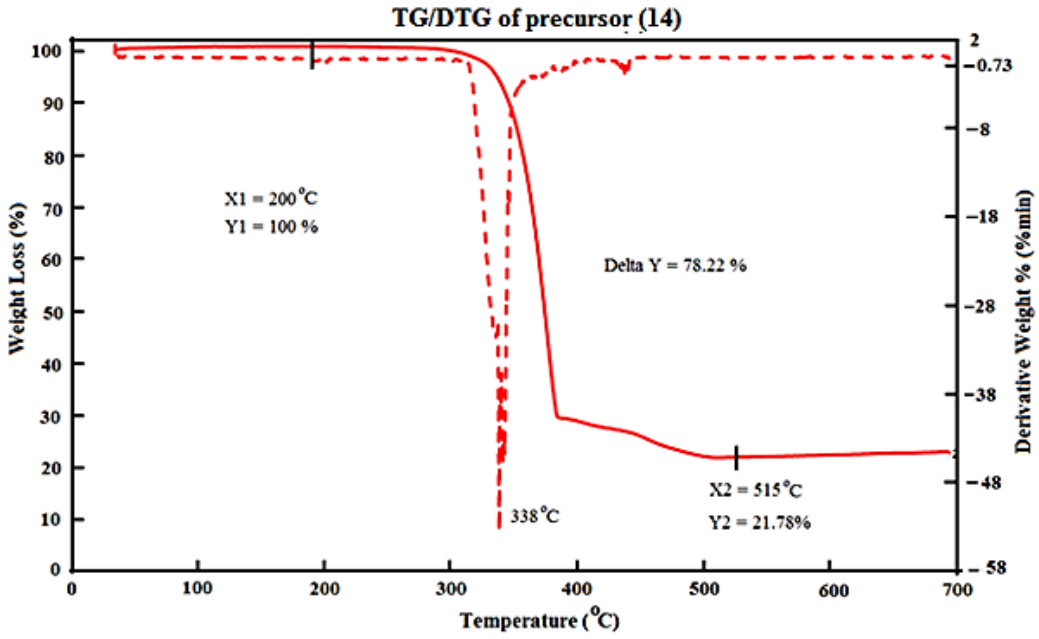

Appendix 15: TG/DTG curves presenting losses in weight against temperature for precursor [Pd($S_2CN^nHex_2)_2$] (**14**).

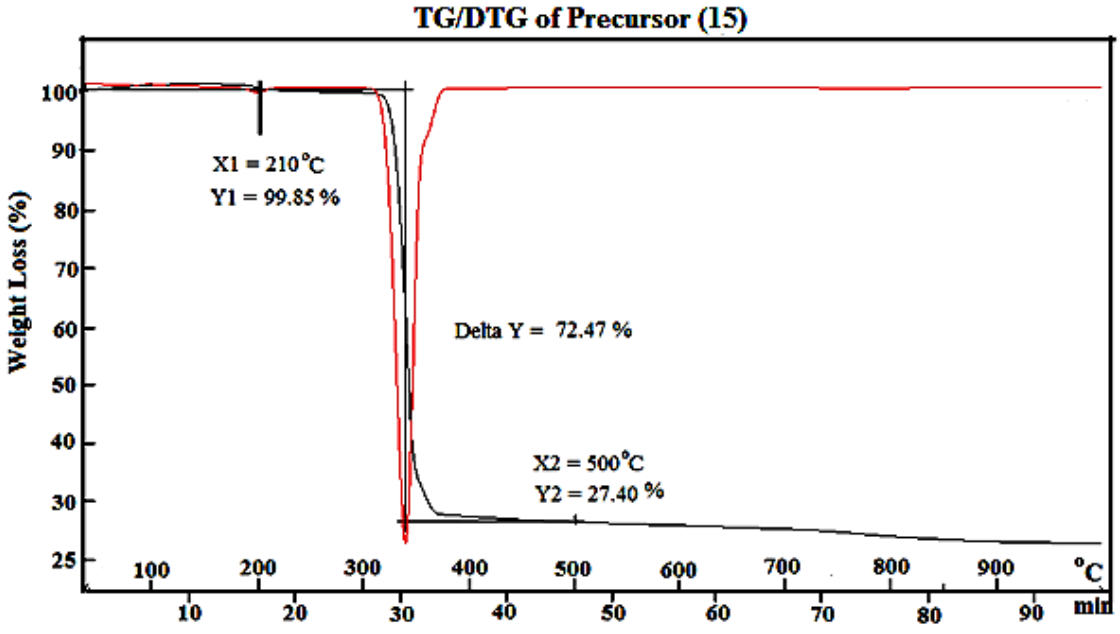

Appendix 16: TG/DTG curves presenting losses in weight against temperature for precursor [Pd($S_2CNCyMe)_2$] (**15**).

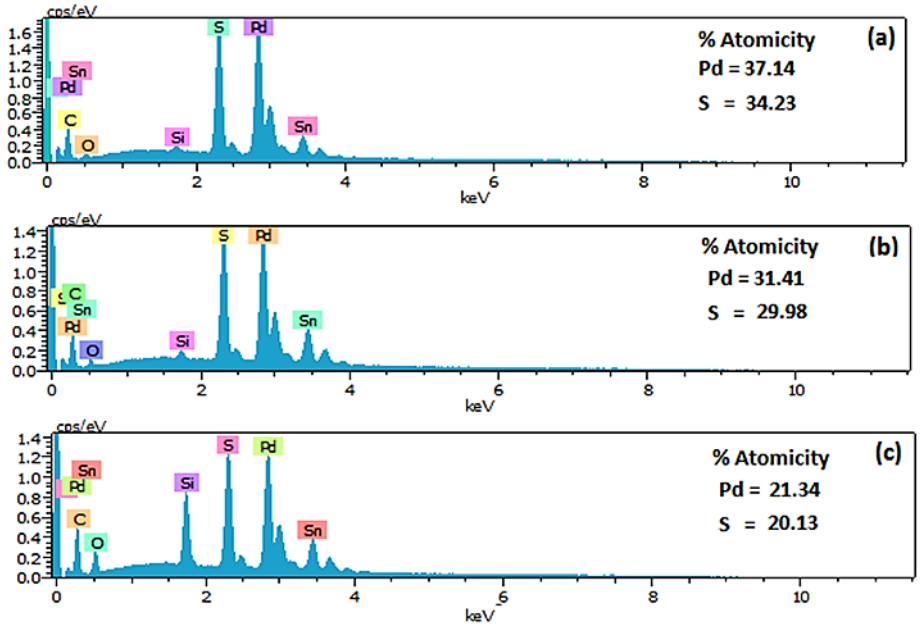

Appendix 17: EDX spectra of PdS thin films deposited using precursor $[Pd(S_2CNBz_2)_2]$•py (**12**) at (a) 400 °C (b) 450 °C (c) 500 °C.

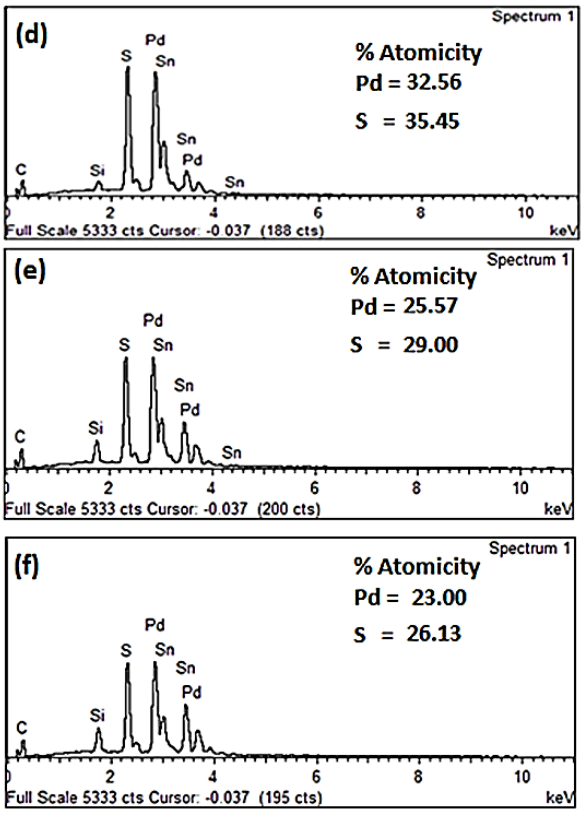

Appendix 18: EDX spectra of PdS thin films deposited using precursors $[Pd(S_2CNCy_2)_2]$•py (**13**) at (d) 400 °C (e) 450 °C (f) 500 °C.

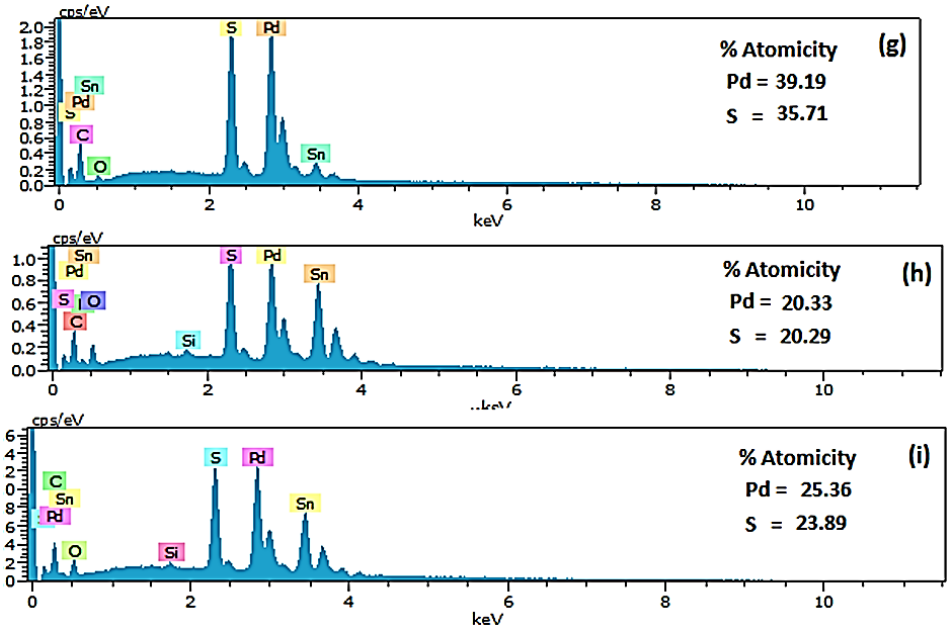

Appendix 19: EDX spectra of PdS thin films deposited using precursors $[Pd(S_2CN^nHex_2)_2]$ (**14**) at (g) 400 °C (h) 450 °C (i) 500 °C.

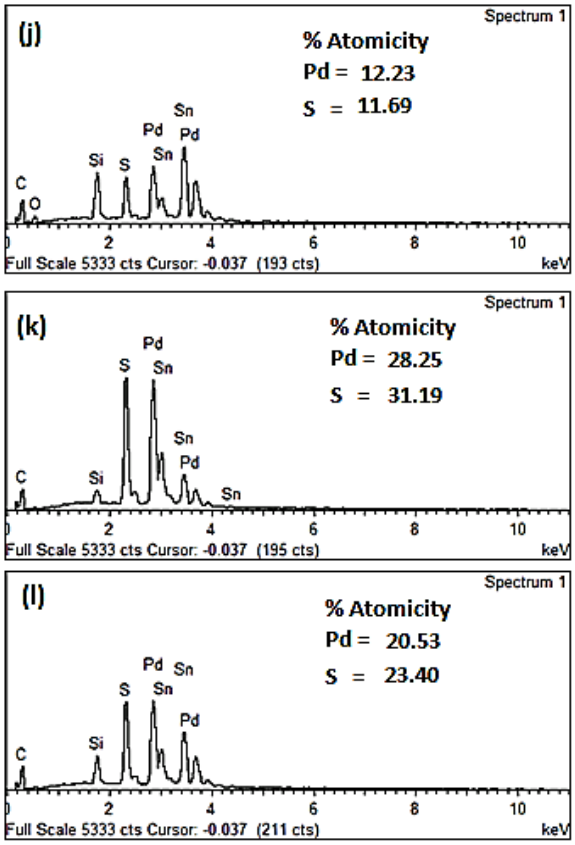

Appendix 20: EDX spectra of PdS thin films deposited using precursors $[Pd(S_2CNCyMe)_2]$ (**15**) at (j) 400 °C (k) 450 °C (l) 500 °C.

LIST OF PUBLICATIONS

(1) **Ehsan, M.A**.; Peiris, T.N.; Wijayantha, K.U.; Olmstead, M.M.; Arifin, Z.; Mazhar, M., . . . McKee, V. (2013). Development of molecular precursors for deposition of indium sulphide thin film electrodes for photoelectrochemical applications. *Dalton Tran., 42*, 10919-10928.

(2) Mansoor, M.A.; Ehsan, M.A.; McKee, V.; Huang, N.-M.; Ebadi, M.; Arifin, Z., . . . Mazhar, M. (2013). Hexagonal structured $Zn_{1-x}Cd_xO$ solid solution thin films: synthesis, characterization and applications in photoelectrochemical water splitting. *J. Mater. Chem. A, 1*, 5284-5292.

(3) **Ehsan, M.A**.; Peiris, T.; Wijayantha, K.; Khaledi, H.; Ming, H.N.; Misran, M., . . . Mazhar, M. (2013). Surface morphological and photoelectrochemical studies of ZnS thin films developed from single source precursors by aerosol assisted chemical vapour deposition. *Thin Solid Films, 540*, 1-9.

(4) **Ehsan, M.A**.; Khaledi, H.; Tahir, A.A.; Ming, H.N.; Wijayantha, K.; Mazhar, M. (2013a). Synthesis and characterization of silver diethyldithiocarbamate cluster for the deposition of acanthite (Ag_2S) thin films for photoelectrochemical applications. *Thin Solid Films, 536*, 124-129.

(5) **Ehsan, M.A**.; Ming, H.N.; Misran, M.; Arifin, Z.; Tiekink, E.R.; Safwan, A.P., . . . Mazhar, M. (2012). Effect of AACVD Processing Parameters on the Growth of Greenockite (CdS) Thin Films using a Single-Source Cadmium Precursor. *Chem. Vap. Deposition, 18*, 191-200.

(6) **Ehsan, M.A**.; Mansoor, M.A.; Mazhar, M.; Tahir, A.A.; Hamid, M.; Upul Wijayantha, K. (2012). Cobalt titanate–cobalt oxide composite thin films deposited from heterobimetallic precursor. *Appl. Organometal. Chem., 26*, 493.

(7) **Ehsan, M.A**.; Tahir, A.A.; Hamid, M.; Mazhar, M.; Wijayantha, K.; Zeller, M. (2011). Deposition of iron titanate/titania ceramic composite thin films from a single molecular precursor. *Inorg. Chim. Acta, 376*, 189-194.

(8) Tahir, A.A.; **Ehsan, M.A**.; Mazhar, M.; Wijayantha, K.U.; Zeller, M.; Hunter, A. (2010). Photoelectrochemical and photoresponsive properties of Bi_2S_3 nanotube and nanoparticle thin films. *Chem. of Mater., 22*, 5084-5092.

(9) **Ehsan, M.A.;** Ming, H.N.; McKee, V.; Peiris, T.N.; Wijayantha, K.U., . . . Mazhar, M. Photo-absorber Vysotskite structured palladium sulphide thin films from dithiocarbamate precursor.. New J. Chem., 2014, DOI:10.1039/c4nj00564c

NJC

PAPER

View Article Online
View Journal

Vysotskite structured photoactive palladium sulphide thin films from dithiocarbamate derivatives†

Cite this: DOI: 10.1039/c4nj00564c

Muhammad Ali Ehsan,[a] Huang Nay Ming,[b] Vickie McKee,[c] Thalge Anton Nirmal Peiris,[c] Upul Wijayantha-Kahagala-Gamage,[c] Zainudin Arifin[a] and Muhammad Mazhar*[a]

A series of palladium(II) dithiocarbamate complexes $[Pd(S_2CNRR')_2]\cdot n(py)$ [where py = pyridine; RR′ = Bz, n = 1 (**1**); Cy, n = 1 (2); ^{n}Hex, n = 0 (**3**) and MeCy, n = 0 (**4**)] have been synthesized and characterized using various physicochemical techniques and their single crystal structures have been established. The decomposition modes and potential of the complexes as single source precursors (SSPs) for the development of palladium sulphide (PdS) thin films were investigated by thermogravimetric and derivative thermogravimetric (TGA/DTG) analyses. The PdS thin films were deposited on FTO conducting glass substrates at 400, 450 and 500 °C by the aerosol-assisted chemical vapour deposition (AACVD) technique and characterized by X-ray diffraction (XRD), scanning electron microscopy (SEM), energy dispersive X-ray analysis (EDX) reveal that the deposit has a tetragonal structure with a 1 : 1 ratio of Pd : S. The shape and size of PdS crystallites and the texture of films depend on the deposition temperatures and the precursor type used. The direct band gap energy of 1.56 eV was estimated from UV-Vis spectroscopy of the PdS films fabricated from precursor (**2**) at 450 °C. The photoelectrochemical (PEC) properties of PdS films were studied by recording the current–voltage plots under alternating dark and illumination conditions. To the best of our knowledge, this is the first demonstration of PEC studies of photoactive PdS thin films fabricated using the AACVD technique using palladium(II) dithiocarbamate complexes as precursors.

Received (in Montpellier, France) 12th April 2014,
Accepted 27th May 2014

DOI: 10.1039/c4nj00564c

www.rsc.org/njc

1. Introduction

Transition metal sulphides exhibit diverse electrical, magnetic and optical properties[1] which are fundamental to a range of technological applications such as solar cells,[2] fuel cells,[3] gas sensors,[4] lithium ion batteries,[5] spintronics light-emitting diodes,[6] non-volatile memory,[6] spin valve transistors light emitting diodes,[6] laser devices, photoconductors[7] and infrared detectors.[7] Palladium sulphides exist in a variety of phases including PdS, PdS_2, $Pd_{2.8}S$, Pd_3S, Pd_4S, $Pd_{2.2}S$ and $Pd_{2.5}S$. Of all these phases, only vystotskite PdS possesses a band gap energy (E_g) < 2 eV[8] to exhibit semiconducting properties, which find potential applications in catalysis,[9,10] ohmic contacts in semiconducting electronic devices, acid resistant high temperature electrodes,[11] recording films in optical discs and lithographic films,[12] and light image receiving materials with silver halides.[13] PdS is a widely explored material and has been largely synthesized in powder forms as well as nano-crystals using a variety of methods. Nano-crystals have been synthesized by solvothermal or thermal decomposition of palladium(II) xanthate and allyl palladium(II) xanthate complexes.[14] The aqueous dispersions of PdS particles have been prepared by the addition of Na_2S solution to $PdCl_2$ or Na_2PdCl_4 solutions.[15] Organosols of PdS have been synthesized by the reaction of metal acetate with hydrogen sulphide.[16] However, relatively few reports have been published on the deposition of PdS thin films using either a chemical vapour deposition (CVD) or a non-CVD technique. The single source precursor (SSP) based CVD synthetic approach has been identified as a potential route for the fabrication of tailor-made thin films that can meet the technology demand in

[a] Department of Chemistry, Faculty of Science, University of Malaya, Lembah Pantai, 50603 Kuala Lumpur, Malaysia. E-mail: maliqau@ymail.com, zainudin@um.edu.my, mazhar42pk@yahoo.com; Tel: +60 (03)79674269
[b] Department of Physics, Faculty of Science, University of Malaya, Lembah Pantai, 50603 Kuala Lumpur, Malaysia. E-mail: huangnayming@gmail.com
[c] Department of Chemistry, Loughborough University, Loughborough, LE11 3TU, UK. E-mail: T.A.N.Peiris@lboro.ac.uk, u.wijayantha@lboro.ac.uk, V.McKee@lboro.ac.uk; Tel: +44 (0)1509222574

† Electronic supplementary information (ESI) available: Microanalysis results, H-NMR spectra, TGA plots, EDX spectra and single crystal X-ray crystallographic information. CCDC 995675–995678. For ESI and crystallographic data in CIF or other electronic format see DOI: 10.1039/c4nj00564c

Dalton Transactions

RSC Publishing

PAPER

View Article Online
View Journal

Cite this: DOI: 10.1039/c3dt50781e

Development of molecular precursors for deposition of indium sulphide thin film electrodes for photoelectrochemical applications†

Muhammad Ali Ehsan,[a] T. A. Nirmal Peiris,[b] K. G. Upul Wijayantha,[b] Marilyn M. Olmstead,[c] Zainudin Arifin,[a] Muhammad Mazhar,*[a] K. M. Lo[a] and Vickie McKee[b]

Symmetrical and unsymmetrical dithiocarbamato pyridine solvated and non-solvated complexes of indium(III) with the general formula $[In(S_2CNRR')_3]{\cdot}n(py)$ [where py = pyridine; R,R′ = Cy, n = 2 (**1**); R,R′ = ^{i}Pr, n = 1.5 (**2**); NRR′ = Pip, n = 0.5 (**3**) and R = Bz, R′ = Me, n = 0 (**4**)] have been synthesized. The compositions, structures and properties of these complexes have been studied by means of microanalysis, IR and ^{1}H-NMR spectroscopy, X-ray single crystal and thermogravimetric (TG/DTG) analyses. The applicability of these complexes as single source precursors (SSPs) for the deposition of β-In_2S_3 thin films on fluorine-doped SnO_2 (FTO) coated conducting glass substrates by aerosol-assisted chemical vapour deposition (AACVD) at temperatures of 300, 350 and 400 °C is studied. All films have been characterized by powder X-ray diffraction (PXRD) and energy dispersive X-ray analysis (EDX) for the detection of phase and stoichiometry of the deposit. Scanning electron microscopy (SEM) studies reveal that precursors **(1)–(4)**, irrespective of different metal ligand design, generate comparable morphologies of β-In_2S_3 thin films at different temperatures. Direct band gap energies of 2.2 eV have been estimated from the UV-vis spectroscopy for the β-In_2S_3 films fabricated from precursors (**1**) and (**4**). The photoelectrochemical (PEC) properties of β-In_2S_3 were confirmed by recording the current–voltage plots under light and dark conditions. The plots showed anodic photocurrent densities of 1.25 and 0.65 mA cm^{-2} at 0.23 V *vs.* Ag/AgCl for the β-In_2S_3 films made at 400 and 350 °C from the precursors (**1**) and (**4**), respectively. The photoelectrochemical performance indicates that the newly synthesised precursors are highly useful in fabricating β-In_2S_3 electrodes for solar energy harvesting and optoelectronic application.

Received 23rd March 2013,
Accepted 22nd May 2013

DOI: 10.1039/c3dt50781e

www.rsc.org/dalton

Introduction

Semiconductors with suitable band gaps and band edges are key to the development of efficient light harvesting applications such as solar cells and solar water splitting.[1,2] The β-polymorph of indium sulphide (β-In_2S_3) is known for its optoelectronic and photoelectrochemical properties and is a promising candidate for many useful applications due to its stability, moderate band gap and photoconductive behaviour.[3] β-Indium sulphide (E_g = 2.0–2.2 eV),[4] having a defect spinel structure, displays excellent properties of high photosensitivity and photoconductivity,[5] stable chemical composition and low toxicity.[6] Thus, it is widely applied for displays,[7] as a photocatalyst for dye degradation,[8] for water splitting[6b] and for solar cells.[9,10] Moreover, β-In_2S_3 solar cell devices exhibit a high 16.4% power conversion efficiency,[11,12] which is comparable to CdS because of their equivalent band gaps and has been considered as a substitute for the highly toxic CdS.[13]

Much effort has been expended to produce β-In_2S_3 films and powders with a variety of structures and morphologies. These methods include chemical bath deposition,[14,15] sonochemical,[16] hydrothermal,[17,18] solvothermal,[19] solution phase synthesis,[20] thermal evaporation,[21] chemical spray,[22] solvent reduction route,[23] electrodeposition[24] and metal–organic chemical vapour deposition (MOCVD).[25] However, increasing

[a]*Department of Chemistry, Faculty of Science, University of Malaya, Lembah Pantai, 50603 Kuala Lumpur, Malaysia. E-mail: maliqau@ymail.com, zainudin@um.edu.my, kmlo@um.edu.my, mazhar42pk@yahoo.com; Tel: +60 (03) 79674269*

[b]*Department of Chemistry, Loughborough University, Loughborough, LE11 3TU, UK. E-mail: T.A.N.Peiris@lboro.ac.uk, u.wijayantha@lboro.ac.uk, V.McKee@lboro.ac.uk; Tel: +44 (0) 1509222574*

[c]*Department of Chemistry, University of California, Davis, CA 95616, USA. E-mail: marilyn_olmstead@hotmail.com*

†Electronic supplementary information (ESI) available: Microanalysis results, figures for NMR, XRD, TGA and EDX analyses. CCDC 924187–924190. For ESI and crystallographic data in CIF or other electronic format see DOI: 10.1039/c3dt50781e

Journal of
Materials Chemistry A

RSC Publishing

PAPER

View Article Online
View Journal

Cite this: DOI: 10.1039/c3ta10558j

Hexagonal structured $Zn_{(1-x)}Cd_xO$ solid solution thin films: synthesis, characterization and applications in photoelectrochemical water splitting†

Muhammad Adil Mansoor,[a] Muhammad Ali Ehsan,[a] Vickie McKee,[b] Nay-Ming Huang,[c] Mehdi Ebadi,[d] Zainudin Arifin,[a] Wan Jeffrey Basirun[a] and Muhammad Mazhar*[a]

Hexagonal nanostructured zinc–cadmium oxide [$Zn_{(1-x)}Cd_xO$ where $x = 0.08$, 0.15, and 0.17] solid solution thin films were deposited on FTO coated glass substrates from a common solution of zinc acetate and a newly developed polymeric cadmium precursor by an aerosol-assisted chemical vapour deposition (AACVD) technique. The polymeric cadmium precursor $[Cd_3(TFA)_4(OAc)_2(THF)_4]_n$ (**1**) was synthesized by the reaction of cadmium(II)acetate dihydrate with triflouroacetic acid in THF solution and characterized by melting point, microanalysis, FTIR, ^{1}H-NMR, thermogravimetry (TG/DTG) and single crystal X-ray analysis. The deposited thin films were characterized by powder XRD, SEM, EDX and UV-visible spectrophotometry, and tested for photoelectrochemical (PEC) water splitting to hydrogen and oxygen. The effect of various thin film deposition parameters such as solvent type, temperature and electrolyte concentration on PEC properties has been investigated. The SEM analysis illustrated that the morphology of the films changes significantly with the change of the solvent. The films deposited from THF solution have a needle-like appearance scattered vertically on the FTO-coated glass substrate. An optical band gap of 2.40 eV has been estimated by UV-visible spectrophotometry. The current–voltage characterization proved that the nanocrystalline hexagonal structured $Zn_{0.83}Cd_{0.17}O$ electrodes exhibit an n-type semiconducting behaviour and the photocurrent was found to be strongly dependent on the deposition solvent, deposition temperature and electrolyte concentration. The maximum photocurrent density of 0.23 mA cm^{-2} at 0.55 V *vs.* Ag/AgCl/3 M KCl (~1.23 V *vs.* RHE) was obtained for the $Zn_{0.83}Cd_{0.17}O$ photoelectrode deposited at 500 °C for 45 min from 0.5 M solution of (**1**) and $Zn(CH_3COO)_2 \cdot 2H_2O$ in THF.

Received 5th February 2013
Accepted 28th February 2013

DOI: 10.1039/c3ta10558j

www.rsc.org/MaterialsA

1 Introduction

Hydrogen is the most desirable source of fuel because it possesses a high energy storage capacity of 120 000 J g^{-1} as compared to 40 000 for oil and 30 000 for coal[1] and its combustion does not result in pollution of the environment. Hydrogen production by water splitting has been an objective of semiconductor photoelectrochemistry for nearly four decades. The energy difference between the oxygen evolution potential and the hydrogen evolution potential is 1.229 eV at 25 °C. Therefore, ideally one would like to have a chemically and optically stable semiconductor, in which the conduction and valence bands are positioned favourably so that they bestride the hydrogen and oxygen evolution potentials. To overcome the overpotential which is mainly associated with oxygen evolution, a semiconductor material with a band gap of 1.8–2.0 eV is preferred.

During the last few years, ZnO and related semiconductors have gained substantial interest in the semiconductor research community. The main focus for the application of ZnO materials is in optoelectronic devices,[2] whereby it is important to modulate the band gap. Doping by other elements is an effective way to adjust the band gap of ZnO.[3,4] Among these doping elements, cadmium is a suitable material for reducing the band gap of ZnO.[5,6] Unfortunately, ZnO and CdO have different crystal structures such as hexagonal and cubic respectively. Moreover, the thermodynamic solubility of Cd in the Zn–CdO

[a]Department of Chemistry, Faculty of Science, University of Malaya, Lembah Pantai, 50603 Kuala Lumpur, Malaysia. E-mail: mazhar42pk@yahoo.com; Tel: +60 (3) 79674269

[b]Department of Chemistry, Loughborough University, Loughborough, Leics LE 11 3TU, UK. Tel: +44 (0)1509 222574

[c]Department of Physics, Faculty of Science, University of Malaya, Lembah Pantai, 50603 Kuala Lumpur, Malaysia

[d]Department of Chemistry, Faculty of Science, Islamic Azad University-Gorgan Branch, Gorgan, Iran

† Electronic supplementary information (ESI) available: X-ray crystallographic data for the compound complex (**1**) and figures for NMR, FTIR, XRD and EDX analysis. CCDC 921755. For ESI and crystallographic data in CIF or other electronic format see DOI: 10.1039/c3ta10558j

Thin Solid Films 536 (2013) 124–129

Contents lists available at SciVerse ScienceDirect

Thin Solid Films

journal homepage: www.elsevier.com/locate/tsf

Synthesis and characterization of silver diethyldithiocarbamate cluster for the deposition of acanthite (Ag_2S) thin films for photoelectrochemical applications

Muhammad Ali Ehsan [a], Hamid Khaledi [a], Asif Ali Tahir [c], Huang Nay Ming [b], K.G. Upul Wijayantha [c], Muhammad Mazhar [a,*]

[a] Department of Chemistry, Faculty of Science, University of Malaya, Lembah Pantai, 50603 Kuala Lumpur, Malaysia
[b] Department of Physics, Faculty of Science, University of Malaya, Lembah Pantai, 50603 Kuala Lumpur, Malaysia
[c] Department of Chemistry, Loughborough University, Loughborough LE 11 3TU, UK

ARTICLE INFO

Article history:
Received 22 July 2012
Received in revised form 26 March 2013
Accepted 27 March 2013
Available online 6 April 2013

Keywords:
Silver dithiocarbamate
Single source precursor
Acanthite
Thin films
Aerosol-assisted chemical vapor deposition
Optical band gap
Photoelectrochemical cells

ABSTRACT

Acanthite (Ag_2S) thin films were fabricated on fluorine doped tin oxide coated conducting glass substrates by aerosol assisted chemical vapor deposition (AACVD) using silver cluster $[Ag_4\{S_2CN(C_2H_5)_2\}_3(C_5H_5N)_2]_n \cdot nNO_3 \cdot 2nH_2O$ (**1**) [where $(S_2CN(C_2H_5)_2)$ = diethyldithiocarbamate, C_5H_5N = pyridine] as a single source precursor. Cluster (**1**) was synthesized by the reaction of sodium diethyldithiocarbamate with silver nitrate in a mixture of acetone and pyridine. (**1**) was analyzed by melting point, elemental analysis, Fourier transform infrared spectroscopy, proton nuclear magnetic resonance spectroscopy, thermogravimetry and single crystal X-ray studies. Single crystal X-ray studies showed that (**1**) crystallizes in the triclinic crystal system with a = 11.4372(3), b = 11.6768(3), and c = 16.3672(4) Å and α = 105.817(3), β = 97.891(3), and γ = 93.274(3)° in the space group P-1. Thermogravimetric analysis revealed that (**1**) undergoes facile thermal decomposition at 400 °C to give a stable residual mass consistent with the formation of Ag_2S. Thin films grown from a 0.02 M solution of (**1**) in pyridine at 350 and 400 °C using AACVD technique were characterized by powder X-ray diffraction, field emission scanning electron microscopy (FESEM), energy dispersive X-ray and ultraviolet-visible spectrophotometry. FESEM images of the films exhibited well-defined nanorods with length >1000 nm and diameter 100–150 nm grown without any cracks, fractures or directional preference. A band gap of 1.05 eV was estimated by extrapolating the linear part of a Tauc plot recorded for the films. The photoelectrochemical (PEC) characteristics recorded under Air Mass 1.5 illumination indicated a photocurrent density of 220 μA cm^{-2} at 0.0 V vs Ag/AgCl/3 M KCl. The optical and PEC characteristics of the deposited thin films proved their suitability for PEC applications.

1. Introduction

Metal sulfide semiconductors with narrow band gaps have found utility as photoelectrode materials in photoelectrochemical (PEC) cells that are used for conversion of solar light into chemical energy such as hydrogen generation by water splitting [1]. Silver (I) sulfide Ag_2S has an absorption in the entire visible region of the solar spectrum and as such it is a promising material as a photosensitizer for photocatalysis [2,3] and for water splitting in PEC cells [4]. A major limitation for its wide practical use as a water oxidation photocatalyst is photo corrosion upon irradiation [1] but its narrow band gap of only 1 eV makes it possible to use in infrared (IR) detectors, as a photoconductor [5], as a photosensitive material for recording media [6] for solar selective coatings [7] and in ion-selective electrode membranes [8]. Various approaches have been investigated to produce finely divided silver sulfide nanoparticles [9,10]. However, synthesis of monodispersed Ag_2S nanoparticles is difficult due to the fact that Ag_2S particles have a strong tendency to agglomerate to form clusters [11].

In view of the potential applications of Ag_2S in PEC, several methods have been employed to grow silver sulfide particles with diverse morphologies and sizes [12], such as nanowires [13,14], nanocrystals, and faceted and cubic silver sulfide nanocrystals [15,16]. Several single-source molecular precursors based methods involving pyrolysis in refluxing trioctylphosphine [17], or in alkylamine solvents under solvothermal [18] or refluxing conditions have been investigated to form the Ag_2S powders. Thin films of silver sulfide have also been prepared by chemical bath deposition [19,20], spray pyrolysis [21], thermal evaporation [22], successive sol–gel ionic layer adsorption and reaction (SILAR) [23], molecular beam epitaxy [24] and by electrochemical ion-exchange processes [25]. These deposition techniques do however suffer from multiple drawbacks such as poor conformality, low throughput, restricted directional variation and low compositional control. Several of these problems can be overcome by using aerosol assisted chemical vapor deposition (AACVD) technique. This method only requires the precursor to be soluble in any solvent suitable for aerosol generation. The precursor is dissolved in a solvent and an aerosol of the solution is generated

* Corresponding author. Tel.: +60 3 79674269.
E-mail address: mazhar42pk@yahoo.com (M. Mazhar).

0040-6090/$ – see front matter © 2013 Elsevier B.V. All rights reserved.
http://dx.doi.org/10.1016/j.tsf.2013.03.092

Thin Solid Films 540 (2013) 1–9

Contents lists available at SciVerse ScienceDirect

Thin Solid Films

journal homepage: www.elsevier.com/locate/tsf

Surface morphological and photoelectrochemical studies of ZnS thin films developed from single source precursors by aerosol assisted chemical vapour deposition

Muhammad Ali Ehsan [a], T.A. Nirmal Peiris [b], K.G. Upul Wijayantha [b], Hamid Khaledi [a], Huang Nay Ming [c], Misni Misran [a], Zainudin Arifin [a], Muhammad Mazhar [a,*]

[a] Faculty of Science, Department of Chemistry, University of Malaya, Lembah Pantai, 50603 Kuala Lumpur, Malaysia
[b] Department of Chemistry, Loughborough University, Loughborough, LE11 3TU, UK
[c] Faculty of Science, Department of Physics, University of Malaya, Lembah Pantai, 50603 Kuala Lumpur, Malaysia

ARTICLE INFO

Article history:
Received 1 August 2012
Received in revised form 15 May 2013
Accepted 27 May 2013
Available online 11 June 2013

Keywords:
Zinc sulphide
Thin films
Single source
Band gap
Photoelectrochemical

ABSTRACT

Zinc sulphide (ZnS) thin films have been deposited on fluorine-doped tin oxide-coated conducting glass substrates at 375, 425 and 475 °C temperatures from single source adduct precursors [$Zn(S_2CNCy_2)_2(py)$] (**1**) [where, Cy = cyclohexyl, py = pyridine] and [$Zn\{S_2CN(CH_2Ph)(Me)\}_2(py)$] (**2**) [where, Ph = Phenyl, Me = Methyl] using aerosol assisted chemical vapour deposition (AACVD). The precursor complexes have been characterized by microanalysis, infrared spectroscopy, proton nuclear magnetic resonance spectroscopy, X-ray single crystal and thermogravimetric analysis. Thermal analysis showed that both precursors (**1**) and (**2**) undergo thermal decomposition at 375 °C to produce ZnS residues. The deposited ZnS films have been characterized by X-ray diffraction and energy dispersive X-ray spectroscopy. Scanning electron microscopic studies indicated that the surface morphology of ZnS films strongly depends on the nature of the precursor and the deposition temperature, regardless of marginal variation in thermal stability of the precursors. Direct band gap energies of 3.36 and 3.40 eV have been estimated from the ultraviolet–visible spectroscopy for the ZnS films fabricated from precursors (**1**) and (**2**), respectively. The current–voltage characteristics recorded under air mass 1.5 illumination confirmed that the deposited ZnS thin films are photoactive under anodic bias conditions. Furthermore, the photoelectrochemical (PEC) results indicate that these synthesised single source precursors are suitable for obtaining ZnS thin films by AACVD method. The ZnS thin film electrode prepared in this study are very promising for solar energy conversion and optoelectronic applications. The PEC properties of ZnS electrodes prepared from (**2**) are superior to that of the ZnS electrode prepared from precursor (**1**).

1. Introduction

Nanocrystalline zinc sulphide (ZnS) thin films have found applications in wide range of areas such as electronic and optoelectronic industry, photovoltaic cells, optical sensors, lasers, infrared windows, electroluminescent and photoluminescent devices, antireflection coatings, reflectors and interference filters and displays [1–3]. Diverse thin film deposition techniques [4–6] have been applied to develop ZnS thin films. Such methods have their inherent advantages and disadvantages. From a commercial and technological view point, many of these techniques entitle to high operating cost and often require complicated operational steps and instrumentations with less guarantee of high reproducibility. Therefore, extensive studies have been focused to study other routes which may produce high quality ZnS thin films at low cost in a reproducible manner.

The requirements for deposition of ZnS films for many applications are very stringent and require particular crystalline phases, stoichiometric elemental composition, desirable microstructure and film uniformity. It may be achieved by thermal decomposition of single source precursor compounds through appropriate metal ligand design which are easy to handle, low toxic and able to be purified to high levels through crystallization [7,8]. Hence, numerous classes of precursor complexes including dialkyldithiocarbamates [9,10], alkyl xanthates [11,12], dichalcogenophosphinate [13], dialkylthiocarbamtes and monothiocarboxylates [14], thio- and dithio-biuret [15] have been synthesized and employed to deposit ZnS thin films using chemical vapour deposition (CVD) based techniques. *Bis*(diethyldithiocarbamato) zinc(II) [$Zn(S_2CNEt_2)_2$] was the first precursor compound employed for the deposition of ZnS by low-pressure chemical vapour deposition technique and the deposited films were not of good quality. Later, the same precursor was used to make ZnS thin films by using organometallic

* Corresponding author. Tel.: +60 3 79674269, +60 162796040 (mobile); fax: +60 3 79674193.
E-mail address: mazhar42pk@yahoo.com (M. Mazhar).

0040-6090/$ – see front matter © 2013 Elsevier B.V. All rights reserved.
http://dx.doi.org/10.1016/j.tsf.2013.05.117

Full Paper

Applied Organometallic Chemistry

Received: 19 April 2012 Revised: 7 May 2012 Accepted: 21 May 2012 Published online in Wiley Online Library

(wileyonlinelibrary.com) DOI 10.1002/aoc.2893

Cobalt titanate–cobalt oxide composite thin films deposited from heterobimetallic precursor

Muhammad Ali Ehsan[a], Muhammad Adil Mansoor[a], Muhammad Mazhar[a]*, Asif Ali Tahir[b], Mazhar Hamid[c] and K. G. Upul Wijayantha[b]

A single molecular heterobimetallic complex, $[Co_2Ti(\mu_3\text{-}O)(TFA)_6(THF)_3]$ (1) [TFA = trifluoroacetate, THF = tetrahydrofuran], was synthesized, structurally and spectroscopically characterized and implemented as a single-source precursor for the preparation of $CoTiO_3$–CoO composite thin films by aerosol-assisted chemical vapour deposition (AACVD). The precursor complex was prepared by interaction of $Co(OAc)_2.4H_2O$ [OAc = (CH_3COO^-)] with Ti(iso-propoxide)$_4$ in the presence of trifluoroacetic acid in THF, and was analysed by melting point, CHN, FT-IR, single-crystal X-ray diffraction and thermogravimetric analysis. The precursor complex thermally decomposed at 480 °C to give a residual mass corresponding to a $CoTiO_3$–CoO composite material. Good-quality crystalline $CoTiO_3$–CoO composite thin films deposited at 500 °C by AACVD and characterized through powder X-ray diffraction and scanning electron microscopy/energy-dispersive X-ray spectroscopy show that the crystallites have a rose-flower-like morphology with an average petal size in the range of 2–6 μm. Copyright © 2012 John Wiley & Sons, Ltd.

Keywords: cobalt titanate–cobalt oxide; polynuclear bimetallic complex; composite; thin films

Introduction

High-purity titanates are sought for dye-sensitized solar cells[1,2] as photocatalysts for water splitting to hydrogen and oxygen, degradation of air pollutants,[3] for self-cleaning and energy efficient windows,[4] gas sensors[5] and photoluminescent materials.[6] Ferromagnetic cobalt titanium oxide systems[7–10] have been investigated as materials for dynamic random access memory,[11] as dilute magnetic semiconductors and dilute magnetic dielectrics[12] and for metal oxide semiconductor field-effect transistors. Cobalt titanium-based oxides systems are also employed as catalysts, e.g. in hydrogenation processes, Fisher–Tropsch reactions[13] and the oxidative dehydrogenation of ethane.[14] Cobalt titanate ($CoTiO_3$) is used in the preparation of magnetic, ferroelectric nano-composite materials and nano-particulate gas sensors. Particularly, cobalt titanate plays an important role in the production of semiconductor devices, since with this oxide it is possible to manufacture thin films with a very high κ-constant.[15,16] The growing interest of researchers in $CoTiO_3$ materials is also due to a series of its physiochemical properties permitting its application as pigments, magnetic recording media[17] and gas sensors for alcohol, as humidity sensors and as catalysts.[18]

Cobalt titanium oxide powders have been prepared via different synthetic routes, such as conventional solid-state reactions between fine powders,[19] sol–gel processes,[20] stearic acid gel methods,[21] aerogel approaches,[22] the Pechini process,[23] co-precipitation of mixed metal oxalates[24] and micelle solution methods.[25] These methods generally involve mechanical mixing of oxides and/or carbonates followed by heating cycles, calcination and ball milling for extended periods. This often yields inhomogeneous mixtures with only low control over the stoichiometry, appearance of undesirable phases, abnormal grain growth and poor reproducibility. Fabrication of thin films from these powders is often a formidable task, usually requiring high temperatures and some kind of sophisticated equipment. When using low-melting materials as the substrate the high processing temperatures not only affect the quality of the thin films, but the thermal stability of the substrate also becomes a problem. To overcome these challenges associated with the fabrication of ceramic thin films we focused our work on the design and synthesis of soluble single-phase precursor materials that are capable of delivering all the components of the target material to a substrate in the required ratio, where they then can be decomposed under mild conditions to form the desired thin films. Aerosol-assisted chemical vapour deposition (AACVD) is a versatile technique ideally suited for this purpose. Its only requisite is for the precursor to be soluble in a suitable solvent, and the resulting solution can then be used to fabricate multi-component material layers while at the same time ensuring both reproducibility and stoichiometry in the deposited layer(s). Moreover, high-quality thin films can be obtained by AACVD as the homogeneity of the aerosol depends on the size of the aerosol droplets, which can be controlled through the frequency of the ultrasonic generator. In continuation of our previous work[26–28] and taking advantage of carboxylate ligand which coordinates

* *Correspondence to: Muhammad Mazhar, Department of Chemistry, Faculty of Science, University of Malaya, Lembah Pantai, 50603 Kuala Lumpur, Malaysia. E-mail: mazhar42pk@yahoo.com*

a *Department of Chemistry, Faculty of Science, University of Malaya, Lembah Pantai, 50603 Kuala Lumpur, Malaysia*

b *Department of Chemistry, Loughborough University, Loughborough LE11 3TU, UK*

c *Department of Chemistry, Quaid-I-Azam University, Islamabad 45320, Pakistan*

Chemical Vapor Deposition

DOI: 10.1002/cvde.201206988

Full Paper

Effect of AACVD Processing Parameters on the Growth of Greenockite (CdS) Thin Films using a Single-Source Cadmium Precursor**

By *Muhammad Ali Ehsan*, *Huang Nay Ming*, *Misni Misran*, *Zainudin Arifin*, *Edward R. T. Tiekink*, *Ahmad P. Safwan*, *Mehdi Ebadi*, *Wan J. Basirun*, and *Muhammad Mazhar**

Greenockite (CdS) nanostructured thin films are deposited on soda and FTO conducting glass substrates by aerosol-assisted (AA)CVD using a single-source precursor bis-(*N*,*N*-dicylcohexyldithiocarbamato)(pyridine)cadmium(II), $Cd[S_2CNCy_2]_2$.py (**1**), in pyridine, toluene, and THF solutions in the temperature range 350–450 °C. The precursor **1**, characterized by physicochemical methods, undergoes facile thermal decomposition at 350 °C to give a stable residual mass of CdS. The thin films deposited from pyridine solution, and characterized by X-ray diffraction (XRD), UV-vis spectroscopy, field-emission scanning electron microscopy (FESEM), and energy dispersive X-ray (EDX) techniques, exhibit a band gap of 2.4 eV and a photocurrent density of 1.3 mA cm^{-2} at 0.4 V versus Ag/AgCl/3M KCl, suggesting their suitability for application in photo-electrochemical (PEC) cells.

Keywords: Cadmium, Nanostructures, S-ligand, Thin films

1. Introduction

Cadmium sulfide (CdS) is probably the most investigated photoelectrode material, after TiO_2, because of its particular band gap of 2.4 eV[1] that enables the harvesting of most of the photons in the solar spectrum. Having met most of the stringent requirements for the ideal photocatalyst,[2] CdS however undergoes photo-corrosion and suffers from instability upon prolonged irradiation,[3] which mitigates its utility as a photoelectrode in photo-electrochemical water-splitting devices. Nevertheless, CdS still has many potential applications in optoelectronic materials, solar cells and photo-detectors, optical filters, multilayer light emitting diodes, flat panel display photodiodes, phototransistors, and window-layered heterojunction solar cells.[4,5] In view of the aforementioned applications, the investigation of new methods for the fabrication of nanoparticles, nanowires, and nanorods of CdS has been extensively conducted in recent years.[6,7] Several studies on the deposition of CdS thin films have been reported, including by electrodeposition,[8] chemical bath deposition,[9] spray pyrolysis techniques,[10] CVD,[11] vacuum evaporation methods,[12] and sputtering.[13] Since all of these methods suffer from high production costs, and often require complicated operations and instrumentation, work continues to explore more facile routes for the fabrication of CdS nanocrystallite thin films at low cost and in scalable ways.

The trend of using hazardous metal alkyls and H_2S for metal sulfide synthesis[14] is being replaced with a single-source molecular precursor approach because of potential advantages.[15] Various cadmium compounds have been reported as single-source precursors for the fabrication of thin films from CVD techniques, but later proved problematic because of their volatility, lack of stoichiometric control, and poor crystallinity of the target material.[15] One of the reasons for the volatility problem is that cadmium chalcogenides usually exist as high molecular weight polymeric complexes in which the metal centre is bridged by the chalcogenolato ligands to give pseudo-tetrahedral coordination at the metal ion,[16] thereby decreasing their value as precursors for metal-organic (MO)CVD applications. As a result, as observed in the past, most investigations on the formation of CdS thin films were made by low-pressure CVD using classes of cadmium molecular pre-

[*] Prof. M. Mazhar, M. A. Ehsan, Dr. M. Misran, Dr. Z. Arifin, Dr. E. R. T. Tiekink, A. P. Safwan, Dr. M. Ebadi, Dr. W. J. Basirun
Department of Chemistry, Faculty of Science,
University of Malaya Lembah Pantai,
50603 Kuala Lumpur (Malaysia)
E-mail: mazhar42pk@yahoo.com

Dr. H. N. Ming
Department of Physics, Faculty of Science,
University of Malaya Lembah Pantai,
50603 Kuala Lumpur (Malaysia)

Dr. M. Ebadi
Department of Chemistry,
Faculty of Sciences,
Islamic Azad University- Gorgan
Branch Gorgan (Iran)

[**] The Ministry of Higher Education (Malaysia) and the University of Malaya are thanked for funding this research through the High-Impact Research scheme (Grant numbers UM.C/625/1/HIR-C/035 and UM.C/HIR/MOHE/SC/03) and through the UMRG scheme (Grant number RG097/10AET).

Inorganica Chimica Acta 376 (2011) 189–194

Contents lists available at ScienceDirect

Inorganica Chimica Acta

journal homepage: www.elsevier.com/locate/ica

Deposition of iron titanate/titania ceramic composite thin films from a single molecular precursor

Muhammad Ali Ehsan [b], Asif Ali Tahir [c], Mazhar Hamid [a], Muhammad Mazhar [b,*], K.G. Upul Wijayantha [c], Matthias Zeller [d]

[a] Department of Chemistry, Quaid-I-Azam University, Islamabad 45320, Pakistan
[b] Department of Chemistry, Faculty of Science, University of Malaya, Lembah Pantai, 50603 Kuala Lumpur, Malaysia
[c] Department of Chemistry, Loughborough University, Loughborough LE11 3TU, UK
[d] Department of Chemistry, Youngstown State University, 1 University Plaza, Youngstown, OH 44555-3663, USA

ARTICLE INFO

Article history:
Received 22 December 2010
Received in revised form 23 May 2011
Accepted 8 June 2011
Available online 24 June 2011

Keywords:
Heterobimetallic precursor
AACVD
Fe_2TiO_5
TiO_2
Composite
Thin film

ABSTRACT

A heterobimetallic single molecular precursor, $[Fe_2Ti_4(\mu\text{-}O)_6(TFA)_8(THF)_6]$ (1) [TFA = trifluoroacetate, THF = tetrahydrofuran], was synthesized by the simple reaction of $[Fe_3O(OAc)_6(H_2O)_3]NO_3{\cdot}4H_2O$ [OAc = acetato] with tetrakis(2-ethoxyethanalato)titanium(IV) in the presence of trifluoroacetic acid in THF. The synthesized precursor was analyzed by melting point, CHN analysis, FTIR, single crystal X-ray diffraction and thermogravimetric analysis. Complex (1) crystallizes in the orthorhombic space group $Pca2_1$ with cell dimensions $a = 19.2114(14)$, $b = 20.4804(15)$ and $c = 17.2504(12)$ Å, and the complex undergoes thermal decomposition at 490 °C to give a residual mass corresponding to an Fe_2TiO_5–TiO_2 composite mixture. The synthesized precursor was utilized for deposition of Fe_2TiO_5–TiO_2 composite thin films by aerosol-assisted chemical vapor deposition (AACVD) on glass substrates at 500 °C using argon as the carrier gas. Scanning electron microscopy (SEM), energy dispersive X-ray (EDX) and X-ray powder diffraction (XRD) analyses of the thin films suggest the formation of good quality crystalline thin films of an Fe_2TiO_5–TiO_2 composite with an average grain size of 0.105–0.120 μm.

1. Introduction

Mixed metal oxide composites and their applications have become an important research theme due to their unique magnetic, electrical, optical, and catalytic properties, which are distinctly different from those of pure bulk oxides [1]. Mixed metal oxides composites involving transition metals also have extensive applications as catalysts because of their unique textural and acid–base characteristics, which often lead to enhanced catalytic activities as compared with corresponding pure and supported oxide analogues [2].

The iron–titanium oxide composites, for example, have wide applications in the fields of magnetic semiconductors [3], magneto-optical semiconductors [4], and especially in catalysis [5,6], such as photocatalytic degradation of organic pollutants, photoelectrochemical water splitting [7,8], catalytic isomerization [9], and catalytic oxidation [10,11]. Fe_2TiO_5–TiO_2 has been found to possess unique catalytic activity in several reactions such as the oxidation of cyclohexane [2], α-pinene oxide isomerization [9], *o*-cresol photo-degradation and methanol oxidation [10]. Pure iron titanates are commonly known in three different forms, as the minerals ilmenite ($FeTiO_3$), pseudo-brookite (Fe_2TiO_5) and ulvospinel (Fe_2TiO_4), and which of the three is formed largely depends on the preparation method, composition of the precursor, and the calcination temperature [12].

Several methods have been reported for synthesizing iron titanium oxide composites such as wet impregnation [13], hydrolysis freezing [14], hydrothermal [12], co-precipitation [15], sol–gel processes, ultrasound irradiation [16], and chemical vapor deposition [17]. Fe_2TiO_5 has been typically prepared by co-precipitation or sol–gel methods [18,19]. Phani and Santucci [20] have prepared Fe_2TiO_5 from titanium isopropoxide and iron oxalate using a sol–gel technique. Camargo et al. [21] have developed the titanium iron isopropoxide $[FeCl\{Ti_2(OPr^i)_9\}]$ as a single source precursor to prepare an Fe_2TiO_5–TiO_2 composite by the sol–gel route. Using titanium(IV) and iron(III) acetylacetonate, a mixture of anatase and rutile was obtained at 500 °C while pseudo-brookite (Fe_2TiO_5) was formed at temperatures higher than 700 °C [22]. In a more recent study, an aerogel product obtained from titanium(IV) butoxide and iron(III) acetylacetonate also contained pseudo-brookite besides titania [10]. All synthetic procedures for Fe_2TiO_5 powders involve sol–gel acid catalyzed reactions, co-precipitation and/or thermal evaporation drying processes. The resultant powders consist of massive particles with irregular shapes and micron-sized

* Corresponding author.
E-mail addresses: mazhar42pk@yahoo.com (M. Mazhar), u.wijayantha@lboro.ac.uk (K.G.U. Wijayantha).

0020-1693/$ - see front matter © 2011 Elsevier B.V. All rights reserved.
doi:10.1016/j.ica.2011.06.019

5084 *Chem. Mater.* **2010,** *22,* 5084–5092
DOI:10.1021/cm101642b

CHEMISTRY OF MATERIALS
Article

Photoelectrochemical and Photoresponsive Properties of Bi_2S_3 Nanotube and Nanoparticle Thin Films

Asif Ali Tahir,[§] Muhammad Ali Ehsan,[†] Muhammad Mazhar,*[,‡] K. G. Upul Wijayantha,*[,§] Matthias Zeller,[∥] and A. D. Hunter[∥]

[†]*Department of Chemistry, Quaid-I-Azam University, Islamabad-45320, Pakistan,* [‡]*Department of Chemistry, Faculty of Science, University of Malaya, Lembah Pantai, 50603-Kuala Lumpur, Malaysia,* [§]*Department of Chemistry, Loughborough University, Loughborough LE11 3TU, U.K., and* [∥]*STaRBURSTT-Cyberdiffraction Consortium at YSU and Department of Chemistry, Youngstown State University, 1 University Plaza, Youngstown, Ohio 44555-3663*

Received June 12, 2010. Revised Manuscript Received July 15, 2010

Bi_2S_3 nanotubes and nanoparticle in the form of thin films were deposited on fluorine doped SnO_2 (FTO) coated conducting glass substrates by Aerosol Assisted Chemical Vapor Deposition (AACVD) using tris-(*N*,*N*-diethyldithiocarbamato)bismuth(III), $[Bi(S_2CN(C_2H_5)_2)_3]_2$ (**1**) as a precursor. Thin films were deposited from solutions of (**1**) in either chloroform, dichloromethane, or a 1:1 mixture of chloroform and toluene at temperature between 350 to 450 °C and characterized by X-ray diffraction (XRD), UV−vis spectroscopy, field emission gun scanning electron microscopy (FEGSEM), and energy dispersive X-ray (EDX) analysis. FEGSEM images of films deposited from chloroform or dichloromethane exhibit well-defined and evenly distributed nanotubes with an average internal diameter of 40 nm. Films deposited from chloroform/toluene, on the other hand, have compact nanostuctured morphology. Bandgaps of 1.85 and 1.8 eV were estimated for nanotubes and nanoparticles, respectively, by extrapolating the linear part of the Tauc plot recorded for the films. The *n*-type Bi_2S_3 thin films display a reasonable photoactivity under illumination and are thus promising candidates for photoelectrochemical applications. The photoelectrochemical characteristics recorded under AM 1.5 illumination indicated photocurrent density of 1.9 mA/cm^2 and 1.0 mA/cm^2 at 0.23 V versus Ag/AgCl/3 M KCl for the films deposited from chloroform and chloroform/toluene, respectively. The photocurrent is among the highest reported for any Bi_2S_3 photoelectrode to date. Repeated illumination cycles show that the Bi_2S_3 thin films display a reasonable photosensitivity and response indicating their potential to be used in photodetector and optoelectronic nanodevice applications.

Introduction

Starting with the first discovery of carbon nanotubes, inorganic one-dimensional (1D) nanostructures have been at the center of attention in many areas of research from fundamental sciences to industrial systems engineering. Initial interest was targeted on the intrinsic properties of these fascinating material structures, however, the recent focus is aimed at their unusual physical and chemical properties as well as possible applications.[1,2] Inorganic nanostructures have shown great potential and applications are in the research and development of nanodevices.[3] Nanotubes and nanowires, for example, possess several different areas of contact (borders, inner and outer surfaces, and structured tube walls) that in principle can be functionalized in several ways such as by using of nanorods, tubes, and wires as, for example, nanoscale host materials.[4,5]

Binary metal chalcogenides $A_2^{V}B_3^{VI}$ (A = As, Sb, Bi; B = S, Se, Te) have drawn extensive attention as they are an important class of semiconductors that are already used in numerous technological components as, for example, photoconducting targets, electronic and optoelectronic devices,[6] thermoelectric devices,[7] hydrogen storage materials,[8,9] and sensors.[10] For application in photoelectrochemical (PEC) solar cells, the photoelectrode material should have appropriate band energetics, so that it can

*To whom correspondence should be addressed. E-mail: u.wijayantha@lboro.ac.uk (K.G.U.W.), mazhar42pk@yahoo.com (M.M.).

(1) Remškar, M. *Adv. Mater.* **2004,** *16,* 1497–1504.
(2) Patzke, G. R.; Krumeich, F.; Nesper, R. *Angew. Chem., Int. Ed.* **2002,** *41,* 2446–2461.
(3) Hu, J.; Odom, T. W.; Lieber, C. M. *Acc. Chem. Res.* **1999,** *32,* 435–445.
(4) Bao, H.; Li, C. M. X.; Cui; Song, Q.; Yang, H.; Guo, J. *Nanotechnology* **2008,** *19,* 335302.
(5) Bao, H.; Li, C. M.; Cui, X.; Gan, Y.; Song, Q.; Guo, J. *Small* **2008,** *4,* 1125–1129.
(6) Suarez, R.; Nair, P. K.; Kamat, P. V. *Langmuir* **1998,** *14,* 3236–3241.
(7) Chen, B. X.; Uher, C.; Iordanidis, L.; Kanatzidis, M. G. *Chem. Mater.* **1997,** *9,* 1655–1658.
(8) Li, L.; Sun, N.; Huang, Y.; Qin, Y.; Zhao, N.; Gao, J.; Li, M.; Zhou, H.; Qi, L. *Adv. Funct. Mater.* **2008,** *18,* 1194–1201.
(9) Zhang, B.; Ye, X.; Hou, W.; Zhao, Y.; Xei, Y. *J. Phys. Chem. B* **2006,** *110,* 8978–8985.
(10) Grigas, J.; Talik, E.; Lazauskas, V. *Phys. Status Solidi B* **2002,** *232,* 220–230.

Published on Web 08/09/2010